DEVELOPMENT OF X-RAY ABSORPTION DIAGNOSTICS FOR GAS-PHASE REACTING FLOWS

A DISSERTATION
SUBMITTED TO THE DEPARTMENT OF MECHANICAL ENGINEERING
AND THE COMMITTEE ON GRADUATE STUDIES
OF STANFORD UNIVERSITY
IN PARTIAL FULFILLMENT OF THE REQUIREMENTS
FOR THE DEGREE OF
DOCTOR OF PHILOSOPHY

Jared Alexander Dunnmon
September 2017

This dissertation is online at: http://purl.stanford.edu/fk069hr3117

I certify that I have read this dissertation and that, in my opinion, it is fully adequate in scope and quality as a dissertation for the degree of Doctor of Philosophy.

Matthias Ihme, Primary Adviser

I certify that I have read this dissertation and that, in my opinion, it is fully adequate in scope and quality as a dissertation for the degree of Doctor of Philosophy.

Craig Bowman

I certify that I have read this dissertation and that, in my opinion, it is fully adequate in scope and quality as a dissertation for the degree of Doctor of Philosophy.

John Eaton

I certify that I have read this dissertation and that, in my opinion, it is fully adequate in scope and quality as a dissertation for the degree of Doctor of Philosophy.

Norbert Pelc

Approved for the Stanford University Committee on Graduate Studies.

Patricia J. Gumport, Vice Provost for Graduate Education

This signature page was generated electronically upon submission of this dissertation in electronic format. An original signed hard copy of the signature page is on file in University Archives.

Abstract

Accurate experimental measurements are critical to the design and understanding of efficient combustion systems. While new heterogeneous combustion technologies such as Porous Media Burners (PMBs) have demonstrated favorable combustion properties including an extended lean flammability limit, low emissions, and wide dynamic power range, they also pose challenges for traditional experimental techniques. Because combustion occurs within a porous ceramic matrix, physical probes can disturb the combustion environment while engineering optical access becomes difficult. Further, data provided by existing methods is generally of insufficient spatial dimensionality to fully describe complex internal PMB physics. In this context, the development of new diagnostics that can provide measurements of relevant physical quantities non-intrusively, without optical access, and with high spatial resolution becomes a challenge in creating experimental datasets that improve fundamental physical understanding of PMB systems.

In this work, a diagnostic for gas-phase reacting flows is developed based on the principles of X-ray computed Tomography (XCT) at clinical energies, and applied to three different systems of interest. Clinical fan-beam XCT is first applied to a turbulent gas-phase krypton jet, and it is shown that X-ray attenuation measurements can resolve krypton mole fraction within the jet in three dimensions with high quantitative accuracy.

A cone-beam X-ray system is then used to image a krypton-diluted, premixed Bunsen flame via XCT. Simultaneous data series describing visual emission and X-ray attenuation are performed, and scanner noise trends are evaluated via both experiment and simulation. Comparison of experimental data to an axisymmetric simulation with detailed chemistry is demonstrative of both the utility and phenomenology of the X-ray attenuation signal as a density surrogate in reacting flow measurements. Effects of the krypton contrast agent on

important combustion quantities such as flame speed and temperature are also evaluated.

Finally, measurements of a porous media burner are performed with cone-beam XCT, and theory is developed to relate X-ray attenuation to gas-phase temperature. Using this method, experiments are performed to demonstrate temperature measurement of a krypton-diluted flame within the optically opaque porous ceramic matrix of the PMB. Temperature measurements in the gas phase are contrasted with direct thermocouple measurements, and the effect of imaging artifacts and experimental uncertainties is analyzed in detail.

Acknowledgments

I would like to acknowledge the generous financial support from the National Aeronautics and Space Administration under its Leading Edge Aeronautics Research for NASA (LEARN) program, as well as the contributions of our partners at Bosch and Alzeta Corporation. I was also supported by the National Defense Science and Engineering Graduate (NDSEG) Fellowship program.

The work presented in this thesis could not have been accomplished without the guidance, support, and engagement from many individuals. Firstly, I would like to express my sincere gratitude to my advisor, Prof. Matthias Ihme, who has supported me throughout my doctoral work and contributed greatly to the contents of this thesis. I would also like to extend my thanks to a number of collaborators, including Sadaf Sobhani, Dr. Yee Chee See, Dr. Meng Wu, Dr. Waldo Hinshaw, and Dr. Tae Wook Kim. Particular thanks are also extended to Dr. Chris Elkins, Prof. John Eaton and Prof. Tom Bowman in Mechanical Engineering; Prof. Anthony Kovscek in Energy Resources Engineering; Prof. Rebecca Fahrig and Prof. Norbert Pelc in Radiology; and Dave Bartz and Bret Haley from Alzeta corporation.

I would also like to acknowledge the support of Lakhbir Johal in the Thermosciences Machine Shop and Rika Bosmans, Rosa Fernandez, Corinne Beck, and Susan Dorman in Flow Physics and Computational Engineering in contributing to this research.

Last, but not least, words do not exist to adequately express my thanks for the way in which my father Preston, mother Kara, and brother Evan have supported me throughout the PhD – I could not have asked for a more generous, a more good natured, or a more loving family.

Nomenclature

Variables

α	Thermal diffusivity	m^2/s
$\mathcal{D}$	Diffusion coefficient	m^2/s
δ	Dirac delta function	-
ε	Porosity	-
γ	Ratio of specific heats	-
γ	X-ray spectrum density function	-
κ	Spatial frequency	1/m
λ	Thermal conductivity	W/m-K
$\mathcal{F}_\alpha(q)\{\psi\}$	α-dim. Fourier transform of ψ w.r.t. q	-
μ	Linear attenuation coefficient	cm^{-1}
ν	Kinematic viscosity	m^2/s
Φ	Equivalence ratio	-
ϕ	Scan angle	rad
ρ	Density	kg/m^3
σ	Standard deviation	-
τ	Timescale	s
θ	Schlieren deflection	rad
$\underline{e}_i$	Unit vector in i direction	-
ξ	Mass attenuation coefficient	cm^2/g
ζ	Jet buoyancy parameter	-
a	Mean Planck absorption coefficient	$m^{-1}Pa^{-1}$
B_l	Spatial bandlimit	1/m

D	Diameter	m
D	Source-to-axis distance	m
d	Source-to-detector distance	m
E	X-ray energy	eV
Fr	Froude number	-
g	Gravitational acceleration	m/s^2
g	X-ray projection	-
H_R	Apodization filter	-
h_R	Impulse response of apodization filter	-
I	Intensity	$Photons/m^2$
I_T	Tube current	A
K	Detector spacing	m
L	Integral length scale	m
l	Coordinate parallel to source plane	m
M	Measurement vector	-
M	Number of projections	-
n	Number of samples	-
N_s	Number of species	-
N_{ph}	Number of photons	-
P	Pressure	Pa
Q	Volumetric flow rate	m^3/s
r	Radial coordinate	m
R_u	Universal Gas constant	8.314 J/mol-K
Re	Reynolds number	-
s	Coordinate perpendicular to source plane	-
s	Uncertainty parameter	-
S_L^0	Unstretched laminar flame speed	m/s
SE	Standard error	-
T	Temperature	K
U	Uncertainty vector	-
u	Axial velocity	m/s

W	Molar mass	g/mol
w	Pixel width	m
X	Mole fraction	-
x, y, z	Cartesian coordinate system	m
Y	Mass fraction	-

Accents, Subscripts, and Operators

0	X-ray source location
$\bar{\cdot}$	Spectral average
$\hat{\cdot}$	Fourier transform
∞	Far-field condition
$\langle \cdot \rangle$	Arithmetic average
$\tilde{\cdot}$	Fluctuating quantity
Air	Air background
C	Centerline
d	X-ray detector location
E	Turbulent Eddy
g	Gas phase
M	Mixture
$Meas$	Measured data quantity
o	Jet orifice condition
T	Turbulent
u	Unburned gas

Contents

List of Tables

List of Figures

Chapter 1

Introduction

1.1 Motivation and Objectives

As global energy consumption continues to increase with growing population and larger average energy intensities, efficient and fuel-flexible energy generation technologies will be required to sustain the world economy. While emerging technologies such as solar photovoltaics, wind turbines, and modern nuclear energy reactors hold promise in addressing these needs, combustion-based systems are expected to provide a substantial portion of global energy through the next century (Department of Energy, 2017).

In light of this reality, the development of novel combustion methodologies that reduce pollutants, increase power density, and enable fuel flexibility would represent an important step towards energy sustainability. A promising technology that has the potential to accomplish these goals is the Porous Media Burner (PMB), which facilitates combustion of a gas mixture within the voids of a solid matrix, thereby resulting in chemical and physical characteristics different than those observed in conventional, gas-phase combustion systems. The flame is actually stabilized inside the porous material, where the superior thermal conductivity and radiation properties of the solid compared to those of the gas mixture alone result in higher consumption rates and enhanced heat transfer, leading to lower nitrogen oxide (NO_x) emissions and higher power densities at ultra-lean conditions (Wood and Harris, 2008). Specifically, internal heat recirculation resultant from radiation and conduction driven the solid phase enables a regime known as “excess

enthalpy combustion," wherein preheated reactants allow for increased flame speeds while removal of heat from the reaction and post-flame zones decreases thermal NO_x production (Hardesty and Weinberg, 1973). Furthermore, the large interfacial surface area of the porous matrix and its high heat capacity provide enhanced combustion stability in a manner that could enable both enhanced operating range and fuel-flexible operation (Trimis and Durst, 1996). Due to these favorable properties, interest in porous media combustion technology has continued to advance. PMBs can serve as a more efficient, robust, and environmentally friendly alternative for a wide variety of current combustion systems, including surface heaters, domestic heating units, afterburners in solid oxide fuel cells, and potentially even gas turbines (Mujeebu et al., 2009; Noordally et al., 2004).

While understanding of porous media combustion has improved over recent decades to the point that several designs have been suggested for PMBs, we still lack an adequate fundamental understanding of detailed physical processes and internal flame structure inside the porous media. Current experimental methods are primarily hindered by the opaque solid structure obscuring the flame region (Bedoya et al., 2015; Stelzner et al., 2015). To address these challenges, the goal of this work is to develop an experimental diagnostic technique based on X-ray Computed Tomography (XCT) at clinical energies that enables interrogation of the heterogeneous combustion processes within optically inaccessible PMBs.

We pursue this objective by exploring the development of XCT diagnostics for gas-phase flows using lab-scale sources in three separate applications:

Nonreacting Scalar Mixing

We first utilize a turbulent jet configuration to demonstrate and evaluate the ability of a clinical scanner to extract mixing field data describing a radiodense contrast agent in a dynamic flowfield at inert conditions.

Free Flame Combustion

The second stage of this work focuses on assessing both the ability of X-ray absorption techniques to image combustion phenomena, as well as the expected effect of radiodense gaseous contrast agent on the combustion process. This requires modification of an existing X-ray facility to contain a rotating combustion device as well as thorough facility

characterization in the context of low-contrast objects.

Porous Media Combustion

In the context of porous media combustion, a realistic combustor system that is compatible with the X-ray diagnostic system must be designed and operated. The third portion of this work aims to demonstrate the viability of obtaining non-intrusive 3-D measurements of contrast agent number density that can be related to gas temperature. This task requires careful materials characterization, development of experimental and postprocessing procedures, and quantitative consideration of important aspects of lab-scale XCT reconstruction such as beam hardening artifact mitigation and signal-to-noise ratio improvement.

1.2 Review of Related Diagnostics

In the following section, we contextualize the present work by briefly outlining the state of current gas-phase diagnostics for scalar mixing, free-flame combustion, and porous media combustion with an emphasis on creating 3-D field data.

1.2.1 Scalar Mixing

Measurements of scalar mixing in fluid mechanics have become an important tool in understanding the structure of a wide variety of flow phenomena. In particular, scalar concentration measurements in turbulent gas-phase shear flows have yielded both quantitative and qualitative information that has significantly enhanced fundamental understanding of the underlying flow physics. While common methods such as Schlieren imaging (Crow and Champagne, 1971; Meier, 2002), Rayleigh scattering (Dowling and Dimotakis, 1990; Pitts, 1991; Richards and Pitts, 1993; Su et al., 2010), Raman scattering (Birch et al., 1978), and Planar Laser-Induced Fluorescence (PLIF) (Hiller and Hanson, 1988) yield pointwise, one-dimensional, or two-dimensional results, advances in interrogation of flow-field complexity have lent increased importance to the development of three-dimensional measurement techniques.

Current options for three-dimensional visualization of scalar quantities are limited, and most of these are based on various types of optical tomography. Optical tomographic methods were first proposed by Stuck (1977) and Byer and Shepp (1979) for determining

spatial concentration of air pollutants via tomographic reconstruction of laser absorption data. In the nearly 40 years since, methods such as holographic interferometry (Feng et al., 2002; Snyder and Hesselink, 1988; Watt and Vest, 1990), laser absorption (Bennett and Byer, 1984; Lavinskaya et al., 2006; Mohamad et al., 2006; Santoro and Semerjian, 1981; Wright et al., 2006), chemiluminescence (Floyd et al., 2011), and rainbow Schlieren (Agrawal et al., 1997) have all been used in combination with tomographic reconstruction algorithms to yield three-dimensional scalar field data, usually describing species concentrations, in gas-phase applications.

While optical tomographic methods have performed well in many situations, there exist a wide variety of optically inaccessible flow geometries for which they would not be applicable. The general approach to this problem has been attempting to artificially design optical access ports into experimental and industrial environments with varying levels of success (Mohamad et al., 2006; Wright et al., 2006). Further, many experimental setups contain equipment that for practical or cost reasons restricts either view number or available view angles, each of which requires the use of limited-view reconstruction algorithms that are not always as accurate as those used in the high-view limit (Hsieh, 2009; Lavinskaya et al., 2006). Reported work in areas of tomographic chemiluminescence, tomographic Particle Image Velocimetry (PIV), and tomographic measurement of species concentration have, for instance, used camera numbers ranging from 4 to 50 cameras (Elsinga et al., 2006; Floyd et al., 2011; Wright et al., 2006). In an ideal case, one would be able to obtain quantitative data for scalar quantities in optically inaccessible gas-phase flow environments without resorting to such limited-view techniques.

1.2.2 Free Flame Combustion

Optical diagnostics have also been critical to the development of modern combustion science. What originally began as visual observation of flames eventually gave rise to modern methods based on quantitative laser and chemiluminescence techniques that have improved understanding of combustion processes by providing non-intrusive assessments of flame structure (Kohse-Höinghaus et al., 2005). While even visual inspection of chemiluminescence yields insight into phenomena including flame topology and sooting,

for instance, methods such as Schlieren imaging have enabled direct visualization of gradients and curvature in the density field of reacting flows (Andrews and Bradley, 1972; Law, 1989). More recently, laser diagnostics such as Raman scattering, Rayleigh scattering, and various types of PLIF have provided insight into gas-phase combustion via measurements of both composition and temperature (Blevins et al., 1999; Bouvet et al., 2011; Hassel and Linow, 2000; Hiller and Hanson, 1988; Kohse-Höinghaus et al., 2005; Law, 2010). Phenomenologically, Raman and Rayleigh scattering respectively rely on the inelastic and elastic scattering of monochromatic light as it passes through a gas with multiple species. Because Rayleigh scattering is temperature dependent while Raman scattering is composition-dependent, combined Rayleigh-Raman measurements are a preferred method for simultaneous measurement of multiple major species and temperature data (Hassel and Linow, 2000). PLIF, on the other hand, is generally used when a single species is of particular interest, and relies on targeted excitation of a particular molecule by laser photons at common spatial resolutions on the order of 10^{-4} m, laser pulse lengths on the order of 10^{-8} s, and imaging repetition rates on the order of 10^{-4} s (Böhm et al., 2009; Kohse-Höinghaus et al., 2005; Shimura et al., 2011). More recently, techniques such as Coherent Anti-Stokes Raman spectroscopy have also been used to simultaneously measure temperature (with $\pm$ 50 K) and concentration in larger volumes with pollution by particles, but at the cost of decreased spatial resolution on the order of 10^{-3} m (Hassel and Linow, 2000). In addition to the continuing evolution of laser-based techniques, an enhanced understanding of chemical kinetics has enabled the use of detailed chemiluminescence signals to be used for combustion control and measurement of species concentrations such as CH^*, OH^*, and CO^*, even in harsh gas turbine environments (Petersen et al., 2012). Each of these non-intrusive diagnostic capabilities is particularly useful in modern combustion environments, wherein intrusive techniques such as hot wire anemometry, thermocouple measurements, and exhaust gas chromatography can affect behavior of the experimental system while being subject to uncertainties due to high temperature, radiation loss, catalysis, and inadequate quenching (Heitor and Moreira, 1993). While probe-based measurements will likely always remain an important part of combustion science, the ability to measure important quantities without disturbing the combustion environment has enabled significant advances in our

understanding of these phenomena.

1.2.3 Porous Media Combustion

Porous media combustion represents a difficult diagnostic environment for common techniques used in free-flame combustion because the flame is contained within a porous ceramic matrix that does not admit physical or optical access. Common methods for obtaining data include temperature measurements from thermocouples and analysis of exhaust gas composition (Brenner et al., 2000; Liu and Hsieh, 2004; Smucker and Ellzey, 2004). Such measurement techniques continue to be quite successful in characterizing a variety of important aspects of PMB operation and design, including pollutant formation, fuel flexibility, reaction zone thickness, and response to wide variation in operating conditions (Al-Hamamre et al., 2009; Keramiotis et al., 2012; Voss et al., 2013). Engineered access for optical techniques such as CARS (Kiefer et al., 2009) and PLIF (Stelzner et al., 2015) has also been successful in obtaining useful data describing temperature and concentration inside operating PMB. However, none of these techniques existing techniques can produce 3-D field data, and all require some combination of painstaking design or substantial modification to the combustion system itself.

1.3 X-ray Diagnostics in Fluid Mechanics

A potential avenue for creating 3-D field data for optically inaccessible gas-phase fluid mechanics emplacements such as PMBs that remains sparsely explored involves the consideration of lab-scale X-ray Computed Tomography (XCT) systems. These devices were fundamentally designed to volumetrically image internal structures through an optically opaque outer shell, and similar systems have already been successfully utilized to measure mean flow structures in the context of fuel sprays and multiphase flows (Chaouki et al., 1997; Coletti et al., 2014; Duke et al., 2017; Eberhart et al., 2013; Escudero and Heindel, 2014; Linne, 2013; Schumaker et al., 2014). X-ray absorption techniques are particularly useful in this context due to the fact that dense fluids tend to strongly scatter common optical signals (Kastengren et al., 2012; Sick and Stojkovic, 2001). The recent work of Heindel (2011) provides a detailed overview of applications of X-ray absorption diagnostics to multiphase flows, with an emphasis on tomographic

methods.

While the same principle could be applied to optically inaccessible gas-phase flow phenomena, the major reason that lab-scale XCT systems are not generally used to study dynamic gas-phase flow phenomena is that gases are effectively transparent to photons at commonly used lab-scale X-ray energies, rendering X-ray absorption measurements impractical for most gases using these systems. In contrast, soft X-rays from low-energy coherent synchrotron radiation represent a more typical source for X-ray measurements of gas-phase phenomena. The work of Kastengren and Powell (2014) highlights the potential advantages of synchrotron sources over lab-scale X-ray sources in providing bright, monochromatic beams. However, synchrotron sources generally have small fields of view and are not usually not designed for use in three-dimensional tomographic techniques, making laboratory-scale sources preferable for demonstrating the application of XCT to gas-phase flows. In particular, broad-spectrum lab-scale sources do not require raster scanning by a point source as a synchrotron would, and are more easily adapted to house fluid delivery apparati (Halls et al., 2014). According to Meyer et al. (2010), even the most rudimentary tomographic acquisition using a synchrotron source would take on the order of 45 minutes.

Soft X-ray fluorescence techniques represent another class of methods that have been investigated for such applications as visualization of turbulent gas-phase mixing, and are effective even with weakly absorbing samples (Duke et al., 2016; Kastengren et al., 2011). X-ray fluorescence involves exciting an element with X-rays higher than a particular ionization energy appropriate for enabling re-emission of characteristic radiation in the X-ray spectrum. As described in the review of Kastengren and Powell (2014), this technique also requires a specialized low-energy synchrotron source, is generally characterized by low emitted photon counts, and requires complex system modeling to account for re-absorption of emitted photons (Schumaker et al., 2015). Thus, X-ray fluorescence, while useful for spectroscopy or tracking fluid streams containing different tracer molecules, is generally not used in three-dimensional tomographic applications.

As far as combustion environments are concerned, the most familiar applications of X-ray techniques have focused on hard X-ray absorption measurements for applications including shock characterization in high-pressure environments (MacPhee et al., 2002),

understanding liquid fuel atomization in spray injection (Schumaker et al., 2012; Som and Aggarwal, 2010), monitoring in-situ reaction front progress within rock formations (Hasçakir et al., 2011), and detecting soot or particles (Peña et al., 2016). Recent work has also seen the demonstration of soft X-ray diagnostics as a method for spectroscopy of gas-phase flames. The work of Frank et al. (2014), for instance, demonstrated the ability of low-energy, high-flux synchrotron radiation to interrogate a free flame at very low pressure. While Frank et al. (2014) successfully demonstrate the use of soft X-ray diagnostics for flame spectroscopy, however, a facility-scale synchrotron source was required, and low pressures were necessary to ensure that the low-energy X-rays were not attenuated by gas surrounding the subject of interest. Finally, X-ray fluorescence has recently been applied to a combustion system – Schumaker et al. (2015), for instance, utilized a low-energy synchrotron source (7-15 keV) to map density within an axisymmetric coaxial jet flame via X-ray fluorescence, but were unable to obtain a tomographic dataset using this technique.

1.4 Accomplishments

The work presented here has resulted in the following accomplishments:

1. Demonstration of the viability of lab-scale X-ray absorption techniques for measurement of scalar concentration and mixing in dynamic gas-phase flowfields.

2. Development of theory relating X-ray attenuation values and noise quantities to gas-phase variables such as temperature, pressure, and composition.

3. Application of X-ray absorption tomography to map the density field of a gas-phase free flame.

4. Development of facility design, PMB modifications, experimental procedures, and postprocessing techniques to enable lab-scale X-ray diagnostics of gas-phase porous media combustion.

5. Demonstration that XCT can non-intrusively yield 3-D internal PMB attenuation fields that can be related to an inferred internal temperature field.

6. Assessment and mitigation of reconstruction artifacts to enable quantitative interpretation of gas-phase XCT data.

Chapter 2

X-ray Computed Tomography (XCT): Theory, Systems, and Practical Considerations

2.1 Fundamentals of X-ray Attenuation

X-ray absorption diagnostics are enabled by the fact that X-ray photons are attenuated when they interact with matter. The difference between the X-ray diagnostics under consideration here and the laser diagnostics often used in gas-phase flows is that X-ray photons interact with both outer and core electrons via mechanisms including Rayleigh scattering, the photoelectric effect, and Compton scattering, whereas laser diagnostics are dominated by scattering interactions with valence electrons (Bushberg et al., 2011). In general, the interaction between X-ray photons and an object scanned with a polychromatic X-ray beam follows the Beer-Lambert law (Hsieh, 2009),

$$I_d = I_0 \int \gamma(E) e^{-\int \mu(E,s) ds} dE \tag{2.1.1}$$

where I_0 is the incident X-ray intensity, I_d is the detected X-ray intensity, s is the path length through the object, E is the photon energy, γ is the spectral distribution function, and μ is the linear attenuation coefficient of the object. In X-ray Computed Tomography (XCT) measurements, the value reconstructed is approximately the effective monoenergetic

attenuation $\bar{\mu}$, defined such that,

$$e^{-\int \bar{\mu}(s)ds} = \int \gamma(E) e^{-\int \mu(E,s)ds} dE, \tag{2.1.2}$$

where the effective energy $\bar{E}$ is the energy at which the attenuation is $\bar{\mu}$ – this value can be computed via interpolation from known attenuation data Wu et al. (2016). Thus, combining Eqs. 2.1.1 and 2.1.2, the integrated effective attenuation can be directly obtained from projection measurements as (Hsieh, 2009),

$$\int \bar{\mu}(s)ds = -\ln\left(\frac{I_d}{I_0}\right), \tag{2.1.3}$$

We will refer to values obtained at the effective photon energy $\bar{E}$ throughout this manuscript with an overbar. XCT measurements allow for reconstruction of the effective attenuation field $\bar{\mu}$ in three spatial dimensions from a set of projections taken over a large number of angles (Macovski, 1983). The linear attenuation coefficient may be expressed in terms of the mass attenuation coefficient ξ and the density ρ of the material (Macovski, 1983),

$$\mu = \xi\rho, \tag{2.1.4}$$

where ξ is a nonlinear function of the photon energy that varies with material composition. Note that ξ is an atomic quantity that increases with electron density while decreasing with E, and can be determined via measurements of both μ and ρ at reference conditions.

2.2 XCT Theory and Reconstruction Techniques

2.2.1 Filtered Backprojection for 2-D CT

X-ray computed tomography refers to the process of reconstructing an n-dimensional field function from its X-ray absorption projections in $n-1$ dimensions. The following summary of the mathematics behind the reconstruction process closely tracks the presentation in the textbook ofMacovski (1983). In the 2-D case, the 1-D projection function $g(l,\phi)$ can be written in terms of ϕ, the angle between the horizontal and the source-detector axis, and l,

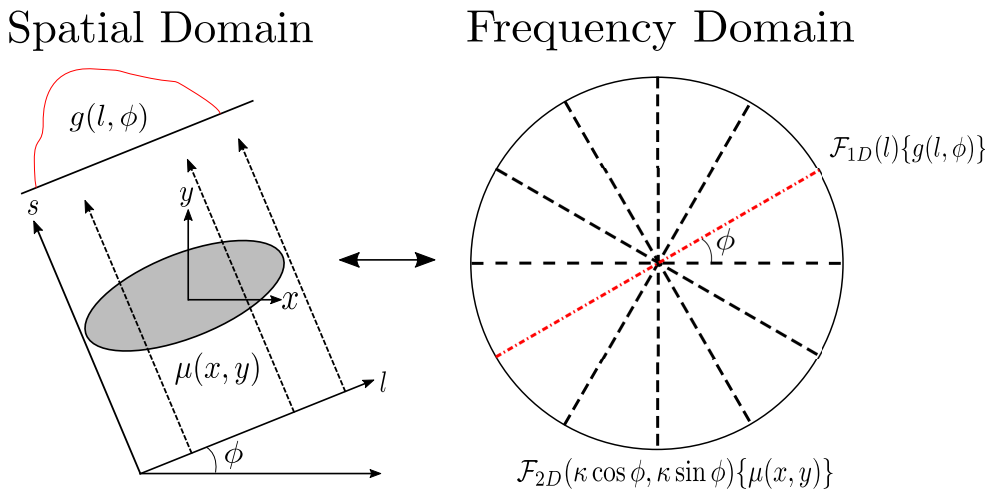

Figure 2.1: Graphical illustration of the projection-slice theorem (Hsieh, 2009)

the coordinate parallel to the detector plane (Prince and Links, 2006),

$$g(l,\phi) = \int \mu(s(\phi,l))\mathrm{d}s. \tag{2.2.5}$$

To implement the XCT imaging procedure, a source-detector assembly is, for instance, rotated around the object and the projection function is sampled at a collection of angles that depends on the scanner geometry (Macovski, 1983). The sinogram representing $g(l,\phi)$ can then be defined as the Radon transform of the attenuation field function $\mu(x,y)$ (Macovski, 1983),

$$g(l,\phi) = \iint \mu(x,y)\delta(x\cos\phi + y\sin\phi - l)\mathrm{d}x\mathrm{d}y, \tag{2.2.6}$$

where δ is the Dirac delta function, x is the horizontal in-plane coordinate, and y is the vertical in-plane coordinate as shown in Fig. 2.1. Note that Eq. (2.2.6) represents the expression appropriate for a simple, monoenergetic, parallel-beam geometry, and that extension to the polyenergetic case requires only replacement of μ with $\bar{\mu}$ in each expression. While this derivation will be presented in a parallel-beam context for mathematical simplicity, scanners used in this work generally use either a fan-beam or a cone-beam geometry, which give similar, but more complex expressions found in, for instance, the textbook of Hsieh (2009).

The inverse Radon transform required to reconstruct $\mu(x,y)$ from $g(l,\phi)$ relies on the

projection-slice theorem to relate $g(l,\phi)$ and $\mu(x,y)$ in the following manner in terms of $\hat{G}(\kappa,\phi)$, the one-dimensional Fourier transform of the projection function with respect to l, and the spatial frequency κ (Macovski, 1983; Prince and Links, 2006),

$$\begin{aligned}
\hat{G}(\kappa,\phi) &= \mathcal{F}_{1D}(l)\{g(l,\phi)\}, \\
&= \int g(l,\phi)e^{-2i\pi\kappa l}\mathrm{d}l, \\
&= \iiint \mu(x,y)\delta(x\cos\phi + y\sin\phi - l)e^{-2i\pi\kappa l}\mathrm{d}x\mathrm{d}y\mathrm{d}l, \\
&= \iint \mu(x,y)e^{-2i\pi\kappa(x\cos\phi+y\sin\phi)}\mathrm{d}x\mathrm{d}y, \\
&= \mathcal{F}_{2D}(\kappa\cos\phi,\kappa\sin\phi)\{\mu(x,y)\}. \qquad (2.2.7)
\end{aligned}$$

Figure 2.1 illustrates this relation graphically. Thus, the attenuation field can be directly written as,

$$\mu(x,y) = \mathcal{F}_{2D}^{-1}(\kappa\cos\phi,\kappa\sin\phi)[\mathcal{F}_{1D}(l)\{g(l,\phi)\}]. \qquad (2.2.8)$$

In many 2-D XCT applications, the inverse Radon transform required to compute μ from g using Eq. (2.2.7) is implemented via a Filtered Backprojection (FBP) method that takes advantage of the projection-slice theorem to express the reconstructed field $\mu(x,y)$ as (Macovski, 1983; Prince and Links, 2006),

$$\mu(x,y) = \int_0^{\pi}\int_{-\infty}^{\infty} H_R(\kappa)\hat{G}(\kappa,\phi)e^{2i\pi\kappa l}\mathrm{d}\kappa\mathrm{d}\phi\big|_{l=x\cos\phi+y\sin\phi}, \qquad (2.2.9)$$

where the spectral apodization filter $H_R(\kappa)$ is introduced to ensure proper relative weighting of signals with low and high spatial frequencies (Hsieh, 2009). It is common to multiply the ramp kernel $H_R = |\kappa|$ that results from theoretical analysis with a filter that accounts for the spatial bandlimit of a physical detector (Hsieh, 2009). For example, the Hamming filter is often used such that H_R can be written as,

$$H_R(\kappa) = |\kappa|\left[0.54 + 0.46\cos\left(\frac{2\pi\kappa}{\kappa_{\max}}\right)\right],\ \kappa < \kappa_{\max}. \qquad (2.2.10)$$

In physical space, Eq. 2.2.9 can be expressed as (Hsieh, 2009),

$$\mu(x,y) = \int_0^{\pi} \int_{-\infty}^{\infty} g(l',\phi) h_R(l-l') dl' d\phi, \tag{2.2.11}$$

where h_R is the inverse Fourier transform of the spatial apodization filter $H_R(\kappa)$. In practice, the backprojection operator is generally applied to each projection individually and the backprojections at all sampled values of ϕ are summed to give the reconstructed attenuation field. Thus, the implementation process for Eq. 2.2.9 involves evaluation of $\mathcal{F}_{1D}[g(l,\phi)]$ at each ϕ to obtain $\hat{G}(\kappa,\phi)$, filtering of $\hat{G}(\kappa,\phi)$ in Fourier space with H_R for each ϕ, evaluation of the inverse Fourier transform to obtain the filtered projection for each ϕ, backprojection of the filtered projection at each ϕ, and summation of the filtered backprojections over ϕ to numerically evaluate the azimuthal integral. As usual, backprojection involves painting the entire ray path with the measured projection intensity, as the distribution of the attenuation along the ray path is unknown a priori (Hsieh, 2009). This FBP reconstruction technique is often utilized due to its analytic robustness and computational efficiency (Hsieh, 2009). Further details on the implementation of FBP can be found in the standard texts of Macovski (1983) or Hsieh (2009). When a 2-D scanner is used, three-dimensional images can be formed by stacking multiple two-dimensional slices taken in succession.

2.2.2 FBP Algorithm for Fan-Beam CT

The standard derivation of the fan-beam reconstruction algorithm for equiangular spacing presented in such textbooks as Hsieh (2009) utilizes substitution of the variables (l,ϕ) with (γ,β) in Eq. (2.2.11), with γ the angle formed between a given ray and the iso-ray (the ray connecting the source with the center of the detector) and β the projection angle. Note that to relate fan-beam and cone-beam sampling, the identity $\phi = \beta + \gamma$ must hold. Performing a standard set of algebraic substitutions and manipulations to account for the fan-beam geometry allows for the specification of the fan-beam version of the FBP algorithm as

(Hsieh, 2009),

$$\mu(x,y) = \int_0^{2\pi} \int_{-\gamma_m}^{\gamma_m} L^{-2} g(\gamma,\beta) h_R''(\gamma'-\gamma) D\cos\gamma d\gamma d\beta, \tag{2.2.12}$$

$$h_R''(\gamma) = \frac{1}{2}\left(\frac{\gamma}{\sin\gamma}\right)^2 h_R(\gamma), \tag{2.2.13}$$

where L is the distance between the X-ray source and the point of reconstruction, D is the source-to-axis distance, and γ_m is the maximum γ beyond which projection values are zero. The derivation of Eq. (2.2.12) is presented in detail in Appendix A.1.

2.2.3 Feldkamp-Davis-Kress Algorithm for Cone-Beam CT

The Feldkamp-Davis-Kress (FDK) reconstruction method originally derived by Feldkamp et al. (1984) represents a natural extension of the 2-D FBP method to a cone-beam geometry with flat panel detector, demonstrated in Fig. 2.2 (Hsieh, 2009). Additional analysis is provided by Hu (1996), Grass et al. (2000), and Zhu et al. (2008). The key result for the reconstructed value of $\mu(x,y,z)$ with respect to the coordinate system defined in Fig. 2.2 can be written as,

$$\mu(x,y,z) = \frac{1}{2}\int_0^{2\pi} \left(\frac{D}{x+D}\right)_\beta^2 g_F\left(\left(\frac{Dy}{x+D}\right)_\beta, \left(\frac{Dz}{x+D}\right)_\beta, \beta\right) d\beta \tag{2.2.14}$$

$$g_F(u,v,\beta) = \int_{-\infty}^{\infty} \frac{D}{\sqrt{u'^2+v^2+D^2}} g_v(u',v,\beta) h_R(u-u') du' \tag{2.2.15}$$

$$g_v(u,v,\beta) = g\left(u\frac{d}{D}, v\frac{d}{D}, \beta\right) \tag{2.2.16}$$

where D is the source-to-axis distance, d is the source-to-detector distance, β is the scan angle, u and v are detector-plane coordinates, g_F is the filtered and weighted projection set, and g_v represents the projection set at the virtual detector that passes through the axis of rotation (Zhu et al., 2008). The derivation of Eqs. (2.2.14)-(2.2.16) is presented in detail in Appendix A.2.

Importantly, FDK does represent a mathematical approximation in the reconstruction process. Consider, for instance, the situation demonstrated in Fig. 2.2. For a circular source trajectory, the path of point A lies directly in the horizontal plane and is thus exactly

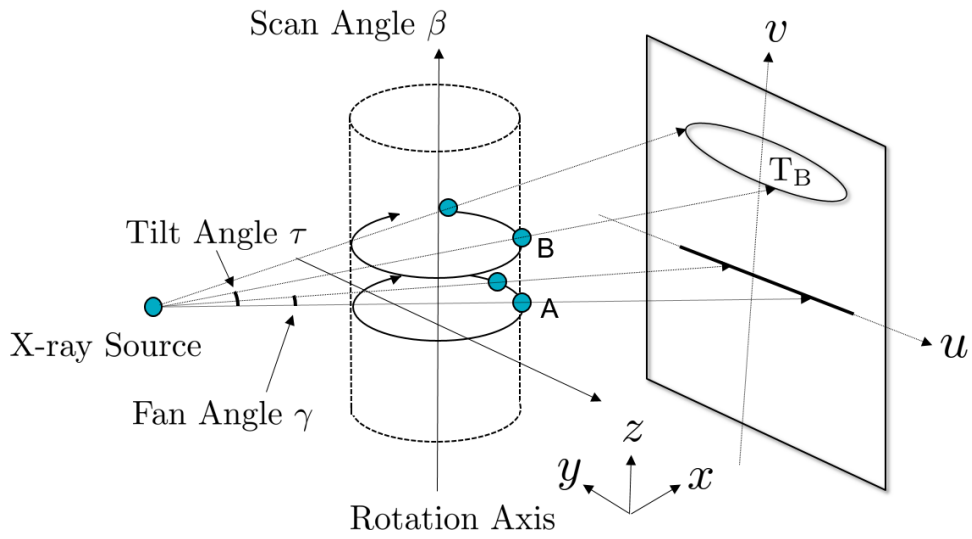

Figure 2.2: Diagram of FDK reconstruction process (Xue et al., 2015).

the same as what would be expected for a 2-D fan-beam measurement, for which FBP is analytically exact. The trajectory of point B, however, forms an ellipse of varying height on the detector, and the row-by-row operation of Eq. (2.2.15) that filters only in the transaxial direction does not accurately describe this geometry. FDK exactness and potential artifacts that may result will be touched upon further in Sec. 2.5.5.

2.3 Application of XCT to Gas-Phase Subjects

2.3.1 Physical Interpretation of Gas-Phase Attenuation

To write the X-ray attenuation expression of Eq. (2.1.4) for a mixture of gases, we can utilize the standard attenuation mixture rule to write the mixture attenuation coefficient as (Jackson and Hawkes, 1981; Macovski, 1983; Thompson and Vaughan, 2005),

$$\bar{\mu} = \rho \sum_{j=1}^{N_s} \bar{\xi}_j Y_j, \tag{2.3.17}$$

with Y_j the mass fraction of component j, N_s the number of components in the mixture, and the overbar indicates the effective energy as described in the discussion around Eq. (2.1.3). Rewriting the mass fraction $Y_j = \rho_j/\rho$ in terms of a partial density ρ_j and invoking the

ideal gas law gives,

$$\bar{\mu} = \sum_{j=1}^{N} \bar{\xi}_j \rho_j = \frac{P}{R_u T} \sum_{j=1}^{N} \bar{\xi}_j X_j W_j = \eta \sum_{j=1}^{N_s} \bar{\xi}_j X_j W_j, \tag{2.3.18}$$

taking P as pressure, T as temperature, W_j as the molar mass of species j, R_u as the universal gas constant, η as the overall number density, and X_j as the mole fraction of species j.

In the case of a radiodense gaseous contrast agent such as krypton combined with low-$\bar{\xi}$ gases, one may treat Eq. (2.3.18) as the combination of attenuation from the gaseous contrast agent and from the balance of the system. In this case, one may extend Eq. (2.3.18) to yield the following simple expression for gas attenuation in terms of material parameters and thermophysical state variables,

$$\Delta\bar{\mu} = \frac{P W_{Kr} X_{Kr} \bar{\xi}_{Kr}}{R_u T}, \tag{2.3.19}$$

where $\Delta\bar{\mu} = \bar{\mu}_M - \bar{\mu}_B$, $\bar{\mu}_B$ is the attenuation measured in a background scan (with only non-attenuating species in the burner), and $\bar{\mu}_M$ is the attenuation of a krypton-augmented gas mixture. Because atomically light gases such as combustion products and ambient air effectively do not attenuate X-rays at clinical energies, the $\bar{\mu}_B$ value is a good measurement of the appropriate signal to be subtracted to isolate the attenuation resultant from the radiodense gaesous contrast agent (Dunnmon et al., 2015).

Importantly, one may further extend Eq. (2.3.19) to yield the following simple expression for gas temperature in terms of known and measured quantities,

$$T = \frac{P W_{Kr} X_{Kr} \bar{\xi}_{Kr}}{R_u \Delta\bar{\mu}}. \tag{2.3.20}$$

We will use this relation in Chap. 5 to demonstrate the utility of XCT in providing measurements that can be related to gas-phase temperature in a straightforward manner.

2.3.2 Static Noise Relation for Gas-Phase XCT

In addition to relating the attenuation signal to key state variables, for application of this technique to combustion systems, it is critical to understand how SNR is affected by various physical parameters. The analysis of Macovski (1983) yields the following relation for SNR of XCT data obtained in a non-attenuating background medium such as air,

$$SNR = \frac{\Delta\bar{\mu}}{\sigma_\mu} \propto \Delta\bar{\mu}\sqrt{N_{ph}M} \propto \Delta\bar{\mu}\sqrt{MI_T w^3 h\tau}, \tag{2.3.21}$$

where σ_μ is the standard deviation of the attenuation measurements, N_{ph} is the average photon count per detector pixel measurement, M is the number of projections contributing to the reconstruction, I_T is the tube current, w is the in-plane resolution, h is the slice thickness, and τ is the exposure time per projection (Hsieh, 2009; Macovski, 1983). Combining Eqs. (2.3.19) and (2.3.21) and assuming that one averages over n different reconstructions to improve SNR yields the following expression relating expected image noise levels to both scan parameters and physical state variables,

$$SNR \propto \frac{PW_{Kr}X_{Kr}\bar{\xi}_{Kr}}{R_u T}\sqrt{MI_T w^3 h\tau n}. \tag{2.3.22}$$

This equation shows that any physical change that increases the number density of krypton atoms in the flow will increase SNR – this includes pressure increases, temperature decreases and krypton mole fraction increases. In addition, increasing tube current, effective pixel size, exposure time, number of reconstructions averaged over, reconstruction slice thickness, and number of projections per reconstruction further increase SNR. Considering the effects of each of these variables on overall measurement quality will be critical in designing effective combustion experiments utilizing XCT diagnostics.

2.4 Overview of XCT Systems

Several different experimental facilities and software packages were used during the course of this work for data acquisition, processing, reconstruction, and analysis. Below we present a detailed description of these tools and facilities.

2.4.1 Hardware Overview

Data obtained for this work was sourced from both clinical fan-beam and tabletop cone-beam scanners. Each of these systems has several characteristic attributes that are worth describing in detail.

Clinical Scanner

The first set of results for gas-phase XCT presented in Sec. 3 utilize a GE HiSpeed CT/i single-slice helical CT scanner housed in the Stanford Earth Sciences department. An image of this scanner can be found in Fig. 2.3. This system has an energy range of 80-120 kVp, where the term "kVp" is standard notation for "kilovolts peak," which determines the maximum energy in keV of photons generated by the X-ray tube (Dunlee) via the standard relation $E = eV$ with e the electron charge and V the tube voltage. The photon beam will realistically have a polyenergetic distribution with the maximum energy value in keV determined by the kVp value of the tube. A tube current of 200 mA was used for all experiments performed in this facility, and reconstruction was performed via 2-D fan-beam filtered backprojection. This fan-beam geometry, wherein axially thin (effectively one-dimensional) projections of adjustable thickness are reconstructed in two dimensions at different positions and then stacked to form a three-dimensional reconstruction, is typical of the simplest clinical 3rd generation XCT geometry (modern clinical XCT scanners have multiple detector rows and produce many images). Note that this scanner is technologically obsolete, meaning that many of the challenges that characterize the measurements presented here may be mitigated in modern machines; the minimum adjustable axial slice thickness of this scanner, for instance, is only 1 mm. In a clinical CT scanner such as this one, all experiments must be able to fit within the source-detector aperture and be robust to bed movement. To perform a scan at several locations, the CT scanner is pre-programmed with a specific bed movement and scan protocol. Bed alignment and scanner control are performed from an outside console, necessitating that any system operated within the CT room during scanning be designed with remote controls and safeguards. Rapid "scout" procedures allow for precise positioning of experimental apparati on the CT bed, and inbuilt laser sights enable precise alignment along multiple axes. Scan time for each axial slice was one second.

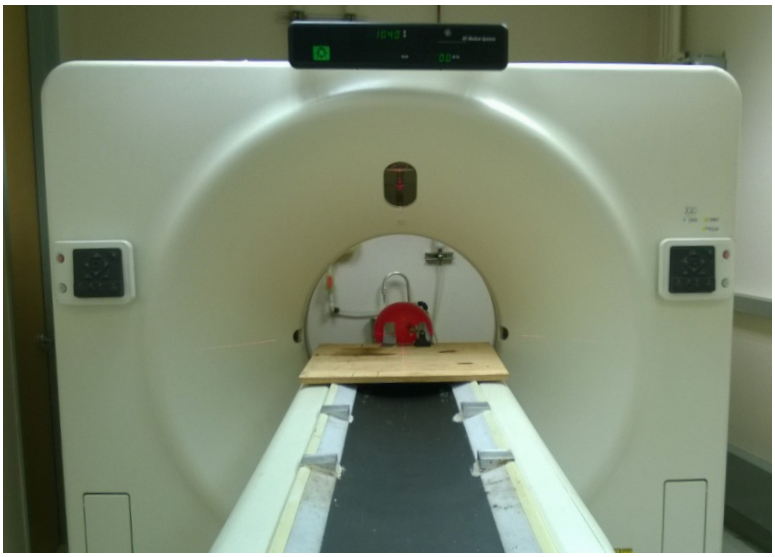

Figure 2.3: GE HiSpeed CT/i scanner with calibration balloon.

Cone Beam Scanner

The second scanner used for this work was the Stanford Tabletop X-ray Facility shown in Fig. 2.4, which contains a fluoroscopic X-ray source, precision rotary table, and flat panel detector with pixel spacing of 0.388 mm. A CPI Indico 100 fluoroscopic X-ray source with energy range $45 - 120$ kVp was utilized along with a Huestis Model 150A collimator. Sample filtered and unfiltered spectra at 60 kVp are presented in Fig. 2.7. X-ray signals were collected at 15 frames per second using a Varian Model 4030B detector with a cesium-iodide scintillator and amorphous silicon type n-i-p photodiodes. As shown in Figure 2.4, the object to be imaged is placed between the source-collimator assembly (left) and detector (right) on a precision rotating table (Parker) to acquire a large number of projections over 360 degrees of rotation. Data from the detector is logged directly on Varian ViVa software, while both gain and offset calibrations must be performed manually during the course of the scan procedure (Hsieh, 2009). Reconstruction requires use of the IsoCal geometry calibration procedure to obtain such metrics as source-to-detector distance and detector offset at sub-millimeter scale. Scans in this facility are performed by initiating motor movement and obtaining X-ray absorption measurements (flat-panel X-ray projections) while the object is spinning at a known

angular velocity within the flat panel field of view. In this way, datasets amenable to tomographic reconstruction can be created.

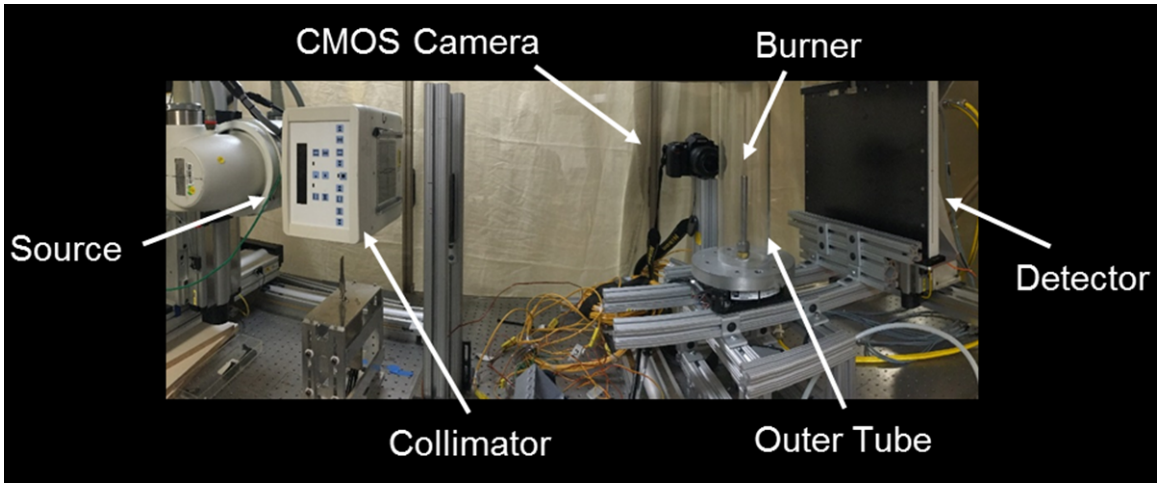

Figure 2.4: Stanford Tabletop X-ray scanner containing Bunsen burner phantom.

The facility as shown in Fig. 2.4 was modified for these experiments to include a instrumentation mount for a camera or thermocouple assembly, thermal radiation shielding, rotating gas-phase flow infrastructure, and a robust exhaust system. The exhaust system consisted of a duct fan rated for 240 LPM attached to a fume hood (Vent-a-Kiln). The flow infrastructure was designed specifically for this facility. An aluminum frame was created to ensure precise motor placement and accessibility, and a specially designed plate was constructed to mate tightly with the motor housing while allowing gas to flow in a well-controlled fashion through a one-inch circular hole in the middle of the motor. Specifically, the center of the aluminum plate was drilled directly through to create a flow pathway, with both top and bottom faces being tapped and threaded to receive male NPT piping; drawings of this apparatus may be found in Fig. C.1 in Appendix C. A flashback arrestor (Superflash), rotary union (DSTI), and connecting tubing were suspended through the motor hole from the female NPT fitting at the bottom of the aluminum plate – in this way, the precision motor could spin the entire flow path in a manner that did not impede or impact field of view. The inlet of the rotary union was connected via a 40 cm section of tubing and series of check valves and junctions to a set of rotameters that controlled gas flow rates originating from compressed gas cylinders. Dual-stage regulators (Prostar)

were used to ensure consistent upstream pressure throughout even long-duration experiments. A piping infrastructure diagram of the flow system can be found in Fig. 2.5, a cross-section schematic of the full apparatus with a porous media burner installed can be found in Fig. 5.13, and detailed design drawings for the flow system and optical table setup can be found in Appendix C.

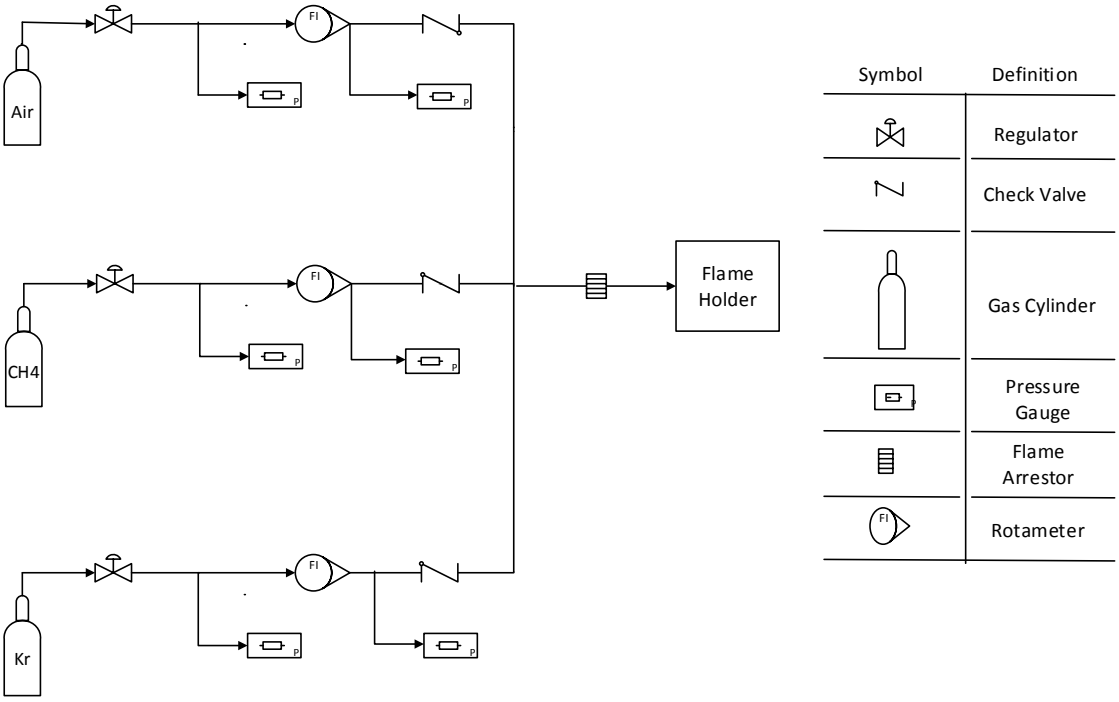

Figure 2.5: Piping infrastructure diagram for Stanford Tabletop X-ray facility flow system.

2.4.2 Software and Deployment

The differences in these systems necessitated the use of different approaches to data acquision, processing, and reconstruction. The GE clinical scanner, for instance, is only capable of outputting reconstructed data as opposed to projection data. The in-house CTAnalyze package supplied by Prof. Anthony Kovscek's group was particularly helpful in postprocessing output from this scanner (output in native DICOM format) such that it would be easily accessible in programs such as MATLAB that could be used for more

intensive quantitative analysis. The Stanford Tabletop X-ray facility, however, represents a much more versatile system. Because projection data are obtained directly from the flat-panel detector, a wide variety of reconstruction techniques, artifact reduction methods, and postprocessing procedures become possible. We employed the CTSim code package developed by the Fahrig Group at Stanford, and most recently maintained by Dr. Meng Wu (Wu et al., 2016).[1]

2.5 Practical Measurement Considerations

A critical aspect of XCT systems is that a combination of hardware limits, physical limits, and image generation complications can cause degradation in the quantitative accuracy of the reconstructed attenuation field. In this section, we detail important points in XCT scanner construction and operation that affect image quality. A thorough treatment of this subject can be found in Hsieh (2009).

2.5.1 Physical System Limitations

Physical limitations in XCT systems play an important role in determining noise levels, resolution, and image uniformity. The source, for instance, generates X-rays via thermally inefficient bombardment of a metal anode (often tungsten) with an electron beam created via thermionic emission from a hot cathode filament (Hsieh, 2009). Emitted electrons are focused onto a small region on the anode target, also known as a "focal spot." Interaction of the electron beam with the atoms in the target enables emission of X-rays from the anode. Over 99% of the energy in the beam directly heats the anode, often above 2500^{o}C, while only 1% of the input energy is converted to X-ray photons (Hsieh, 2009). To avoid melting the tungsten anode, spinning anode disks are generally rotated at high speeds of up to 10,000 RPM, and the outside portion of the disk is manufactured at an angle (often around 7^{o}) such that the impact area of the electron beam can be increased. The effective focal spot can, as a result, be several times larger than the electron beam cross-section, and differential hardening of the emitted X-ray beam can occur as X-rays emitted from different parts of the anode travel through different lengths of tungsten as they exit. This

[1] The CTSim code package has yet to be published; documentation is available upon request from the original author.

phenomenon, known as the "heel effect," can be shown diagrammatically as in Fig. 2.6 (Hsieh, 2009).

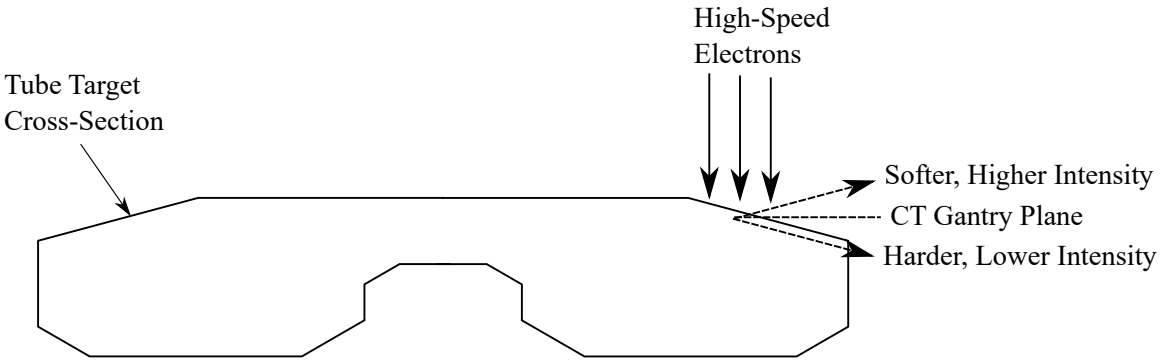

Figure 2.6: Schematic of typical anode (Hsieh, 2009).

As a result of tube heating, the size of the focal spot can change over the course of a measurement, thereby affecting resolution, and scan protocols must be rigorously designed to account for tube cooling requirements. Tube heating specification is generally described in Heat Units (HU) such that,

$$1 \text{ HU} = 0.75 \text{ Joule}, \tag{2.5.23}$$

and tube heating measurements will become important in ensuring repeatable scan protocols for the cone beam scanner of Sec. 2.4.1 in particular. Additionally, as X-ray tubes age, rotor shaft whirl may begin to occur, causing degradation in image quality due to the deviation of the X-ray beam position from that assumed by the reconstruction algorithm.

The X-ray detector is another major system component that must be considered in analyzing overall image quality. All detectors, for instance, are characterized by a dark current of random magnitude that is dependent on time, temperature, and channel number. Consistent channel-to-channel variation in particular can cause a variety of image artifacts described below. This type of variation can be compensated for by an "offset calibration" run before each scan, which computes the offset values for each channel (Hsieh, 2009). Each detector channel is also slightly different from a manufacturing point of view. Thus,

the gain in each detector cell that defines the response magnitude of the cell to impacting X-ray photons is not consistent across channels. To compensate for this type of nonuniformity, a "gain calibration" is often performed by taking several images with no phantom inside the system, and using these flood field images to determine the gain on a channel-by-channel basis (Hsieh, 2009). A new gain calibration must be performed every time scanner conditions change, which includes adjustments to tube voltage, current, collimator settings, and other parameters. A final set of detector characteristics that is of importance to this work is cumulative radiation damage and afterglow, which are observed in flat panel detectors such as that used in the tabletop system. As a scintillator is exposed to radiation over the course of its lifetime, detector gain may vary to the point that there exists significant bias in the reported detector signal. Several such degradation artifacts can be noted in some of the scans performed here, and the avoidance of spurious localized spotting on the detector was considered in experimental design. Further, upon exposure to X-rays, detector output does not immediately return to zero – given that detector elements change response depending on previous exposure levels, if one scans an object and then immediately performs an air scan with no phantom in the system, the outline of the previously scanned object will remain on the detector. Such issues can be adjusted via offset calibration, and must be accounted for in experimental procedures.

2.5.2 System Noise Characteristics

There exist three major contributors to noise in X-ray data acquired on a static subject (Hsieh, 2009):

Quantum Noise

Quantum noise is determined by x-ray flux or the number of X-ray photons detected. This is influenced by two main factors: scanning technique (tube current, voltage, slice thickness, scan speed, etc.), scanner efficiency (detector quantum detection efficiency (QDE), geometric detection efficiency (GDE), etc.), and reconstruction resolution. Scanning technique generally affects the number of photons received at a detector element, which directly influences Signal-to-Noise Ratio (SNR). Increasing the effective photon count received at a detector element is a major effort in our experimental design.

Physical System Noise

The X-ray system itself can introduce various sources of random noise. These include electronic noise in the detector photodiode, electronic noise in the data acquisition system, and scattered radiation that can spuriously impact the detector. While these sources are for the most part a function of the X-ray system itself, it is important to be aware of their potential contributions when analyzing resultant data.

Reconstruction Process

The reconstruction process can also introduce variation into XCT reconstructions. Considerations include reconstruction algorithms, reconstruction parameters, filter kernels, field-of-view and image size. In general, high-resolution kernels produce increased levels of image variation because they preserve or enhance high-frequency content in the projection data.

2.5.3 Beam Hardening Artifacts

Phenomenology

Beam hardening artifacts result from the fact that the various photon energies in a polyenergetic X-ray beams are differentially attenuated by interaction with matter (Hsieh, 2009). Generally, attenuation coefficients for all materials are higher at lower energies, meaning that lower energy X-ray photons are attenuated more strongly than higher energy X-ray photons. Thus, when interacting with an object, the portion of the phantom nearest to the X-ray source encounters a spectrum of lower effective energy, or a "softer" beam, while the portion of the phantom furthest from the X-ray source encounters a higher-energy, or "harder" beam. Importantly, then, each detector channel receives an X-ray spectrum that been hardened differently than that of other channels, as the attenuation field encountered by the beam is spatially dependent. These beam hardening artifacts tend to result in cupping within an image of a cylindrical object, wherein reconstructed attenuation values are lower at the center of an image than at the edges because the beam travels through an increasing amount of attenuative material with decreasing angle from the horizontal (Hsieh, 2009). Beam hardening artifacts can also cause streaks connecting high-density objects, which corrupt the quantitiative accuracy of

the reconstructed attenuation field at specific spatial locations. Finally, beam hardening artifacts are particularly apparent in phantoms with large absolute changes in density or attenuation, meaning that gas-phase portions of an object are much less susceptible to beam hardening than the solid-phase sections. We will describe two important methods for minimizing beam hardening artifacts.

Pre-filtering

The first, and perhaps the simplest, method for mitigating beam hardening artifacts involves pre-hardening the emitted X-ray spectrum with a highly attenuative filter. Common filter materials include aluminum, copper, and other metals. The scanner of Sec. 2.4.1, for instance, contains a 2 mm flat aluminum filter directly after the source. The difference in the expected X-ray spectrum with peak energy of 60 kVp encountered by the phantom as a result of this pre-hardening filter is computed as in Fig. 2.7 using data appropriate for this particular scanner (Wu et al., 2016). Note the substantial decrease in photon density below 20 keV. By hardening the beam in this fashion, the phantom itself is subject to a diminished beam hardening effect.

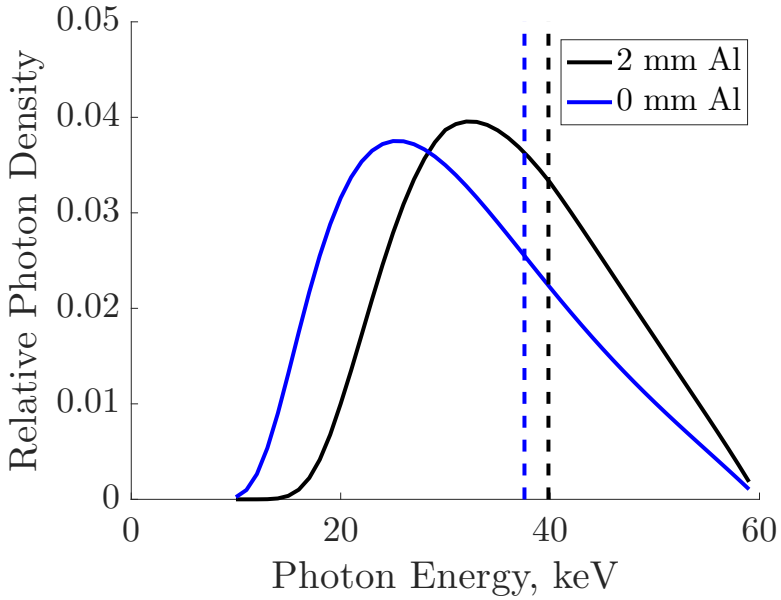

Figure 2.7: Effect of pre-hardening filter. Note that both curves represent normalized PDFs.

Polynomial Beam Hardening Correction

Before reconstructing attenuation data, it is often important to account for the effects of beam hardening directly. Beam hardening fundamentally results from the fact that the monoenergetic and polyenergetic ray sums will be different when a set of heterogeneous materials is in the beamline. This can be observed in the following manner. Following Herman (1979), the monoenergetic ray sum m can be written as,

$$m = \int_0^d (\bar{\mu}_b - \bar{\mu}_a) ds \tag{2.5.24}$$

where μ_a represents the attenuation of the reference (background) material at the effective photon energy $\bar{E}$, μ_b represents the attenuation of the material of interest, and d represents the distance between source and detector. In similar notation, the polyenergetic ray sum p can be written in terms of the spectral distribution function $\gamma(E)$ and photon energy E as,

$$p = -\ln\left\{\int_0^\infty \gamma(E)\exp\left(-\int_0^d [\mu_b(E,s) - \mu_a(E,s)]ds\right)dE\right\}. \tag{2.5.25}$$

In the case where material a and material b both have length of B, Eqs. (2.5.24) and (2.5.25) give:

$$m = B(\bar{\mu}_b - \bar{\mu}_a) \tag{2.5.26}$$

and

$$p = -\ln\left\{\int_0^\infty \gamma(E)\exp\left(-B[\mu_b(E) - \mu_a(E)]\right)dE\right\} \tag{2.5.27}$$

which implies that,

$$p = -\ln\left\{\int_0^{E_{max}} \gamma(E)\exp\left(-\frac{\mu_b(E) - \mu_a(E)}{\bar{\mu}_b - \bar{\mu}_a}m\right)dE\right\}. \tag{2.5.28}$$

Thus, as observed by Herman (1979), it is evident that as long as $\mu_b(E) > \mu_a(E)\ \forall\ E$, the right hand side of Eq. (2.5.28) is monotonically increasing as a function of m. Therefore,

given any value of p, there will be only one value of m that will satisfy Eq. (2.5.28).

While useful in theory, the above approach reflects overly restrictive conditions on the reconstruction volume, as it is obtained assuming only two different materials are contained. However, a more general approach suggested by this analysis is often used in practice to correct for beam hardening—specifically, one may specify a function $f(p)$ of the polyenergetic ray sum such that if $f(p)$ is used to estimate m, a reasonably accurate reconstruction of the spectrally averaged $\bar{\mu}$ field is obtained. Specifying $f(p)$ to be a polynomial function (Hsieh, 2009),

$$f(p) = a_n p^n + a_{n-1} p^{n-1} + ... + a_2 p^2 + a_1 p + a_0, \tag{2.5.29}$$

represents a natural choice due to ease of evaluation and coefficient specification, and beam hardening corrections based on this method have been experimentally validated and are widely utilized in both medical and industrial XCT (Wildenschild and Sheppard, 2013). Note that the constant offset a_0 is often set to zero in such analyses to reflect the fact that zero polyenergetic attenuation must physically imply zero monoenergetic attenuation.

2.5.4 Ring Artifacts

Ring artifacts are caused by consistent errors in a single detector channel (or set of detector channels) across projections. These artifacts are well-known in the clinical XCT literature and can result from a myriad of sources including, but not limited to, local temperature variations, radiation damage, and heterogeneous scintillator thickness (Prell et al., 2009; Sijbers and Postnov, 2004). Such errors will create lines on a sinogram in projection space that will be converted to noticeable rings in reconstruction space during the backprojection process. A variety of methods for addressing ring artifacts exists – notable amongst these are the reconstruction-space filtering approach of Prell et al. (2009), the polar-coordinate line identification strategy of (Sijbers and Postnov, 2004), and rigorous gain and offset calibrations to avoid channel-to-channel variations. In this work, we attempt to minimize ring artifacts via calibration, particularly for results on which quantitative analysis is performed, but do occasionally make use of the Prell et al. (2009) filter in the clinical facility described in Sec. 2.4.1 and the Sijbers and Postnov

(2004) algorithm for data from the tabletop facility described in Sec. 2.4.1. While these methods are well-described in the literature, we will provide a brief summary below.

Ring Correction in Polar Coordinates (RCP) Method

This ring artifact correction of Prell et al. (2009)is based on the concept that median filtration in the radial direction smooths out ring artifacts, but also smooths parts of the image that are uncorrupted. The procedure therefore uses the difference between the reconstructed image and a median-filtered version of the image to create an artifact template that can be subtracted from the original reconstruction. The implementation of this approach in the CTSim code used in this work can be summarized as (Prell et al., 2009; Wu et al., 2016),

1. Transform reconstruction $\mu_{Cart}(x,y)$ to polar coordinates $\mu_{Pol}(r,\phi)$
2. Apply radial median filter M of size $\mathrm{M}_{Rad},\mathrm{M}_{Azi}$ voxels to create the filtered image $\mu_M(r,\phi) = f_{Thresh} * M_{\mathrm{M}_{Rad},\mathrm{M}_{Azi}}$, where M_{Azi} increases with radius to account for increased pixel number at larger radii
3. Compute $\Delta\mu(r,\phi) = \mu(r,\phi) - \mu_M(r,\phi)$ to create an artifact template
4. Threshold $\Delta\mu(r,\phi)$ to values below some constant value T to ensure that true object features are not included in the artifact template $\mu_{Art}(r,\phi) = \Delta\mu(r,\phi)\cdot \mathrm{I}(\mu(r,\phi) < T)$ with I the indicator function
5. Convert the artifact template $\mu_{Art}(r,\phi)$ back to Cartesian coordinates $\mu_{Art}(x,y)$
6. Compute corrected reconstruction $\mu_{Cor}(x,y) = \mu(x,y) - \mu_{Art}(x,y)$

As documented by Prell et al. (2009), this procedure reliably identifies global artifact structures and enables improvement of image quality via direct artifact subtraction.

Method of Sijbers and Postnov (2004)

The artifact correction strategy of Sijbers and Postnov (2004) uses a conceptually similar approach to that of Prell et al. (2009) in that it constructs a global artifact template that can be subtracted from the reconstruction in a manner that does not affect SNR. Major

differences are that that the Sijbers and Postnov (2004) strategy for identifying artifact template relies on a sliding window approach to demarcate spurious lines in the polar domain and that the artifact templates are subtracted in the polar domain. This procedure entails the following steps, and is implemented in this fashion within the CTSim code (Wu et al., 2016),

1. Transform reconstruction $\mu_{Cart}(x,y)$ to polar coordinates $\mu_{Pol}(r,\phi)$
2. Slide a window of size W in the radial direction across the image, and compute the signal variance σ^2 for each row; if $\sigma^2 < T$ for an appropriate threshold value T, append the mean-subtracted value of this row to an artifact matrix $\mathbf{A}_j$ for $j \in [0, J-W]$ with J the number of image voxels in the radial direction
3. Compute the median value for each column in $\mathbf{A}_j$, which results in an artifact template for the window in question; by considering artifact templates from each position of the sliding window, define a global artifact template vector $\mathbf{a}$ that describes all radial locations
4. Subtract the global artifact template vector a of length J from each row i of $\mu(r,\phi)$, creating the corrected reconstruction $\mu_{Cor}(r,\phi)_i = \mu(r,\phi)_i - \mathbf{a}$
5. Convert the corrected reconstruction $\mu_{Cor}(r,\phi)$ back to Cartesian coordinates $\mu_{Cor}(x,y)$

2.5.5 Other Artifacts

In addition to ring and beam hardening artifacts, to which substantial attention is given in this work, there also exist a variety of other artifacts of which practitioners should be aware.

Streaking and Shading

Streaking artifacts refer to sharp lines across a reconstructed image, often caused by an isolated pixel error in a single projection, which are magnified in intensity by the ramp filtering process during backprojection. Shading artifacts describe more diffuse, lower-magnitude errors that can affect entire groups of pixels, causing wider swathes of altered attenuation within an image. In addition to detector inhomogeneity, streaking and

shading can often be caused by X-ray scattering, as photons scattered from different surfaces cause increased or decreased photon counts within a given area. Streaks can also occur in reconstructions of scans that are subtracted in projection space, but contain single projections that are slightly misregistered. Streaks do not appear in any of the data series presented here, and the reader is directed to the textbook of Hsieh (2009) for more detail on such artifacts.

Cone-Beam Artifacts for Circular Trajectories

A variety of artifacts specific to the FDK cone-beam reconstruction algorithm have been reported in the literature. It has, for instance, been theoretically shown that a circular trajectory for cone-beam CT will always result in incomplete reconstruction information (Smith, 1985; Tuy, 1983). In particular, FDK is susceptible to distortions at high-density interfaces (Nagarajappa et al., 2015), inaccuracies at large cone angles (Hu, 1996), and drops in average intensity with axial deviation from the center plane (Zhu et al., 2008). While these artifacts are often mild in practical systems where cone angles are small, it is important to consider them in quantitative analysis of XCT data from cone-beam systems.

Chapter 3

Characterization of Turbulent Mixing via XCT

3.1 Introduction

In this study, we develop a method for measuring scalar fields of a turbulent gaseous jet using widely available clinical XCT technology. Tomographic reconstruction of carefully acquired X-ray attenuation data using inbuilt scanner software yields easily attainable measurements of the mean scalar concentration field in three dimensions with high spatial resolution. The coupling of this high spatial granularity with both rapid scan times and the feasibility of measurements in optically inaccessible environments gives XCT several unique advantages in the context of gas-phase flow diagnostics. Sec. 3.2 will discuss critical aspects of experimental design, calibration, and uncertainty analysis before results are analyzed in Sec.tion 3.3. Finally, Sec. 3.4 will summarize key conclusions and propose future directions for work in gas-phase XCT.

3.2 XCT Diagnostics for Gas-Phase Fluid Phenomena

3.2.1 XCT of a Binary Gas Mixture

In this study, we consider an inert binary mixture containing components 1 and 2 at known pressure and temperature. Rearranging Eq. (2.3.18), writing out the summation for a two-component mixture, and solving for the mole fraction of component 1 in terms of the

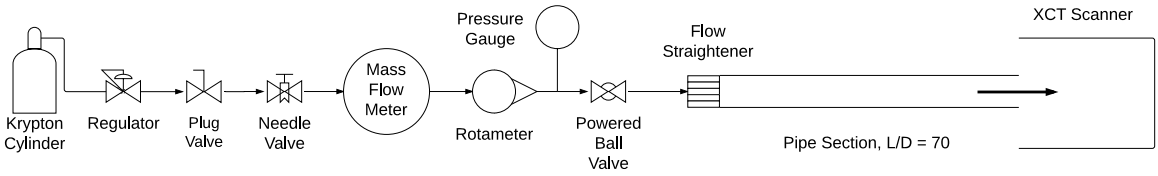

Figure 3.1: Schematic of experimental setup

mixture attenuation $\bar{\mu}_M$ yields,

$$X_1 = \frac{\bar{\mu}_M - \frac{PW_2}{R_u T}\bar{\xi}_2}{\frac{PW_1}{R_u T}\bar{\xi}_1 - \frac{PW_2}{R_u T}\bar{\xi}_2}, \tag{3.2.1}$$

which expresses X_1 in terms of only measured quantities and known physical constants, where XCT measures $\bar{\mu}_M$. Finally, substitution of Eq. (2.3.18) into Eq. (3.2.1) directly relates the mole fraction to the measured attenuation $\bar{\mu}_M$ through the following linear mixing law,

$$X_1 = \frac{\bar{\mu}_M - \bar{\mu}_2}{\bar{\mu}_1 - \bar{\mu}_2}, \tag{3.2.2}$$

where $\bar{\mu}_1$ and $\bar{\mu}_2$ are the measured linear attenuation values of components 1 and 2 at pressure P and temperature T. This result is identical to that of such work as Vega et al. (2014) and Glatz et al. (2016).

3.2.2 Theoretical Implications for Experimental Design

The analytical formulation in Section 3.2.1 could theoretically be applied to measure scalar transport in any number of gas-phase flows if X-ray diagnostic systems were sensitive enough to detect changes in attenuation resultant from variations in the composition or density of any gaseous compound of interest. In reality, however, such diagnostics will be contrast-limited because most ambient gases are effectively transparent to X-rays at energies characteristic of clinical scanners (40-120 keV). Thus, because gas densities will always be orders of magnitude lower than those of solid and liquid phases normally imaged via clinical XCT, it is necessary to utilize a high-ξ gas for gas-phase absorption measurements. In light of this requirement, krypton gas was chosen as the

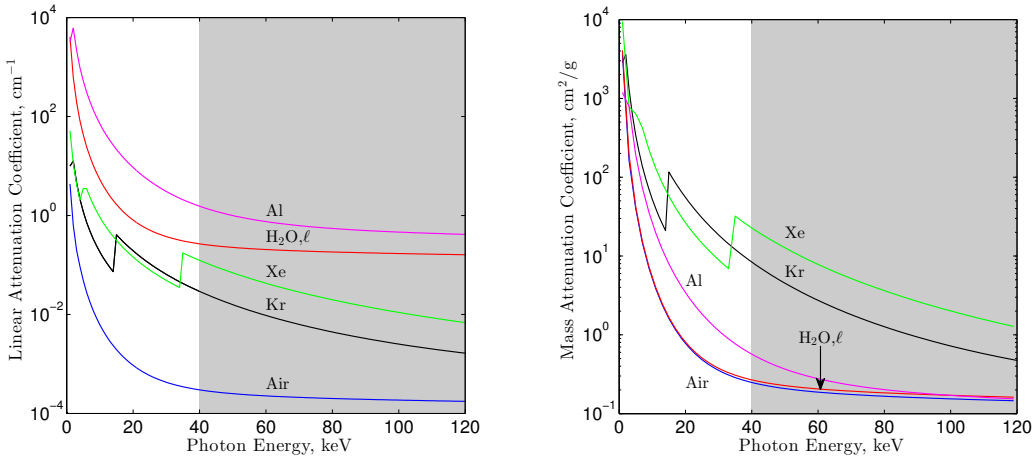

(a) Linear Attenuation Coefficients (b) Mass Attenuation Coefficients

Figure 3.2: Attenuation coefficients of representative materials vs. photon energy; shading shows energy range of clinical XCT.

working fluid for this study due to its high mass attenuation coefficient and relatively low cost. Krypton has previously been used with great success as a contrast agent in XCT studies of pulmonary absorption in the medical field (Chae et al., 2008; Simon, 2005; Thieme et al., 2011) and rock porosity in the context of petroleum engineering (Mayo et al., 2015; Vega et al., 2014). Krypton was also used as a gas-phase contrast agent for 2D X-ray fluorescence measurements of a coaxial jet flame in the contemporaneous work of Schumaker et al. (2015). Linear and mass attenuation coefficients for krypton and other pertinent materials are illustrated in Fig. 3.2. Note that the sharp discontinuities observed in the curves for krypton and xenon occur at energies characteristic of the inner K electron shells of each atom; at these energies, a sharp jump in attenuation is observed because incoming photons above the K edge begin to contain enough energy to interact with K-electrons via the photoelectric effect (Macovski, 1983).

Demonstrating the viability of XCT as a diagnostic tool for gas-phase mixing is best accomplished using a well-known flow configuration. Gas-phase jet flows represent a classic test case for a wide variety of diagnostics, and for tomographic methods in particular, because they are relatively simple to set up while being theoretically, experimentally, and computationally well-characterized (Birch et al., 1978; Dowling and

Dimotakis, 1990; Emmerman et al., 1980; Mi et al., 2001; Su et al., 2010; Watt and Vest, 1990; Yip and Long, 1986). Vertical gaseous jets are especially common in experimental work due to symmetry, well-developed similarity laws, and ease of setup (Chen and Rodi, 1980), but the geometry of common clinical XCT scanners requires the use of a horizontal jet. While experimentally convenient for the present work, however, a horizontal krypton jet exhausted into ambient surroundings will by nature be negatively buoyant due to the high specific gravity of krypton. Negatively buoyant inclined and horizontal jets have been previously studied, often in the context of submerged liquid discharges (Fan, 1967; Jirka, 2004; Papakonstantis et al., 2011), but literature on such flows in gas-phase phenomena is sparse (Britter, 1989; Wang and Andreopoulos, 2010).

3.2.3 Experimental Design and Facility Specifications

All experiments were performed on the GE HiSpeed CT/i XCT scanner described in Sec. 2.4.1 using a fan-beam geometry. Several characterization scans were undertaken to determine the best scan parameters at which to run each experiment. System response was tested over all possible scanner energies, axial resolutions, and tube currents. The experimental apparatus, illustrated in Fig. 3.1, consisted of a krypton gas cylinder connected to a long tube section via a plug valve, metering valve, Aalborg GFM mass flowmeter, and actuated ball valve. The flow was controlled by adjusting the metering valve to a particular setting and varying the pressure supplied by the krypton regulator such that desired values were read by the mass flowmeter. In this way, flow conditions could be precisely replicated over a long series of trials. Alignment of the pipe and jet exit with the axis of the XCT scanner to within 0.4 degrees was performed using laser sights built into the scanner and confirmed via scout scans of the entire apparatus.

A set of two different jet characterization experiments was performed by exhausting a krypton jet from a copper tube of 76.2 cm in length having an inner diameter of $D =$ 1.09 cm, resulting in a development length of approximately $70D$ for the pipe flow. A flow straightener was placed at the entrance to the tube to ensure a well-developed pipe flow. This experimental setup was used to create several datasets describing a krypton jet exhausted into ambient air at bulk velocity of $u_o = 9.5$ m/s. This results in an exit Reynolds

number of $Re_o = 16,000$ with Re_o defined as,

$$Re_o = \frac{u_o D}{\nu_o}, \tag{3.2.3}$$

where the subscript o indicates reference to the condition at the exit orifice.

All scans were performed at a tube voltage of 80 kVp a tube current of 200 mA, 1 mm axial resolution, and 200 μm in-plane resolution. Each axial slice was reconstructed over a radial domain of 10 cm in diameter using 972 views taken over a total time of one second. Flow rate data from the mass flowmeter and ambient temperature data from a type K thermocouple were logged using LabView software. Further, the actuated ball valve was controlled in such a way that the flow could be stopped or started immediately from the LabView console.

The first jet experiment involved obtaining ten scan sets consisting of 67 axial slices at 3 mm spacing over a 20 cm domain. These scans were conducted in order to enable uniform spatial coverage of the jet while obtaining a large enough sample size for useful multiple-trial averaging. This first set of experiments was conducted using the scanner's baseline calibration settings that are appropriate for water-based objects, while later experiments utilized an air-based calibration that improves data quality.

The second experiment involved obtaining more detailed data at five specific axial locations, each of which was scanned 20 times in order to enhance statistical convergence of the results. Moreover, minimization of imaging artifacts via the combination of air-based calibration and background subtraction allows for quantitative reconstruction of the krypton concentration field for this dataset. Pertinent results from each of these experiments, along with a full discussion of the detailed air calibration data, are discussed next.

3.2.4 Presentation of Detailed Calibration Data

In order to fully characterize scanner behavior and allow for quantitative interpretation of the data, a set of calibration data describing scanner response to various krypton mole fractions was obtained. In particular, it is important to ensure that the detector operates in spatially uniform linear fashion in the low-contrast region we consider in order to

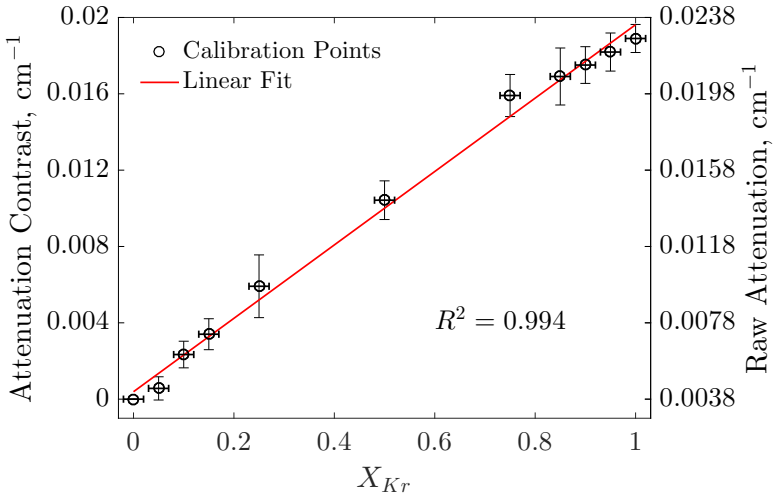

Figure 3.3: Krypton XCT calibration curve; vertical and horizontal bars indicate 95% confidence intervals.

implement the linear mixing law of Eq. (3.2.2) with confidence. The calibration curve illustrated in Fig. 3.3 was created using five scans of thin plastic balloons filled to various krypton concentrations using a pulmonary syringe with air as the bath gas. Error bars in Fig. 3.3 are 2% for the mole fraction measurement (horizontal direction, estimated effect of syringe filling procedure) and the 95% confidence interval of the XCT measurements over all reconstructed voxels in all five scans, assuming a Gaussian distribution on the variation (vertical direction). Acceptably linear behavior is observed throughout the domain, even at low krypton mole fractions, indicating that the scanner is indeed sensitive enough to allow for resolution of a wide domain of krypton mole fractions. It is also useful to observe that at low mole fractions, the estimated spread in the filling procedure can become large compared to the nominal mole fraction. Further, using a simple estimate such that $dX_{Kr} = (\partial X_{Kr}/\partial \bar{\mu}) d\bar{\mu}$, Fig. 3.3 implies a typical 95 % confidence interval width of 0.075 and maximum confidence interval width of 0.15 in mole fraction space for a five-scan averaging procedure; thus, increasing scan number will be important in reducing expected spread in krypton mole fraction values inferred from attenuation measurements. Note that the path length in the calibration scans was 20 cm through the various krypton-air mixtures inside the balloons, while in the jet experiments the path length through the gas mixture would be between 1 cm and 5 cm with krypton concentration

depending on axial position.

To compliment this calibration procedure, data from the X-ray tube manufacturer (Dunlee) was used in combination with the SpekCalc software package (Poludniowski et al., 2009) to compute a theoretical spectrum for the XCT device. This probability density function, reproduced in Fig. 3.4, can be used to compute a theoretical value for the dynamic range in the denominator of Eq. (3.2.2), which can be compared to the value obtained via direct calibration. Note that the sharp peaks in the spectrum result from characteristic radiation concentrated at energies analogous to the transition energies between electron orbitals in the tungsten target (Prince and Links, 2006).

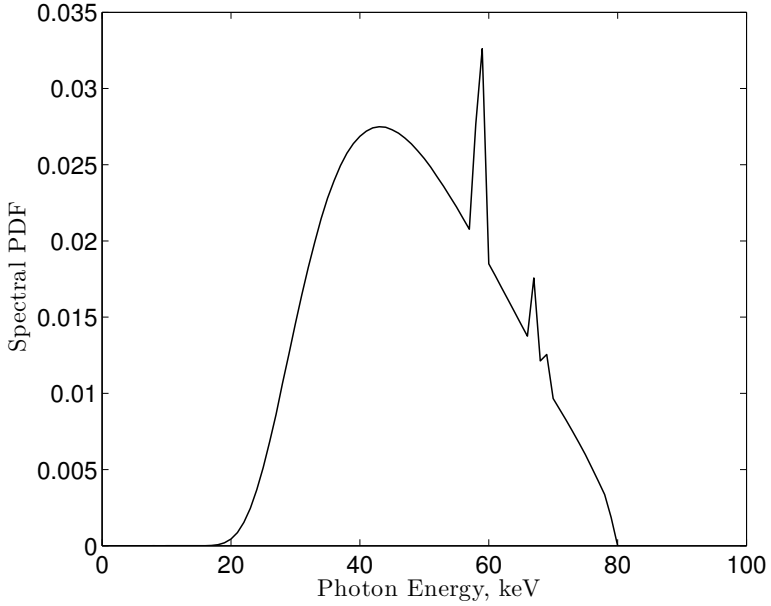

Figure 3.4: GE HiSpeed CT/i theoretical spectrum calculated from SpekCalc (Poludniowski et al., 2009).

It is apparent from Fig. 3.3, for instance, that we report the average attenuation for pure krypton as 0.02259 cm^{-1} while air registers at an average of 0.0038 cm^{-1}, which is higher than the value of 0.0005 cm^{-1} predicted by the CT theory using Eqns. (2.1.4) and (2.1.2) along with the spectrum illustrated in Fig. 3.4. Similarly, the measured value of krypton at 0.02259 cm^{-1} compares reasonably to the theoretical value of 0.02462 cm^{-1} computed using scanner hardware data and SpekCalc. This type of discrepancy is not unexpected given that we are operating in the extreme low contrast regime of the scanner,

and that the constant offset error between theoretical and experimental attenuation values when measuring pure air is often on the order of 0.002, even for newer scanners (ImPACT Group, 2009). These differences are mostly the result of the clinical context of most XCT scanners, wherein internal reconstruction parameters are optimized for reconstruction of objects whose density is similar to water rather than air. However, despite this slight misalignment between theoretical attenuation results and actual scanner readings, the calibration data of Fig. 3.3 allows us to utilize Eq. (3.2.2) in the following manner on a voxel-by-voxel basis,

$$X_{Kr} = \frac{\bar{\mu}_{Meas} - \bar{\mu}_{Bk}}{\bar{\mu}_{Kr} - \bar{\mu}_{Air}}, \tag{3.2.4}$$

where $\bar{\mu}_{Meas}$ is the jet experiment attenuation, $\bar{\mu}_{Bk}$ is the attenuation from a background scan taken with only air in the scanner, $\bar{\mu}_{Kr}$ is the average krypton attenuation value from the balloon calibration procedure, and $\bar{\mu}_{Air}$ is the average air attenuation value from the balloon calibration procedure.

3.2.5 Uncertainty Analysis

When evaluating the various results presented here, it is important to understand associated measurement uncertainties in the context of both the turbulent flowfield and scanner behavior as described in Sec. 2.5. Uncertainties associated with gas-phase XCT can be placed into several categories: intrinsic detector variation error, systematic reconstruction error, flowfield fluctuation error, and physical noise mechanisms (Boas and Fleischmann, 2012; Hsieh, 2009). Each of these is explored below in detail.

Intrinsic Detector Variation Error

The first type of error that one would consider in an experimental system is the variation caused by nonuniform hardware operation. The manufacturer of the GE HiSpeed CT/i scanner used in this experiment reported a nominal standard deviation of $\pm$ 0.0008 cm^{-1} on a voxel-by-voxel basis. As reflected in Fig. 3.3, standard deviations were generally below 0.0005 cm^{-1} in each individual scan in the dataset presented here. Note that this standard deviation remains constant regardless of the number of scans considered, and that there exists minimal correlation between standard deviation and the absolute attenuation value.

Thus, we conservatively take the measurement error due to random detector variation as $\sigma_{Det} = 0.0005$ cm^{-1}.

In addition to random detector variation, a systematic change in detector response over time was observed in the facility used for these experiments. These changes resulted in an average decrease of 1×10^{-5} cm^{-1} per scan at the center of the region of interest over the first 100 scans of a procedure in which 150 consecutive scans of a krypton-containing balloon were recorded using an initially cool scanner. This type of detector response drift is common in fan-beam geometries because all detector elements do not consistently receive an unattenuated signal that can be used for self-calibration at each point in time as the system hardware heats up; rather, unimpeded channels at the edge of the detector array are used to monitor changes in system behavior and infer analogous changes at the center of the array (Macovski, 1983). Because we would like to maximize computed X_{Kr} accuracy along the centerline of the jet, we take the attenuation contrast reported in Fig. 3.3 to be the baseline "warm scanner" value and adjust the value used for $\bar{\mu}_{Kr}$ in Eq. (3.2.4) using a linear approximation,

$$\bar{\mu}_{Kr} = \bar{\mu}_{Kr}^{Cal} - 10^{-5} n \text{ cm}^{-1}, \tag{3.2.5}$$

where $\bar{\mu}_{Kr}^{Cal}$ is the value obtained from calibration and n is the number of scans previously performed in a given trial. Importantly, as shown in Fig. 3.5, we found the value of the drift to be dependent on the distance from the center of the reconstructed domain, but utilize the 1×10^{-5} cm^{-1} value observed along the centerline in these calculations in order to simplify the analysis procedure while ensuring that the centerline mole fraction is accurately represented. Because drift becomes less negative towards larger radii, we would expect krypton mole fractions at large jet radii computed by Eqs. (3.2.4) and (3.2.5) to be slightly higher than their true values. We account for any potential error that this treatment may introduce by conservatively taking the resultant uncertainty as $\sigma_{Deg} = 0.0003$ cm^{-1}.

Reconstruction Error

The major contribution of reconstruction error in this experiment is the presence of ring artifacts of the type discussed in Sec. 2.5.4. The Ring Correction in Polar coordinates

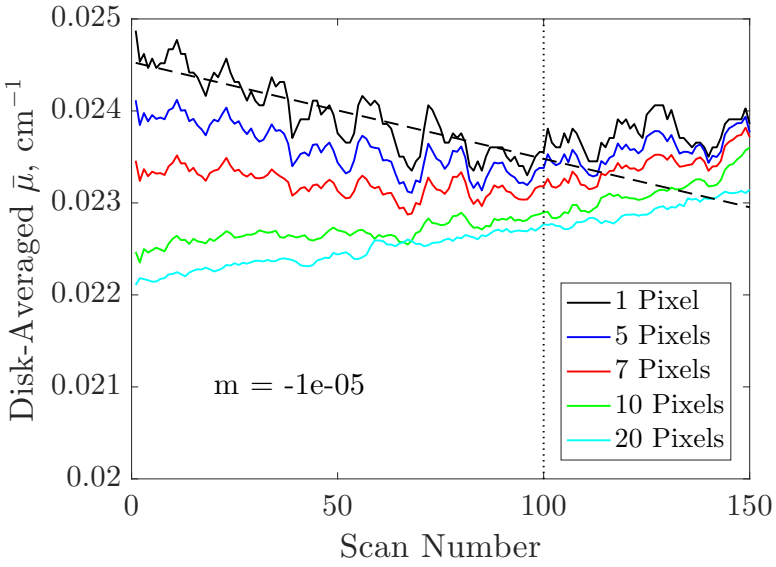

Figure 3.5: Averaged attenuation value versus scan number within disks of different size around the center of the region of interest; drift value used here computed at center pixel over the first 100 scans wherein a consistent trend is observed.

(RCP) algorithm detailed in Prell et al. (2009) seems to apply well to this case, and has thus been used to remove spurious artifacts from the data when appropriate. Note that the air-calibrated results for the second experiment do not require this correction, but that it is useful in processing the results of the first jet experiment, which was more susceptible to ring artifacts due to use of a baseline system calibration.

Flowfield Fluctuation Error: Analysis of Time-Varying XCT

A third source of potential error stems from the fact that XCT reconstruction is performed using a set of projections that represent integral images of a temporally varying field at slightly different points in time. In this case, reconstructions for each axial slice were computed from 972 linear projections taken over a total time period of one second, meaning that a scan of the full domain (67 slices during the first experiment) took just over one minute. Note that the scanner used in this study only outputs reconstruction (not projection) data, meaning that all analysis performed here references exclusively reconstruction data. Thus, it is important to note that the reconstructions presented here are “time-averaged” in the sense of Heindel (2011) in that while each projection is recorded at a timescale on the

order of a millisecond, the reconstruction is computed from a set of 972 projections that took a total of one second to record.

Errors associated with XCT reconstruction of time-dependent data were originally analyzed by Willis and Bresler (1990) in the context of situations such as cardiac XCT wherein a time-varying, aperiodic phantom must be imaged. For this particular application, a simplified approach was pursued to assess how the Radon transformation performs on a transient signal. For this, we considered a disk with diameter of 1 cm and unity attenuation coefficient that homogeneously oscillates with frequencies up to 10 kHz and magnitude of 0.2 commensurate with the expected jet turbulence intensity I_T. The reconstructed results were compared to those of a static disk at the corresponding mean field. As shown in Fig. 3.6, it was observed that the average voxel-to-voxel error was below 1% of the mean field for nearly all frequencies not in phase with the projection sampling frequency, and, further, that there was no directional bias to these errors. The error formulation presented in Fig. 3.6 is the global error metric recommended by Cai et al. (2013),

$$e = \frac{\sum_i |F^{rec} - F|}{\sum_i F}, \tag{3.2.6}$$

where F is a ground truth attenuation field, F^{rec} is the reconstruction, and i indexes all voxels in the reconstructed field of view. Thus, these results suggest that temporal variations should not contribute to systematic error in this study because it is focused on resolution of the mean field.

We can obtain useful quantitative insight into this issue by comparing the characteristic timescales of the system under consideration. The timescale defining the axial slice scan time, τ_{Scan}, can be approximated as,

$$\tau_{Scan} \sim 1 \text{ s}, \tag{3.2.7}$$

from observed scanner operation. The large eddy turnover time, τ_E, would be the appropriate metric for defining the timescale over which large-scale turbulent fluctuations occur. We can estimate this quantity in terms of representative values of an integral length scale L, turbulence intensity I_T, and a velocity scale. Taking $L \sim D$, a reasonable value of $I_T \approx 0.2$ along the centerline (Birch et al., 1978; Panchapakesan and Lumley, 1993; Pope,

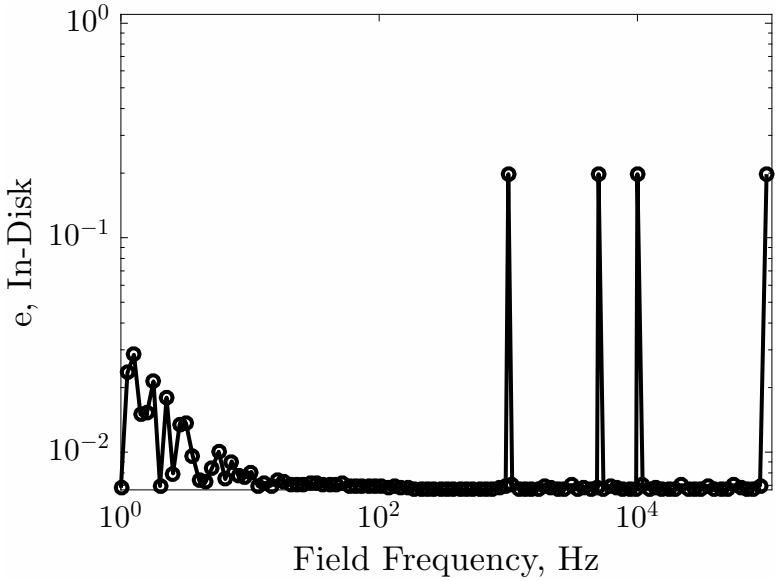

Figure 3.6: Relative error e of reconstructed fields oscillating at various frequencies with respect to mean field value; projection acquisition frequency is 1 kHz, tomographic acquisition time is 1 second for 1000 projections.

2000), and u_o as an applicable velocity scale yields,

$$\tau_E \sim \frac{D}{I_T u_o} = 0.005 \text{ s}. \tag{3.2.8}$$

In this case, we see that the ratio between the scan and eddy turnover timescales is approximately,

$$\frac{\tau_{Scan}}{\tau_E} \sim O\left(10^2\right), \tag{3.2.9}$$

meaning that the timescale over which projections are taken is several orders of magnitude longer than that on which large-scale turbulent fluctuations occur. Due to the difference in scales between the total scan time and eddy turnover times, a full set of projections contains data from over 100 eddy turnovers. Thus, data in a given projection should be minimally correlated in time with data from the majority of the other projections (taken during different eddy turnovers) that contribute to the reconstruction. This result implies that reconstructing a field from these projections would lead to a reasonable estimation of

the statistically converged mean field (Heindel, 2011). Averaging over many uncorrelated reconstructions as we do in the present work further mitigates any error introduced via reconstruction of the stationary mean field from instantaneous projections taken at different times. Nonetheless, the measurement variation resultant from this phenomenon is conservatively estimated as $\sigma_{Turb} = 0.0005$ cm^{-1} to account for any non-stationarity in the reconstruction of the time-varying flowfield.

Photon Noise

In most XCT modalities, Poisson-distributed variation from the photon generation process contributes to the noise (Macovski, 1983). However, in the context of low-attenuation gas-phase flows, photon counts will be quite high, and thus the variance of this Poisson distribution, σ^2_{Pho}, will be small compared to variations in attenuation resulting from mole fraction fluctuations in the turbulent flowfield. We therefore assume $\sigma_{Pho} = 0$ cm^{-1} in our error estimates.

3.2.6 Approach to Uncertainty Analysis

A wide variety of literature on the analysis of uncertainty in experimental measurements has been established for some time (Kline, 1985; Moffat et al., 1982; Moffat, 1985, 1988). In particular, the work of Moffat (1988) has come to represent a seminal approach to this task. The most immediately pertinent concepts from this work are both the general form for measurement uncertainty in a measurement R as a function of measurands x_i,

$$\delta R = \left\{ \Sigma_{i=1}^{N} \left(\frac{\partial R}{\partial x_i} \delta x_i \right)^2 \right\}^{1/2}, \tag{3.2.10}$$

with the reduction such that if $R = x_1^a x_2^b \cdots x_M^m$,

$$\frac{\delta R}{R} = \left\{ \left(a \frac{\delta x_1}{x_1} \right)^2 + \left(b \frac{\delta x_2}{x_2} \right)^2 + \cdots + \left(m \frac{\delta x_M}{x_M} \right)^2 \right\}^{1/2}. \tag{3.2.11}$$

The above equations generally apply under the assumptions of measurement independence, Gaussian variation in each measurand, and that each measurement error is expressed with the same confidence level. We will apply this framework to a variety of quantities computed

both here in the remainder of this work.

Standard Error Estimation

Considering the sources of potential uncertainty presented above, we construct an estimation of the measurement variance that will be used to create error bars for quantitative krypton mole fraction measurements. Here, we have assumed that uncertainty introduced via detector degradation is not mitigated by the averaging procedure (i.e. does not vary inversely with scan number n),

$$\sigma_{Tot}^2 = \frac{\sigma_{Det}^2 + \sigma_{Pho}^2 + \sigma_{Turb}^2}{n} + \sigma_{Deg}^2. \tag{3.2.12}$$

Note that we would separately consider systematic errors such as artifacts in this framework. Using values estimated above for contributions to the total error from these different sources, we can estimate the standard error of the mean of n measurements of the average krypton mole fraction at each pixel over the 0.01904 cm^{-1} dynamic range observed in Fig. 3.3, SE_n, as,

$$SE_n = \frac{1}{0.01904\ \text{cm}^{-1}} \sqrt{\frac{\sigma_{Turb}^2 + \sigma_{Pho}^2 + \sigma_{Det}^2}{n} + \sigma_{Deg}^2}. \tag{3.2.13}$$

Note that contributions to SE_n arising from σ_{Turb}, σ_{Pho}, and σ_{Det} can be controlled by increasing the number of scans. In this study, we have chosen $n = 20$ in order to ensure that the reported standard error of $SE_{20} = 0.02$ is relatively insensitive to uncertainties in the estimates of σ_{Turb}, σ_{Pho}, and σ_{Det}. We utilize this estimate of the standard error when presenting error bars on experimental measurements in later sections. Indeed, many of these values are reported as azimuthal averages over many pixels, and thus these error bars will be particularly conservative given that additional reduction in standard error resultant from azimuthal averaging is not considered.

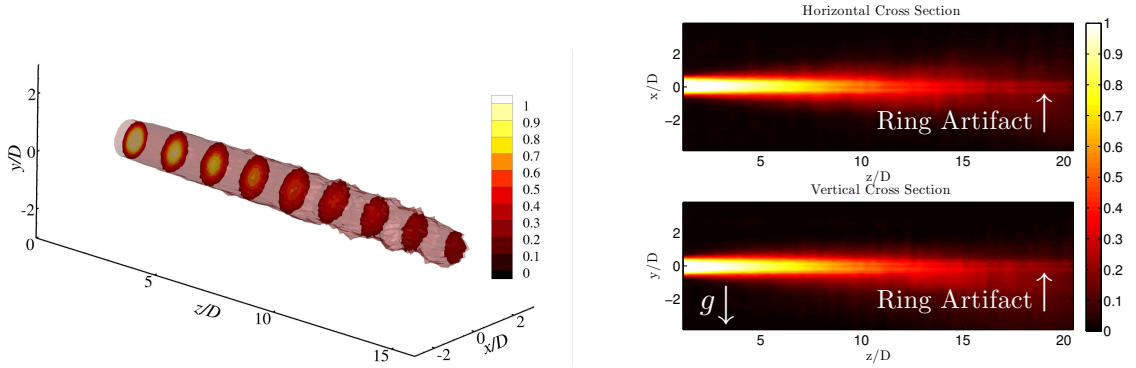

(a) Isosurface at $\langle X_{Kr} \rangle_{10} = 0.25$ and axial cross sections

(b) Horizontal (top) and vertical (bottom) $\langle X_{Kr} \rangle_{10}$ cross sections

Figure 3.7: XCT visualizations of the krypton jet concentration field.

3.3 Results and Discussion

3.3.1 Full-Length Jet Visualization and Buoyancy Analysis

We now proceed to analyze the data from the first jet experiment, which was conducted using the baseline water-phantom calibration for the XCT scanner. In the following sections, it will be useful to present several different types of X_{Kr} data. We therefore utilize $\langle X_{Kr} \rangle_n$ to represent krypton mole fraction averaged over n reconstructions, $\langle X_{Kr} \rangle_\theta$ to denote an average in the azimuthal direction, and $X_{Kr,C}$ to indicate mole fraction along the jet centerline. To illustrate the level of detail obtained from this diagnostic, we present a 3-D reconstruction of average data from the first experiment over ten scans in Fig. 3.7. Note in particular the well-visualized inner structure of the jet as well as the effective capture of the jet buoyancy effect as the outer isosurface begins to bend in the downward direction near the far portion of the axial domain. This trend is apparent both in the 3-D data and in the relative shapes of the horizontal and vertical cross-sections, as the horizontal cross-section remains symmetric while the vertical cross-section has higher krypton mole fractions in the direction of gravity.

It is also apparent from these data that scans using the baseline water-phantom calibration result in a noticeable ring artifact near the center of the domain, which can be observed as two lines symmetrically placed about the center of the horizontal and vertical

cross-sections. Thus, as mentioned above, we have applied the RCP filter of Prell et al. (2009) to mitigate the effects of these errors on our reconstructed fields for results from the first experiment. To understand the errors that this routine, which is fundamentally based on intelligent application of median filters and thresholding, might introduce, we present in Fig. 3.8 a comparison between an unfiltered and a filtered dataset describing the radial krypton mole fraction profile at $z/D = 10$ along the vertical centerline of the jet. Several key observations arise from this data. First, the filter performs well in eliminating noise resultant from ring artifacts near the outer region of the jet, as the line traces the appropriate smooth curve through the original unfiltered data. Note that these small ridges near the outer part of the y domain in Fig. 3.8 can be directly correlated with rings in the axial cross-sections of this data. Further, the ring artifact near the center of the jet (visible as a small depression in Fig. 3.8 near $y/D = 0$) remains throughout this particular dataset. Fundamentally, this occurs both because ring artifacts tend to be of larger magnitude towards the center of the domain and because pixel count decreases with radius from the center of the jet, meaning that the filter has fewer uncorrupted pixels over which to take a median near the center of the domain. We show in later results that this type of error can be mitigated via rigorous calibration procedures.

Despite the existence of the central ring artifact, this dataset can nonetheless give useful qualitative and quantitative insight into the effects of buoyancy on the heavy gaseous jet. For instance, Becker and Yamakazi (1978) analyze the behavior of a propane jet diffusion flame using a nondimensional coordinate that can be approximated as (See and Ihme, 2014),

$$\zeta \approx \frac{z}{D}\left(\frac{\rho_\infty}{\rho_o} Fr^{-2}\right)^{1/3}, \tag{3.3.14}$$

where z is defined from the jet orifice and $Fr = u_o/\sqrt{gD}$ with g the gravitational constant. The criterion $\zeta < 1$ is applied to define the forced convection limit wherein buoyancy effects are negligible. While the situation modeled here is certainly different in character than that of the vertical alignment of Becker and Yamakazi (1978) in the sense that gravity does not directly oppose the motion of the fluid, we can nonetheless use this criterion as an estimate of the point at which buoyancy becomes important in this flow. Setting $\zeta = 1$

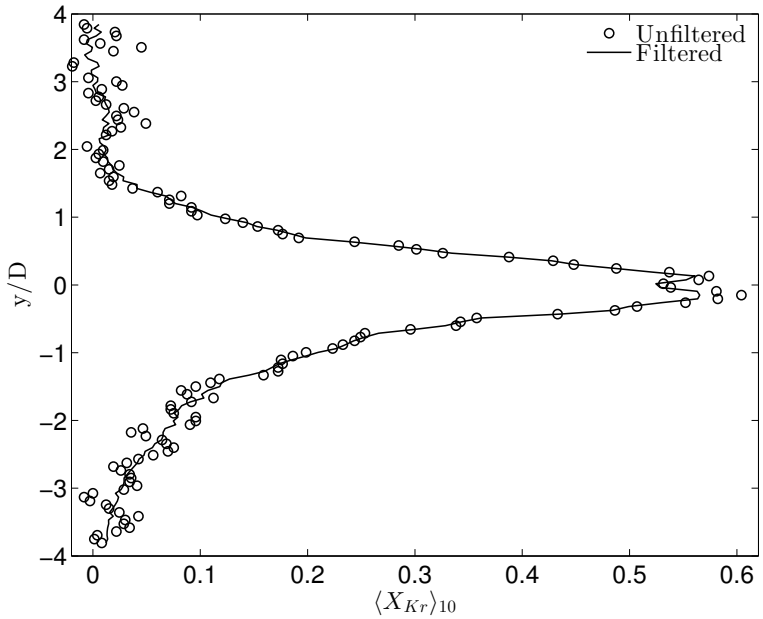

Figure 3.8: Effect of RCP filter on $\langle X_{Kr} \rangle_{10}$ data for radial profile at $z/D = 10$

and solving for the location at which buoyancy becomes important yields a critical value of $z/D \sim 14$. Qualitative agreement with this trend is best observed in Fig. 3.7. Note the expected symmetry in jet development out to just before $z/D = 10$ before substantial downward-biased asymmetric spreading begins to occur between $z/D = 10$ and $z/D = 15$. The work of Pitts (1991) demonstrates that the jet density ratio may significantly affect the measurement of the virtual origin, and thus we perform only a brief analysis here to illustrate approximate qualitative agreement between this experiment and the buoyancy criterion of Becker and Yamakazi (1978).

3.3.2 Quantitative Analysis of Jet Concentration Data and Comparison to Similar Measurements

As a final piece of analysis for this experiment, we extract krypton mole fraction profiles from the second jet experiment and compare these data to relevant experimental and computational results. This dataset was obtained after air-based scanner calibration and was recorded within 24 hours of the original balloon calibration experiment, meaning that the scanner behavior exactly replicates that observed in Fig. 3.3. Both calibration and jet

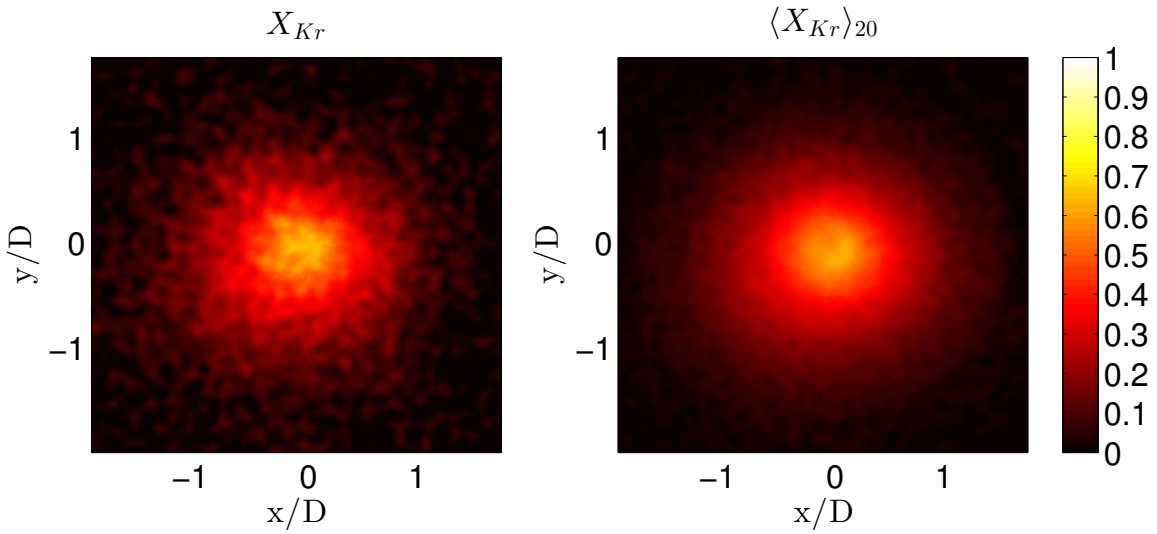

Figure 3.9: Comparison of X_{Kr} and $\langle X_{Kr}\rangle_{20}$ at $z/D = 10$.

data indicate the absence of persistent ring artifacts—such behavior is expected given that the air calibration conditions are much closer to actual operating conditions than water phantom calibration conditions would be. This implies that systematic detector channel errors should be smaller in the former case. In order to maximize statistical convergence of mean field measurements within tube heating limits, 20 scans were taken at each of five axial locations ($z/D = 0.5$, 2.5, 5, 10, 15). Comparison of a single reconstruction to an average over twenty reconstructions can be found in Fig. 3.9.

Numerical integration of the reconstructed attenuation field commensurate with the mole fraction data at $z/D = 0.5$ indicates an estimated peak krypton absorbance of 0.025 through centerline of the jet.[1] To arrive at this estimate, spectrally averaged linear attenuation coefficients were computed using Eq. (2.1.2), linear attenuation data from Fig. 3.2(a), and the scanner spectrum from Fig. 3.4. Attenuation at each pixel was then computed from Eq. (2.3.18), and absorbance profiles were calculated directly via Eq. (2.1.3). Absorbance values were generally insensitive to the angle of line integration due to axisymmetry. We report the krypton absorbance as the difference between the centerline jet absorbance value and absorbance computed along a line containing pure air in order to specifically isolate the impact of the krypton.

[1] Absorbance is defined here as $\int \bar{\mu} ds = -\ln(I_d/I_0)$.

Re-Matched Methane Jet

We also compare data from the current experiment to that of Birch et al. (1978), who investigated an axisymmetric methane jet exhausted with a fully developed pipe flow profile at Re = 16,000. While the buoyancy and preferential diffusion aspects of the current setup are not replicated by the experiment of Birch et al. (1978), nearly all other parameters are exactly the same, making it a useful case to which to compare our data. Specifically, it is reasonable to expect axial concentration patterns to be relatively similar between the two jets (particularly at axial positions before buoyacy begins to take effect in the krypton jet). Radial profiles should show some level of qualitative agreement, but the radial data of Birch et al. (1978) is taken from the fully-developed far field of the jet, whereas the krypton jet data will necessarily be taken from the near field. In general, though, this represents the most pertinent dataset in the literature and, crucially, contains data in the near field describing axial concentration decay.

Comparison of Results

Results from the literature allow us to perform an analysis to confirm that the obtained XCT data reproduces species concentration profiles that are in reasonable alignment with results from other modalities. Figure 3.10(a) illustrates vertical profiles of $\langle X_{Kr} \rangle_{20}$ at the horizontal centerline, Fig. 3.10(b) shows analogous profiles in the horizontal direction, and Fig. 3.10(c) compares the mean centerline profile, $\langle X_{Kr,C} \rangle_{20}$, from this experiment to that of a CH_4/air jet from the work of Birch et al. (1978). Note that each data point in Fig. 3.10 represents a single voxel that is 200 μm x 200 μm x 1 mm in size in the horizontal, vertical, and axial direction, respectively. Figure 3.10(a) directly illustrates that the XCT data quantitatively captures the negative buoyancy of the jet, with profiles near the jet orifice being nearly symmetric before the heavy krypton gas begins to sink towards the bottom of the jet at downstream positions. In particular, buoyancy is difficult to observe before $z/D = 10$, while the difference in the distance between the $z/D = 10$ and $z/D = 15$ profiles between the top and bottom portions of the jet is directly indicative of negative buoyancy. Note that data shown in Figs. 3.10(a) - 3.10(c) do not require utilization of the RCP ring artifact filter, with the only applied transformations being the linear mixing law of Eq. (3.2.4) to extract krypton mole fraction from the attenuation measurement and a

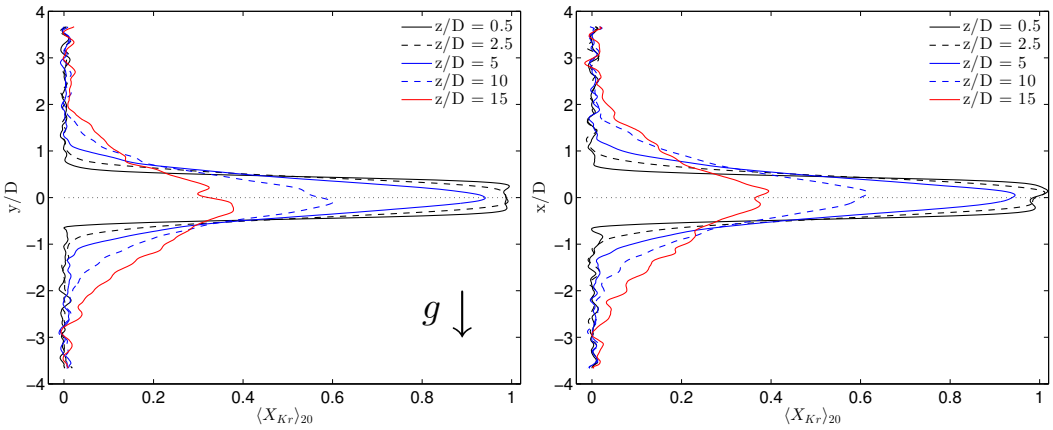

(a) Vertical $\langle X_{Kr}\rangle_{20}$ profiles

(b) Horizontal $\langle X_{Kr}\rangle_{20}$ profiles

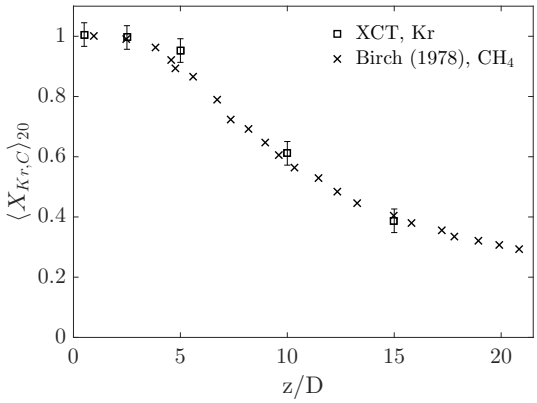

(c) Centerline $\langle X_{Kr,C}\rangle_{20}$ profiles

Figure 3.10: Averaged $\langle X_{Kr}\rangle_{20}$ profiles in (a) vertical, (b) horizontal, and (c) axial directions.

moving average smoothing operation. Variations in the data observed in Fig. 3.10(a) near the centerline of the profiles for $z/D = 10$ and $z/D = 15$ result from the fact that the air scans used to compute $\bar{\mu}_{Air}$ in Eq. (3.2.4) were conducted with a "cool" scanner, which gives smooth subtracted results at early scan times ($z/D < 10$), but causes the observed variation in computed $\langle X_{Kr}\rangle_{20}$ near the centerline, where detector drift is most pronounced, at later times. Importantly, investigation of nearby pixels confirms that the peak krypton mole fraction value is minimally affected. For consistency, the same air background is used for all calculations performed here, but one could also work to create a temporally

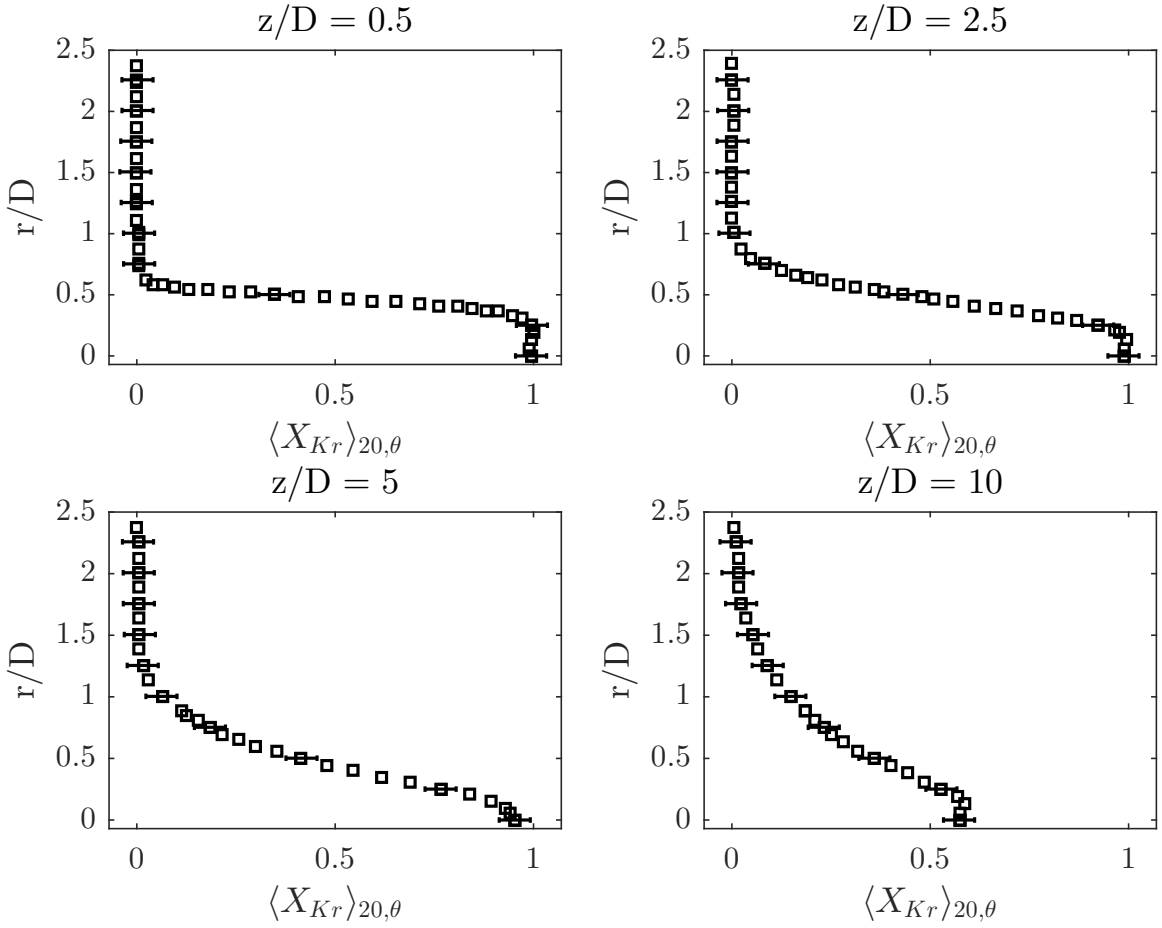

Figure 3.11: Comparisons of azimuthally averaged radial $\langle X_{Kr} \rangle_{20,\theta}$ profiles from experiments and simulations of the krypton-air jet.

resolved air background if further precision was required. Note that subsequent quantitative comparisons feature azimuthally averaged datasets that eliminate much of the variation associated with these raw pixel measurements.

In Fig. 3.10(c), we observe the expected general scaling of the maximum jet krypton mole fraction with $1/z$, even in the horizontal geometry, and see that the centerline concentration falloff takes a slightly different form in the krypton-air jet than in the lower density ratio methane-air jet. Note that error bars in Fig. 3.10(c), as they do throughout this section, represent 95% confidence intervals assuming Gaussian distribution of the overall error and the standard error estimate of Eq. (3.2.13).

We can also use this dataset to extract radial concentration profiles in the near field of the negatively buoyant horizontal jet, as shown in Fig. 3.11. The radial profile data shown in Fig. 3.11 reflect the expected behavior of the near field of a turbulent jet, and the work of Dunnmon et al. (2015) illustrates good agreement between these profiles and those of an LES calculation obtained by Sadaf Sobhani.

3.4 Conclusions and Future Directions

We have demonstrated the successful application of clinical XCT methods to measuring gas-phase mole fractions in a statistically stationary turbulent flowfield. Through the use of radiodense krypton gas, it was possible to quantitatively and qualitatively visualize mixing of a negatively buoyant krypton-air jet. This diagnostic shows potential in allowing for easy tomographic visualization of mean scalar concentration fields using well-established clinical XCT scanners.

We have also identified potential sources of uncertainty in this diagnostic, which arise from intrinsic detector variation, detector degradation, systematic reconstruction error, flowfield fluctuations, and physical mechanisms such as photon noise. Random detector variations are well-documented and easily incorporated into our analysis, while temporal variability and artifact-induced reconstruction errors require more intensive consideration. Measurements of the mean flow will have errors that are fundamentally related to the relationship between scanner frequency and the underlying temporal power spectrum of the turbulent jet, but such errors are diminished via reconstruction using many uncorrelated projections and further averaging over multiple uncorrelated trials. Additionally, due to the low attenuation of gas-phase flows, photon fluence variations are not a major source of error in the gas-phase XCT results presented here. Finally, artifact errors are spatially localized and somewhat predictable, but need to be carefully treated to ensure that other quantitatively important data is not corrupted by standard filtering algorithms. At present, lower-magnitude artifacts near the edges of the reconstructed domain may be easily removed via the filter of Prell et al. (2009), providing substantial reduction of these spurious signals. However, the central ring artifact will often not be completely removed by this procedure. Nonetheless, we have shown that air-based calibration reduces both the probability and magnitude of error in the detector elements.

Chapter 4

XCT Characterization of a Premixed Bunsen Flame

4.1 Introduction and Background

Before applying X-ray diagnostics to a PMB system, it is important to assess their ability to visualize a conventional combustion phenomenon in three dimensions and to understand the effect of the krypton gaseous contrast agent on the combustion process. Further, in addition to having potential utility as a PMB-specific diagnostic, X-ray absorption techniques may also have merit as a standalone method for interrogating experimental combustion systems. In the spirit of recent work in the field of optical Tomographic Chemiluminescence (TC) (Cai et al., 2013; Li and Ma, 2014; Xu et al., 2015), for instance, XCT can provide a complementary measurement mechanism fundamentally based on thermophysical state of a gas, as opposed to the reaction progress information generally indicated by chemiluminescence. Further, given the fundamentally different phenomenologies and energy levels of X-ray and optical diagnostics, it is possible to perform X-ray measurements simultaneously with nearly any other optical diagnostic method to obtain an additional data series describing the same flame. The fact that flames do not naturally emit or absorb high-energy X-rays minimizes interference that could pollute other optical signals via such phenomena as beam steering (Schumaker et al., 2015). Importantly, X-ray diagnostics have the capability to penetrate many

optically opaque surfaces, which allows for measurements within systems such as PMBs that are inaccessible to optical diagnostics.

In this chapter, we utilize a simple Bunsen flame to present what is to our knowledge the first application of hard X-ray absorption techniques at clinical energies to characterization of a gas-phase free flame. A Bunsen flame was used for this study due to the simplicity of associated experimental design, low required flow rates, the ability to leverage axisymmetry in comparing tomography to traditional line-of-sight analyses, and ease of comparison to 2-D axisymmetric simulation. This experiment allows us to explicitly demonstrate several important aspects of XCT applicability to combustion measurements:

1. Measurement of attenuation fields of free flames is viable within an attenuative outer casing using hard X-ray absorption techniques

2. Changes in X-ray attenuation signal within a flame containing a radiodense gaseous contrast agent are dominated by thermal expansion of the gas

3. Addition of the radiodense gaseous contrast agent causes several physical effects that should be considered when utilizing this diagnostic – these include changes in adiabatic flame temperature, laminar flame speed, and Lewis number

4. The combination of X-ray and chemiluminescence measurements enables simultaneous experimental assessment of different flame quantities

5. SNR converges consistently with increased effective photon counts, though the X-ray system may be limited by a noise floor characteristic of its specific hardware

This chapter will proceed as follows. Section 4.2 will first detail the experimental setup and procedure. Analysis will proceed in Sec. 4.3, which describes the effects of the krypton contrast agent on flame dynamics via radiography measurements and computation, and further in Sec. 4.4, which analyzes the reconstructed tomographic data, makes comparisons to 2-D computations, and assesses simultaneous XCT-chemiluminescence data. Before concluding, a complete analysis of measurement noise from the X-ray system will be presented in Sec. 4.5.

4.2 Experimental Setup and Procedure

4.2.1 Burner and Scanner Setup

In the present work, we utilize a Bunsen flame to analyze the applicability of XCT diagnostics for free flames. A straight tube of 175 mm in length and 9.5 mm inner diameter with a flow straightener at its inlet was mounted to a rotating flow system contained within a tabletop X-ray enclosure – both the rotating flow system and X-ray hardware are described in detail in Sec. 2.4.1, while Fig. 2.4 illustrates the experimental setup of the XCT system that was utilized in this study. A variety of fuel-rich radiodense Kr/Air/CH_4 mixtures were created by mixing streams of methane, air, and krypton. Combustion was initiated at fuel-rich conditions in order to ensure stability of the flame as krypton concentration was varied. Component gases in the premixed stream were combined using a set of tee junctions, and flow rates were controlled using a set of rotameters for each constituent gas. Rotameter accuracy was $\pm 8\%$ for methane and $\pm 5\%$ for all other gases.

The burner was housed inside a transparent polycarbonate tube of radius 93 mm and thickness 3 mm. This tube served both to shield the flame from ambient drafts to minimize transient unsteadiness and to provide an outer attenuative casing to emulate what would be expected in a porous media burner. The transparent tube also allowed for simultaneous recording of chemiluminescence (CL) data in addition to XCT data with a Nikon D90 CMOS DSLR camera mounted orthogonally to the X-ray source-detector axis, as shown in Fig. 2.4. Such commodity cameras have recently been shown to enable spectrally coarse, yet faithful CL-style measurements of signals correlated with different excited radical species (Huang and Zhang, 2008, 2011). Note that the axisymmetry of the Bunsen flame allows for collection of CL and X-ray data describing the same points in time using instrumentation mounted along different spatial axes. During XCT trials, the camera was remotely activated to record images of the flame, yielding simultaneously acquired data series describing visual emission and X-ray attenuation.

As shown in Figure 2.4, the burner is placed between the source-collimator assembly (left) and detector (right) on the precision rotating table to acquire 625 projections over 360 degrees for tomographic acquisitions, with each projection integrated over 40 ms in

time. Source-to-isocenter distance was 944.8 mm and source-to-detector distance was measured at 1255.5 mm. Scans were conducted with a 45 kVp and 30 mA X-ray beam to optimize SNR by minimizing photon energy while maximizing tube current at a setting that would allow for many sequential tomographic acquisitions without overheating the X-ray source hardware. Note that source-to-isocenter and source-to-detector distance were minimized to the degree possible given facility constraints with the intent of maximizing X-ray intensities. The 3-D reconstruction volume is $256\times256\times480$ voxels in size with 300 μm isotropic spacing. The 3-D images were reconstructed using the Feldkamp-Davis-Kress (FDK) method with a Hamming windowed ramp kernel to eliminate high-frequency noise (Feldkamp et al., 1984; Hsieh, 2009). Ring artifacts are removed using the standard algorithm of Sijbers and Postnov (2004) summarized in Sec. 2.5.4; this process was originally applied to Bunsen flame data by Dunnmon et al. (2017b).

4.2.2 Facility Characterization

Before proceeding to flame experiments, it was important to characterize the X-ray facility in the context of low-contrast gas-phase attenuation experiments. As a first test to ensure absorbance linearity with krypton mole fraction, we use a plastic syringe to create gas mixtures at several different krypton mole fractions and extract the absorbance value from a Region Of Interest (ROI) along the centerline of the syringe. A sample projection from this procedure with the measurement and background ROIs indicated can be found in Fig. 4.1.

This calibration procedure yields the curve in Fig. 4.2(a), which demonstrates response linearity. Note that each point on this curve was obtained from a single projection, and that error bars represent 95% confidence intervals on each value computed from standard deviations within the ROI. Given that reconstructions from this system utilize projection data, it is important to ensure a reasonable level of source consistency over the course of a scan procedure. As shown in Fig. 4.2(b), the source exhibits increasing average output (uniform over the entire detector) both as projection number increases and with different tomographic acquisitions, though the effect of this trend on computed absorbance values can be minimized by using an unimpeded segment of the flat panel detector to estimate I_0 on a projection-by-projection basis, which we do for all data taken from this facility. The

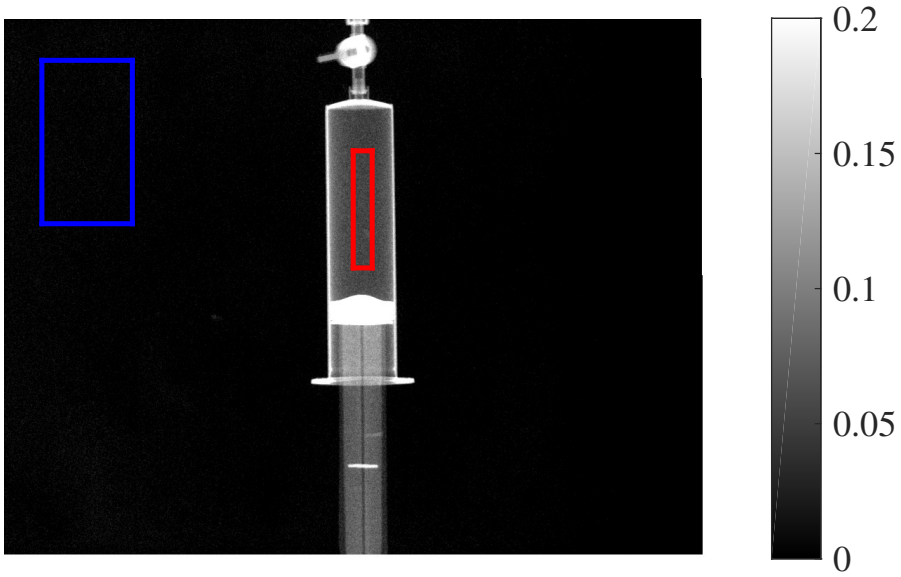

Figure 4.1: Projection containing syringe containing a krypton-air mixture; blue rectangle indicates area used to obtain background photon counts while red rectangle indicates area used for calibration. Color axis is absorbance.

blue square in Fig. 4.1 illustrates an area of the detector that was used for measurement of I_0; note that this approach is viable because appropriate gain and offset calibrations ensure a uniform flat field measurement across the detector.

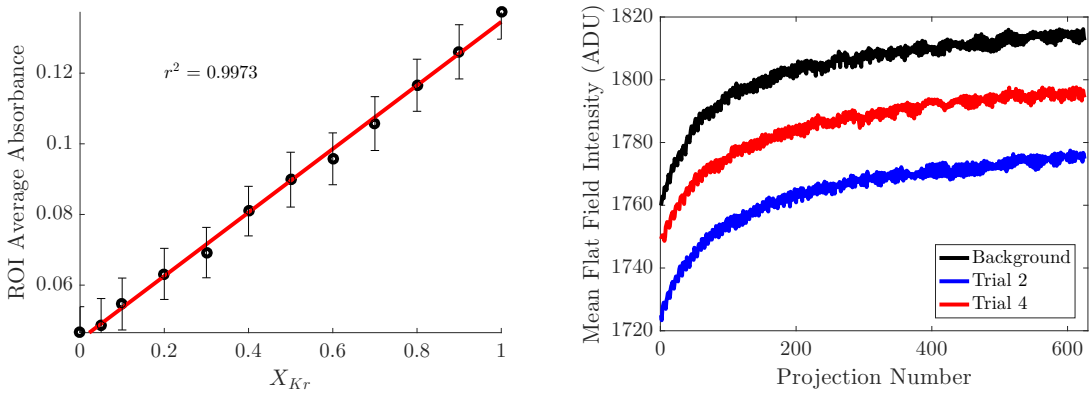

(a) Krypton calibration curve

(b) CBCT system calibration

Figure 4.2: Facility characterization: (a) krypton calibration and (b) source stability.

4.2.3 Experimental Procedure

The Bunsen flame experiments were performed in several stages. First, a set of projection radiography measurements were taken at various different conditions to evaluate how the addition of krypton to a particular flame would affect observed flame topology and X-ray contrast. These measurements are also intended to demonstrate the type of data series that can be obtained from radiography as a contrast to those achievable via XCT. A methane-air flame was established at the outlet of the Bunsen burner, with ignition provided via a small torch, and allowed to stabilize for 30 minutes to minimize thermal transience. Note that this 30 minute duration was still relatively small compared to the five-hour total duration of the combustion portion of the experiment. At this point, 625 projection images of the methane-air flame were obtained at a rate of 15 fps – this represents condition (a) in Table 4.1. An identical projection set was taken at each condition in Table 4.1, where conditions (a)-(c) were arrived at by increasing the krypton volumetric flow rate Q_{Kr} at constant Q_{CH_4} and Q_{Air} and conditions (c)-(e) were attained by lowering Q_{Air} with all else held constant. Finally, a set of background data was recorded in order to allow for isolation of the signal resultant from the krypton contrast agent. Results from this experiment will be analyzed in Section 4.3.

Condition	Φ	X_{Kr}	u_o	Re
(a)	1.18	0.00	19 cm/s	118
(b)	1.18	0.22	25 cm/s	188
(c)	1.18	0.35	30 cm/s	252
(d)	1.63	0.44	24 cm/s	218
(e)	3.27	0.57	18 cm/s	182

Table 4.1: Projection radiography conditions. Krypton was added from (a)-(c) while air was reduced from (c)-(e). Values reported are nominal measurements. Reynolds numbers are calculated at jet exit conditions using Eq. 3.2.3, and u_o values represent bulk outlet velocities.

In the second experiment, a steady flow of premixed gas was established and ignited on the burner at nominal condition (c) from Table 4.1, with a mixture of $X_{Kr} = 0.351$, $X_{N_2} = 0.456$, $X_{O_2} = 0.121$, and $X_{CH_4} = 0.072$ at a bulk velocity of $u_o = 30 \pm 2$ cm/s, equivalence ratio of $\Phi = 1.18 \pm 0.24$, and dilution ratio $X_{Kr} = 0.35 \pm 0.03$. At these

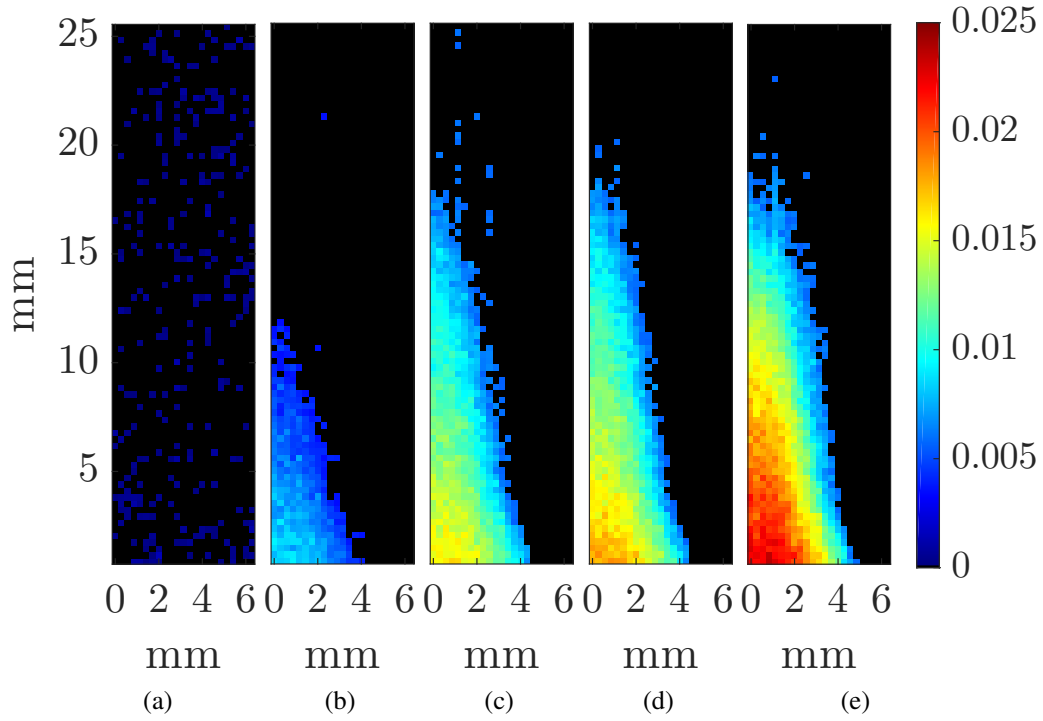

Figure 4.3: Projection radiography visualizations of integrated attenuation signal for conditions in Table 4.1. Absorbance values represent integrated attenuation, $\int \Delta\bar{\mu} ds$.

conditions, visual emission surface had a height of 21 mm. Uncertainties on these values are computed from given rated flowmeter uncertainties and worst-case variation – for equivalence ratio, for instance, the maximum increase is computed using the maximum possible methane flow rate within rated uncertainty and minimum possible air flow rate within rated uncertainty. Such large variations in equivalence ratio would imply $\pm 25\%$ variation in the flame speed and $\pm$ 100 K variation in the adiabatic flame temperature. Values in Table 4.1 are characterized by similar levels of experimental uncertainty, though this reality does not affect qualitative conclusions about the effect of changes in equivalence ratio and krypton mole fraction on trends in X-ray absorption signal and flame topology.

Given these conditions, we compute a Reynolds number of $Re = 252$, which is well in the laminar regime–we therefore expect this flame to behave in laminar fashion throughout the course of the experiment. To enable well-resolved attenuation measurements and

convergence studies, a set of 100 tomographic acquisitions was performed, with 50 taken with the burner operating and 50 more taken as background to ensure converged noise statistics under averaging and background subtraction. This dataset was collected via 10 hours of continuous system use during a single day, ensuring that no variability in environmental conditions, flow rates, or hardware state would contribute to any observed inter-acquisition variation. Results from this procedure will be presented in Section 4.4.

In the present study, it is important to note that no natural coflow was provided due to experimental constraints of the rotating flow apparatus and small physical space in the X-ray scanner, though small amounts of air could be drawn into the plastic tube through the unsealed junction between the tube and motor base. Given these conditions, the flames considered here and associated X-ray attenuation measurements should be negligibly affected by large quantities of air entrainment. This is particularly true given that the inner cone of the rich Bunsen flame is the subject of our measurements. Stability is critically important in this application, because for accurate subtraction, the setup cannot be moved at all during the scanning procedure – thus, if the flame were to extinguish, the process of removing the tube to relight it would irreparably corrupt the dataset.

4.3 Analysis of Contrast Gas Effects

4.3.1 Radiography Data

As in most techniques intended for tomographic reconstruction, substantial information can generally be gleaned from the underlying projection measurements. In the case of XCT, it is useful to demonstrate how background-subtracted projection radiography measurements can be useful in assessing flame behavior. Consider, for instance, the projection radiography results presented in Fig. 4.3, which represent an average over 625 frames, each of which was obtained with a 40 ms X-ray exposure time. These flames are visualized within the plastic tube – subtraction of measurements taken with the tube only (no flow) enable clear visualization of the flame via projection imaging. While dark field and flat field data for gain and offset calibrations were used directly by internal Varian software and not generally recorded, raw projections describing both raw Analog-to-Digital Unit (ADU) and attenuation values characteristic of the background in

this setup can be found in Fig. 4.4. As expected, attenuation strength improves in the

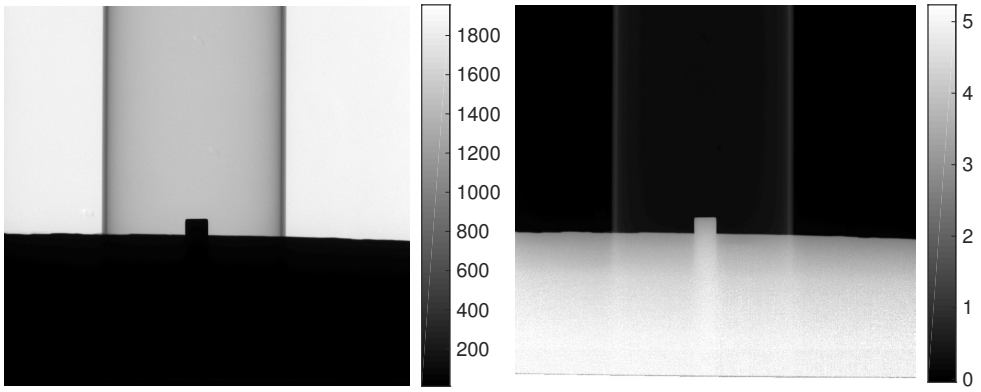

(a) Raw ADU (b) Absorbance, $\int \bar{\mu} ds$

Figure 4.4: Background (a) Analog-to-Digital Unit and (b) absorbance data for Bunsen experiment

flame radiography data with increasing krypton mole fraction, and the premixed flames in Figs. 4.3(b) - 4.3(e) exhibit the conical attenuation profile expected of a Bunsen flame. The random noise shown in Fig. 4.3(a) demonstrates that the flame is not visible on X-ray without the krypton contrast agent. As krypton flow rate is increased from condition (a) to condition (c) at constant air and methane flow rates, flame height increases due to a combination of increased flow rate and decreased flame speed resultant from increased diluent fraction. As air is subsequently removed from the flow from condition (c) to condition (e), contrast improves due to the increased krypton mole fraction, and a small extension of the flame profile is observed, as is commensurate with the expected drop in laminar flame speed with increasing richness of the reaction mixture.

4.3.2 Physical Analysis of Contrast Gas Effects

This radiography study confirms the theoretical expectation that flame characteristics should change substantially with krypton addition. To understand how the addition of krypton to the combustible mixture should affect fundamental flame parameters, we perform several 1-D premixed flame calculations using the Cantera software package (Goodwin and Moffat, 2006). These calculations utilize a version of the GRI 3.0 methane combustion mechanism modified to incorporate krypton and CH^* chemistry. Krypton

molecular parameters were obtained from the work of Burcat (1984), and the CH^* mechanism, which is used to simulate the peak location of the excited CH radical that emits in the visible spectrum, can be found in Kojima et al. (2005). Krypton was assumed to be approximately equivalent to argon, both in terms of three-body reaction participation and efficiencies. The work of Jasper et al. (2015) suggests that third-body efficiencies for krypton should be on the order of 0.9 ± 0.05 with respect to that of argon. We performed a sensitivity analysis at appropriate conditions to assess this effect on the flame speed, and observed a 1% increase as a result of lowering the third-body reaction efficiencies from being equal to argon to being 90% of the argon values. Thus, in the calculations that follow, we neglect this effect and use krypton third body efficiencies equivalent to those of argon.

Interesting points to examine include the effect of the krypton diluent on the unstretched laminar flame speed, S_u^0, the adiabatic flame temperature T_{ad}, and the effective Lewis number, Le_{Eff}. Figures 4.5(a) and 4.5(b) demonstrate the expected effect of substitution of both krypton and argon for nitrogen in methane-air combustion. The convention "X-air" indicates a gas mixture where nitrogen has been replaced completely by compound X as measured by mole fraction – Ar-air, for instance, is 79% argon and 21% oxygen in terms of mole fraction. Results for Kr-air, for which there is no published experimental data, indicate a slight decrease in the flame speed compared to that of Ar-air at all equivalence ratios. This trend likely results from the fact that krypton does have the low heat capacity characteristic of a monoatomic species, which results in the similar adiabatic flame temperature values shown in Fig. 4.5(b), but also a higher density and lower conductivity, which would tend to slightly decrease flame speed via decreased thermal diffusivity.

As shown in Fig. 4.5(c), continuing addition of a krypton diluent causes a decrease in the laminar flame speed. The low heat capacity of the krypton, which contributes to a raised adiabatic flame temperature relative to a diatomic diluent, likely contributes to the ability of krypton-diluted flames to be maintained at the high diluent fractions shown here. In similar fashion, adding krypton to the mixture decreases Lewis number due to changes in the mixture species diffusivity and mixture thermal diffusivity, which is altered due to density, thermal conductivity, and heat capacity effects. In the present experiment, ρc_p

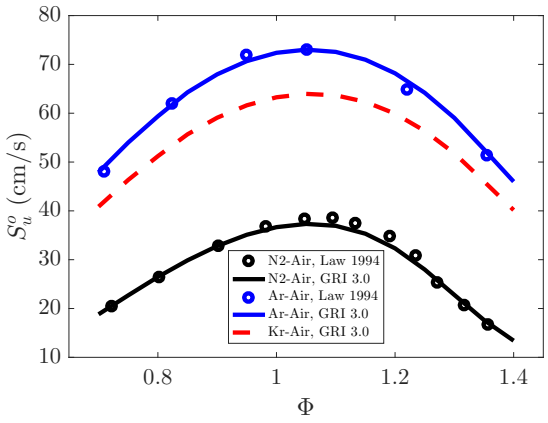

(a) CH_4/Air flame speeds with different inerts at a 79 % - 21 % volumetric inert-oxidizer ratio.

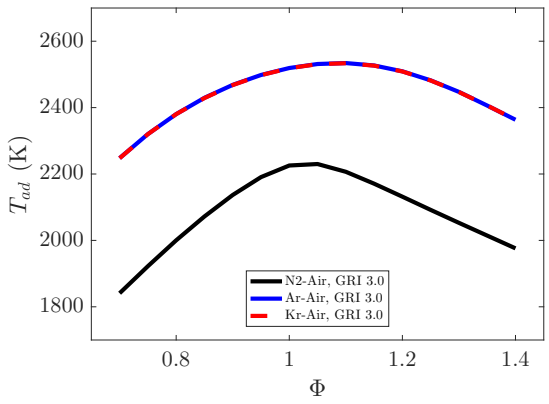

(b) CH_4/Air adiabatic flame temperatures with different inerts at a 79 % - 21 % volumetric inert-oxidizer ratio.

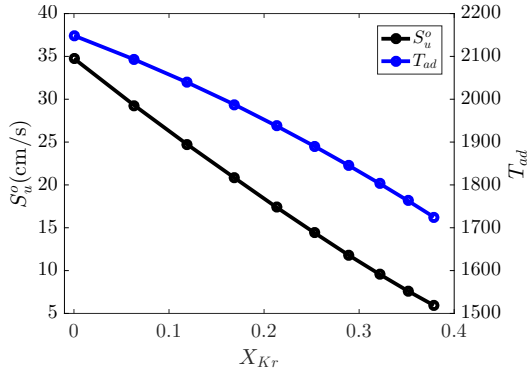

(c) CH_4/air flame speed and adiabatic flame temperature vs. krypton mole fraction (dilution ratio) at $\Phi = 1.18$.

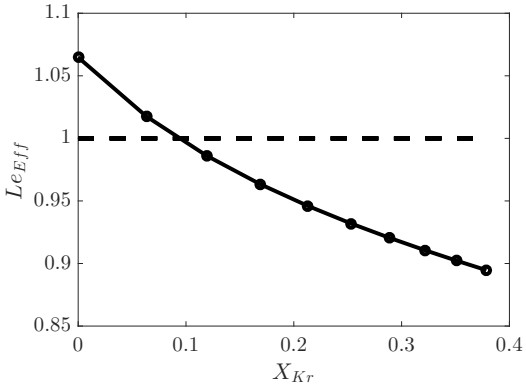

(d) CH_4/air Lewis number vs. krypton mole fraction (dilution ratio) at $\Phi = 1.18$.

Figure 4.5: Premixed flame calculations: (a) flame speed with different inerts (b) flame temperature with different inerts (c) effect of krypton dilution on flame speed and temperature (d) effect of dilution on Lewis number.

remains relatively unchanged when krypton is added, while the thermal conductivity λ decreases substantially (by a factor of three) between air and krypton, leading to a decrease in $Le_{Eff} = \lambda_u/\rho_u c_{p,u}\mathcal{D}_{i,m}$ from 1.1 at $X_{Kr} = 0$ to 0.9 at $X_{Kr} = 0.35$ and $\Phi = 1.18$, where $\mathcal{D}_{i,m}$ is the effective diffusion coefficient of the deficient reactant and all other mixture properties are evaluated in the unburned freestream (Law, 2010).

These changes in diffusive character, such as the crossing of the $Le = 1$ boundary, can

have important effects on flame behavior. From a physical standpoint, for instance, the general integral analysis of Sun et al. (1999) that includes thermal expansion effects gives the following result characterizing the relationship between the unburned laminar flame speed S_u^0 and the value expected for a curved flame in a nonuniform flow field, S_u,

$$\frac{S_u}{S_u^0} = 1 + \frac{Ze}{2}\left(\frac{1}{Le} - 1\right)\frac{\alpha^0 \kappa \delta_T^0}{S_u^0} + \zeta \delta_T^0. \tag{4.3.1}$$

with $Ze = E_A(T_b - T_u)/R_u T_b^2$ the Zeldovich number, E_A the activation energy, κ the strain rate, ζ the curvature, and δ_T the flame thickness. As demonstrated by Eq. 4.3.1, the decrease in *Le* resultant from krypton dilution (as shown in Fig. 4.5(d)) can cause reversal of expected Lewis number effects in mixtures with $Le > 1$ and enhance such effects in mixtures with $Le < 1$.

Finally, looking towards later 2-D simulations and experimental analysis in Sec. 4.4.2, it is useful to assess the effect of krypton dilution on the structure of the flame as well as to evaluate the importance of detailed diffusion models in simulating these effects. Figure 4.6, for instance, presents the results of 1-D premixed flame calculations at $\Phi = 1.18$ for dilution ratios of $X_{Kr} = 0$ and $X_{Kr} = 0.35$. Decrease in the the peak temperature and extension of the flame region with added krypton can be directly observed, while both thermodiffusion and full multicomponent diffusion minimally affect the results of the krypton-diluted case. Additionally, it is helpful to note that the krypton mole fraction does change significantly across the flame front, and particularly so in rich combustion, due to an increase in the overall particle density resultant from the combustion reaction. In Fig. 4.6(b), this drop has a maximum value of 2.8% of the nominal X_{Kr} while the post-flame equilibrium value represents a 2.3% drop with respect to the nominal value. This observation will become particularly important when assessing sources of uncertainty in inferred temperature measurements in Chap. 5.

As a useful secondary investigation, we present 1-D results analogous to those in Fig. 4.6(b) for conditions (b)-(e) of Table 4.1 in Fig. 4.7. Note that condition (a) contains no krypton, and thus is not represented in these results, and condition (e) contains so much krypton and so little oxidizer that it is most appropriate to use a diffusion flame calculation assuming reaction with small amounts of entrained air as opposed to a premixed flame

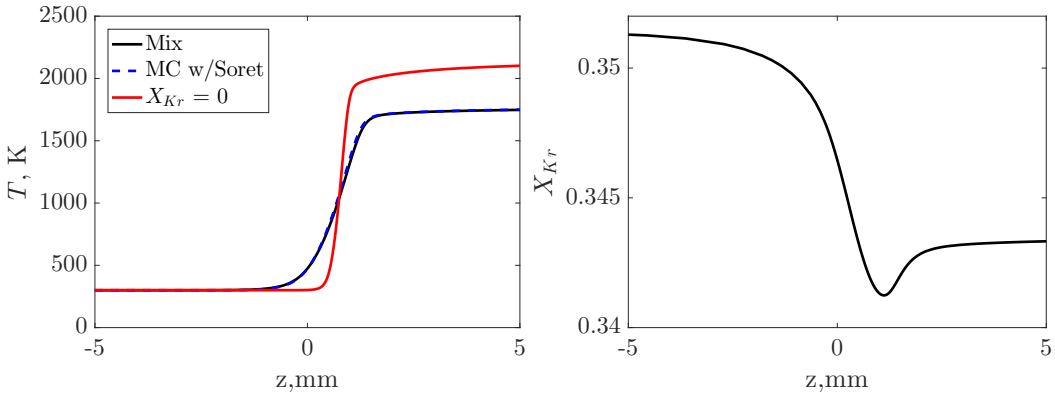

(a) Temperature (b) X_{Kr}, Condition (c)

Figure 4.6: Premixed flame calculation results showing (a) the effects of krypton dilution and multicomponent diffusion on flame temperature profile and (b) drop in krypton mole fraction across the flame due to intermediate production and non-equimolarity. Profiles are centered at the point of maximum density decrease for the $X_{Kr} = 0.35$, $\Phi = 1.18$ case.

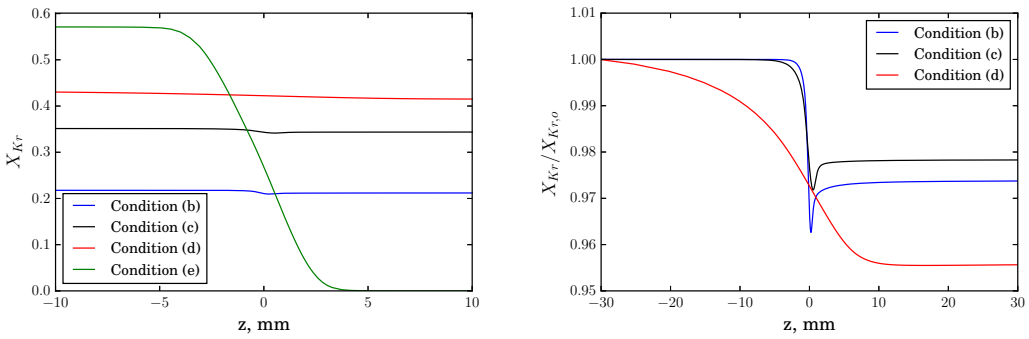

(a) X_{Kr}, Conditions (b)-(e) (b) $X_{Kr}/X_{Kr,o}$, Conditions (b)-(d)

Figure 4.7: Changes in X_{Kr} across the flame front in terms of absolute (a) for conditions (b)-(e) from Table 4.1 and normalized (b) quantities for premixed calculations at conditions (b) - (d) from Table 4.1. Normalization is performed by dividing X_{Kr} at each point by the nominal inlet value given in Table 4.1.

calculation. In Fig. 4.7(a), we observe that the drop in krypton mole fraction across the flame front occurs for each flame, but is substantially more spatially compact for conditions (b) and (c), where the equivalence ratio is relatively near to stoichiometric. As the air is removed from condition (c) to condition (d), flame speed decreases due to

increases in both diluent concentration and excess fuel. Finally, at condition (e), the predicted diffusion flame front is elongated, as would be expected – note that oxidizer (air) mass flux was set at 25% of the fuel stream mass flux. As shown in the normalized results of Fig. 4.7(b), the elongated flame at condition (d) also exhibits a larger relative krypton drop across the flame front than do the flames at conditions (b) and (c), which behave in relatively similar fashion to one another.

4.4 Analysis of Reconstructed Tomographic Data

We proceed by analyzing the reconstructed attenuation fields from these experiments. Note that the long-duration tomographic experiments were performed at condition (c) from the radiography study in Table 4.1.

4.4.1 3-D Reconstructions and Simultaneous Chemiluminescence

In the context of the long-duration tomographic experiment, Figs. 4.8 and 4.9 demonstrate reconstructed attenuation fields using averages of one, ten, and fifty tomographic acquisitions, as will be analyzed further in Section 4.5. For comparison, we also show an Abel inversion computed from the average of all 31250 registered projections from the fifty-acquisition tomographic dataset. As Fig. 4.9 clearly shows, the expected spatial profile of the conical Bunsen flame is apparent. A cone angle of 12^o can be extracted from the shoulder region of any of various attenuation isosurfaces in the vicinity of the flame front, and this is well in line with the average expected angle given the observed height and known diameter of the flame. Note that the reduced flame speed resultant from the krypton diluent enables support of such a small cone angle at laminar conditions. Further, while for the axisymmetric Bunsen flame the Abel inversion shown in Fig. 4.9(d) is a natural reconstruction procedure, the equivalent tomographic reconstruction found in Fig. 4.9(c) has the advantage of general applicability to non-axisymmetric subjects.

To better visualize spatial changes within the attenuation field, we approximate the gradient of the attenuation field in three Cartesian dimensions via a Sobel operator to obtain an experimental attenuation gradient magnitude field shown in Fig. 4.10. The Sobel operator, described in detail by Danielsson and Seger (1990), is an isotropic discrete differentiation operator that is often used to compute gradients in the field of image

processing. The Sobel gradient in a given direction represents the convolution of a central-difference kernel in the derivative direction with a triangle filter in the transverse directions (Danielsson and Seger, 1990). In the x, direction, for instance, the kernel h_x is:

$$h_x(-1,:,:) = \begin{bmatrix} -1 & -3 & -1 \\ -3 & -6 & -3 \\ -1 & -3 & -1 \end{bmatrix}, \; h_x(0,:,:) = \begin{bmatrix} 0 & 0 & 0 \\ 0 & 0 & 0 \\ 0 & 0 & 0 \end{bmatrix}, h_x(1,:,:) = \begin{bmatrix} 1 & 3 & 1 \\ 3 & 6 & 3 \\ 1 & 3 & 1 \end{bmatrix} \quad (4.4.2)$$

The Sobel transform is commonly used in image processing to compute image gradients efficiently and isotropically while minimizing high-frequency noise via smoothing provided by the triangle filter (Danielsson and Seger, 1990). Thus, while the gradient magnitude field presented here is computed numerically from an experimental field and may therefore contain some spurious noise and smoothing, the purpose of this procedure is to demonstrate the spatial locations of most rapid attenuation change. As expected, the Abel inversion in Fig. 4.10(b) using all 31250 projections gives a less noisy result than tomographic reconstruction of those exact same projections shown in Fig. 4.10(a), but this comes at the cost of requiring the assumption of axisymmetry. As is also apparent from Figs. 4.9(d) and 4.10(b), the Abel inversion procedure can also enhance small artifacts, particularly near the centerline. This gradient visualization yields several useful insights. First, the average value of the X-ray gradient magnitude within the flame region tends to decrease with height – this is in agreement with the physical reality that as unburned gas moves upwards within the negatively curved Bunsen flame, each element of gas is closer in proximity to a larger flame surface area, meaning that preheat is expected to slightly increase with vertical position in the flame while reactant diffusion is also enhanced (Mungal et al., 1995). Very similar observations regarding the presence and phenomenology of increased preheat thickness near the flame tip have been made in such work as the experiments of Mungal et al. (1995) and the numerical calculations of Poinsot et al. (1992). This is particularly true at the flame tip, where we see an attenuation gradient value less than half of that observed at the base. Note that despite the reduced gradient signal at the top of the flame, flame tip opening of the type described by Law et al. (1982) was not observed in these experiments.

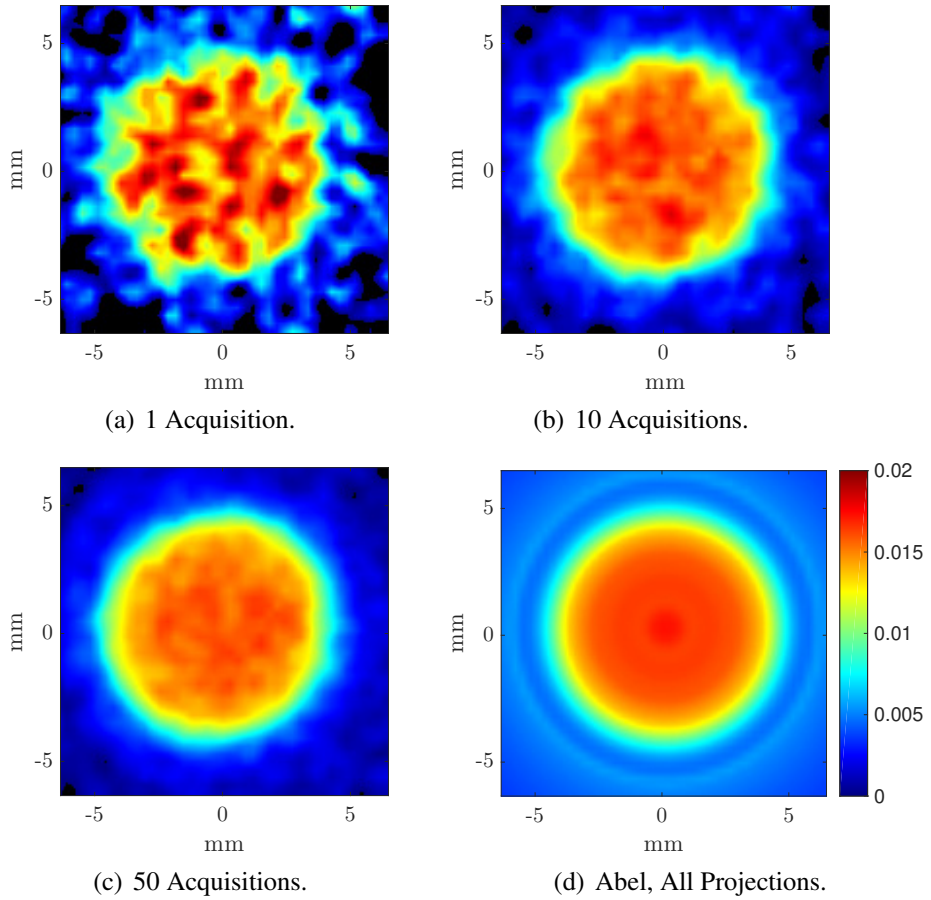

(a) 1 Acquisition.

(b) 10 Acquisitions.

(c) 50 Acquisitions.

(d) Abel, All Projections.

Figure 4.8: Horizontal cross-sections of $\Delta\bar{\mu}$ in cm^{-1} at a height of 1.2 mm above the burner exit. Each acquisition contains 625 projections. These images describe experiments nominally performed at condition (c) in Table 4.1.

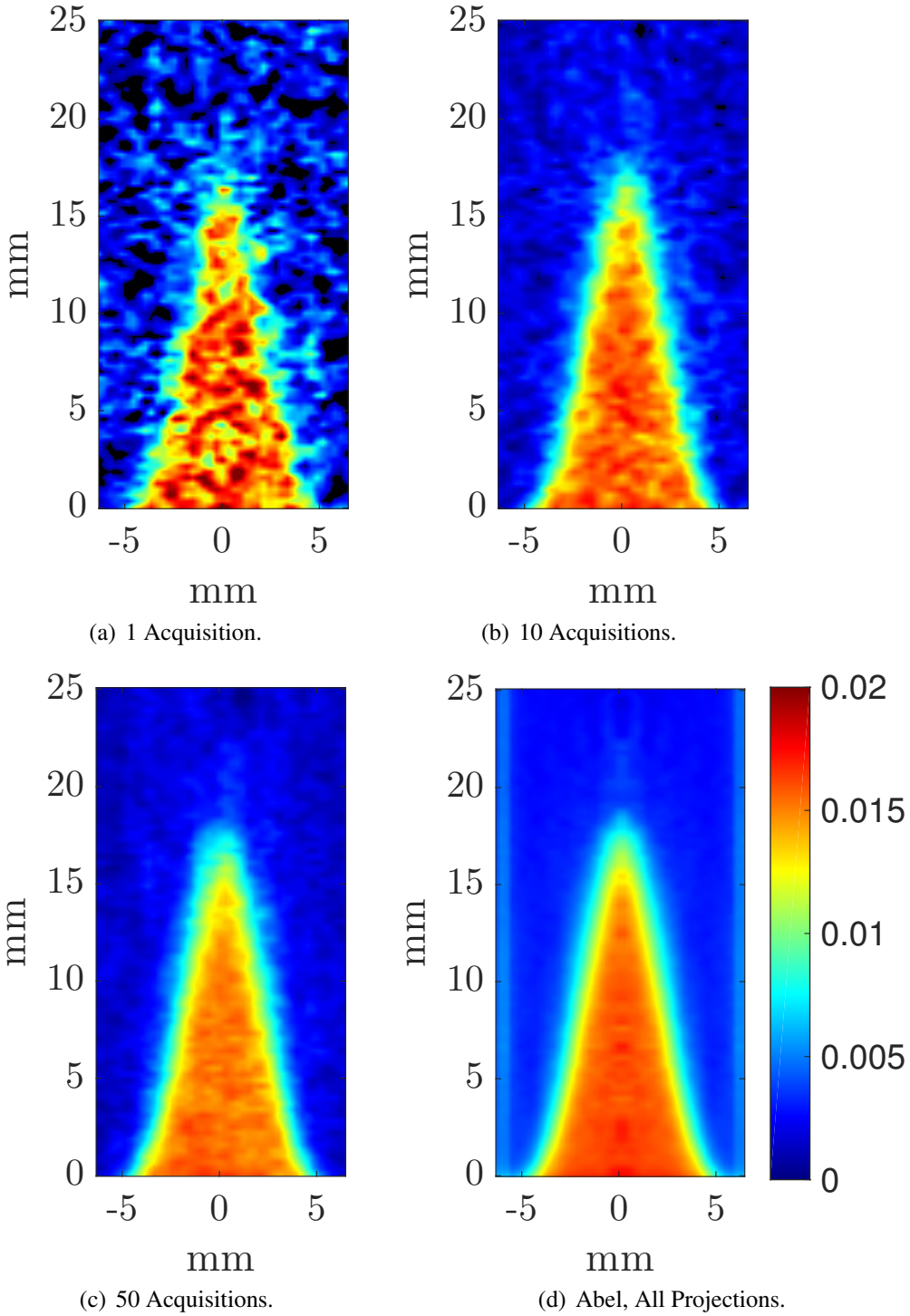

(a) 1 Acquisition.

(b) 10 Acquisitions.

(c) 50 Acquisitions.

(d) Abel, All Projections.

Figure 4.9: Vertical centerline cross-sections of $\Delta\bar{\mu}$ in cm^{-1}. Each acquisition contains 625 projections. These images describe experiments nominally performed at condition (c) in Table 4.1.

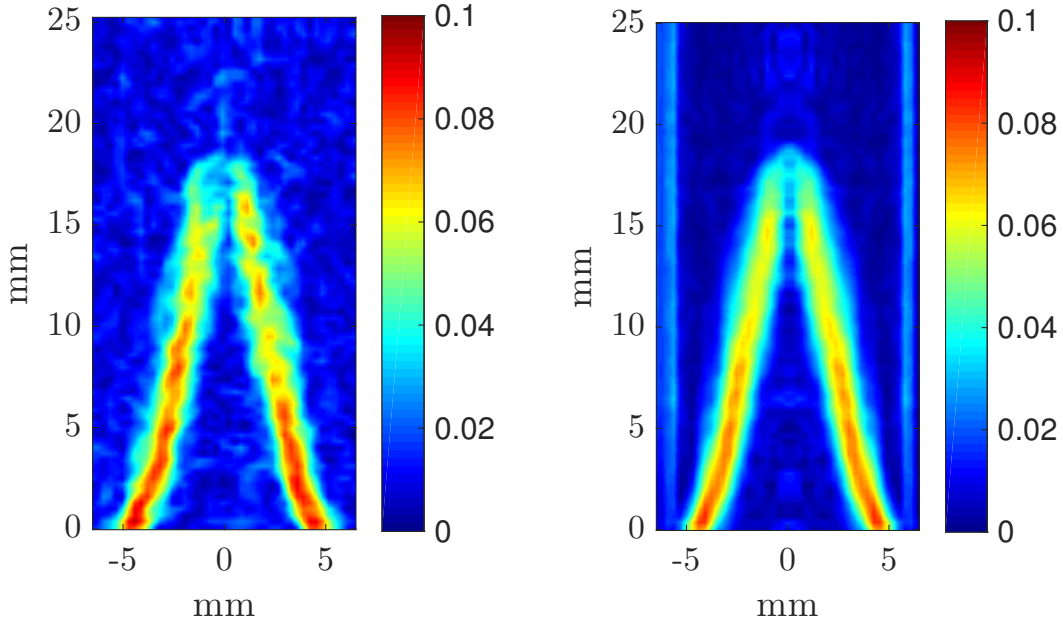

(a) 50 Acquisitions. (b) Abel, All Projections.

Figure 4.10: Cross sections of $|\nabla(\Delta\bar{\mu})|$ in cm^{-2} from (a) tomography and (b) Abel inversion from all 31250 registered projections. These fields were computed numerically using a 3-D Sobel transform. These images describe experiments nominally performed at condition (c) in Table 4.1.

At this point, we proceed to a comparison between XCT results and those of visible chemiluminescence in the style of Xu et al. (2015), who use simultaneous Mie scattering and tomographic chemiluminescence data to demonstrate the physical differences between these two diagnostics. Comparison between a chemiluminescence signal representing the reaction zone and that of a secondary method such as PIV or Mie scattering wherein a particle-based tracer can be used to identify the upstream vicinity of the zone of rapid temperature rise has also been previously demonstrated by such workers as Mungal et al. (1995). In the case of the X-ray diagnostics shown here, we have suggested that the maximum X-ray gradient surface should occur near to the location at which temperature begins to rise rapidly. Note that in this region, reactions have not yet occurred beyond negligible levels, and composition (and thus X_{Kr}) remains constant to good approximation. As a complement to these X-ray measurements, visible chemiluminescence images were simultaneously recorded using a CMOS camera in order

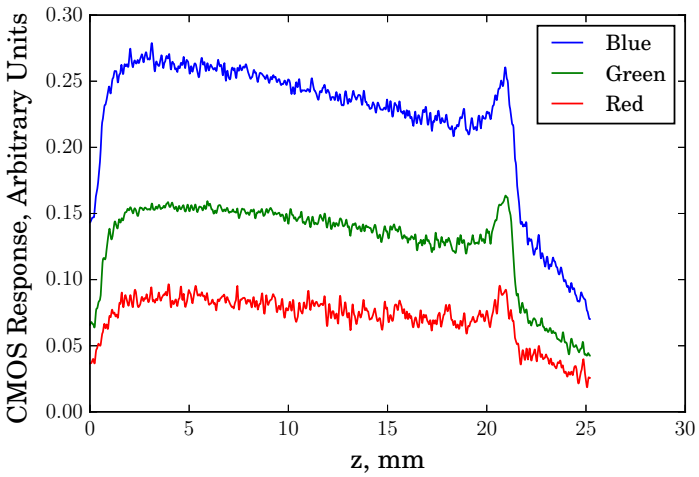

Figure 4.11: Centerline profiles from different CMOS chip channels. These images describe experiments nominally performed at condition (c) in Table 4.1.

to locate the reaction zone. As shown in Fig. 4.11, all channels show sharp falloff at the same height along the axial centerline, which is indicative of the axial extent of the reaction zone. The fact that large emission values are recorded near the base of the flame as well as the tip may result from the line-of-sight nature of this measurement and the fact that the emitting flame area is larger at the base of the flame than near the tip. As in other work such as that of Bouvet et al. (2011) describing optical diagnostics of Bunsen flames, a rapid drop in intensity is expected directly downstream of the reaction zone, and such phenomenology is indeed observed in Fig. 4.11. Increased signal near the peak is in keeping with increased reaction intensity often observed near the tip of Bunsen flames due to the large negative curvature and increased preheating.

Figure 4.12 illustrates the superposition of the experimental X-ray and chemiluminescence profiles, where we use the blue CMOS channel correlated with CH^* emission for the visual signal (Huang and Zhang, 2011). It is immediately apparent that the X-ray profiles are more compact than the chemiluminescence profile in all dimensions, which is reasonable given that the two locations occur near to the unburned and burned gas, respectively. We also observe differences in position between the maximum X-ray gradient and maximum chemiluminescence surfaces of between 1.5 mm and 3 mm, with separation increasing towards the tip of the flame.

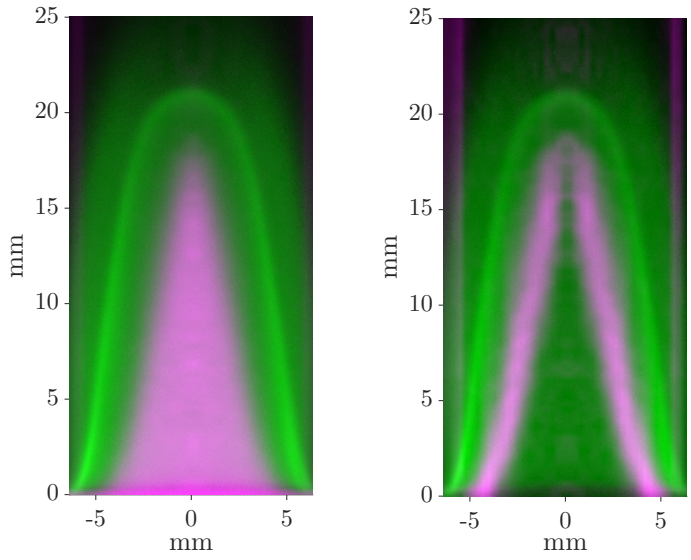

(a) $\Delta\bar{\mu}$+CL (b) $|\nabla(\Delta\bar{\mu})|$+CL

Figure 4.12: Superimposed experimental attenuation and chemiluminescence profiles. Gradient fields were computed numerically using a 3-D Sobel transform. These images describe experiments nominally performed at condition (c) in Table 4.1.

4.4.2 Comparison to Axisymmetric Simulation

At this point, it is useful to utilize high-dimensional simulation capabilities to investigate the effect of krypton addition on laminar flame structure in two dimensions, which will account for such phenomena as flame stretch and strain in comparing to the axisymmetric 3-D results of Sec. 4.4. In particular, it is instructive to investigate experimental observations such as the offset between the X-ray attenuation surface and the visual emission surface correlated with CH^* production via direct simulation. As shown in the 1-D calculations presented above, krypton dilution is generally expected to decrease local laminar flame speeds, increase flame thickness, and reduce flame temperature.

Computational Setup

The computational approach pursued here makes use of the FLUENT solver (Ansys, Inc., 2009), and verification was performed via comparison of the current modeling procedure to both the free-flame case of Chander and Ray (2008) as well as the detailed species, temperature, and velocity fields reported by Bennett et al. (1999) in their computational

analysis of a rich, axisymmetric Bunsen flame. The verification case, procedure, and results are described in detail in Appendix B. The general setup of the problem of interest here can be observed in Fig. 4.13. We consider a premixed, axisymmetric Bunsen flame stabilized on a burner head. The computational domain spans $-175 < z < 250$ mm in the axial direction and $0 < r < 46$ mm in the radial direction, where $z = 0$ is the burner exit plane. Boundary conditions are enforced as follows, with the goal of maximizing alignment between experimental and computational configurations:

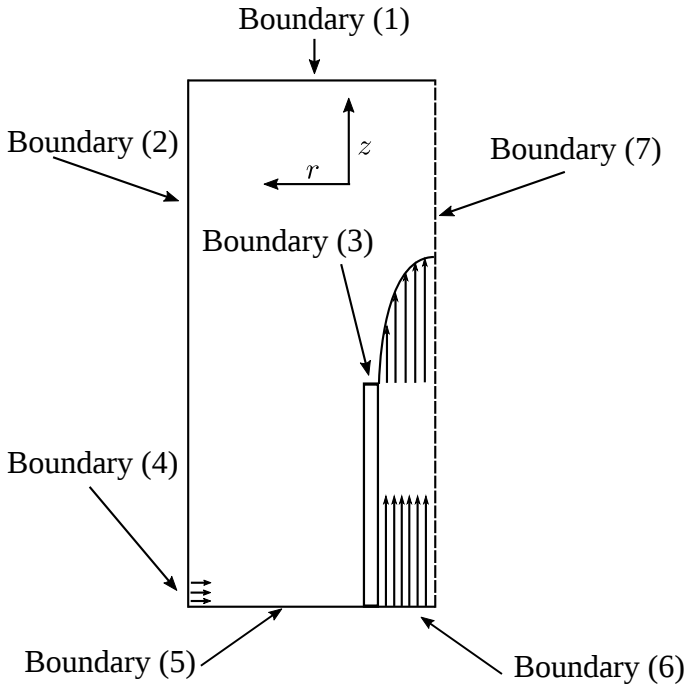

Figure 4.13: Calculation schematic.

- Boundary (1): Outflow, $0 < r < 46$ mm, $z = 250$ mm; $\partial()/\partial_z = 0$, p is extrapolated. In addition to being a reasonable replication of the experimental setup, the 250 mm post-burner axial location of the outflow boundary has been shown to be of sufficient extent to be sufficiently far away from the flame for practical purposes (Bennett et al., 1999).

- Boundary (2): Wall (no-slip); $r = 46$ mm, $-175 < z < 250$ mm; $T = 300$ K, $X = X_{air}$.

- Boundary (3): Wall (no-slip); $4.75 < r < 6.25$ mm, $-175 < z < 0$ mm; $T = 300$ K (enforced at base), steel material properties; conjugate heat transfer and zero species diffusion enforced at fluid interfaces in order to model interaction between the flame and burner head.

- Boundary (4): Velocity inlet, $r = 46$ mm, $-175 < z < -174$ mm, $T = 300$ K, $X = X_{air}$, $v_r = -0.01$ m/s; this inlet models the unsealed junction between the plastic tube and rotary motor plate.

- Boundary (5): Wall, $T = 300$ K, $X = X_{air}$; $6.25 < r < 46$ mm, $z = -175$ mm; This wall models the rotary motor plate.

- Boundary (6): Velocity Inlet; $0 < r < 4.75$ mm, $z = -175$ mm, $T = 300$ K, $\Phi = 1.18 \pm 0.24$, $X_{Kr} = 0.35 \pm 0.03$, $v_r = 0$, $v_z = 30 \pm 2$ cm/s (indicated as nominal conditions $\pm$ experimental uncertainty); this inlet models the flow exiting the through-motor-plate section into the burner tube. Simulating this uniform inlet over the length of the tube leads to a burner outlet that is very nearly fully developed with $v_z(z = 0) \approx 2v_z(z = -175 \text{ mm}) \left[1 - \left(\frac{r}{R}\right)^2\right]$ for $R = 4.75$ mm.

- Boundary (7): Axisymmetry, $\partial()/\partial_r = 0$, $v_r = 0$; $r = 0$ mm, $-175 < z < 250$ mm

The computational mesh utilized here was very similar to that of Chander and Ray (2008), which was in turn based on that of Kleijn (2001). A fine mesh of size $\Delta r = 50\mu$m x $\Delta z = 100\mu$m was utilized for the flame region ($0 < r < 10$ mm and $0 < z < 25$ mm), with smooth expansion from to a cell size of $30\Delta r$ as $r \to 46$ mm and an expansion to $30\Delta z$ as $z \to 250$ mm. A similar rate of expansion was enforced in the $-z$ direction from $-175 < z < 0$ mm. Following Chander and Ray (2008), second order upwinding was used for all spatial discretizations, and an implicit, double-precision, segregated solver using the SIMPLE algorithm was utilized. Finite-rate chemistry is modeled using the same augmented GRI 3.0 mechanism developed for the the above 1-D calculations. This mechanism contains 56 species and adds the krypton atom and the CH^* sub-mechanism of Kojima et al. (2005) to the baseline GRI 3.0 mechanism. Kinetic theory expressions were

used to compute the viscosity and thermal conductivity λ as,

$$\mu = 2.67 \times 10^{-6} \frac{\sqrt{WT}}{\sigma^2 \Omega_\mu} \tag{4.4.3}$$

$$\lambda = \frac{15}{4} \frac{R_u}{W} \mu \left[\frac{4}{15} \frac{c_p W}{R_u} + \frac{1}{3} \right] \tag{4.4.4}$$

where $\Omega_\mu = \Omega_\mu(T^*)$, $T^* = \varepsilon/k_B$, and ε/k_B and σ are the Lennard-Jones energy parameter and characteristic length, respectively. Mixture values for these properties are computed using the Wilke approximation,

$$\mu = \sum_i \frac{X_i \mu_i}{\sum_j X_i \phi_{ij}} \tag{4.4.5}$$

$$\lambda = \sum_i \frac{X_i \lambda_i}{\sum_j X_i \phi_{ij}} \tag{4.4.6}$$

$$\text{where } \phi_{ij} = \frac{\left[1 + \frac{\mu_i}{\mu_j}^{1/2} + \frac{W_j}{W_i}^{1/4} \right]^2}{\left[8 \left(1 + \frac{W_i}{W_j} \right) \right]^{1/2}} \tag{4.4.7}$$

Heat capacities for each species are computed using the tabulated NASA polynomials of the form (Burcat, 1984),

$$c_p = \sum_{i=-2}^{5} a_i T^i, \tag{4.4.8}$$

while mixture values are computed using the simple mixing rule,

$$c_p = \sum_i Y_i c_{p,i}. \tag{4.4.9}$$

Mass diffusivities are computed from the Chapman-Enskog equation derived from kinetic theory McGee (1991),

$$\mathcal{D}_{ij} = 0.00188 \frac{\left[T^3 \left(\frac{1}{W_i} + \frac{1}{W_j} \right) \right]^{1/2}}{p \sigma_{ij}^2 \Omega_D} \tag{4.4.10}$$

where Ω_D is a temperature-dependent collision integral related to the Lennard-Jones energy parameters of species i and j and σ_{ij} is the arithmetic average of their characteristic Lennard-Jones length. Similarly to the 1-D calculations, initial results showed little sensitivity to different approximations for diffusive mass flux, including full multicomponent diffusion, mixture-averaged diffusion with the Soret effect, and mixture-averaged diffusion without the Soret effect. Thus, we neglect the Soret and Dufour effects and utilize a purely Fickian diffusion model to calculate the diffusive mass flux j_i of species i,

$$j_i = -\rho \mathcal{D}_{i,m} \nabla Y_i, \tag{4.4.11}$$

where the diffusion coefficient of species i into the mixture is,

$$\mathcal{D}_{i,m} = \frac{1 - Y_i}{\sum_{j \neq i} (X_j / \mathcal{D}_{ij})}. \tag{4.4.12}$$

We also enforce gravitational acceleration in this simulation to accurately represent buoyancy forces. Finally, we model radiation using a narrow-band optically thin radiation model due to Grosshandler (1993), which has been shown to be appropriate for a variety of optically-thin combustion environments as a less expensive alternative to more complex methods such as discrete ordinates (Bennett et al., 1999; Chen et al., 2007; Coelho et al., 2003). In this model, the radiative flux can be written,

$$Q = 4\sigma \sum_{\alpha} a_{p,\alpha} p_\alpha (T^4 - T_B^2) \tag{4.4.13}$$

with σ the Stefan-Boltzmann constant, T the local temperature, T_B the background temperature, and $a_{p,\alpha}$ the mean Planck absorption coefficient of species α, for $\alpha \in \{\mathrm{CO}, \mathrm{CO_2}, \mathrm{H_2O}, \mathrm{CH_4}\}$.

Solution Procedure

The procedure for this calculation was heavily based on that of Chander and Ray (2008). First, initial values for velocity, temperature, mass fractions of oxygen and methane set to

constant values over entire computational domain. The non-reacting flowfield was then calculated with species and mass/momentum conservation active. The solution was run for several thousand iterations until the residuals for velocities ceased changing. A spark of radius 2 mm was then provided directly above the burner at a position of $z = 5$ mm. Once ignition took place, under-relaxation factors were set to 0.5 and 0.3 respectively, and the simulation was run for several thousand iterations until residuals began to stabilize. Under-relaxation factors were then increased to unity, and the solution was then iterated to convergence. For parametric studies, previous solutions were used to initialize solutions for new conditions. Convergence guidance for the FLUENT solver is given in the solver documentation; for these calculations, the following criteria were observed, which are similar to those in Chander and Ray (2008):

- Scaled continuity residuals are below 10^{-5}
- Scaled energy residuals are below 10^{-6}
- Scaled species residuals for all species are below 10^{-5} – this is limited by the most minor species, meaning that most species residuals are O(10^{-6}) when calculations are completed.
- Integrated mass flux imbalance is negligible

Note that for the pressure-based FLUENT solver, scaled residuals R^{ϕ} are computed as follows (Ansys, Inc., 2009),

$$R^{\phi} = \frac{\sum_P |\sum_{nb} a_{nb}\phi_{nb} + b - a_P\phi_P|}{\sum_P |a_P\phi_P|}, \tag{4.4.14}$$

where P is an index over cells, nb indicates all neighbors of a cell, and the general conservation equation for a variable ϕ at cell P is expressed as (Ansys, Inc., 2009),

$$a_P\phi_P = \sum_{nb} a_{nb}\phi_{nb} + b. \tag{4.4.15}$$

For context, the FLUENT documentation prescribes a decrease in the scaled residual to 10^{-6} for the energy equation and 10^{-3} for all other equations as sufficient for convergence in most problems (Ansys, Inc., 2009).

Simulation Analysis and Comparison to Experiment

A this point, we will compare and contrast the experiments and computations performed at condition (c) from Table 4.1. Before beginning such an analysis, however, it is important to comment on the impact of uncertainty in experimental inlet conditions on simulation results. Specifically, due to hardware constraints, variation within rated rotameter limits leads to worst-case flow rate variations on the order of 6% of the mean, worst-case krypton mole fraction variations on the order of 10% of the mean, and worst-case variations in the equivalence ratio of 20% of the mean. As discussed in Sec. 4.2.3, this leads to uncertainties of ± 0.24 on the equivalence ratio, ± 2 cm/s on the inlet velocity, and ± 0.03 on the krypton mole fraction, which can have substantial effects on the agreement between the simulated and experimental data.

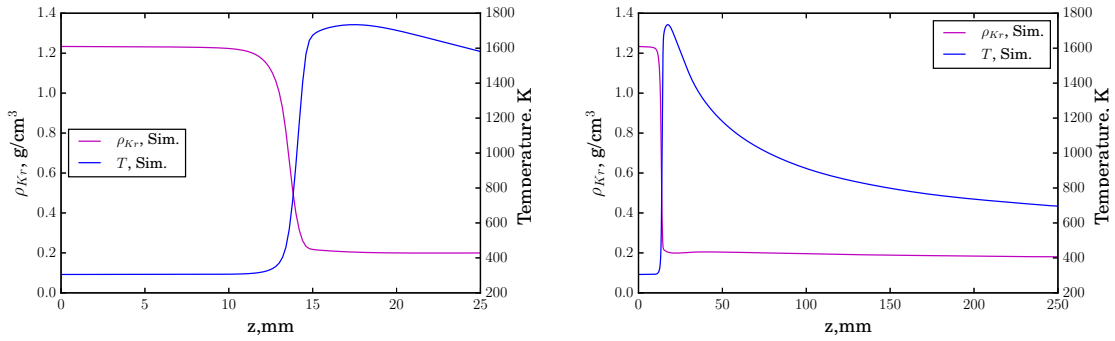

(a) Reduced Domain (b) Full Domain

Figure 4.14: Temperature and partial krypton density curves for simulation of condition (c) from Table 4.1.

Results of FLUENT calculations at condition (c) of Table 4.1 along the axial centerline can be found in Fig. 4.14, where Fig. 4.14(a) shows the domain of experimental interest and Fig. 4.14(b) shows the entire simulated domain downstream of the burner head. Importantly, as expected, simulated partial density of krypton scales directly with $1/T$. As shown in Fig. 4.5(c), at these high krypton dilution ratios, absolute flame speeds are very low and sensitive to the equivalence ratio, which is the parameter that varies most as a result of rotameter uncertainty. For example, computed unstretched laminar flame speed for condition (c) from Table 4.1 with $\Phi = 1.18$ is $S_L^0 = 7.8$ cm/s while the condition

incorporating maximum experimental uncerainty would have a flame speed of $S_L^0 = 2.1$ cm/s at $\Phi = 1.42$ and $X_{Kr} = 0.38$.

A useful comparison to experiment can be made along the axial centerline of the Bunsen flame due to the direct analogy between the simulated krypton partial density ρ_{Kr} and the experimental gas attenuation $\Delta\bar{\mu}$. Specifically, recalling Eq. 2.1.4, ρ_{Kr} and $\Delta\bar{\mu}$ are directly proportional, with the mass attenuation coefficient $\bar{\xi}_{Kr}$ the appropriate constant of proportionality. To compare the simulated ρ_{Kr} and experimental $\Delta\bar{\mu}$ values, we compute a 95% confidence interval on the krypton attenuation from a reconstruction of five scans of a krypton balloon, which yields values of $\Delta\bar{\mu} = 0.042 \pm 0.0058$ cm^{-1}. Using the density of krypton at ambient conditions, we can then leverage Eq. 2.1.4 to calculate an experimental value of $\bar{\xi}_{Kr} = 12.1 \pm 3.3$ cm^2/g, which is in reasonable agreement with direct integration of tabulated ξ_{Kr} values over the 45 kVp scanner spectrum, which yields a value of $\bar{\xi}_{Kr} = 17.6$. Thus, when plotting ρ_{Kr} from experiment, we use the value given by $\rho_{Kr} = \Delta\bar{\mu}/\bar{\xi}_{Kr}$, with uncertainties on $\bar{\xi}$ presented as appropriate. Results describing simulated and experimental

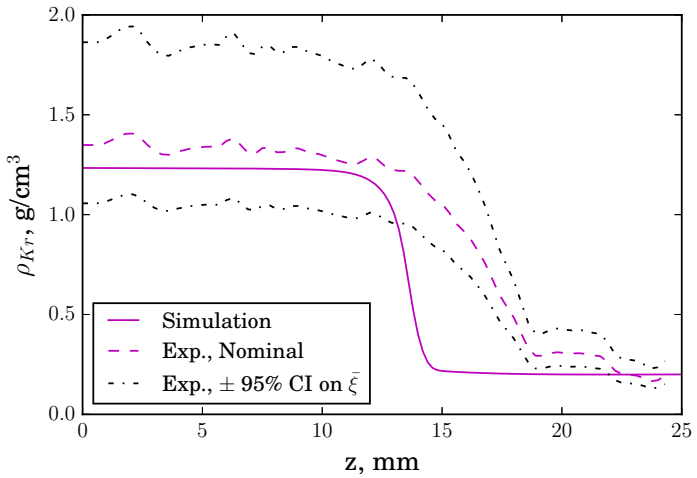

Figure 4.15: Krypton partial density (ρ_{Kr}) quantities for condition (c) from Table 4.1 computed from experiment and simulation with the mass attenuation coefficient indicated.

ρ_{Kr} values with appropriate spread on each quantity can be found in Fig. 4.15. Several trends are immediately noticeable. First, the spread in density resultant from potential spread in the computed mass attenuation coefficient is substantial, but the mean value used here gives ρ_{Kr} results that align well with what is expected given the inlet conditions for this

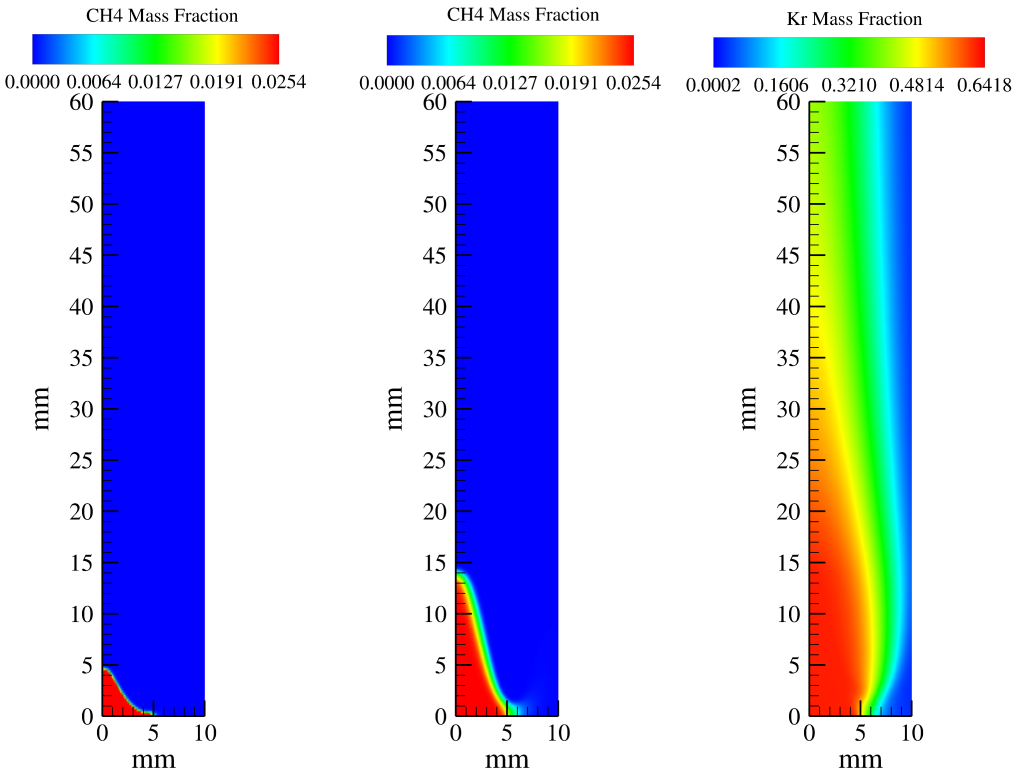

(a) $Y_{CH_4}, X_{Kr} = 0$ (b) Y_{CH_4} (c) Y_{Kr}

Figure 4.16: Contours of Y_{CH_4} and Y_{Kr} for condition (c) from Table 4.1. Note that in (a) the Reynolds number and equivalence ratio are are held constant at $Re = 252$, $\Phi = 1.18$ while the composition changes such that $X_{Kr} = 0$.

condition. Because the $\bar{\xi}$ measurement is indeed a mean over many pixels describing the same material, the error bounds we have prescribed here are conservatively large. Note that due to large uncertainties in the inlet conditions, only qualitative comparison to simulation will be performed here.

At this point, it is useful to present more detailed simulation results both to assess the effect of krypton on the flame in 2-D as well as to enable direct visual comparison to experiment. A natural question to investigate in the context of simulation is the difference between running these calculations with and without a krypton diluent to understand the effect of this diluent directly. Results for the 2-D methane field of the simulation at condition (c) from Table 4.1 both without ($X_{Kr} = 0$) and with ($X_{Kr} = 0.35$) a krypton

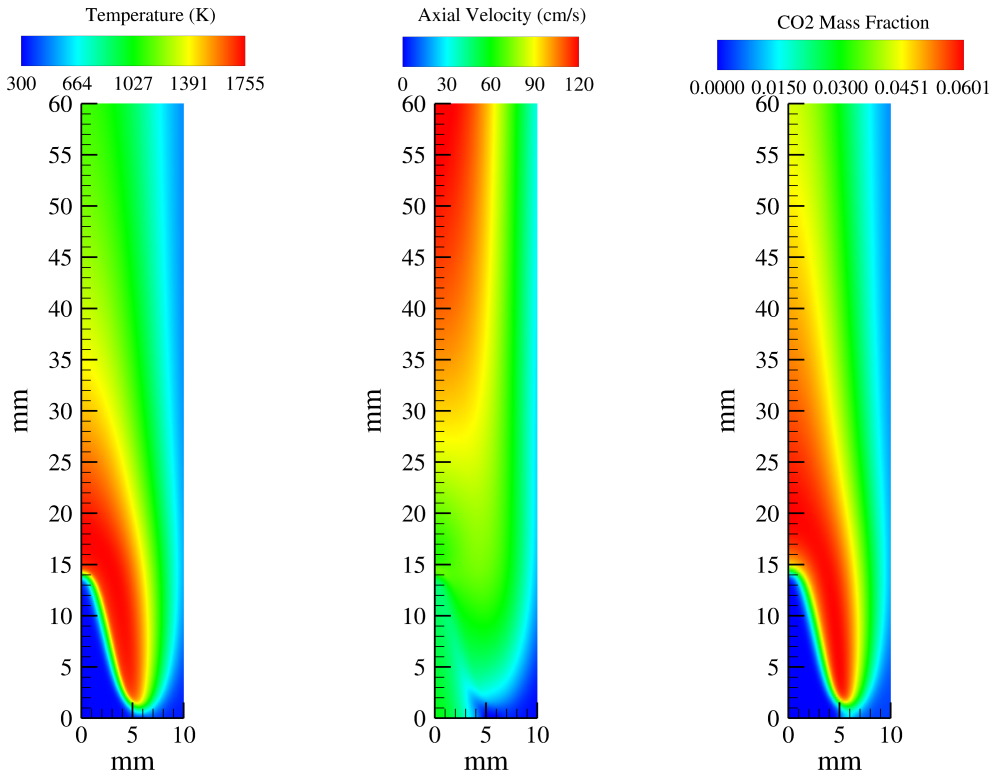

(a) Temperature. (b) Axial Velocity. (c) Y_{CO_2}.

Figure 4.17: Contours of temperature, axial velocity, and Y_{CO_2} for condition (c) from Table 4.1.

diluent are respectively presented in Figs. 4.16(a) and 4.16(b). Note that conditions were maintained at $Re = 252$ and $\Phi = 1.18$ for both cases. Clearly, as expected, the krypton-containing case has a significantly lower flame speed due to dilution with an inert species, though this effect is somewhat mitigated by the low molar heat capacity of krypton resultant from its monatomicity. This same trend is observed in experimental projection radiography data, where flame height increases markedly with krypton addition. We also observe reasonable axial velocity and Y_{CO_2} fields in Figs. 4.17(b) and 4.17(c), respectively. Notably, the temperature field in Fig. 4.17(a) indicates that the inner reaction zone is contained almost entirely by a region of nearly constant krypton mass fraction (as shown in Fig. 4.16(c)), meaning that temperature changes will dominate changes in the attenuation signal, as implied by Fig. 4.14. Additionally, development of a

parabolic burner exit profile can be observed in Fig. 4.18.

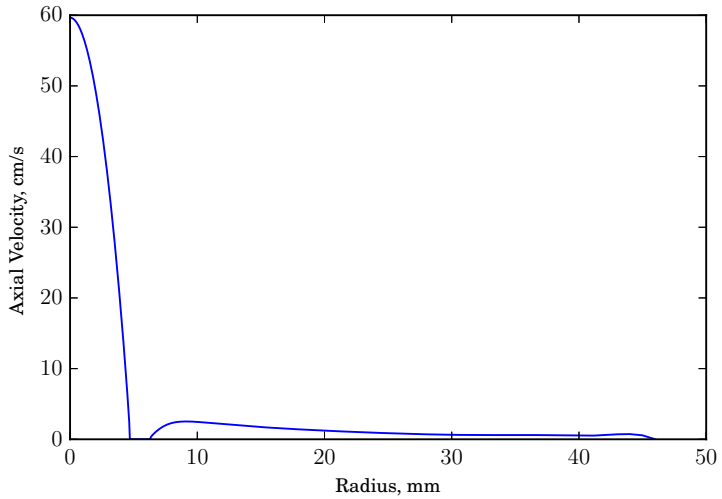

Figure 4.18: Inlet velocity profile for case (c) from Table 4.1.

Finally, Fig. 4.19(a) shows the simulated fields of krypton partial density ($\rho_{Kr} = Y_{Kr}\rho = \Delta\bar{\mu}/\bar{\xi}_{Kr}$) for condition (c) from Table 4.1 superimposed on those of Y_{CH^*}, the activated radical of CH that is correlated with the blue CMOS chip response (Huang and Zhang, 2011). As a reminder, $\Delta\bar{\mu}$ describes the linear X-ray attenuation while $\bar{\xi}_{Kr}$ refers to the mass attenuation coefficient of krypton. Note that the individual CMOS elements of the Nikon D90 camera utilized here have been well documented to have peak blue response between 410 nm and 490 nm, peak green response between 510 and 530 nm, and peak red response between 590 and 610 nm Lesnichii et al. (2013). As documented by Huang and Zhang (2011), these ranges compare favorably with the expected bands of CH^* emission at 430 ± 5 nm and C_2^* at approximately 510 nm documented by Petersen et al. (2012), though it is also expected that activated CO_2 will be a substantial (and potentially dominant) contributor to chemiluminescence in these bands (Petersen et al., 2012). Figure 4.19(b), on the other hand, shows the $\Delta\bar{\mu}$ field reconstructed at the center slice of the experimental krypton-diluted Bunsen flame run at condition (c) from Table 4.1 superimposed on the simultaneously recorded visible luminescence field from the blue channel of the CMOS chip. Clearly, visual emissions correlated with this signal occur significantly downstream of the zone of rapid X-ray attenuation (or partial density) falloff – this is expected, as activated radicals

tend to appear near the downstream end of the reaction zone, while thermal expansion of the gas occurs in the preheat zone. Thus, we see that the spatial relationship between these two experimental surfaces is supported by direct laminar flame calculation. Qualitatively similar trends with respect to the relative location of the CH^* and partial density fields are observed in experiment and in simulations at both conditions, with separation between the two surfaces increasing along the shoulder of the flame with increasing height.

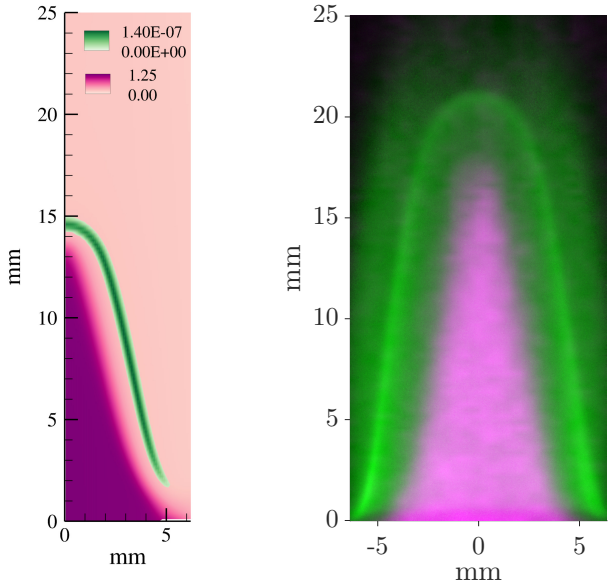

(a) Simulation (b) Experiment

Figure 4.19: Comparison between simulation and experiment, Y_{CH^*}/visual emission (green) and partial density/attenuation (violet) for (a) simulation and (b) experiment at nominal condition (c) from Table 4.1.

At this point, we can draw several useful conclusions from the combination of the X-ray and chemiluminescence signals. A superimposition of experimental and simulated profiles describing both partial krypton density and mass fraction of the CH^* radical can be found in Fig. 4.20. This figure yields several important insights. It is clear from the simulated data, for instance, that the gradient of the X-ray attenuation signal is maximized near to the upstream end of the zone of rapid density decrease (and temperature increase) that defines the thermal flame thickness. Similarly, it is expected that the simulated CH^* radical concentration should spike just as the temperature reaches its maximum – this is supported

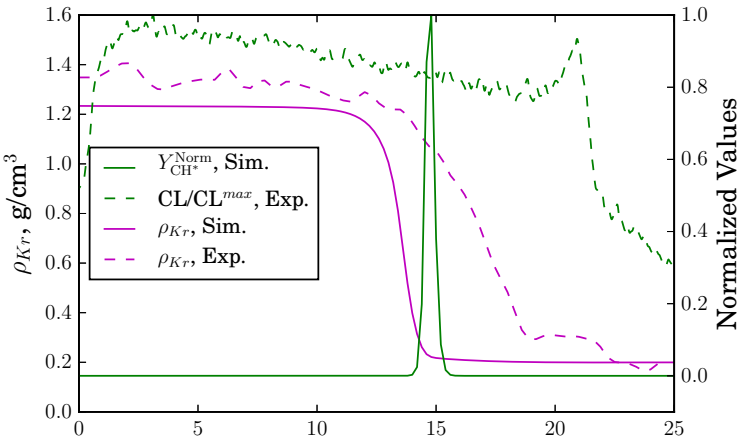

Figure 4.20: Comparison of experimental and simulated centerline quantities describing ρ_{Kr} and visual emission for condition (c) in Table 4.1. Uncertainties on experimental values are shown in Fig. 4.15, and are omitted here for clarity.

by the fact that in both simulated and experimental cases, the large increase in either visual emission or Y_{CH^*} occurs just as density reaches its nearly-burned value.

Following this line of reasoning, the simulation results in Fig. 4.21 enable direct insight into how the combination of X-ray and chemiluminescence data can be used to obtain physically insightful measurements. Specifically, the solid blue line in Fig. 4.21 demonstrates the temperature profile of the simulated case at condition (c) from Table 4.1 with the solid green and violet lines respectively indicating the location of the maximum gradient in the partial density signal and the location of the maximum CH^* mass fraction. Taking z as the coordinate in the flame propagation direction (e.g. the axial coordinate in Fig. 4.21), we can define the X-ray-Chemiluminescence flame thickness as,

$$\delta_{XCL} = z(Y_{\mathrm{CH}^*} = Y^{max}_{\mathrm{CH}^*}) - z(|\nabla\rho| = |\nabla\rho|^{\max}) \tag{4.4.16}$$

and compare this to the traditional thermal flame thickness,

$$\delta_T = (T_b - T_u)/(dT/dz)_{\max}. \tag{4.4.17}$$

In the case simulated above, Fig. 4.16(c) shows that changes in krypton mass fraction are small in the pre-flame region, meaning that,

$$|\nabla \rho_{Kr}| = Y_{Kr}|\nabla \rho| + \rho|\nabla Y_{Kr}| \sim |\nabla \rho|, \tag{4.4.18}$$

and thus that the location of maximum krypton partial density gradient will be a good

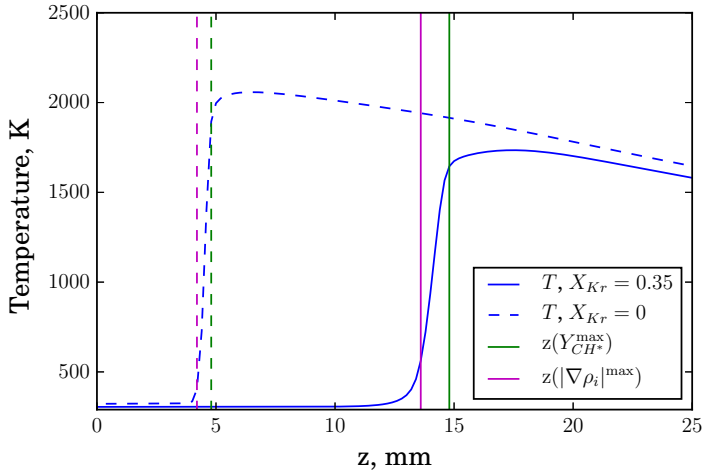

Figure 4.21: Comparison of $X_{Kr} = 0$ (dashed) vs. $X_{Kr} = 0.35$ (solid) cases for $\Phi = 1.18$, $Re = 252$ as in condition (c) of Table 4.1.

approximation of the location of maximum overall density gradient. For case (c) from Table 4.1), we compute $\delta_{XCL} = 1.20$ mm while $\delta_T = 1.29$ mm. As shown in the dashed lines in Fig. 4.21, which represents the equivalent of case (c) with $X_{Kr} = 0$, $\Phi = 1.18$, and Reynolds number held constant at $Re = 252$, we can compute this exact same set of metrics by directly using $|\nabla \rho|$ instead of $|\nabla \rho_{Kr}|$. Again, we see that the two values are very similar, with $\delta_{XCL} = 0.60$ mm and $\delta_T = 0.56$ mm. Differences between δ_{XCL} and δ_T are on the order of 7% in both cases, indicating that this agreement is insensitive to krypton diluent concentration.

Using these ideas, we can re-examine the results of Fig. 4.12, which shows that the distance between the X-ray and optical surfaces increases towards the tip of the flame. Specifically, in light of this analysis, as the distance between the X-ray gradient surface and the visible emission surface increases towards the top of the flame, the thickness of

the flame region itself is increasing, which can result from a variety of physical effects. In particular, these results are reminiscent of those of Mungal et al. (1995), who observed a consistent distance of 0.3 mm between a surface defined by seeded particles and that of a flame image along the shoulder of the flame, but also observed a larger difference of 1.4 mm at the flame tip. Mungal et al. (1995) explain this phenomenon by pointing out that merging of the preheat zones near the tip of the Bunsen flame leads to velocity and temperature changes that occur well upstream of the visual emission surface. Also worth considering is the work of Xu et al. (2015), who show that the surface obtained from oil droplet evaporation (via Mie scattering) in a methane-air flame behaves similarly to the X-ray gradient surface in terms of positioning relative to the optical signal. In their work, the difference between the two signals is shown to lie between 0.5 mm and 1.5 mm. In addition to the high equivalence ratio, a major reason that the X-ray gradient and chemiluminescence surfaces are separated by larger distances here than observed between by Xu et al. (2015) or Mungal et al. (1995) is the fact that, as shown in Fig. 4.21, diluting the mixture with additional inert causes substantial decrease in the flame speed and extension of the preheat zone compared to the undiluted case studied in other contexts.

4.4.3 Model Assessment

Before proceeding on from this section, it is helpful to clarify the fact that while radiation and conjugate heat transfer models were included in these calculations due to their relative lack of expense in a fully-laminar calculation performed using commercial code and potential to improve physical accuracy, these phenomena were not necessarily expected to have a dominant effect on the results shown here. Estimates of the importance of each of these heat transfer modes can be performed by relating the expected heat loss from each mode to the total heat released by the flame, in the spirit of analyses such as Lee et al. (2011). We consider the following nondimensional quantities here,

$$\mathcal{C} = \frac{\text{Heat Loss to Surface}}{\text{Heat Release}} = \frac{Q_{BH}}{Q_{HR}} = \frac{q_{TSF} A_{BH}}{Q_{HR}}, \tag{4.4.19}$$

$$\mathcal{R} = \frac{\text{Radiative Heat Loss}}{\text{Heat Release}} = \frac{Q_R}{Q_{HR}} = \frac{q_R'^{max} A_{\mathrm{F}} \delta_T}{Q_{HR}}, \tag{4.4.20}$$

Quantity	Variable	Value	Source
Inner Radius	r_i	4.75 mm	Burner measurement
Outer Radius	r_o	6.25 mm	Burner measurement
Flame Height	h	15 mm	Simulation
CH_4 Mole Fraction	X_{CH_4}	0.072	Flow rate measurement
Inlet Velocity	u_o	0.3 m/s	Flow rate measurement
Surface Heat Flux	q_{TSF}	1.773×10^4 W/m^2	Simulation
Thermal Flame Thickness	δ_T	1.29 mm	Simulation
Volumetric Radiative Loss	$q_R^{\prime\, max}$	3.5×10^6 W/m^3	Simulation
CH_4 Lower Heating Value	LHV_{CH_4}	50 MJ/kg	Standard
CH_4 Density	ρ_{CH_4}	0.656 kg/m^3	Standard

Table 4.2: Table of values for heat transfer analysis.

where Q_{BH} is the total rate of heat loss to the burner head, q_{TSF} is the total surface heat flux flux at the burner head, A_{BF} is the area of the the burner head, Q_R is the total rate of heat loss to radiation, $q_R^{\prime\, max}$ is the maximum simulated value of the volumetric rate of radiative heat loss, A_F is the flame surface area, δ_T is the thermal flame thickness, and Q_{HR} is the total rate of heat release. Computing the relevant heat transfer rates using values given in Table 4.2 gives,

$$Q_R = q_R^{\prime\, max} \delta_T \pi r_i \left(r_i + \sqrt{r_i^2 + h^2} \right) = 1.4 \text{ W}, \tag{4.4.21}$$

$$Q_{BH} = q_{TSF} \times \pi (r_o^2 - r_i^2) = 0.91 \text{ W}, \tag{4.4.22}$$

$$Q_{HR} = q_{CH_4} LHV_{CH_4} \rho_{CH_4} = u_o X_{CH_4} \pi r_i^2 LHV_{CH_4} \rho_{CH_4} = 50.1 \text{ W}. \tag{4.4.23}$$

Thus, from these values, we have $\mathcal{R} = 2.8\%$ and $\mathcal{C} = 1.8\%$. Given that the magnitude of heat transfer to the burner head is only 2% of the overall heat release, it appears that conjugate heat transfer is likely not a modeling necessity to obtain reasonably accurate results for these simulations from a thermodynamic point of view. However, it is important to note that even small amounts of conjugate heat transfer may be important for flame stabilization, and less diluted flames (e.g. the $X_{Kr} = 0$ cases) showed substantially higher surface heat fluxes than the krypton-containing cases. As far as radiation is concerned, we again see only a small contribution to the physics of this problem, and the radiation estimate

presented here certainly overpredicts heat loss because it does not consider self-radiation and uses the full thermal flame thickness when computing the volume of fluid radiating at maximum simulated intensity. Importantly, then, even if radiation and conjugate heat transfer were neglected for this particular set of calculations, overall heat transfer errors would be at most 5%, indicating that detailed consideration of radiation and conjugate heat transfer are not necessarily required for accurate simulation results for the particular flame under consideration here.

4.5 Noise Analysis

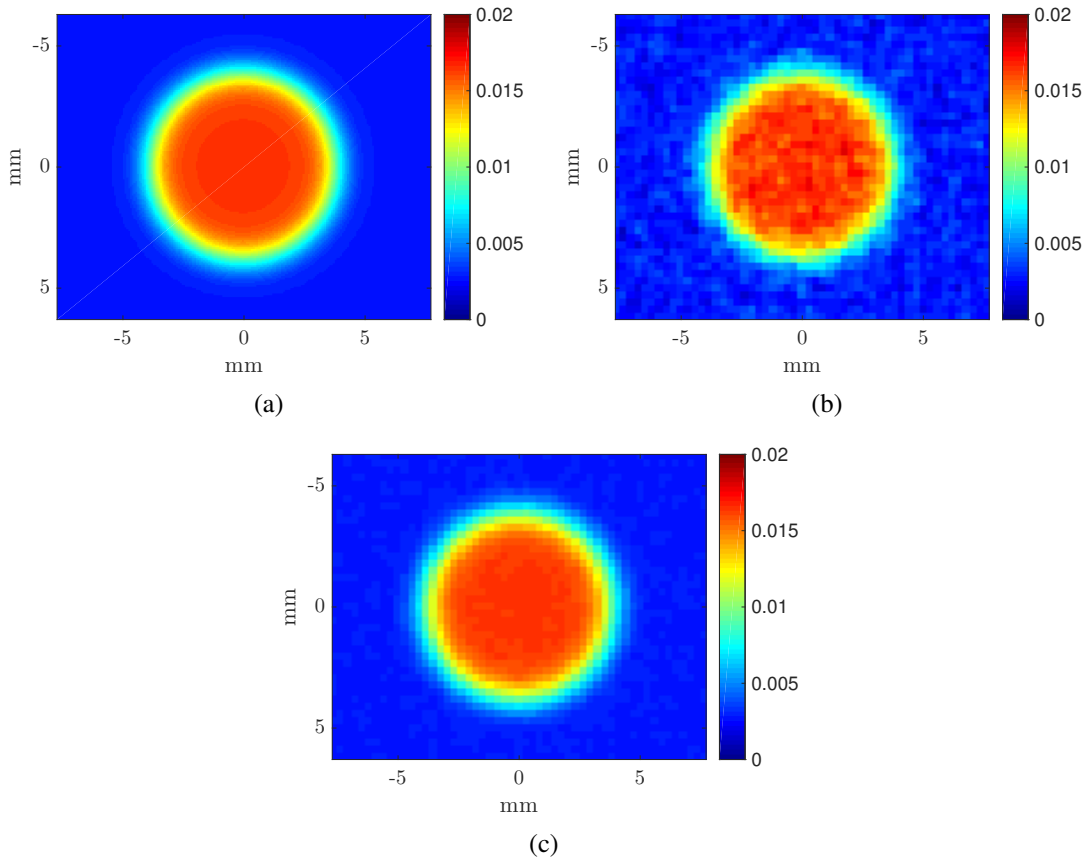

Figure 4.22: Phantom study results: (a) phantom, (b) one acquisition reconstruction, and (c) 50 acquisition reconstruction.

We now analyze noise trends in the experimental data while focusing on the

contributions of X-ray system noise to the expected error in this experiment. A standard method in assessing expected reconstruction behavior is the use of a computational phantom to enable evaluations of reconstruction performance that incorporate a ground truth value (Xu et al., 2015). In this case, we utilize a phantom created by rotating the computational attenuation signal $\Delta\bar{\mu} = Y_{Kr}\rho\bar{\xi}_{Kr}$ from the krypton-diluted calculation of Fig. 4.6 about the center axis such that a flame with radius similar to that at the base of the Bunsen flame is created – this phantom can be observed in Fig. 4.22(a). Note that the maximum attenuation values recovered here are very similar to those observed experimentally, meaning that assessments of error should have quantitative interpretations. We then perform several computational projection and reconstruction procedures, wherein synthetic datasets are created and reconstructed to demonstrate the effect of averaging multiple acquisitions under the assumption of minimal noise from flow unsteadiness. Importantly, we model the noise added to each pixel as,

$$N \sim Poisson\left(N_0 \exp\left[-\int \Delta\bar{\mu} ds\right]\right), \tag{4.5.24}$$

where $N_0 = 7.6 \times 10^5$ is the number of expected photons from the source at each pixel computed from the 45 kVp spectrum used for all experiments in this study. Reconstructions of cases containing both one and fifty averaged tomographic datasets are presented in Figs 4.22(b) and 4.22(c). The substantially higher photon noise distortions observed in Fig. 4.22(b) versus Fig. 4.22(c) indicate that increasing the aggregate photon count does have a noticeable effect on these results. Absolute reconstruction errors on a pixel-by-pixel basis are computed for these two cases in Figs. 4.23(a) and 4.23(b) using the phantom as ground truth. Thus, the values presented in Figs. 4.23(a) and 4.23(b) define the difference between the atteunation values of the reconstruction and those of the ground-truth phantom. These figures clearly show that in the case of a single scan, photon noise is large enough that the induced error profile is uniform across the reconstructed volume. These errors have a maximum magnitudes of of $2 \times 10^{-3}\text{cm}^{-1}$, or 10% of the maximum phantom attenuation value of $0.02\,\text{cm}^{-1}$. In the fifty scan case, we see a reduction of this maximum characteristic error to a smaller value around $5 \times 10^{-4}\ \text{cm}^{-1}$ (3 % of the maximum phantom attenuation), and also observe that the errors are now

spatially localized around the region of attenuation change within the flame.

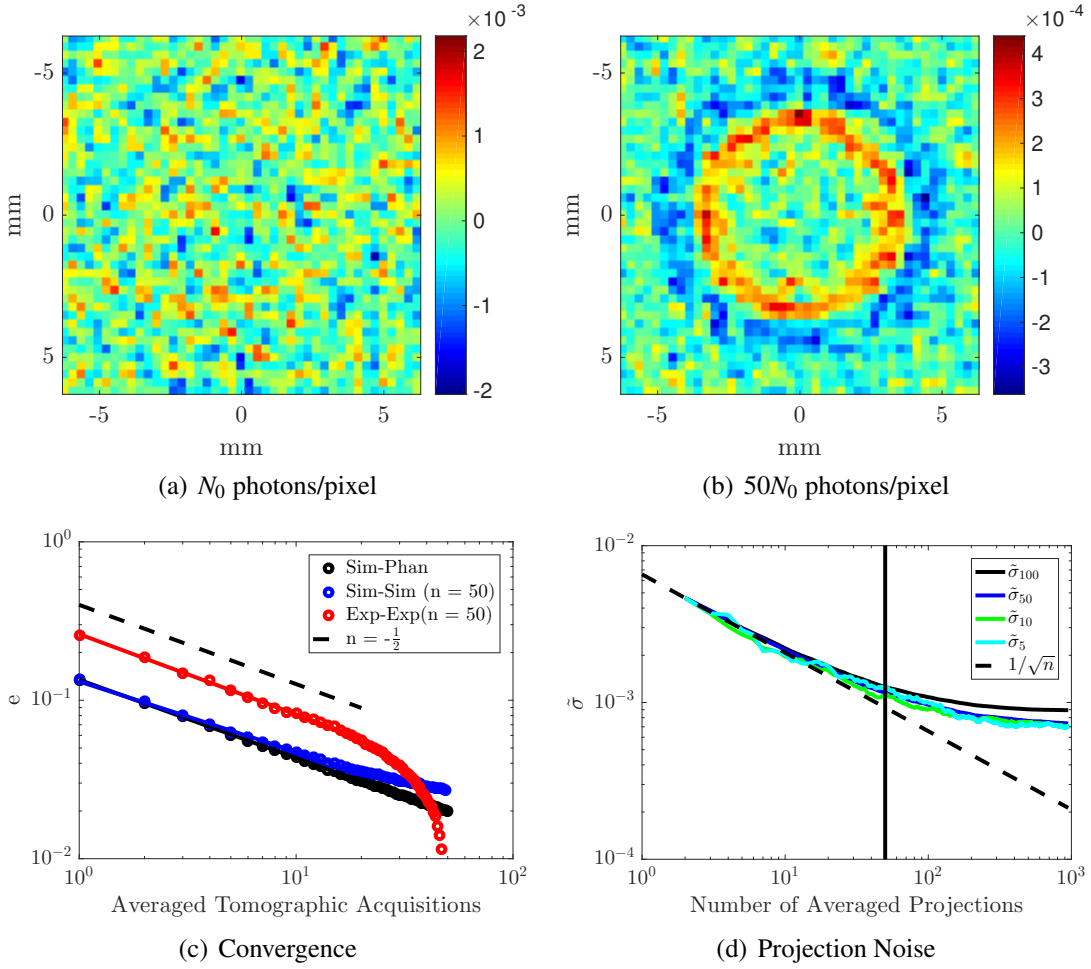

(a) N_0 photons/pixel (b) $50N_0$ photons/pixel

(c) Convergence (d) Projection Noise

Figure 4.23: Absolute reconstruction errors with respect to computational phantom for (a) one acquisition and (b) fifty acquisitions, along with (c) convergence behavior defined using the error metric of (Cai et al., 2013) presented in Eq. (3.2.6). Panel (d) shows experimental noise reduction with increasing projection number.

We can also analyze convergence behavior as part of this study, where we utilize the global error metric suggested by (Cai et al., 2013), presented above in Eq. 3.2.6.As implied by Eq. (2.3.22), we would expect reconstruction error to decrease with $\sqrt{n}$ – we see that this result is indeed obtained when simulated reconstruction convergence is assessed using the phantom as ground truth. In addition to demonstrating this convergence behavior in the simulation, however, it is also helpful to do so using the actual experimental data, for which

no ground truth is available. Thus, we use the $n = 50$ case as ground truth and evaluate experimental convergence to this reconstructed field. Performing this study of convergence to the $n = 50$ result on the computational reconstructions (blue line in Fig. 4.23(c)) yields very similar results to those obtained using the phantom as ground truth (black line in Fig. 4.23(c)), indicating the validity of this $n = 50$ convergence study procedure. This experimental convergence study to the experimental $n = 50$ reconstruction shows that a $n^{-1/2}$ convergence trend is indeed observed – note that experimental convergence behavior at higher n is biased by the fact that we are using the $n = 50$ scan as a baseline, and that the early (low n) portion of the curve should be used to assess convergence rate.

As an additional point, it is useful to quantitatively assess noise reduction in the projection data as a function of increasing scan numbers. To accomplish this task, we perform an explicit projection noise study in which we take 1000 projection images and compute the standard deviation within square boxes of varying sizes for averages over different numbers of projections. These boxes are located in areas of the image that are not occluded by any objects, meaning that they should exhibit uniform attenuation values. We refer to the standard deviation of the projection value of size m as $\tilde{\sigma}_m$. The results of this projection noise study, shown in Fig. 4.23(d), indicate that the majority of the denoising benefit at a given angle is gained from the first 50 projections. Specifically, we observe that while averaging over the first 50 projections yields a 69 % decrease in $\tilde{\sigma}_m$ across multiple values of m, averaging over 1000 projections gives only a 5 % additional decrease in $\tilde{\sigma}_m$. This reality hints at an underlying noise floor imposed by the X-ray system hardware, and implies that the 50 projections recorded at each angle during this study are sufficient to capture the majority of possible denoising gains.

These findings describing the underlying variation in the projection images also have direct impact on the expected noise from reconstruction, as is implied by the increased SNR observed with additional averaged projections. From a theoretical standpoint, the analysis presented in (Prince and Links, 2006) defines the approximate variance in reconstructed values of μ resultant from photon noise, $\sigma^2_{\mu,Phot}$, as,

$$\sigma^2_{\mu,Phot} \approx \frac{2\pi^2 B_\ell^3}{3} \frac{K}{M} \frac{1}{N_{ph}}, \tag{4.5.25}$$

where N_{ph} is the average number of photons counted at a detector, B_ℓ is a spatial bandlimit, M is the number of projections, and K is the physical detector spacing. Importantly, the derivation of Eq. (4.5.25) assumes that the statistical variation in photon fluence as measured by a Poisson distribution with mean value N_{ph} and variance $1/N_{ph}$ is constant for all detector channels, in which case it simply becomes a constant term that is carried forth in the analysis (Prince and Links, 2006). If we assume that a similar constant variance characterizes the experimental system, then this quantity is exactly that measured by $\tilde{\sigma}_m$ and reported in Fig. 4.23(d), which describes the variation in many detector channels that should report the same value at different numbers of tomographic acquisitions. Ideally, in the future, facility changes to enable smaller source-axis and source-detector distances, brighter photon sources, and more sensitive detectors would enable increases in photon count and decreases in noise levels without requiring additional acquisitions.

4.6 Conclusions

At this point, we have demonstrated the applicability of X-ray diagnostics in free-flame environments via intensive study of a krypton-diluted Bunsen flame. Changes in the X-ray attenuation signal of the krypton contrast agent have been demonstrated to yield combustion-relevant datasets at high resolution, in three dimensions, without assumptions of axisymmetry, and within an attenuative outer casing. Effects of the krypton contrast agent on key free flame parameters including flame speed, Lewis number, and flame temperature have been elucidated and discussed through lenses of experiment, computation, and theory. Analysis also suggests that the difference between the maximum X-ray gradient surface and maximum visible chemiluminescence surface locations can be indicative of the thermal flame thickness, though the experimental flame thickness measured here may be increased due to the contribution of CO_2^* to the visible signal, which results from the wide absorption band of the optical system used to conduct these measurements.

Finally, a thorough analysis of error in the X-ray reconstruction resultant from photon noise was conducted in the context of increasing photon counts via averaging of multiple tomographic acquisitions. While not optimal for fluid mechanics applications due to

steady state requirements, these results indicate that increasing aggregate photon counts via multiple tomographic acquisitions does indeed have a useful noise-reducing effect on XCT data. Further, simulation of a phantom analogous to the experimental setup has enabled the use of the $n = 50$ reconstruction as an approximation of ground truth that enables a baseline convergence analysis to be performed. Using this metric, we observe experimental convergence at the expected rate of $n^{-1/2}$ – this conclusion is nontrivial because it indicates a level of stationarity in the X-ray noise distribution (drawn from a complex set of linear systems including the source, detector, photodiode, etc.) that enables statistical convergence with increased sampling up to a certain point. Observed levels of convergence explain the decrease in standard deviation and increase in SNR (in both internal and edge regions of the flame) experimentally observed with increasing scan number.

In the end, it is hoped that this study will provide a fundamental basis of theoretical, experimental, and physical understanding that will inform future application of hard X-ray absorption diagnostics to combustion subjects. The ability of XCT to non-intrusively interrogate flames in high-resolution 3D within non-axisymmetric, optically inaccessible environments, to provide improved performance at high pressures, and to allow for inexpensive simulation makes it a useful addition to the toolset of experimental combustion. In the long run, hardware and software improvements such as brighter X-ray sources that increase photon count, photon-counting detectors that enable single-pass, multiple-energy studies, advanced statistical reconstruction methods that reduce noise, and multiple source-detector systems that would enable the time-resolved XCT measurements required for generating insight into turbulent or highly unsteady flames could substantially enhance the utility of these diagnostics for the combustion community.

Chapter 5

Analysis of Porous Media Combustion via XCT

5.1 Introduction

Having at this point demonstrated the quantitative capability of XCT to measure krypton density in Chap. 3 and applied this technique to successfully measure the attenuation field within a Bunsen flame in Chap. 4, we now proceed to apply this diagnostic to its intended purpose: making 3-D measurements within an optically inaccessible porous media burner (PMB) that can be directly related to temperature, as described by the result developed in Eq. (2.3.20). In this work, we utilize an extension of the two-zone PMB design first proposed by Trimis and Durst (1996), in which stability is achieved via pore-scale quenching as governed by a critical Peclet number (Babkin et al., 1991). Using this two-zone porous burner design, Khanna et al. (1994) successfully demonstrated that PMBs are characterized by particularly low CO and NO_x emissions when compared to free-flame systems. Barra et al. (2003) complemented this work by performing a numerical investigation of the optimal conditions for flame stabilization in the two-zone burner design, in which it was found that heat conductivity and volumetric heat transfer coefficient of the solid structure are critical in determining heat re-circulation levels and stability boundaries. Using a 1-D time-dependent formulation with detailed reaction chemistry, Barra and Ellzey (2004) later showed that the heat re-circulation efficiency

Property	Al_2O_3	SiC	ZrO_2
Thermal application limit (^{o}C)	1900	1600	1800
Thermal conductivity (W/m-K) at 1000^{o}C	5-30	80-160	2-5
Total emissivity at 2000 K	0.28	0.9	0.31
Coefficient of thermal expansion ($10^{-6}K^{-1}$) from 20-1000^{o}C	8	4.7-5.2	10-13
Thermal shock parameter ($10^{-3}Wm^{-1}$)	3	28	1.5
Mass attenuation coefficient (cm^2/g) at 40 keV	0.37	0.49	8.23
Linear attenuation coefficient (cm^{-1}) at 40 keV	1.46	1.57	46.75

Table 5.1: Porous media material parameters for design consideration (Fuessel et al., 2011; Wood and Harris, 2008).

decreases with increasing equivalence ratio, and that the heat transfer properties were primarily independent of the burner length.

We proceed by first describing the process of hardware design and set of experiments used to test these ideas in Secs. 5.2 and 5.3. Key details of data analysis are discussed in Sec. 5.4 while important results are presented and analyzed to draw useful conclusions about this PMB system in Sec. 5.5.

5.2 Burner Design and Characterization

In order to perform XCT on a PMB phantom, it is imperative to design the burner in a manner that maximizes transmitted photon counts while mitigating artifacts caused by beam hardening, low photon counts, and other phenomena mentioned in Sec. 2.5. In this section, we describe the process of designing a burner that would fulfill these criteria and characterizing this design to ensure compatibility with XCT.

5.2.1 Burner Material Characterization

In order to create a burner design that is both operationally viable and X-ray compatible, serious consideration must be given to construction materials. In general, combustion systems tend to be constructed from heat-resistant metals such as steel, aluminum, or ceramic. PMBs in particular often contain porous sections comprised of such materials as zirconia (ZrO_2), alumina (Al_2O_3), or silicon carbide (Fuessel et al., 2011; Wood and Harris, 2008). Key properties of these materials can be found in Table 5.1.

In terms of design criteria, an X-ray compatible PMB needs to fulfill several key constraints. Firstly, the thermal application limit should be high enough for the material to maintain integrity in a combustion environment. All of these materials meet this requirement for methane-air flames within the usual flame temperature range, so this is not a significantly limiting factor. Thermal conductivity should be maximized for optimum internal heat recirculation in the combustion zone of a two-zone burner, but minimized to enable enhanced quenching in the upstream fine-pore section. In this context, SiC is optimal for the combustion zone, while alumina and zirconia are well-suited for the quenching zone. Total emissivity affects total radiative heat transfer – it is unclear a priori what the optimal choice would be, but it is important to note that SiC differs significantly from the other two materials. Resistance to thermal shock and coefficient of thermal expansion are both important metrics given that the porous media will be embedded within an outer tube. Minimizing the coefficient of thermal expansion while maximizing thermal shock resistance will lead to a burner that is maximally resistant to degradation via intense thermal cycling while maintaining its designed shape as closely as possible to avoid misregistration in subtracted scans due to thermal expansion. Finally, given that porous media is specified in units of Pores-Per-Inch (PPI), and that the volume of material is relatively constant across different PPI values, it is critically important to minimize the linear attenuation coefficient of the porous material. Note that PPI, which describes pore diameter, is a different metric than the porosity ε, which defines the void fraction within a porous medium. In this context, zirconia is a poor option if we wish to make measurements within the porous media section given its extremely high attenuation coefficient. Other materials including vitreous carbon foam and copper foam were also considered – copper was ruled out due to its high attenuation coefficient, while vitreous carbon foam was too brittle for burner installation, and tended to disintegrate upon use.

In addition to theoretical considerations, burner design methods were confirmed and investigated empirically. Figure 5.1(a) illustrates a projection measurement of several different porous media materials. The copper (at right) is several times more attenuative than the other pieces. The alumina (far left) and SiC are well-visualized even within an aluminum casing, while the vitreous carbon foam displays minimal attenuation. Figure 5.2 shows complementary reconstructions of a 3 PPI SiC porous section and a 40 PPI

yttria-stabilized-zirconia (YZA) section, which is a more complex ceramic containing a significant amount of zirconia. Note that the overall attenuation value observed in the YZA is nearly three times that found in the SiC at 120 kVp – given the nonlinear nature of attenuation-vs-energy curves, this difference will only get worse at lower energies, confirming that YZA would not be a good choice for X-ray compatibility.

In a similar fashion, characterizing potential materials for the outer casing is critically important, as these materials can be the major source of beam hardening and photon loss in this type of an experiment. Figure 5.3 illustrates the mass and linear attenuation coefficients of candidate casing materials such as quartz (SiO_2), iron, and aluminum. As implied by these values, steel is extremely attenuative, to the point of being impractical for lab-scale photon sources, while other metals and ceramics show promise. Further, Fig. 5.1(b) shows a projection of tubes composed of aluminum, titanium, and ceramic. Even though the titanium is half the thickness of the other two tubes, its attenuation value is nonetheless substantially higher. Finally, to confirm that either aluminum or ceramic would be the optimal choice, a projection study was performed at many different X-ray energies to assess whether or not porous media could be observed through an outer metal casing. As shown in Fig. 5.4, a steel casing composed of a size 3 pipe completely obscures contained porous media at 60 kVp, while the aluminum casing allows the porous media to be well-visualized.

In light of these design constraints, it was decided to utilize a quartz outer tube containing silicon carbide porous inserts secured via a compression fit between the porous sections, the outer tube, and a layer of ceramic fiber insulation between the two (mostly alumina in composition). The burner was constructed by wrapping the stack of porous media in a single piece of ceramic fiber insulation and manually creating the compression fit. Silicon carbide was chosen over alumina as the porous material due to its superior thermal shock resistance and high conductivity. Quartz was chosen as the outer material over aluminum due to its low coefficient of thermal expansion, high heat tolerance, and transparency, which would enable the user to visually verify flame stability and positioning.

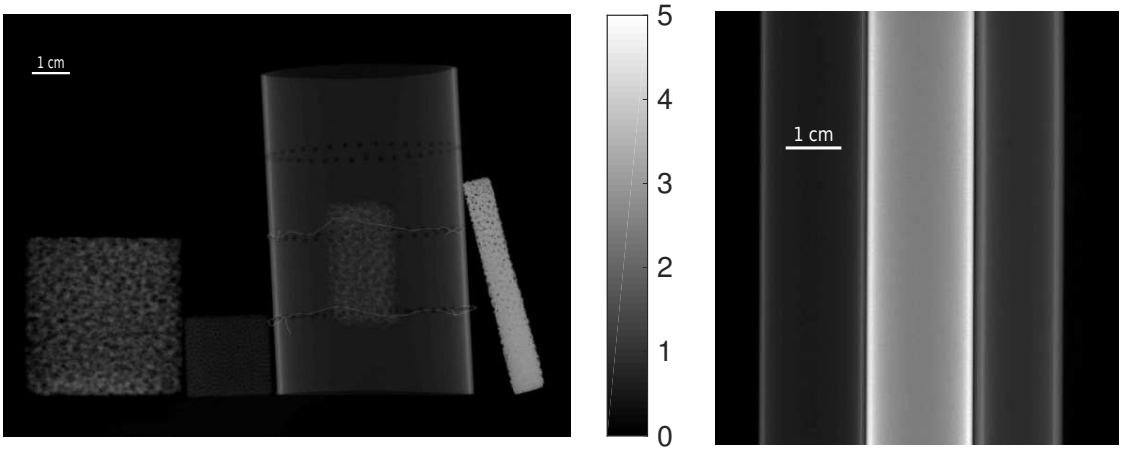

(a) Porous media candidate materials. (b) Casing candidate materials

Figure 5.1: Projections at 60 kVp, 20 mA showing (a) different porous media samples (alumina, vitreous carbon foam, silicon carbide within aluminum case, copper) and (b) different tube materials (aluminum, titanium, ceramic). Color axis is absorbance in cm^{-1}.

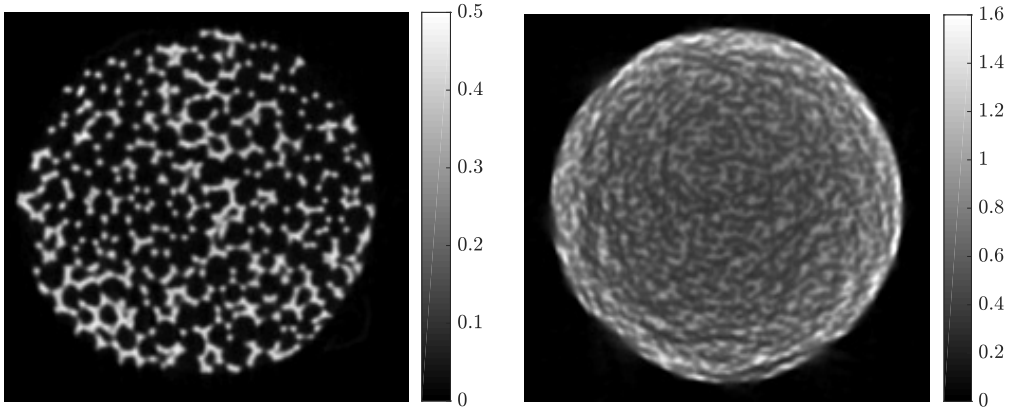

(a) 3 PPI SiC (b) 40 PPI YZA

Figure 5.2: Reconstructed scans at 120 kVp, 8 mA showing (a) 3 PPI SiC (b) 40 PPI YZA. Diameter of each piece is 5 cm.

5.2.2 Burner Specifications

The final burner design consisted of a quartz tube (Western Industrial Ceramics) of 0.41 cm thickness, 5.59 cm inner diameter, and 17.78 cm length surrounding three adjacently placed Silicon Carbide (SiC) disks (Ultramet) of 2.54 cm in height and 5.08 cm in

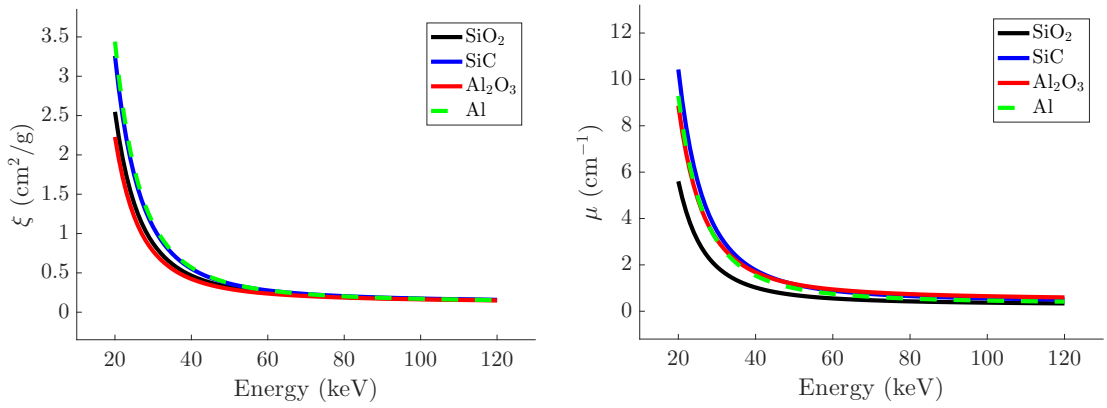

(a) ξ. (b) μ

Figure 5.3: Attenuation coefficients of candidate materials: (a) mass attenuation and (b) linear attenuation (Berger et al., 2010).

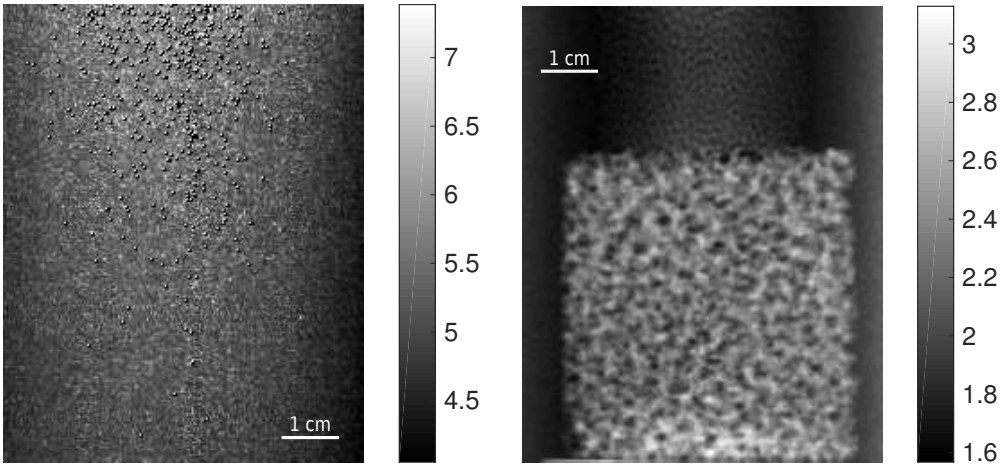

(a) Steel casing. (b) Aluminum casing.

Figure 5.4: Scans at 60 kVp showing (a) porous media inside steel casing (b) porous media inside aluminum casing. Color axis is absorbance in cm^{-1}.

diameter. A fine-pore 100 PPI disk was placed furthest upstream for use as a flashback arrestor and flow homogenizer, followed by a 65 PPI disk for flame quenching and a 3 PPI disk that functioned as the combustion zone. SiC disks were held in place via a compression fit using a ceramic fiber insulation lining (Unifrax, Western Industrial Ceramics). Note that the lowest disk was placed 2.5 cm above the quartz tube inlet in

order to leave a substantial region wherein the unburned gas could be imaged for calibration purposes. Note that in ensuring that the entirety of the burner is X-ray compatible via SiC construction, the upstream 65 PPI quenching section has a much higher thermal conductivity than it would in most two-zone burners; this reality should be considered when assessing burner behavior in comparison to that in the literature.

5.2.3 Phantom Characterization: Beam Hardening, Ring Artifacts, and Axial Consistency

In order to ensure that accurate attenuation measurements could be performed inside the burner, a set of calibration and characterization experiments was conducted in order to assess the presence of artifacts, determine the usefulness of standard beam hardening correction methods, and evaluate the homogeneity of gas attenuation measured within the gas-phase and the various porous media sections. We first describe implementation of a standard beam hardening correction technique before proceeding to burner characterization.

Implementation of Beam Hardening Correction

A polynomial beam hardening correction as described in standard work such as that of Hsieh (2009) is implemented to account specifically for the impact of the quartz tube, ceramic fiber insulation, and silicon carbide porous media. Because all of these materials have extremely similar attenuation characteristics, as shown in Fig. 5.3(a) the correction is implemented using attenuation characteristics for quartz to approximate those of all solid layers in the burner. To accomplish this correction, we compute polyenergetic and monoenergetic line integrals for a set of 256 discrete lengths of quartz l_i with attenuation μ_Q between 0 cm and 3 cm, the maximum estimated length of ceramic material between the source and detector. This 3 cm value was estimated using values of 1.25 cm insulation equivalent compressed into the void between porous media and quartz, 0.41 cm quartz, and 5 cm thick porous media with $\varepsilon \approx 80\%$. Monoenergetic ray sums m_i and polyenergetic ray sums p_i were computed via discrete integration of the following

expressions, (Wu et al., 2016),

$$m_i = -\ln\left(e^{-l_i\bar{\mu}_Q}\right) \tag{5.2.1}$$

$$p_i = -\ln\left(\int \gamma_{EI}(E)e^{-l_i\mu_Q(E)}dE\right). \tag{5.2.2}$$

Note that γ_{EI} denotes the spectral PDF characteristic of an energy integrating detector, which can be written as(Wu et al., 2016),

$$\gamma_{EI}(E) = \frac{EN_0(E)}{\int EN_0(E)dE}, \tag{5.2.3}$$

with $N_0(E)$ the number of emitted photons as a function of energy. A Vandermonde matrix P is then computed with element i, j containing p_i^j for $j = 1...4$, and the coefficient vector a is solved for with m the vector of monoenergetic line integrals m_i via the normal equations such that,

$$a = (P^T P)^{-1} P^T m, \tag{5.2.4}$$

and the corrected sinogram data g^* used for reconstruction can be written as,

$$g^* = \sum_{j=1}^{4} a_j g^j, \tag{5.2.5}$$

where g is the uncorrected sinogram data (Hsieh, 2009; Wu et al., 2016).

Beam Hardening Characterization

A series of experiments were performed in the cone-beam scanner of Sec. 2.4.1 to assess beam hardening behavior, response linearity, and artifact presence within scans of a cool burner. First, a set of five tomographic acquisitions at two different settings (45 kVp, 80 mA and 60 kVp, 60 mA) were performed with krypton gas completely filling the burner. It was ensured that no air would leak into the burner by maintaining a small, constant krypton flow rate through the same flow system described in Sec. 2.4.1. A set of five scans of the burner without air (hereby referred to as “no-krypton” scans to avoid confusion with

the common term “air scans”) were also recorded to allow for complete subtraction of the burner background to isolate the contrast signal resultant from the krypton contrast agent. Reconstructions of the five no-krypton scans were averaged and subtracted from the five krypton scans using the same geometry, reconstruction, and registration parameters ultimately used for the rest of the study, which are detailed in Sec. 5.3.2. A schematic and description of the scanned burner can be found in Fig. 5.5. As a first analysis, the

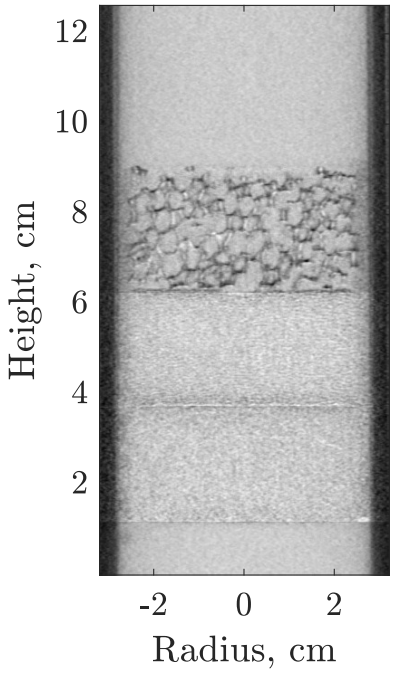

Figure 5.5: Schematic of the porous burner. The bottom section is filled with unburned gas, the lowest porous section is the 100 PPI flashback arrestor, the middle porous section is the 65 PPI quenching section, the top porous section is the 3 PPI combustion region, and the top section of the burner is designed to be filled with burned gas.

attenuation profile along a burner diameter is plotted in Fig. 5.6(a), As expected, overall attenuation is higher in the 45 kVp case, and beam hardening is more pronounced. This is particularly evident in the sharp slope within the quartz sections on either side of the burner. For perspective in interpreting this plot, it is instructive to remember that the porous sections expand out to a radius of 25 mm in each direction, followed by 3.18 mm of insulation and 2.05 mm of quartz. the increased curvature at higher radii observed within the burner is a classic “cupping” artifact often indicative of beam hardening. While

the 60 kVp curve in particular shows improvement with the polynomial beam hardening correction, it is perhaps most instructive for the purposes of the current study to investigate the subtraction of the krypton and no-krypton scans, as shown in Fig. 5.6(b). These scans represent only the signal obtained from a single line of pixels in the krypton gas – notably, for both energies the difference between the cases with and without beam hardening is negligible. However, the 60 kVp case experiences less curvature near the edges of the porous medium than does the 45 kVp case. As a result of these analyses, and the fact that increased photon counts are observed in the 60 kVp case, we choose to use the 60 kVp, 50 mA setting for all experiments conducted during this study.

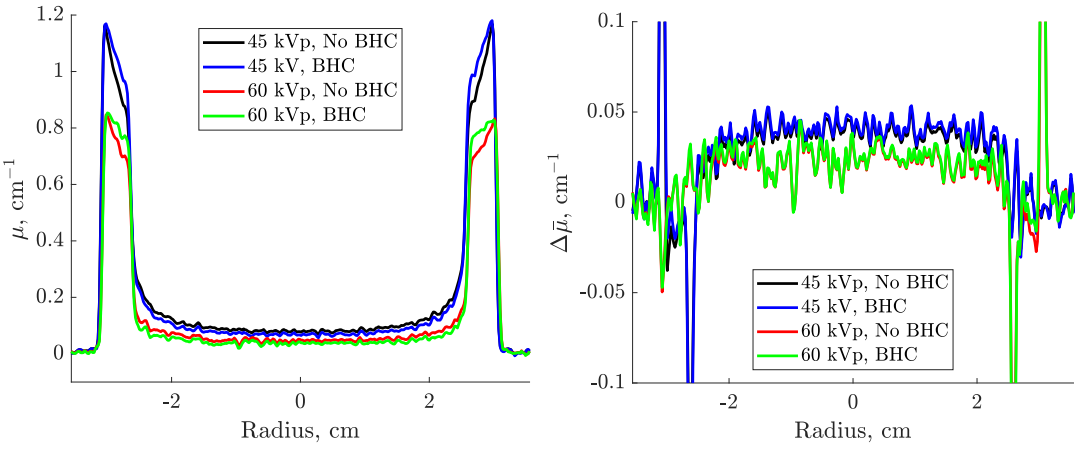

(a) Raw Data (b) Subtracted Data

Figure 5.6: Beam hardening behavior at different energies along transaxial centerline for (a) raw data and (b) subtracted data.

As a next step, we investigate the impact of several different data processing techniques on the raw and subtracted data in Figs. 5.7(a) and 5.7(b). In Fig. 5.7(a), it is apparent that the beam hardening correction shifts the attenuation curve down (between the black and blue lines) by a factor that is dependent on the radius. Applying azimuthal averaging eliminates the vast majority of rapid variation in the signal, and additional ring artifact correction using the algorithm of Sijbers and Postnov (2004) adds little additional signal to the azimuthally averaged data. Thus, we forego explicit ring artifact correction throughout this study, leveraging the rigorous scanner calibration procedure and averaging to remove random variations. Importantly, Fig. 5.7(a) demonstrates that once azimuthal

averaging has taken place, the subtracted krypton attenuation signal is consistent across all radii considered, with larger variation towards the center where there exist fewer pixels over which to average. Effectively, one can conclude that because the solid structure causes the vast majority of the beam hardening in this phantom, subtracting the no-krypton background effectively removes the beam hardening artifact moreso than any explicit correction. This conclusion is both useful and important for the work that follows.

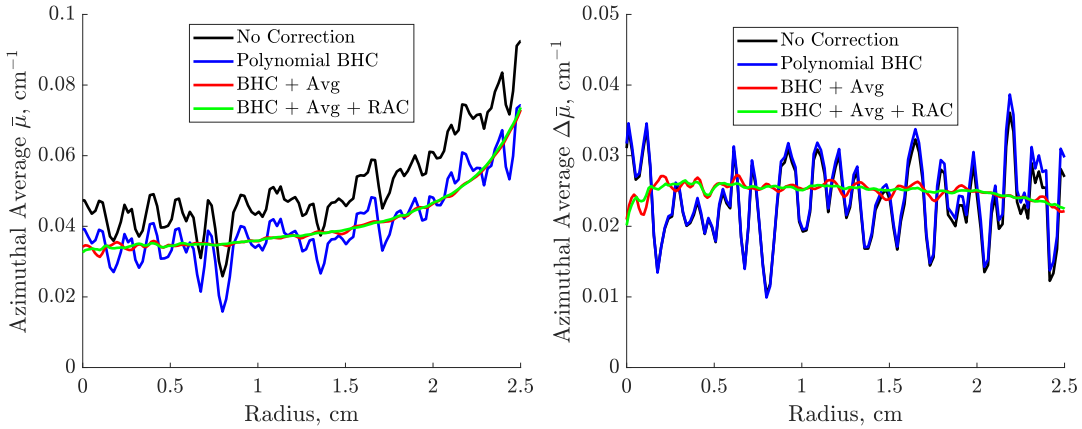

(a) Raw Data (b) Subtracted Data

Figure 5.7: Performance of different corrections for (a) raw data and (b) subtracted data: beam hardening correction (BHC), ring artifact correction (RAC), and azimuthal averaging (Avg).

Porosity Adjustment and Uniformity Assessment

At this point, we address the reality that different data processing procedures will be required to extract an accurate gas-phase attenuation value that can be related to thermodynamic state from different sections of the burner column. For instance, because XCT reconstructions fundamentally give point measurements of $\bar{\mu}$ at each voxel, attenuation measurements in voxels in the gas-phase sections at the top and bottom of the burner tube will reflect the difference between the burned and unburned gas mixture, while those in the porous media sections require more careful consideration. Specifically, pores in the 100 PPI and 65 PPI sections are smaller than the 200-micron reconstruction resolution, meaning that voxels in these domains effectively represent a volume-average of the solid and the gas. In fact, the volume fraction of each porous section can be

extracted by computing the ratio $\Delta\bar{\mu}_{PM}/\Delta\bar{\mu}_{Kr}$ over a large number of voxels (with $\Delta\bar{\mu}_{PM}$ indicating the value obtained in the porous media and $\Delta\bar{\mu}_{Kr}$ that for pure krypton gas), as the ratio of these two attenuation differences will simply reflect the relative amount of krypton gas contained in each segment of the burner tube (i.e. the solid will subtract out, as its attenuation remains constant). Mathematically, this can be written as,

$$\begin{aligned} \Delta\bar{\mu} &= \bar{\mu}_M - \bar{\mu}_B && (5.2.6)\\ &= ([1-\varepsilon]\bar{\mu}^S + \varepsilon\bar{\mu}^{Kr}) - ([1-\varepsilon]\bar{\mu}^S) && (5.2.7)\\ &= \varepsilon\bar{\mu}^{Kr} && (5.2.8)\\ \therefore \Delta\bar{\mu}^g &= \Delta\bar{\mu}/\varepsilon && (5.2.9) \end{aligned}$$

where $\Delta\bar{\mu}^g$ represents the attenuation of the *gas phase*. Thus, to obtain the attenuation resultant from the gas-phase constituents only in areas of the burner with pore sizes smaller than each voxel, it is required to adjust the subtracted signal by dividing out the porosity. Ideally this could be accomplished locally given nonuniformities in manufactured porous sections, but in this work we compute a volume-averaged porosity for both the 65 PPI and 100 PPI pieces over a representative volume comprising over 10000 voxels in the center of the burner. We denote the attenuation signal within any segment i of the burner as $\Delta\bar{\mu}_i$ and the volume-average as $\tilde{\bar{\mu}}_i$. The different sections of the burner are unburned gas UB, 65 PPI $65P$, 100 PPI $100P$, 3 PPI $3P$, and burned gas BG. We therefore estimate the porosity in the 65 PPI section as,

$$\varepsilon_{65P} \approx \frac{\tilde{\bar{\mu}}_{65P}}{\tilde{\bar{\mu}}_{UB}} \qquad (5.2.10)$$

and perform a similar procedure for the 100 PPI section. This yields results of $\varepsilon_{65P} = 0.85$ and $\varepsilon_{100P} = 0.80$, both of which are in reasonable agreement with the results of Nagata et al. (2009), which analyzes SiC porous sections fabricated using the same methods as those used here. Spread in reported average porosity values for SiC reticulated foams of the type used here are presented in Fig. 5.8.

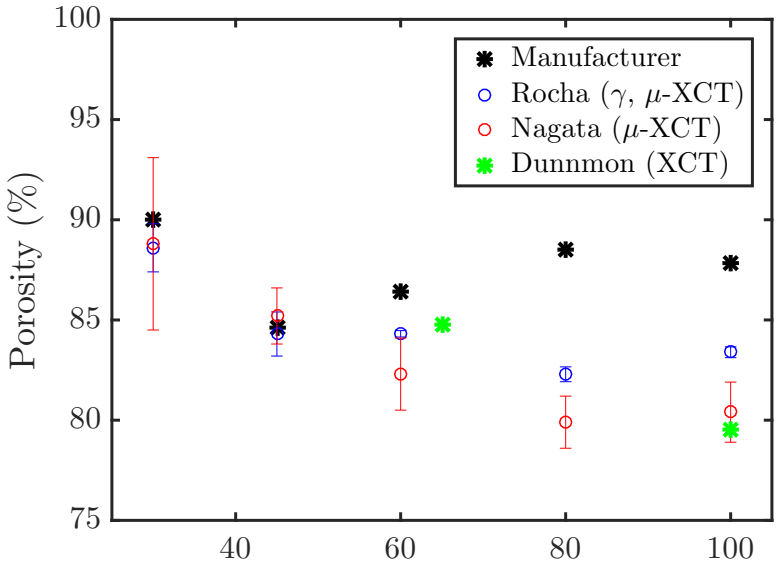

Figure 5.8: Literature, manufacturer, and computed porosity values.

Using this porosity correction, we can compute a value for $\Delta\bar{\mu}^g$ at every point in the burner column and use the resulting attenuation field to assess response uniformity throughout the burner. Averages of all pixels within a 2 cm radius for burner slices within each region can be found in Fig. 5.9. A number of useful conclusions can be drawn from these results. Firstly, in all sections containing purely gas, the median value varies by only 2% across all slices in either the inlet or outlet domains with no trend versus height. This indicates that axial intensity drop should not significantly affect the results. Further, typical interquartile ranges on the order of 4% of the mean and extreme outlier values exhibiting 15% deviation from the mean indicate encouraging homogeneity amongst pixel values. Similarly, median values in the 65 PPI and 10 PPI sections deviate from those in the gas-only sections by a maximum of 2%, indicating the efficacy of the porosity correction. Importantly, pixel values in these regions show a greater spread, part of which is due to inhomogeneity in the physical porosity with spatial position. This issue will be analyzed in further detail in a later section. Finally, the most notable aspect of this data is that the gas values observed in the 3 PPI section demonstrate a 6% drop with respect to those in other sections. These gas-phase pixels were idenified by segmenting out the solid structure and dilating the solid mask by two pixels in each direction to eliminate any

possible contribution of partial volume artifacts or imperfect scan-to-scan registration. The exact reason for this drop is not immediately clear, but the observed 6% deviation from the expected median value will be incorporated within experimental uncertainty analysis. Note that while this segmentation algorithm was used due to its simplicity and practicality and was applied consistently to reduce any potential bias, further study on the effect of different segmentation algorithms would be useful.

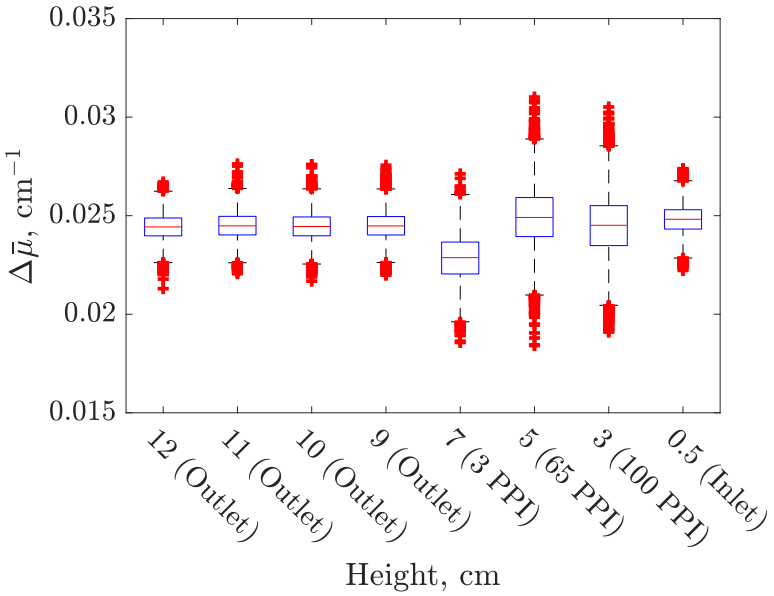

Figure 5.9: 100% krypton gas attenuation statistics at various heights within a burner for gas; 5 scan averages.

Balloon Calibration Procedure

As a final calibration experiment, it is important to establish that expected linearity of the attenuation signal with krypton number density is maintained within the quartz tube. Importantly, XCT is insensitive to why number density changes, be it via reduced krypton mole fraction or decreased bulk density caused by increased temperature. Thus, this procedure will also verify that the attenuation signal will remain proportional to the density (and inversely proportional to temperature) as a combusting flow undergoes thermal expansion. For this experiment, we use a precision syringe to fill several thin plastic balloons with krypton mole fractions of 0%, 25%, 50%, 75%, and 100% and perform a single tomographic scan with each balloon filling the top of the burner column.

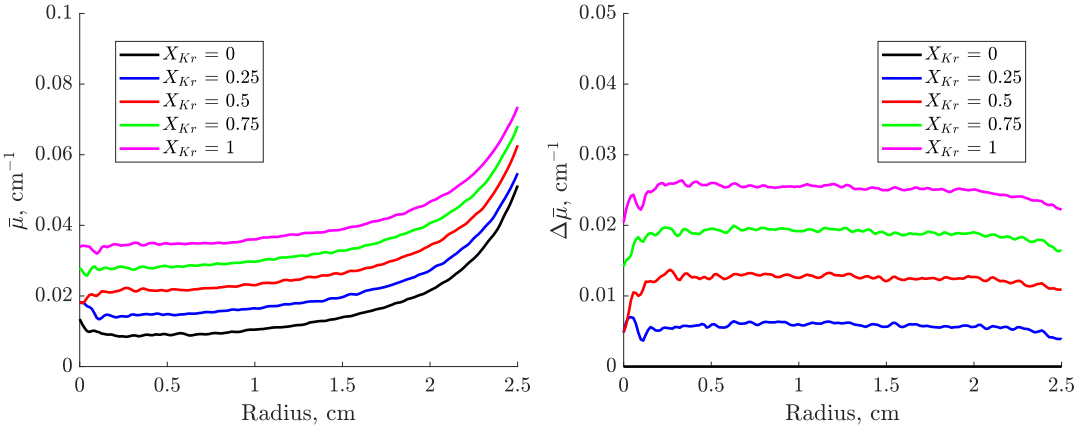

(a) Raw Data (b) Subtracted Data

Figure 5.10: Azimuthally averaged attenuation in a krypton balloon for (a) raw data and (b) subtracted data.

We then extract a slice at a height of 10 cm, subtract the no-krypton scan, and evaluate the average attenuation values. Figure 5.10(a) shows azimuthally averaged raw attenuation values, while Fig. 5.10(b) shows the subtracted data (i.e. subtracting the $X_{Kr} = 0$ curve from all curves in Fig. 5.10(a)). Again, we see that in the subtracted data, krypton values are consistent out to a radius of approximately 2 cm, at which point a slight decrease is observed. All values within 2 cm are then averaged for each case and a line is fit through the five resulting points – as shown in Fig. 5.11, we observe almost exactly linearity with krypton concentration, demonstrating that the outer quartz tube does not affect linearity of krypton response inside the burner. This conclusion will be key to extracting interpretable temperature values from the burner interior.

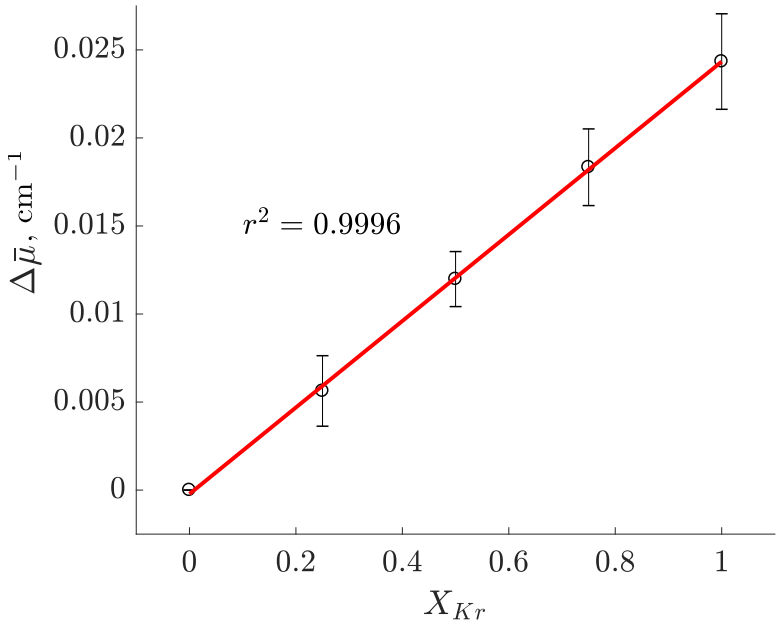

Figure 5.11: Calibration points inside tube using krypton balloons. Error bars are 95 % confidence intervals on average attenuation values.

5.3 Experimental Setup and Procedure

5.3.1 Burner Setup

Figure 5.12 shows the porous burner and the experimental setup of the XCT that was utilized in this study, which was installed in the Stanford Tabletop X-ray facility described in Sec. 2.4.1. A three-stage porous burner emplacement (Fig. 5.12(a)) was constructed such that the flame stabilization point would be directly in the field of view of the X-ray detector, as shown in Fig. 5.12(b).

A radiodense four-component Kr/N_2/O_2/CH_4 mixture was combusted at lean conditions within the PMB. Flow rates were controlled and measured using a set of rotameters for each constituent gas. Rotameter accuracy was $\pm 5\%$ for methane and $\pm 3\%$ for all other gases. As shown in Fig. 5.13, the burner was secured to the precision rotary motor described in Sec. 2.4.1 by bolting the bottom lip of the quartz tube between two aluminum disks padded with ceramic fiber insulation. The 3 PPI - 65 PPI interface where the flame stabilizes in this burner was placed in the center of the detector, and a

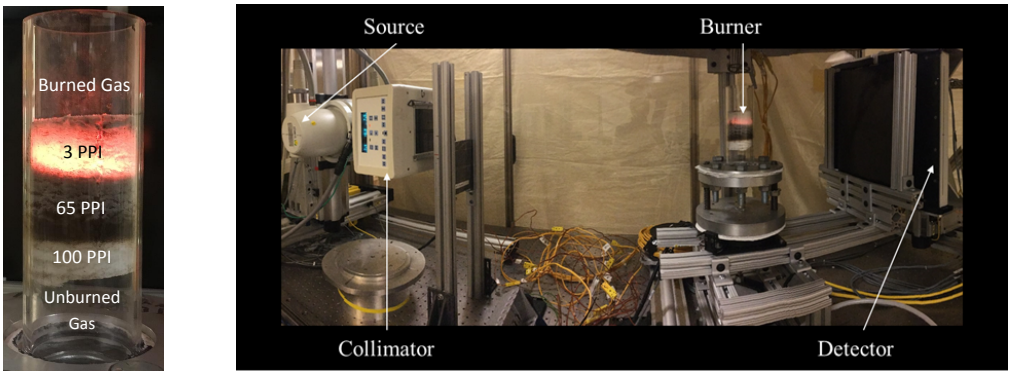

(a) Burner (b) Full setup

Figure 5.12: Experimental setup, showing (a) burner setup and (b) XCT-system

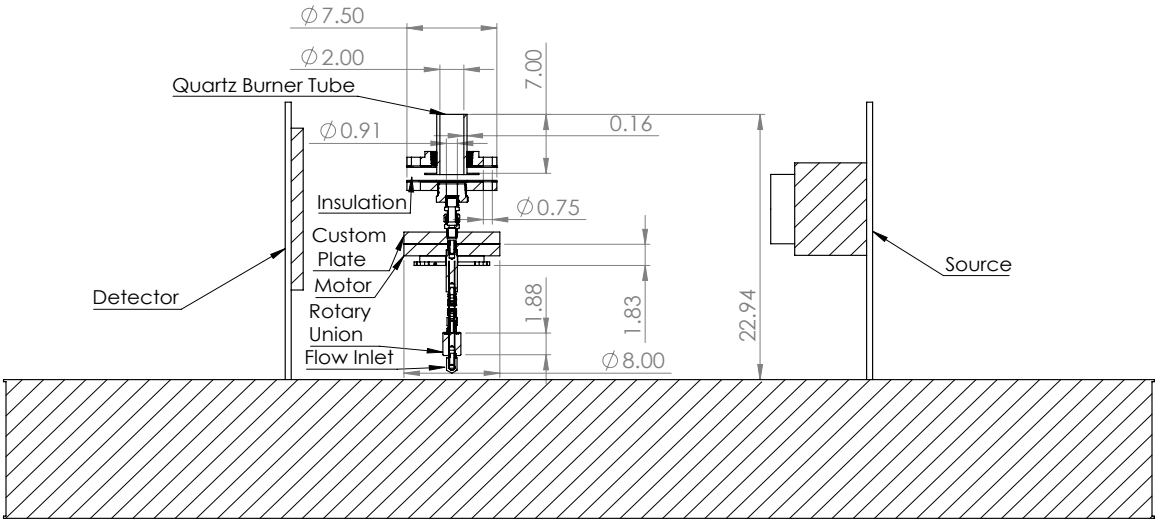

Figure 5.13: Technical drawing of cone-beam XCT setup with PMB installed. Dimensions are in imperial units, which were used for all design tasks on this setup and describe the standard hardware used for construction, delineated in additional drawings in Appendix C.

thermocouple rake containing five sensors at a radial spacing of 5 mm was installed on a linear bearing to enable temperature readings at different heights and radii within the tube. This thermocouple rake had a range of motion large enough to move the thermocouples completely outside the tube during XCT scans, such that they would not cause X-ray artifacts. Note that detailed design drawings for the flow system can be found in Appendix C.

5.3.2 XCT Scan Parameters and Procedure

Before each experiment, the Viva Version 67 data acquisition software is initialized to interface with the flat-panel detector, and data from the most recent geometry calibration is recorded to set reconstruction parameters. Buffers were allocated for the maximum possible value of 1200 projections per acquisition in order to maximize SNR, and the motion tracking system was initialized to rotate at 0.0125 rotations/second to obtain 1200 projections per rotation at the detector's native 15 frame-per-second acquisition rate. The motion tracking system was also programmed to perform two rotations on every activation in order to ensure that the operator has time to turn on the X-rays before the magnetic sensor on the turntable that begins detector acquisition is activated. The X-ray tube is then warmed up such that the Heating Units (HU) value reads 5%. This is a required procedure to ensure baseline source stability before proceeding with any data acquisition. A detector gain calibration is performed before each experimental series with no phantom between the source and detector. During the gain calibration, 128 flood field images and 128 dark field images are recorded in order to calibrate each detector element to give a uniform measurement of the flood field. Gain values for the flat-panel detector remain consistent as long as the X-ray detector is powered on. Before each tomographic acquisition (hereafter referred as a "scan," each of which consists of 1200 "projection" images), an offset (or dark field) calibration is performed, wherein the detector elements are re-adjusted to ensure that no "detector memory" effects pollute the acquisition–simply stated, if this adjustment is not performed, detector elements' response will drift, with the magnitude of the drift roughly correlating with the typical photon count received at that element during the previous acquisition (Hsieh, 2009).

Each scan is recorded at a tube voltage of 60 kVp and tube current of 50 mA to compromise between maintaining high photon counts, avoiding detector elements saturation, and minimizing energy level to maximize krypton mass attenuation coefficient $\bar{\xi}_{Kr}$. This setting requires the use of the "High Intensity Fluoroscopy" (HLF) setting on the X-ray tube – using this setting, the rotor spins three times as fast as it would on the default setting and heats up substantially due to the high intensity of the incoming electron beam. Repeated experimentation has shown that allowing longer times in between HLF

scans increases the number of scans that can be completed before an internal "rotor fault" error, at which point the X-ray tube must be allowed to cool and turned off before it can be reactivated. Avoiding such faults during the course of the experiment is critical to ensuring that background (no-krypton) and contrast (krypton) scans are recorded under exactly the same conditions. Eight minutes were allowed between scans for the anode rotor to consistently cool down, which generally allows for between 15-25 full scans to be completed before anode rotor overheat. In general, tube heating value stabilizes such that it moves between 40% and 55% during each two-minute long acquisition procedure, and returns to 40% after eight minutes' interval (between the beginning of the two scans).

For reconstruction, source-to-isocenter distance was 944.8 mm and source-to-detector distance was measured at 1255.5 mm, resulting in a maximum cone angle of 3.3^o. The 3D reconstruction volume is $384\times384\times700$ voxels in size with 200 μm isotropic spacing. Polynomial beam hardening correction for the outer quartz material was performed in the projection domain as discussed in Sec. 2.5.3. The 3D images were reconstructed using the Feldkamp-Davis-Kress (FDK) method with a Hamming windowed ramp kernel to eliminate high-frequency noise Hsieh (2009).

5.3.3 Detailed Experimental Procedure

In order to obtain XCT data describing the burning PMB, a steady flow of premixed gas was established through the burner with a mixture of $X_{Kr} = 0.375$, $X_{N_2} = 0.368$, $X_{O_2} = 0.192$, and $X_{CH_4} = 0.065$ at a linear bulk velocity of 3.8 cm/s, overall flow rate of 4.6 SLPM, and nominal equivalence ratio of $\Phi = 0.69$. This flow was created by mixing three gas streams: an 80% Kr - 20% O_2 mixture, methane, and air. Given these conditions, we compute a pore-scale Reynolds number on the order of $Re_P = 5$, which is well in the laminar regime– we therefore expect this flame to behave in laminar fashion throughout the course of the experiment. Finally, the flame was ignited at the outlet using a small torch, at which point the flame would travel upstream within the quartz tube and eventually settle at the 3 PPI - 65 PPI interface.

The gas composition utilized here was chosen in order to obtain reasonable X-ray contrast while mitigating the effect of the krypton contrast agent on combustion chemistry and heat transfer. Further, as implied by Eq. (2.3.22), one could conceivably achieve

similar SNR with the same spatial resolution and sample size using a mixture with even smaller X_{Kr} by utilizing an XCT system that allows for higher tube currents, a larger number of projections, or longer exposure times. Each of these improvements is certainly achievable in general, but all were beyond the capability of the specific system utilized in this study. To demonstrate the applicability of these recommendations, we performed a simple experiment wherein a single reconstruction of the burner phantom filled entirely with krypton gas was performed using data acquired at both $I_T = 20$ mA and $I_T = 50$ mA. Based on Eq. (2.3.22), one would expect an SNR ratio of $SNR_{50}/SNR_{20} = \sqrt{50/20} = 1.58$. The actual value calculated from the experiment in a region above the 3 PPI porous media was $SNR_{50}/SNR_{20} = 1.59$. This result supports the validity of the scaling analysis contained in Eq. (2.3.22), and implies that even lower krypton concentrations could be used. For instance, simply utilizing a high-power CT tube with characteristic tube current of at least 200 mA would allow for a 100% SNR increase over the system used here at the same photon energy—this would enable results similar to those shown here to be obtained with an X_{Kr} value half of that used in the current experiment.

Once a flame was established and allowed to reach steady state over a period of thirty minutes, a set of detailed temperature measurements were conducted within the burner using the set of five type-K thermocouples mounted above the burner exit with 5 mm spacing in the radial direction. The thermocouple assembly was mounted on a vertical track to allow for axial temperature traverses — these temperature data taken from the burned gas will be used to provide validation for the implied temperature field extracted from XCT measurements. Such temperature data are also useful for confirming that the burner is at steady state when the XCT data is taken. Specifically, three constant-speed 360 degree rotations were performed with thermocouples directly above the burner surface to assess spatiotemporal homogeneity. The radial thermocouple rake was lowered into the tube while centered on the burner, and the XCT motor was used to rotate the burner underneath these probes. Data obtained from this procedure indicate that the burner was operating at a very consistent state during these experiments, to the point that each of three separate trials taken 2 minutes apart give effectively identical thermocouple signals over a 360 degree traverse at all five radial locations (within 10 K with no predominant trend).

Our goal in the tomographic data acquisition is to obtain subtracted measurements of $\Delta\bar{\mu} = \bar{\mu}_M - \bar{\mu}_B$. Thus, after preheating the X-ray tube to ensure flux stability, we first perform twenty tomographic acquisitions of the burner combusting the $Kr/N_2/O_2/CH_4$ mixture at steady-state to obtain measurements of $\bar{\mu}_M$. Flame stability was confirmed over the duration of the experiment both visually (as in Fig. 5.12(a), flame radiation is visible through the burner insulation) and indirectly with thermocouples situated above the outlet of the quartz tube (so as not to cause X-ray artifacts in the burner tube). Each scan required a duration of approximately eight minutes to acquire data and perform detector offset calibration for the next scan. After these twenty scans of the burning radiodense mixture were recorded, the krypton-containing gases were removed from the gas stream and replaced with an air flow such that the same amount of fuel continued to combust at the interface, but with no radiodense contrast agent in the premixed gas. Twenty scans of the burner running at this $X_{Kr} = 0$ condition were then obtained to measure $\bar{\mu}_B$. It is critical that these scans be taken with a hot burner if Eq. (2.3.20) is to be faithfully applied via background subtraction; specifically, while thermal expansion was minimized in the design of the burner, the SiC porous disks still undergo nontrivial thermal expansion with temperature, and attempting to perform background subtraction between a hot burner scan and cold air scan was shown to result in poor image registration in prior iterations of the experiment. Multiple scans are taken at each condition to ensure that noise levels of both $\bar{\mu}_M$ and $\bar{\mu}_B$ could be equally reduced via averaging over several trials. Finally, note that subtraction is purposely performed in reconstruction (attenuation) space rather than in projection (absorbance) space—while more computationally intensive, this procedure ensures faithful reconstruction of each acquisition and allows registration between reconstructed datasets (mostly based on solid body rotation) to be performed in physical space.

5.4 Data Analysis Methods

As discussed above, image processing is performed inside the 3 PPI section of the background measurement to isolate voxels containing the solid via thresholding and solid mask dilation to subsequently extract all gas phase voxels to be used for evaluation of internal flame structure. Note that typical attenuation values are 0.5 cm^{-1} for solid-phase

SiC, 0.05 cm^{-1} for air reconstructed inside the 3 PPI SiC pores, and 0.06 cm^{-1} for ambient-temperature CH_4/Kr/N_2/O_2 gas mixture inside the 3 PPI SiC pores, meaning that this thresholding procedure is quite robust. The air attenuation value can be considered a constant offset that is eliminated via background subtraction, as air attenuation is physically negligible at these photon energies. Because we are interested in gas-phase attenuation changes that imply information about the thermodynamic state, attenuation differences in the 65 PPI and 100 PPI porous sections are scaled by the appropriate volume fraction to ensure accurate reflection of the gas-phase state, as discussed in Sec. 5.2.3. We will refer to data in which this adjustment has been made by using the superscript g to indicate that we are working with the attenuation only of the *gas phase*.

In the following analysis, an average over twenty air scans is subtracted from an average over twenty burning scans to compute $\Delta\bar{\mu}^g$ at each point in space after volume fraction adjustment. Specifically, each of the 40 tomographic acquisitions is first individually reconstructed. Next, the 20 air scans are each registered to a single air scan via a solid body rotation–this is accomplished via the inbuilt MATLAB `imrotate` function, wherein the image is rotated by a set number of degrees using bilinear interpolation. The miminization problem in Eq. (5.4.11) is solved for each image, where I_{reg}^{temp} represents the chosen axial slice from the reconstruction chosen as the registration template, I_{reg}^{j} represents this same slice from the j^{th} reconstruction, α represents the angle of solid body rotation, and R is a solid body rotation operator. The greedy algorithm used to implement this procedure to register each air scan b to a particular scan a is delineated exactly in Algorithm 1 in Appendix D, while an example set of subtracted reconstructions from both unregistered and registered datasets are shown in Fig. 5.14.

$$\min_{\alpha} ||R(I_{reg}^{j}, \alpha) - I_{reg}^{temp}||_2 \forall\, j \in\ 1 \ldots n \tag{5.4.11}$$

Once the air scans have been registered, the burning scans are each registered to the same baseline air scan, which yields good registration because the solid attenuation dominates gas-phase attenuation, meaning that the random, anisotropic solid alignment will be optimized by the rotation procedure. The set of registered air scans is then

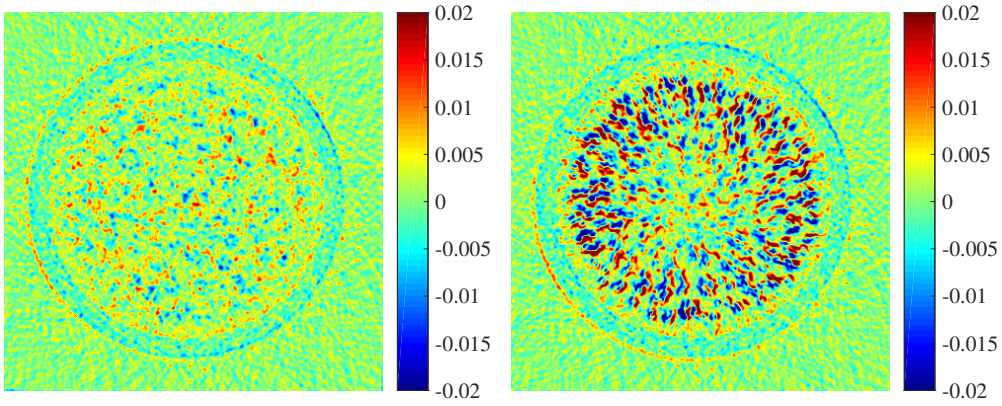

(a) Rotated subtraction (b) Unrotated subtraction

Figure 5.14: $\Delta\bar{\mu}$ [cm^{-1}] for (a) rotated and (b) unrotated reconstructions. Note that the rotation registration algorithm removes most of the spurious subtracted values.

averaged and subtracted from the registered set of burning scans to create a single subtracted dataset representing $\Delta\bar{\mu}$. In addition to averaging in time, a $3\times3\times3$ median filter is applied in order to remove remaining white noise *only* when results are visualized. Note that such a box physically represents a volume of size $0.6\times0.6\times0.6$ mm^3, a value that is substantially smaller than the size of the pores in the 3 PPI section, which typically have diameters on the order of 5 mm. Additionally, after locating solid voxels via thresholding based on $\bar{\mu}_B$ magnitude, the solid voxel regions are dilated by two pixels in all directions to minimize the effect of partial volume artifacts and any scan-to-scan misregistration on the gas phase measurements.

Computations of an implied temperature field can be accomplished at both the pixel and mean levels using Eq. (2.3.20) in combination with known upstream temperature values. Specifically, by Eq. (2.3.20), the quantity $\Delta\bar{\mu}T$ must remain constant at any point in the gas phase under the assumption of constant P and X_{Kr}, which are reasonable here given that the gas is homogeneously mixed, that no entrainment occurs, and that the flame is statistically planar. Note that the validity of assuming constant X_{Kr} in particular will be examined in detail during error analysis. Thus, utilizing spatially resolved attenuation measurements at

each voxel, we can compute a "self-calibrated" temperature at each voxel as,

$$T = T_0 \frac{\Delta\bar{\mu}_0{}^g}{\Delta\bar{\mu}^g}, \tag{5.4.12}$$

where the inlet temperature is measured to be $T_0 = 302$ K and inlet attenuation $\bar{\mu}_0$ is taken to be the average value in the bottom domain of the burner (the transparent portion upstream of the insulation in Fig. 5.12(a)) where the gas is at ambient temperature.

5.5 Results and Discussion

5.5.1 Flame Structure Analysis

At this point, it is useful to examine the internal PMB flame structure using the 3D XCT dataset, where we refer to the horizontal directions as x and y while taking z to be the vertical (axial) direction defined as $z = 0$ at the burner inlet. In Fig. 5.15, we present cross-sectional maps of the subtracted attenuation field along the vertical axis of the burner for both the present experiment with $X_{Kr} = 0.375$ and a previous version of the same experiment run with $X_{Kr} = 0.820$ along with the same equivalence ratio and data processing procedures. As shown in Fig. 5.15, the $X_{Kr} = 0.820$ case clearly gives results with less noise, as implied by Eq. (2.3.22)—however, given our emphasis on performing measurements at practically relevant conditions that are most analogous to fuel-air combustion, we analyze the $X_{Kr} = 0.375$ results in the remainder of this paper.

Given that $\Delta\bar{\mu}^g \sim 1/T$ from Eq. (2.3.20), these results indicate that areas of lower temperature will be indicated by regions of higher attenuation (assuming constant pressure and X_{Kr}). One phenomenon that is immediately apparent is that the X-ray measurements indicate substantial preheating of the incoming gas in the 65 PPI and 100 PPI porous sections, within which there exists a noticeable axial variation in the attenuation field. While uncertainties such as the porosity inhomogeneity discussed above could contribute to this effect, the fact that X-ray measurements indicate increasing temperature not only between porous media pieces, but within them, strongly suggests that the gas is indeed being preheated within the burner. This is, in effect, an observation of excess enthalpy combustion in three dimensions. Specifically, these results suggest that the 65 PPI and 100

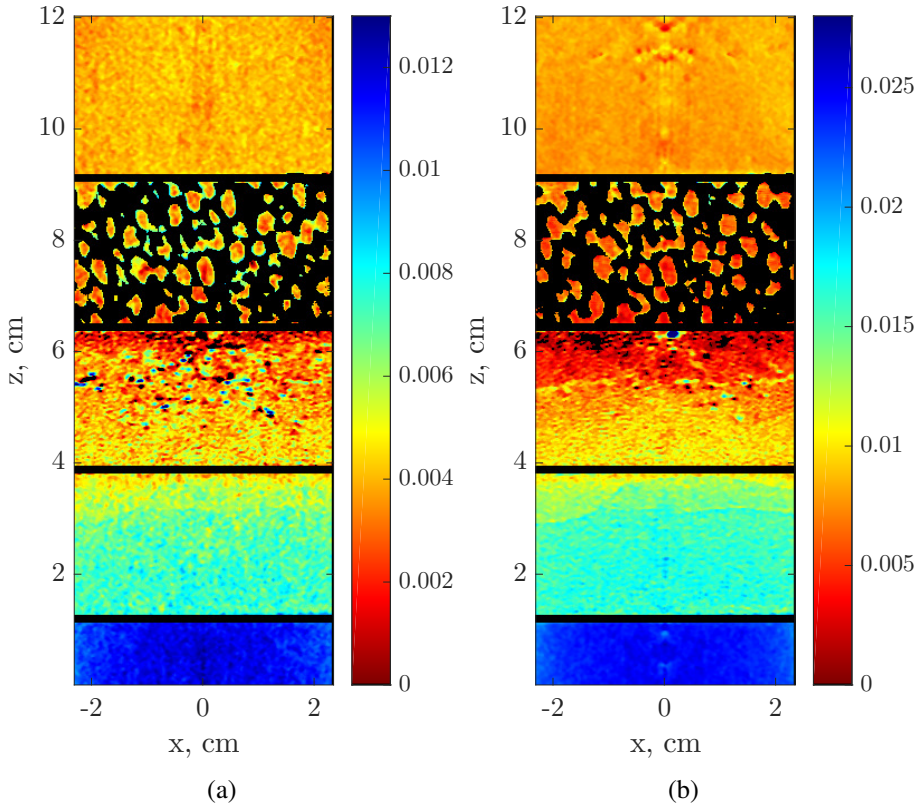

Figure 5.15: Cross-sectional view of linear attenuation field for (a) $X_{Kr} = 0.375$ and (b) $X_{Kr} = 0.820$; $\Delta\bar{\mu}^g$ [cm^{-1}] (solid matrix in black); Black lines delineate the porous sections; Color scale is directly proportional to nominal X_{Kr} in both (a) and (b).

PPI SiC sections, which are composed of a highly conductive solid material, are transporting heat upstream to the incoming gas, which then expands and exhibits lowered attenuation. This effect is likely augmented by the low flow rate characteristic of this experiment, which results in relatively small convective heat transport away from the highly conductive upstream SiC pieces.

Further, one can observe that burning within the porous matrix is not axially homogeneous. As expected, the regions of highest temperature occur nearest to the 3 PPI - 65 PPI interface on the 3 PPI side of the burner in Fig. 5.15, but the degree of homogeneity in the radial and azimuthal directions is better visualized with the in-plane attenuation data shown in Fig. 5.16. As axial coordinate z increases, we see that the gas in the bottom of the 100 PPI section shown in panel (A) is noticeably cooler than that in the

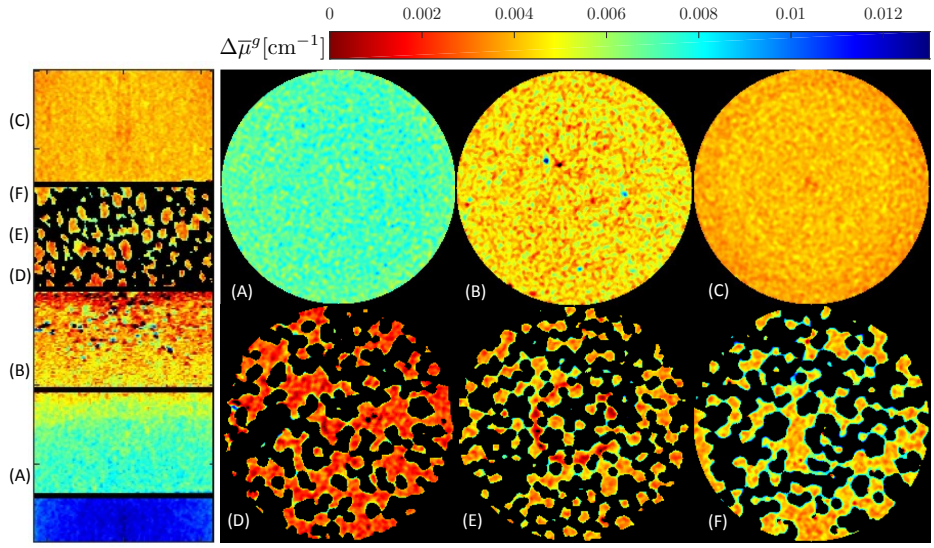

Figure 5.16: Linear attenuation field $\Delta\bar{\mu}^g$ [cm^{-1}] at different sections through the burner (solid matrix in black); Heights are as follows with respect to the axis of Fig. 5.15–(A): 2.4 cm , (B): 4.4 cm, (C): 10.6 cm, (D): 6.5 cm, (E): 7.8 cm, (F): 9.1 cm; Locations are indicated on the vertical cross section. Operating conditions are those with $X_{Kr} = 0.35$ described in Sec. 5.3.3.

more substantially preheated 65 PPI section shown in panel (B) throughout the radial and azimuthal domains. The temperature in the exhaust gas, in panel (C), is also well visualized, and is significantly cooler than the burning zone of panel (D). Comparison of panels (D)-(F) demonstrates variation in combustion behavior through the 3 PPI combustion zone. Specifically, near the interface, we observe distinct homogeneity in the attenuation field, indicative of relatively consistent combustion conditions within this slice of the burner. Additionally, an average temperature decrease (attenuation increase) is observed as we move to the downstream sections of the burner, where the attenuation field appears to become slightly less homogeneous. Further, the development of noticeable spatial inhomogeneity observed in the downstream sections of the burner (such as in panels (E) and (F)) hints at the existence of potentially interesting pore-scale heat transfer physics which may well have an effect on the fundamental operation of PMBs.

Finally, it is worth pointing out that the full 3-D nature of this dataset cannot be over-emphasized in evaluating its utility. As shown in Fig. 5.17, this data enables direct

inspection of the implied temperature field at any point in the 3-D field, which suggests several phenomenological aspects of the current flame. Firstly, it is apparent that the gas cools significantly between the combustion region in the 3 PPI section and the outlet of the burner, which is again indicative of heat recirculation within the burner. Secondly, the flame surface at the 3PPI - 65 PPI interface is well visualized, and there appears to be evidence of axially extended flame kernels at certain spatial locations. Thirdly, at the burner surface, the hottest pockets of gas are separated by cooler area, which indicates that a pore-scale heat transfer mechanism may be of importance in this burner. As expected, these results imply that the solid wall is cooler than the hot gas in the region downstream of the reaction zone, while the reverse would be expected upstream of the reaction zone (Viskanta and Gore, 2000).

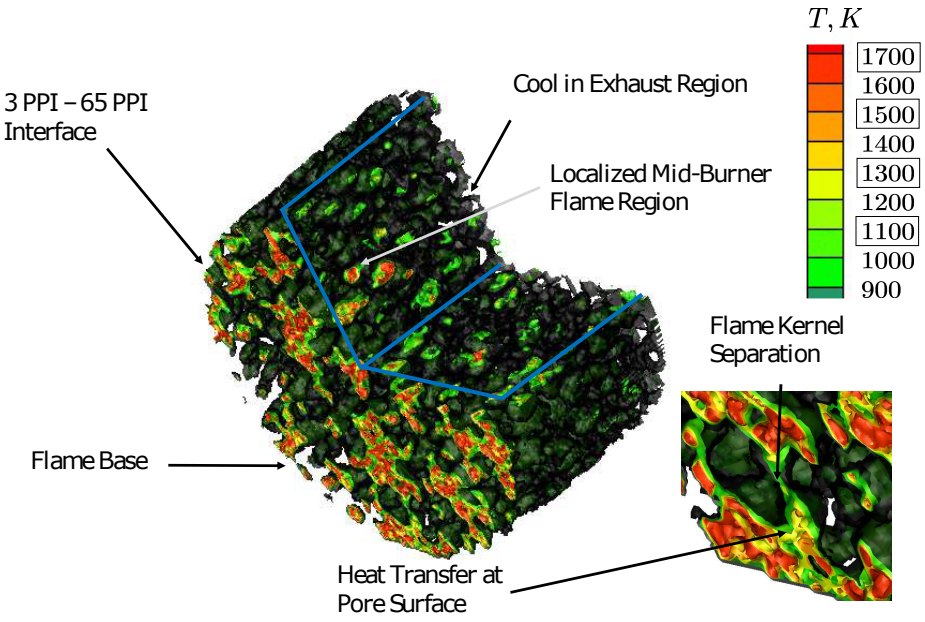

Figure 5.17: 3D cutout of the 3 PPI section. Isosurfaces are shown for boxed temperatures. Operating conditions are those with $X_{Kr} = 0.35$ described in Sec. 5.3.3.

5.5.2 Comparison of Implied Temperature to Thermocouple Measurements

Insulation Thermocouples and Radiation Observations

In order to have another point of comparison, the experimental procedure was later re-run with four thermocouples installed in the ceramic fiber insulation layer surrounding the burner. This was not possible during X-ray scans, as the metal in the thermocouple shaft causes significant artifacts, as shown in Fig. 5.18(a). To record temperature data, the burner was lit using only methane and air, and krypton was then added to arrive at the same conditions as the rest of the burner experiments. The temperature trace from this procedure can be found in Fig 5.18(b) – clearly, even for the same amount of fuel and oxidizer, the thermocouples in the insulation record a larger temperature. This phenomenon can be correlated with an increase in the visual emission of the flame – as shown in Figs. 5.18(c) and 5.18(d), the $X_{Kr} = 0$ case is noticeably less luminous than the $X_{Kr} = 0.375$ case, indicating that the addition of krypton enables increased radiative heat transfer from the flame to other parts of the burner. Thermocouple data obtained in the insulation is also compared to the X-ray data below.

Comparison of Results

When using thermocouple measurements to assess the performance of the XCT diagnostic in the burned gas column, we average over all gas-phase voxels within the appropriate radius at each axial slice. We first obtain 1D attenuation curves by averaging $\Delta\bar{\mu}^g$ at each position in the axial direction for each reconstruction to give 1D volume-averaged $\Delta\bar{\mu}^g$ curves. Importantly, the averaging procedure over twenty scans ensures a reasonable level of statistical convergence in the results. This mean $\Delta\bar{\mu}^g(z)$ curve can be observed over the axial distance in Fig. 5.19(a).

As shown in Fig. 5.19(b), 1D implied temperature calculated from the self-calibration procedure agrees relatively well with both known temperature in the unburned gas section and steady-state thermocouple data obtained in the burned gas section. Note that the thermocouple data has not undergone explicit correction for radiation loss; as demonstrated by Bradley and Matthews (1968), radiation losses can result in

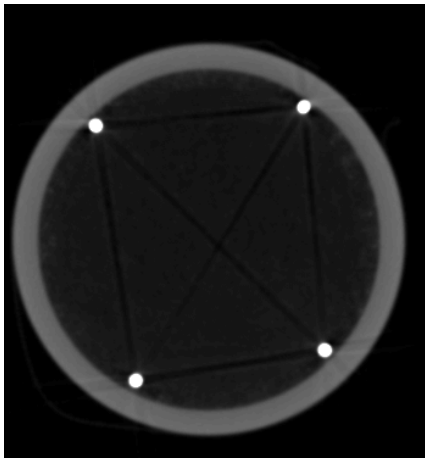

(a) Thermocouple locations

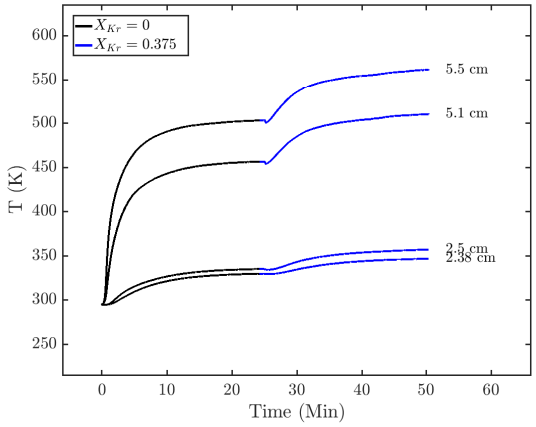

(b) Temperature traces

(c) $X_{Kr} = 0$

(d) $X_{Kr} = 0.375$

Figure 5.18: Thermocouple location and increased visual output with krypton addition. Panel (a) shows thermocouple location, panel (b) shows temperature traces from thermocouples embedded in the insulation, panel (c) shows visual light emission from the 3 PPI section at $X_{Kr} = 0$, and panel (d) shows visual light emission from the 3 PPI section at $X_{Kr} = 0.35$.

thermocouple readings that are on the order of 10-50 K lower than the actual gas temperature that would be recorded by XCT. Error bars on the thermocouple measurements reflect a 30 K radiation loss estimated as in (Glawe et al., 1956). Additionally, the X-ray measurements themselves are subject to some uncertainty—in the 1D comparison, we show 95% confidence intervals using a standard error that takes into account a variety of potential uncertainties detailed explicitly in Sec. 5.6. Note also that small, spatially localized areas in the 65 PPI porous media wherein either $\Delta\overline{\mu}^g < 0$ or $\Delta\overline{\mu}^g > \Delta\overline{\mu}^g_0$ are excluded from the averaging procedure, as these values are fundamentally

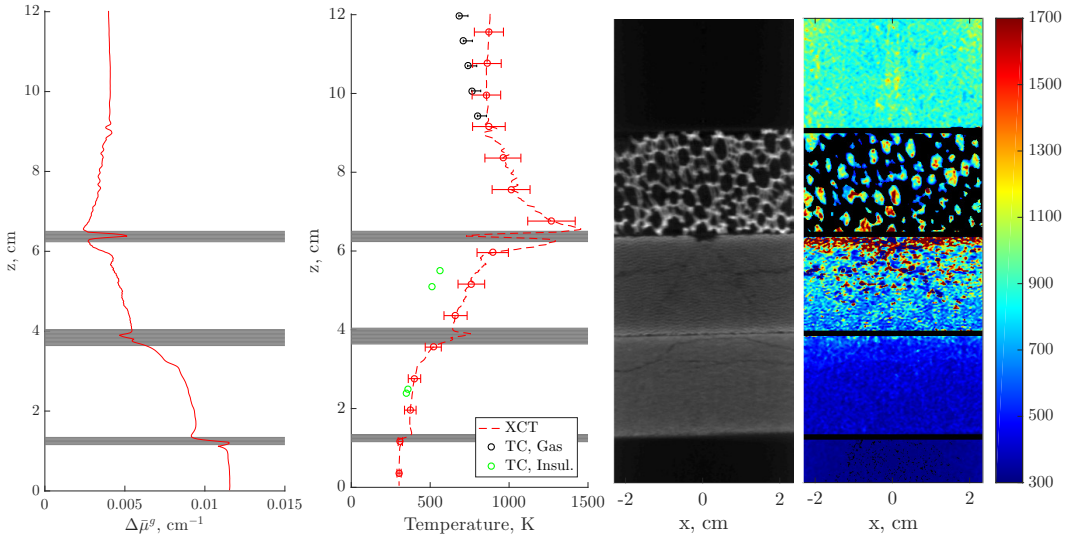

(a) 1D mean attenuation (b) 1D temperature profiles (c) Solid (d) Implied temperature

Figure 5.19: (a) Mean attenuation curve $\Delta\bar{\mu}^g(z), [\text{cm}^{-1}]$; (b) Comparison of implied temperature results to thermocouple (TC) measurements; (c)Visualization of solid structure; (d) Vertical cross section of 3D implied temperature field; Note that all subfigures are on the same z axis and black lines delineate the porous sections. Operating conditions are those with $X_{Kr} = 0.35$ described in Sec. 5.3.3.

unphysical.

Overall, reasonable qualitative agreement with expected behavior is observed in terms of flame position at the interface between the 3 PPI and 65 PPI burner sections. Further, the temperature pattern observed in the downstream portion of the burner agrees to an acceptable degree with thermocouple measurements, and that within the burner shows the expected cooling of the burned gas as it moves through the 3 PPI section. As discussed above, while theory would suggest a flame exactly at the interface with minimal upstream conduction, the experiments explicitly suggest evidence of an extended preheat zone throughout the 65 PPI SiC section, which is indicative of the level of internal heat exchange within the porous burner. The grounded thermocouples in the insulation also indicate a temperature lower than that of the X-ray measurements, which indicates that the degree of preheating indicated by the X-ray measurements may be exaggerated, though heat is clearly being transferred upstream in the 65 PPI section. Further, note that there exist several sharp changes in the mean attenuation curve of Fig. 5.19(a) and the

temperature curves of Fig. 5.19(b). Each of these appears to occur directly at the interface between two different burner segments, and likely results from imperfect registration and axial alignment of the porous sections at the interface combined with particularly low signal in the hottest portion of the burner. Additionally, there exists a section just below the 3 PPI - 65 PPI interface wherein temperatures are high enough that attenuation values become too small to confidently extract a quantitative implied temperature. Thus, these sections of the plots have been grayed out to indicate areas where results are not necessarily reliable.

Several aspects of Figs. 5.19(c) and 5.19(d) bear further discussion. First, the vertical slice of the 3D implied temperature field (or the data presented in Fig. 5.17) yields better visualization of temperature variation than the attenuation map of Fig. 5.15 because we are plotting a quantity that is directly proportional to temperature. The axial extent of the flame zone is substantially more apparent from this data, which indicates that most of the combustion occurs within the bottom third of the burner at these conditions. This is consistent with the observed extent of the radiant flame zone visible through the ceramic fiber insulation between the burner and quartz tube. It is important to note that while these 3D results are encouraging, further work on calibrating temperature to krypton gaseous contrast agent concentration would be helpful in lowering the level of uncertainty surrounding quantitative voxel-to-voxel subtracted measurements, which can be on the order of the measurement at the tail ends of the voxelwise $\Delta\bar{\mu}^g$ distribution. As a final comment, the solid visualization of Fig. 5.19(c) (a scan of the burner containing only air in the gas phase) shows that cracking has occurred in the upstream SiC porous foams over the course of these experiments. While such crack-detection represents a more traditional use of XCT, it is nonetheless useful in working with PMBs due to the fact that questions about potential inhomogeneities in internal flow patterns can be answered without destructive procedures.

5.6 Error and Uncertainty Analysis

We now apply the framework of Eq. (3.2.11) to evaluate the magnitude and importance of varying sources of uncertainty in these measurements.

5.6.1 Uncertainty in Inlet Conditions

Key experimental flow rate values are X_{Kr}, X_{O_2}, X_{N_2}, X_{CH_4}, linear inlet velocity u_0, inlet temperature T_0, and equivalence ratio Φ. Flow quantities are derived using known geometry of the burner tube and measured flow rates. Uncertainty is $\pm 3\%$ of full scale for all flow measurements except for methane, for which it is $\pm 5\%$.

Volumetric flow rates at standard conditions were computed from rotameter indicated flow rates (in ILPM), measured pressures, and measured ambient temperature using the following conversion factor under the assumption of ambient temperature,

$$q_{SLPM} = q_{ILPM} \sqrt{\frac{P_{new}}{P_{cal}} \frac{W_{new}}{W_{cal}} \frac{T_{cal}}{T_{new}}}, \tag{5.6.13}$$

where *cal* indicates the calibration condition, *new* indicates the actual conditions, P indicates the downstream pressure, and T defines the operating temperature. This correction factor is derived from first principles in Appendix E; for more detail on rotameter uncertainty, the reader is directed to the work of Wojtkowiak and Popiel (1996). In our case, the temperature correction is generally negligible, the pressure correction is small, but non-trivial, and the specific gravity correction is quite important given the large molar mass of krypton and small molar mass of methane. Note that, as recommended by the manufacturer, a viscosity correction based on the in-tube Reynolds number was not applied given the low (and relatively similar) gas viscosities used here. Mole fractions were computed as volume fraction of each compound within the premixed gas,

$$X_i = \frac{q_i}{q_{tot}}. \tag{5.6.14}$$

The equivalence ratio was computed in the following manner (Law, 2010),

$$\Phi = \frac{n_{\mathrm{F}}/n_{\mathrm{O}}}{(n_{\mathrm{F}}/n_{\mathrm{O}})_{st}} = 2\frac{n_{\mathrm{F}}}{n_{\mathrm{O}}} = 2\frac{q_{CH_4}}{0.21 q_{Air}}, \tag{5.6.15}$$

and the linear speed was computed as,

$$u_o = \frac{q_{tot}}{A_o}. \tag{5.6.16}$$

Overall uncertainty in key computed quantities may be analyzed via the framework of Moffat (1988). Note that the flowmeter uncertainties are taken such that the $\pm Z\%$ value indicates the 95% confidence level value such that $Z \approx 2\sigma$, with σ the standard deviation for that quantity. Rotameter uncertainty values for each gas are incorporated into this analysis.

$$\begin{aligned}
\frac{\sigma_{u_o}}{u_o} &= \frac{\sigma_{q_{tot}}}{Au_o} \\
&= \frac{1}{Au_o}\sqrt{\sigma_{q_{Air}}^2 + \sigma_{q_{CH_4}}^2 + \sigma_{q_{Kr-O_2}}^2} \\
&= \frac{1}{Au_o}\sqrt{(0.015q_{Air}^{Max})^2 + (0.025q_{CH_4}^{Max})^2 + (0.015q_{Kr-O_2}^{Max})^2} \\
&= \frac{0.16\text{cm/s}}{3.8\text{cm/s}} \\
&= 4.2\%. \\
\therefore u_0 &= 3.8 \pm 0.32\text{cm/s}
\end{aligned} \tag{5.6.17}$$

$$\begin{aligned}
\frac{\sigma_\Phi}{\Phi} &= \sqrt{\left(\frac{\sigma_{q_{CH_4}}}{q_{CH_4}}\right)^2 + \left(\frac{\sigma_{q_{O_2}}}{q_{O_2}}\right)^2} \\
&= \sqrt{\left(\frac{0.015(0.21q_{Air}^{Max})}{0.21q_{Air}}\right)^2 + \left(\frac{0.025(q_{CH_4}^{Max})}{q_{CH_4}}\right)^2} \\
&= 9.8\% \\
\therefore \Phi &= 0.69 \pm 0.14
\end{aligned} \tag{5.6.18}$$

$$\begin{aligned}
\frac{\sigma_{XKr}}{X_{Kr}} &= \sqrt{\left(\frac{\sigma_{q_{Kr}}}{q_{Kr}}\right)^2 + \left(\frac{\sigma_{q_{tot}}}{q_{tot}}\right)^2} \\
&= \sqrt{\left(\frac{0.015(0.8q^{Max}_{Kr-O_2})}{0.8q_{Kr-O_2}}\right)^2 + \left(\frac{\sigma_{q_{tot}}}{q_{tot}}\right)^2} \\
&= 6.3\% \\
\therefore X_{Kr} &= 0.375 \pm 0.047
\end{aligned} \tag{5.6.19}$$

While these uncertainties do not affect the temperature values extracted from the XCT data, they represent nominal spread on the initial conditions for the computational model reported in the work of Dunnmon et al. (2017a).

5.6.2 Sources of Uncertainty and Error in XCT Measurements

In this section, we detail possible contributors to uncertainty in the experimental measurements, and explicitly prescribe the standard error used for error bars on implied temperature values.

Hardware Stability Error

One aspect of the experimental system that could potentially contribute to variation over the course of the different trials is the state of the X-ray hardware, such as the X-ray detector. However, this behavior is relatively easy to compensate for in the present procedure, as a detector offset calibration is performed for the flat panel detector before each scan. Thus, the detector elements will remain well-calibrated over time, even with changes in temperature and afterglow effects (Hsieh, 2009).

Another piece of hardware whose behavior may vary with time and temperature is the X-ray tube. In particular, as the spinning anode in the tube is bombarded by an electron beam, it heats up and slightly expands. If the anode is not at a stable temperature, the focal spot of the beam may move over time, affecting recorded attenuation values. The data processing procedure described above attempts to compensate for this behavior by running the exact same procedure for both burning scans and air scans–the scanner is started from a cold state for each, and twenty-five scans are recorded for each point during the course

of a precisely specified procedure. Reported tube heating value will generally stabilize on the 3rd to 5th scan – to ensure that our results are minimally affected by this behavior, we only use scans that occurred with a stable tube temperature (i.e. the last 20 scans of each 25-scan procedure).

As shown in Fig. 5.20, investigation of the axially averaged attenuation field inside the burner as a function of time has demonstrated that there is a slow decrease in the attenuation signal over time, both in the no-krypton scans and in the burning krypton scans. Averaging these signals should indeed decrease the impact of such drift, as the drift in the averaged scan D_{av} for an average of n scans can be approximated as,

$$D_{av} = \frac{(\mu_{M,n} - \mu_{M,1}) - (\mu_{B,n} - \mu_{B,1})}{n}. \tag{5.6.20}$$

which yields characteristic drift values of $D_{Av,3PPI} = 2.75 \times 10^{-5}$ cm^{-1}, $D_{Av,65PPI} = 1.5 \times 10^{-5}$ cm^{-1}, $D_{Av,100PPI} = 2.0 \times 10^{-5}$ cm^{-1}, and $D_{Av,UB} = 1.9 \times 10^{-5}$ cm^{-1}, $D_{Av,B} = 8 \times 10^{-6}$ cm^{-1}. In terms of characteristic mean values in each section, this results in variation of $\sigma_D = 0.8\%$ in the 3 PPI section, $\sigma_D = 0.4\%$ in the 65 PPI section, $\sigma_D = 0.3\%$ in the 100 PPI section, 0.2% in the unburned gas section, and $\sigma_D = 0.2\%$ in the burned gas section.

Acquisition Noise and Spatial Material Inhomogeneity

Scan technique was optimized to reduce quantum noise by maximizing photon flux. Scanner efficiencies are properties of the system, and were also explored in Sec. 4.5. Further, Baek and Pelc (2011) have characterized the noise power spectrum of the exact system used for this study in the published literature. To account for any variation from photon noise, the results of Fig. 5.9 for the homogeneous gas sections suggest a conservative value of $\sigma_{HG} = 2\%$ of the mean be used to account for variation of the measured mean gas value about its true value pure gas sections. In the 3 PPI section, we use a value of $\sigma_{HG,3PPI} = 6\%$ resultant from the observed drop in the 3 PPI measurement values reported in Fig. 5.9.

As mentioned above, there also exists an uncertainty in the 65 PPI and 100 PPI porous media sections due to manufacturing inhomogeneity in the material combined with the average porosity correction procedure. Specifically, as shown in Fig. 5.21(b), the top and bottom faces of the porous media section appear to be significantly denser than the rest of

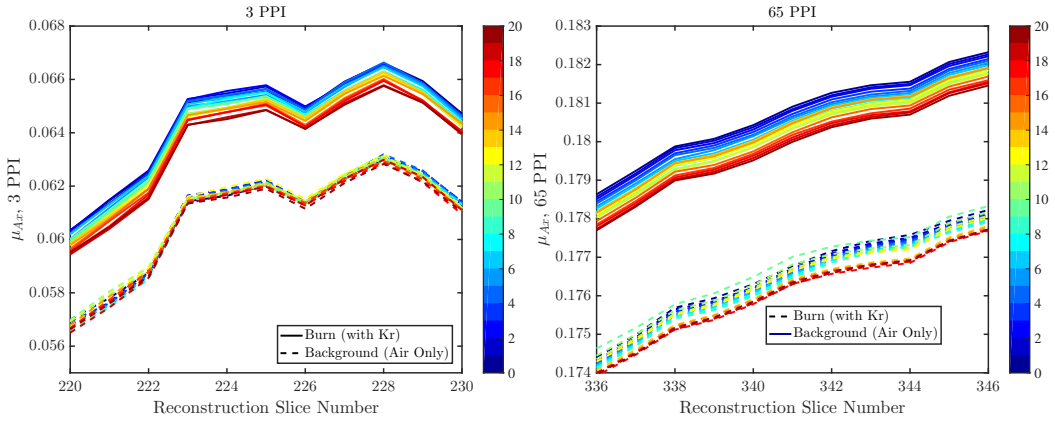

(a) 3 PPI Stability

(b) 65 PPI Stability

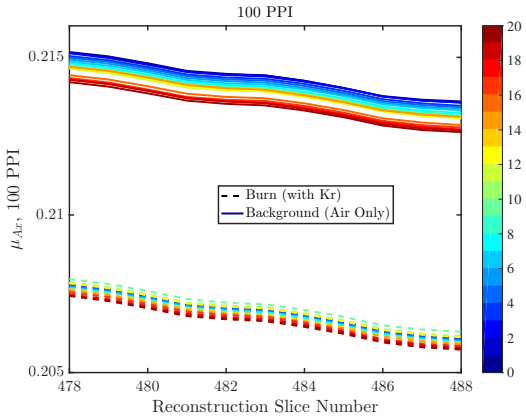

(c) 100 PPI Stability

Figure 5.20: Recorded average attenuation for krypton and air scans over time for gas-containing sections.

the piece, and there appears to be a smooth increase in the density, which in this case is a direct analog for porosity, from left to right. To confirm that the trends in z were not a result of cone-beam artifacts at sharp interfaces, the same scan was repeated with the r and z axes switched (i.e. the flat faces orthogonal to the X-ray beam), and the same results were observed. Given the large density variations observed within the attenuation field of the 65 PPI piece, it is not unexpected that we observe increased uncertainty in the 65 PPI and 100 PPI pieces.

With respect to the 1-D curve uncertainties, however, the results of Figs. 5.9 and 5.16 show that the temperature fields within each slice are often relatively homogeneous.

Given that the spreads observed in the 65 PPI and 100 PPI pieces in Fig. 5.9 are approximately twice those in the pure gas sections, we use a value of $\sigma_{HG,65PPI} = \sigma_{HG,100PPI} = 2\sigma_{HG,UB} = 4\%$ of the mean. Note that these bounds are quite conservative, as averaging over approximately 40000 pixels at each slice will mitigate variation associated with measurement noise (but not that associated spatial inhomogeneity).

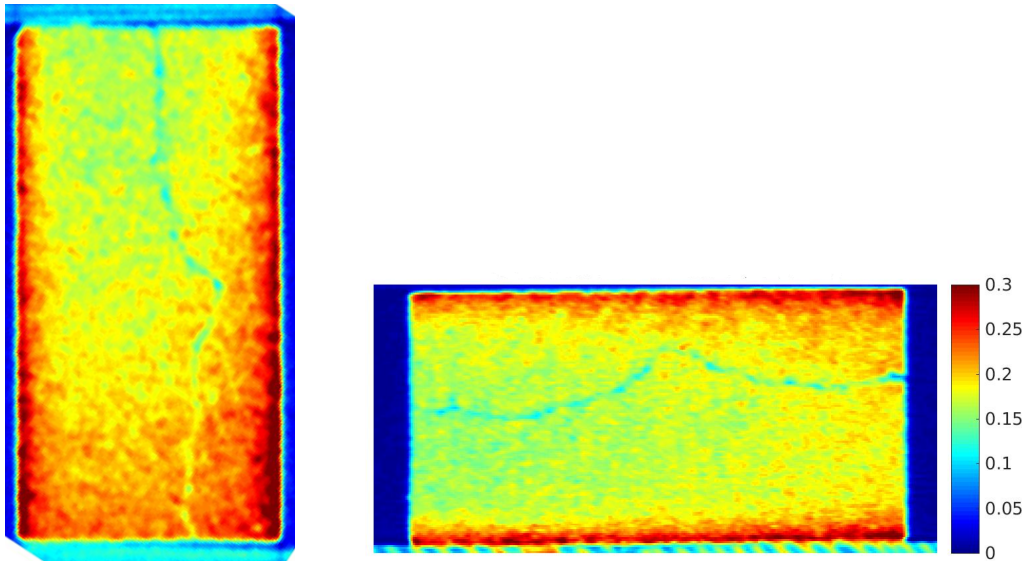

(a) Side-oriented (b) Top-oriented

Figure 5.21: Linear attenuation $\bar{\mu}\,[\mathrm{cm}^{-1}]$ of 100 PPI cross-section with flat face (a) parallel (side-oriented) and (b) perpendicular (top-oriented) to X-ray source.

Interface Imprecision and Burner Erosion Error

As mentioned above, a variety of imprecisions occur at the interface between two porous sections. Known cone-beam artifacts appear at these interfaces, and unavoidable minor rotational misregistrations combined with a slight tilt in the porous media section alignment from perfectly horizontal can result in spurious subtracted pixel values around these interfaces. Thus, we suggest that the accuracy of attenuation values reported near interfaces be discounted.

Another potential uncertainty exists due to the fact that, over the course of burner operation, the SiC porous media sections began to undergo erosion. This is evident, for

instance, in the results of Fig. 5.22, which shows not only the slight interface tilt from the horizontal, but also the development of a hole nearly 1 mm deep in the 65 PPI piece directly in the center of the burner. While this range falls within the range of interface values that we suggest to discount, it is notable that in this situation the average porosity correction would yield a temperature that is too low, as the attenuation values in the center of this slice should not be corrected for the burned-off material. Notably, such phenomena would be nearly impossible to diagnose non-destructively without XCT-based techniques.

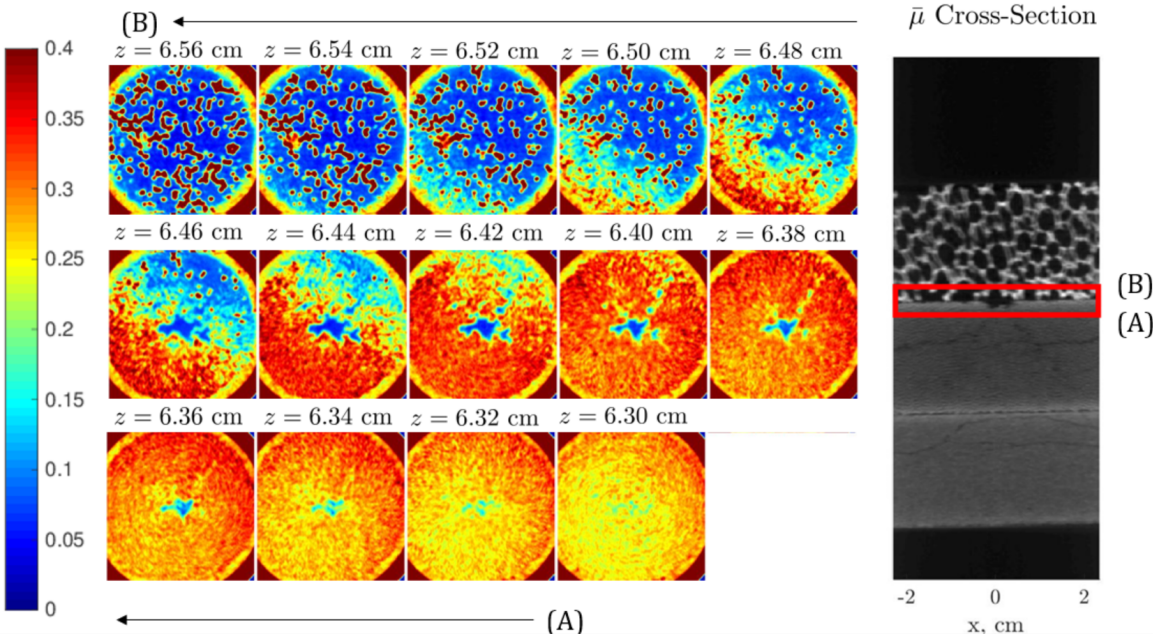

Figure 5.22: Slice-by-slice cross section of linear attenuation $\bar{\mu}[\text{cm}^{-1}]$ near 65 PPI - 3 PPI interface. Erosion of SiC material at surface of 65 PPI section is evident.

Reconstruction Artifact Errors

While the FDK method is relatively well-known and widely used, it is an approximation that is susceptible to a few well-known artifacts, such as axial intensity drop Zhu et al. (2008). Further, traditional CT artifacts such as ring artifacts (resulting from anomalous detector channels), streaking (due to scan misregistration or sharp density gradients), and beam hardening (due to differential attenuation of high and low-energy X-rays) can contribute to quantitative error.

In the context of the present work, beam hardening artifacts have already been

discussed in Sec. 5.2.3. While streaking was observed in early attempts at this experiment, reconstruction-based averaging (as opposed to projection-space averaging) and precise registration ensures that streaking is minimal. Ring artifacts in the current dataset are minimal, particularly when many pixels are averaged (as shown in Sec. 5.2.3). Thus, no ring artifact correction was required for this study – this result is a direct consequence of careful and consistent detector calibration procedures. With respect to cone-beam

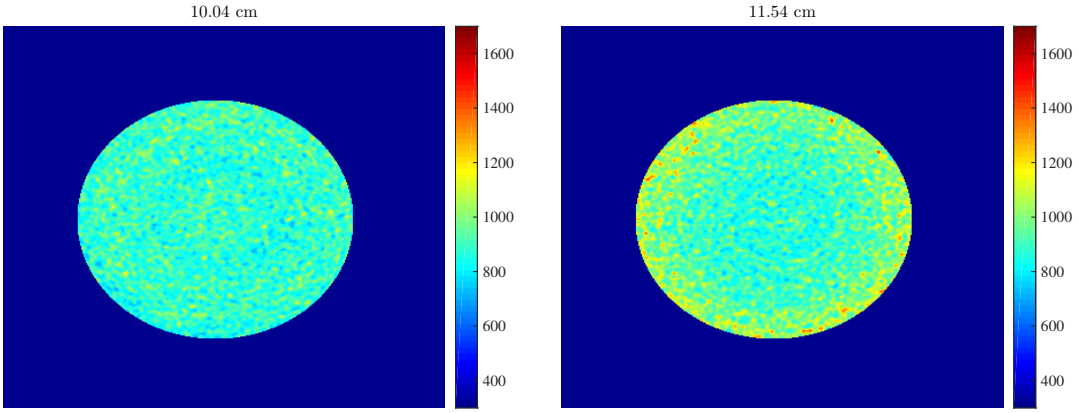

(a) Implied temperature profile at outlet of 3 PPI section (z = 10 cm).

(b) Implied temperature profile near outlet of quartz tube (z = 11.5 cm).

Figure 5.23: Development of cupping artifact with increased height along the burner tube.

artifacts, axial intensity drop is expected (and observed) to be small for this experiment given its maximum cone angle of 3.3^o. The results of Zhu et al. (2008) suggest a theoretical maximum drop of 1% in the attenuation signal near the top of the tube. As discussed above, results at interfaces wherein one could expect cone-beam distortions have been noted in the results presented here. The major artifact observed in this experiment is a cupping artifact near the top and bottom of the tube. While this artifact appears to have little effect on signal homogeneity within the portion of the burner over which the volume average is taken, it may affect values near the top of the tube, which could at least partially explain why the volume-averaged X-ray implied temperature signal does not decrease with height near the top of the tube as the thermocouple measurements do in Fig. 5.19(b). The increase in the magnitude of this artifact with height can be observed as an increase in the implied temperature in the gas near the outer edge of the

tube in Fig. 5.19(d), and is shown more explicitly in Figs. 5.23(a) and 5.23(b), with the field of view (2.5 cm) encompassing the entire porous media section to illustrate the artifact most clearly. Averaging was performed over the inner 60% of this field, which appears substantially less sensitive to the artifact. To account for this artifact explicitly, we add a coarse 5% value to the temperature uncertainty in the burned gas, with the understanding that this may be inadequate near the top of the tube. Note that while this artifact can also be observed near the bottom of the tube (best shown in results presented here as light blue edges in the bottom portion of the burner in Fig. 5.15), the attenuation value in this cool gas region is large enough to effectively mask its quantitative effect. Only when attenuation values become extremely small, as they do in the burned gas, do such artifacts begin to have noticeable impact on quantitative measurements.

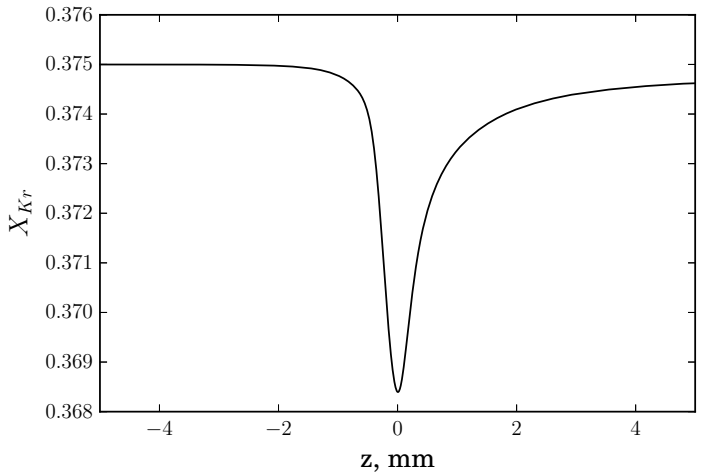

Figure 5.24: Results of premixed flame calculation describing expected variation in X_{Kr} due to combustion reactions. Operating conditions are those with $X_{Kr} = 0.35$ described in Sec. 5.3.3.

X_{Kr} Variation in the Combustion Region

In some cases, it is possible that the mole fraction of krypton would change appreciably as a result of combustion chemistry. A premixed flame calculation at the PMB operating conditions was performed to assess this variation in the context of lean methane combustion, and results can be found in Fig. 5.24. This curve indicates that the maximum

change in X_{Kr} near to the reaction zone is less than 2% of the nominal value), and that this region is highly spatially localized, as X_{Kr} returns to within 0.2% of its nominal value 2 mm downstream of the reaction zone. In the context of the PMB, where we have a more distributed reaction zone, it is prudent to consider the potential for such changes in the bottom third of the 3 PPI section (approximately 8 mm downstream of the interface) and potentially within the portion of the 65 PPI section closest to the flame. This effect results from the fact that local changes in the number of intermediates at constant pressure may cause a slight local decrease in the krypton mole fraction. Overall, this uncertainty is assumed to be negligible outside of spatial regions close to the reaction zone, wherein it will be assumed to contribute a 2% standard error value in implied temperature calculation.

Compound Coefficient of Variation

In order to account for each of the above uncertainties, we compute a the total standard error for each axially averaged temperature point using Eq. (3.2.11). We incorporate uncertainties in gas-phase attenuation using the following general formula with $T = \Delta\bar{\mu}_o^1 T_o^1 \Delta\bar{\mu}^{-1}$ with variation in X_{Kr} explicitly taken into account as an uncertainty,

$$SE_T = T\left\{\left(\frac{\delta\Delta\bar{\mu}_o}{\Delta\bar{\mu}_o}\right)^2 + \left(\frac{\delta\Delta\bar{T}_o}{\Delta\bar{T}_o}\right)^2 + \left(-\frac{\delta\Delta\bar{\mu}}{\Delta\bar{\mu}}\right)^2\right\}^{1/2} \tag{5.6.21}$$

$$= T\frac{\delta\Delta\bar{\mu}}{\Delta\bar{\mu}}. \tag{5.6.22}$$

We see that the measured attenuation values are the only contributor to uncertainty, under the reasonable assumption that measurements at the reference conditions are accurate. We can now define the coefficient of variation in $\Delta\bar{\mu}$ as follows,

$$\frac{\delta\Delta\bar{\mu}}{\Delta\bar{\mu}} = \left\{\left(\frac{\sigma}{\Delta\bar{\mu}}\right)_{HG}^2 + \left(\frac{\sigma}{\Delta\bar{\mu}}\right)_{Rec}^2 + \left(\frac{\sigma}{\Delta\bar{\mu}}\right)_{Drift}^2 + \left(\frac{\sigma}{\Delta\bar{\mu}}\right)_{XKr}^2\right\}^{1/2} \tag{5.6.23}$$

where Rec refers to reconstruction artifacts such as cupping and axial intensity drop, HG refers to variation observed in the slice in question filled with homogeneous gas as analyzed in Sec. 5.2.3, $Drift$ refers to error introduced by hardware drift, and XKr refers

Burner Section	$\left(\frac{\sigma}{\Delta\bar{\mu}}\right)_{HG}$	$\left(\frac{\sigma}{\Delta\bar{\mu}}\right)_{Rec}$	$\left(\frac{\sigma}{\Delta\bar{\mu}}\right)_{Drift}$	$\left(\frac{\sigma}{\Delta\bar{\mu}}\right)_{XKr}$	$\frac{\delta\Delta\bar{\mu}}{\Delta\bar{\mu}}$
Unburned	2.0%	1.0%	0.2%	0.0%	2.3%
100 PPI	4.0%	0.0%	0.3%	0.0%	5.0%
65 PPI	4.0%	0.0%	0.4%	1.0%	5.7%
3 PPI	6.0%	0.0%	0.8%	1.0%	6.1%
Burned	2.0%	5.0%	0.2%	0.0%	5.3%

Table 5.2: Summary of experimental uncertainties in implied temperature measurement.

to error introduced due to local variation in the krypton mole fraction. Note that the XKr contribution is only applied to points within 8 mm of the reaction zone. We define each of these quantities for the different regions of the burner separately in Table 5.2, with values as stated throughout this section. These values are used directly to compute error bars in Fig. 5.19(b), which represent 95% confidence intervals.

Note that due to averaging over over several thousand pixels in each slice, coefficients of variation for the mean value of each slice would be uniformly less than 0.2% if one uses the $n^{-1/2}$ expected scaling from the law of large numbers.

5.6.3 Uncertainty in Thermocouple Measurements

Measuring stochastic uncertainties in thermocouple measurements are relatively straightforward. Data was taken over a long enough period of time that explicit uncertainties can be computed as $\sigma_C = 0.2K$ and $\sigma_H = 1.5K$ for hot H and cold C conditions, respectively. Note that these uncertainties do not take into account bias errors such as those resultant from a radiation loss. As shown in Bradley and Matthews (1968), radiation losses can result in thermocouple readings that are on the order of 10-50 K smaller than the actual gas temperature that would be recorded by XCT. Error bars on the thermocouple measurements reflect a 30 K radiation loss estimated as in (Glawe et al., 1956) in addition to the above stochastic uncertainty. Thus, 95 % confidence bounds are as follows for measured value M:

$$T_C = T_C^M \pm 0.4K, \tag{5.6.24}$$

$$T_H = T_H^M - 30 \pm 3K, \tag{5.6.25}$$

5.6.4 SNR Trends

Finally, in the context of this uncertainty analysis, it is useful to observe changes in SNR with increasing scan numbers. The change in the reconstructed field associated with averaging additional scans can be found in Fig. 5.25, while trends in SNR in a small region in the burned gas directly above the burner outlet are evaluated in Fig. 5.26. Importantly, we again see $n^{1/2}$ scaling of SNR with increasing scan number, reflected by a commensurate improvement in visual image quality.

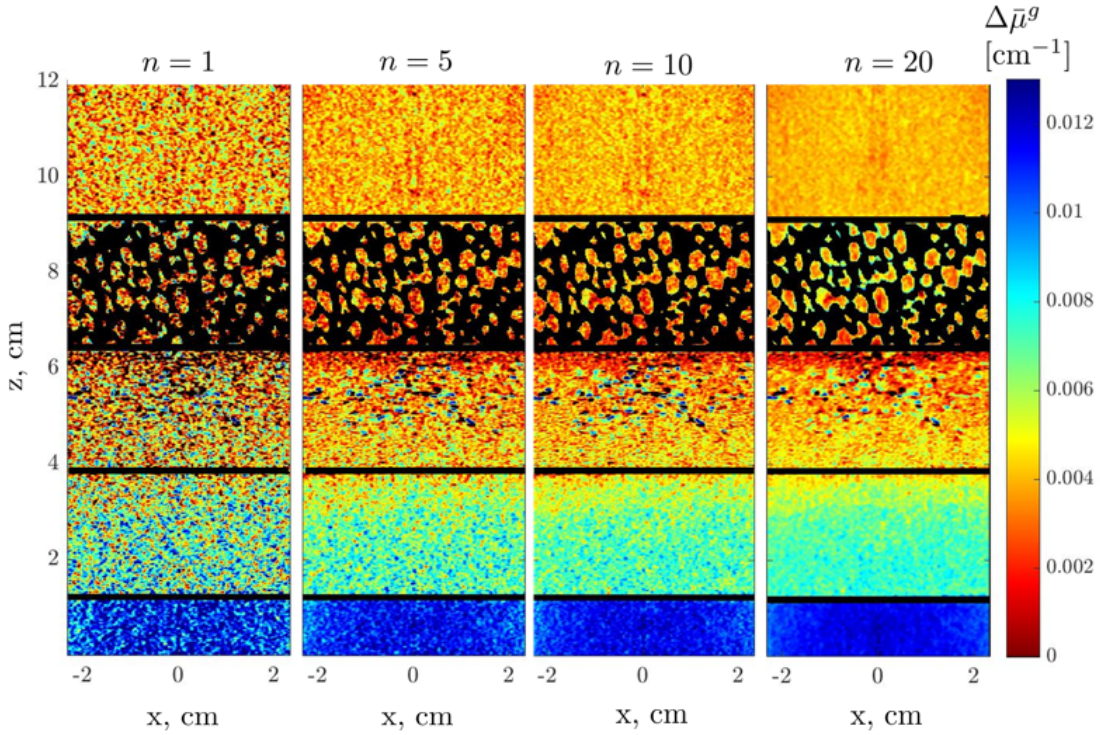

Figure 5.25: Increase in SNR with scan number.

5.7 Conclusions

This study has demonstrated the potential of XCT to provide relatively unique insight into internal processes characteristic of PMBs within a burner specially designed for X-ray compatibility. In addition to allowing for qualitative assessment of internal flame structure, non-intrusive extraction of implied temperature fields from a multi-zone SiC

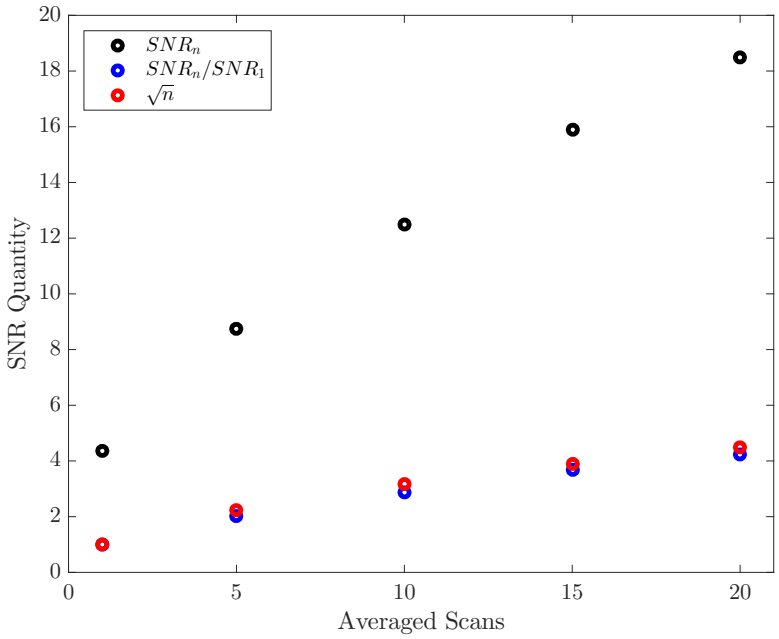

Figure 5.26: SNR in gas phase directly above burner outlet.

PMB yields results that show encouraging agreement with those from traditional thermocouple measurements. Further, the XCT method was able to distinguish the substantial, mostly homogeneous internal preheat zone in the 65 PPI SiC upstream section that is not predicted by most computational models (e.g. Barra and Ellzey (2004)) and would have been very difficult to diagnose using traditional methods. While these first measurements are indicative of the potential of XCT as a combustion diagnostic, detailed uncertainty analysis reveals several key sources of error that should be considered such as hardware drift, reconstruction artifacts, porous media inhomogeneity, and XCT measurement noise.

The fact that PMB systems have relatively high thermal mass and tend to operate near a steady state condition appears to make them particularly amenable to XCT measurements. However, while XCT has a major strength in its ability to non-intrusively yield 3-D field data, its temporal resolution is also hindered by the requirement of inter-scan averaging (on a timescale of several minutes) to achieve reliable measurements at contrast levels characteristic of radiodense gas-phase flows. Developing methods to improve signal-to-noise ratio and scan acquisition rate using a combination of hardware

and software improvements (optimized reconstruction techniques, advanced detectors, brighter sources, etc.) would enhance the attractiveness of this diagnostic tool. Further, improving temporal resolution with a multiple-detector, multiple-source system that would allow XCT measurements to capture transient effects could be quite helpful in developing discrete models of porous media and filtration combustion. In the end, the experiment described here has demonstrated the viability of performing useful combustion experiments within the limitations of available XCT hardware, and suggests that this experimental method holds substantial promise in providing high-resolution 3-D datasets describing implied gas-phase temperature and density fields with minimal (if any) optical access requirements.

Chapter 6

Summary, Conclusions, and Directions for Future Work

The work presented here has demonstrated the systematic development of X-ray absorption techniques at clinical energies for application to gas-phase flows. Notably, these diagnostics are non-intrusive, yield 3-D datasets, are unaffected by the optical environment, and can be set up with relative ease. Beginning with analysis of scalar mixing in a turbulent jet, we have illustrated the viability of using lab-scale X-ray sources for quantitative measurement of attenuation fields within gas-phase flow phenomena at high energies characteristic of non-synchrotron sources. Favorable comparison of XCT data to data from the literature and theoretical expectation reflect encouragingly on the ability of these diagnostics to capture useful information about gas-phase flows.

Extension of these methods to the case of a premixed free flame has demonstrated that the reconstructed X-ray attenuation field provides a quantity that represents a natural surrogate for gas density measurement. Effects of the krypton gaseous contrast agent on flame structure and behavior have been analyzed, and a complete investigation of noise in cone-beam XCT has revealed that increasing aggregate photon count via repeated scans and averaging substantially improves SNR to the point of enabling practical measurements. Additionally, simulation of the krypton-diluted flame in multiple dimensions has yielded reasonable agreement with simultaneous experimental data describing chemiluminescence and X-ray attenuation. The distance between the surfaces defined by the maximum X-ray

gradient surface and maximum visual emission magnitudes has been shown to empirically relate to the thermal flame thickness.

Finally, an X-ray compatible porous media burner has been developed to allow for robust two-zone PMB operation while minimizing X-ray artifacts and maximizing photon count. Importantly, it has been shown that background subtraction mitigates the vast majority of XCT artifacts in this experiment, and a detailed set of procedures to account for such variations as tube heating, thermal expansion, and other uncertainties has been described in detail. XCT scans of the PMB combusting a mixture with half of the nitrogen diluent replaced by krypton have demonstrated the viability of obtaining 3-D X-ray attenuation fields within the PMB that could be directly related to temperature. Importantly, the work presented here was the first to develop the theory relating gas-phase X-ray attenuation to temperature and utilize these ideas in pursuit of a practical diagnostic technique for gas-phase flows. Comparison of implied temperature signals to thermocouple data from the same experiment shows encouraging levels of agreement in the gas-phase section, while the XCT data suggest internal heat recirculation in excess of that predicted by common 1-D computational models. Further, these results have allowed for robust analysis of potential sources of noise and uncertainty, have supported non-destructive analysis of burner robustness, and have suggested the presence nontrivial pore-scale heat transfer physics.

In the end, the work described here has shown that lab-scale, polychromatic X-ray sources are viable for experimental research in both reacting and inert gas-phase fluid mechanics. While the large number of scans required to obtain viable photon counts in the current work creates significant stresses on existing hardware, advances such as brighter sources, faster detector sample rates, and photon-counting detectors could help to remove these barriers in the future. Further, the possibility of multi-directional XCT systems that allow for simultaneous projection acquisition could enable time-resolved 3-D measurements, which would be of substantial utility to the community. Finally, advanced reconstruction techniques could be leveraged to decrease the number of photons required to obtain clean experimental signals.

In many ways, the timing of this work has tracked the progress of the nascent research community applying X-ray diagnostics to gas-phase fluid mechanics. The majority of

such work has taken place at the Advanced Photon Source at Argonne National Laboratory, a powerful synchrotron source that has nicely complemented the research presented here on lab-scale sources with the equivalent at facility scale. Within six months of this writing, Swantek et al. (2017) used ensemble-averaged Abel inversions of absorption radiography to interrogate the internal scalar concentration field of a high-pressure gas-phase jet, Tranter et al. (2017) attempted to map gas density within an SiC tube via X-ray fluorescence coupled with a sophisticated signal trapping model, and Hansen et al. (2017) related 2D X-ray fluorescence measurements within an axisymmetric McKenna flame to temperature in a manner very similar to that of Dunnmon et al. (2017a). While these advances in synchrotron imaging demonstrate the progress of the field in pursuit of X-ray diagnostics for gas-phase flows, the utility of high-energy lab-scale sources in enabling true 3-D tomography, increased penetrating power, rapid scan times, and ease of experimental design remains apparent. As the field of experimental fluid mechanics continues to progress, it is the author's hope that X-ray diagnostics will have a substantial role to play in enabling important new discoveries.

Appendix A

Detailed Derivation of Reconstruction Expressions

In this section, we present a more detailed derivation of the fan-beam reconstruction algorithm of Eq. (2.2.12) and the FDK cone-beam reconstruction algorithm of Eq. (2.2.16) originally derived by (Feldkamp et al., 1984). The style of the derivation shown here follows that of Hsieh (2009) closely.

A.1 Fan-Beam FBP Derivation

In the fan-beam case, we begin by observing that a fan-beam sample can be represented as a parallel-beam sample with,

$$\begin{cases} \phi = \beta + \gamma \\ l = D\sin\gamma, \end{cases} \tag{A.1.1}$$

with D the source-to-axis distance, γ the angle formed between a given ray and the iso-ray (the ray connecting the source with the center of the detector) and β the projection angle. The reconstruction algorithm for this parallel-beam case, presented in Eq. (2.2.11),

is reproduced for convenience,

$$\mu(x,y) = \int_0^{\pi}\int_{-\infty}^{\infty} g(l',\phi)h_R(l-l')dl'd\phi \tag{A.1.2}$$

$$= \int_0^{\pi}\int_{-\infty}^{\infty} g(l',\phi)h_R(x\cos\phi + y\sin\phi - l')dl'd\phi, \tag{A.1.3}$$

$$= \frac{1}{2}\int_0^{2\pi}\int_{-\infty}^{\infty} g(l',\phi)h_R(x\cos\phi + y\sin\phi - l')dl'd\phi, \tag{A.1.4}$$

where we have used the relationship $l = x\cos\phi + y\sin\phi$ demonstrated in Fig. 2.1 and modified the expression such that it covers a full azimuthal domain up to 2π. We now recast this equation in polar coordinates such that (x,y) is represented by (r,θ) and leverage the identity $r\cos(\phi-\theta) = r\cos\theta\cos\phi + r\sin\theta\sin\phi$ such that,

$$\mu(r,\theta) = \frac{1}{2}\int_0^{2\pi}\int_{-\infty}^{\infty} g(l',\phi)h_R[r\cos(\phi-\theta) - l']dl'd\phi, \tag{A.1.5}$$

Now, substituting Eq. (A.1.1) into Eq. (A.1.5), using the fact that $dld\phi = D\cos\gamma d\gamma d\beta$, and observing that functions of β are 2π-periodic, we obtain,

$$\mu(r,\theta) = \frac{1}{2}\int_0^{2\pi}\int_{-\gamma_m}^{\gamma_m} g(\gamma,\beta)h_R[r\cos(\beta+\gamma-\theta) - D\sin\gamma]D\cos\gamma d\gamma d\beta, \tag{A.1.6}$$

where γ_m is again the maximum γ beyond which all projection values are zero. In order to express the argument of h as a convolution, it is useful to use the following identities,

$$r\cos(\beta+\gamma-\theta) - D\sin\gamma = r\cos(\beta-\theta)\cos(\gamma) - [r\sin(\beta-\theta) + D]\sin\gamma, \tag{A.1.7}$$

$$L\cos\gamma' = D + r\sin(\beta-\theta) \tag{A.1.8}$$

$$L\sin\gamma' = r\cos(\beta-\theta), \tag{A.1.9}$$

where L is the distance from the source to a point of reconstruction at (r,θ) that is passed through by a ray at angle γ'. Combining Eqs. (A.1.6) and (A.1.7) yields the following relation,

$$r\cos(\beta+\gamma-\theta) - D\sin\gamma = L\sin(\gamma'-\gamma), \tag{A.1.10}$$

where we have leveraged the fact that $L\sin(\gamma' - \gamma) = L\sin\gamma'\cos\gamma - L\cos\gamma'\sin\gamma$. Substituting Eq. (A.1.10) into Eq. (A.1.6) gives,

$$\mu(r,\theta) = \frac{1}{2}\int_0^{2\pi}\int_{-\gamma_m}^{\gamma_m} g(\gamma,\beta)h_R[L\sin(\gamma'-\gamma)]D\cos\gamma d\gamma d\beta,, \tag{A.1.11}$$

where the integral over γ is now in the form of a convolution. To further refine the expression for the argument of the filter function h. Some simple algebra yields the relation,

$$h_R(L\sin\gamma) = \int_{-\infty}^{\infty} H_R(\kappa)e^{2i\pi\kappa L\sin\gamma}d\kappa \tag{A.1.12}$$

$$= \left(\frac{\gamma}{L\sin\gamma}\right)^2 \int_{-\infty}^{\infty} H_R(\kappa')e^{2i\pi\kappa'\gamma}d\kappa' \tag{A.1.13}$$

$$= \left(\frac{\gamma}{L\sin\gamma}\right)^2 h_R(\gamma), \tag{A.1.14}$$

where we have used a transformation such that $\kappa' = (\kappa L\sin\gamma)/\gamma)$. Finally, because L does not depend on γ, we can combine Eqs. (A.1.11) and (A.1.14) recover the reconstruction formula of Eq. (2.2.12) as,

$$\mu(x,y) = \int_0^{2\pi}\int_{-\gamma_m}^{\gamma_m} L^{-2}g(\gamma,\beta)h_R''(\gamma'-\gamma)D\cos\gamma d\gamma d\beta, \tag{A.1.15}$$

$$h_R''(\gamma) = \frac{1}{2}\left(\frac{\gamma}{\sin\gamma}\right)^2 h_R(\gamma) \tag{A.1.16}$$

A.2 Cone-beam FDK Derivation

To derive the cone-beam reconstruction technique of Feldkamp et al. (1984) that assumes a flat-panel detector with equal spacing, we begin by presenting the fan-beam reconstruction formula for a detector with equal spacing in Eq. (A.2.17),

$$\mu(r,\theta) = \frac{1}{2}\int_0^{2\pi}\int_{-\infty}^{\infty} U^{-2}(r,\theta,\beta)\left(\frac{D}{\sqrt{D^2+l^2}}\right)g(l,\beta)h_R(l'-l)dld\beta, \tag{A.2.17}$$

$$U(r,\theta,\beta) = \frac{D + r\sin(\beta-\theta)}{D}, \tag{A.2.18}$$

where l is the coordinate on the imaginary linear detector parallel to the actual detector and containing the origin, which is exactly equivalent to the definition in both Eq. (2.2.11) and Fig. RadonFig. The similarity between Eqs. (A.2.17) and (A.1.15) is expected, as each expression requires adjusting the projection by a geometric factor and additional weighting of the backprojections Further, U in the this case represents the ratio of the projected distance to the source-to-axis distance, and is thus analogous to L in the equiangular case. Finally, in the context of deriving FDK, it is helpful to note that the geometric weighting factor here is precisely,

$$\frac{D}{\sqrt{D^2+l^2}} = \cos\gamma, \tag{A.2.19}$$

meaning that the reconstruction formula may be rewritten as,

$$\mu(r,\theta) = \frac{1}{2}\int_0^{2\pi}\int_{-\infty}^{\infty} U^{-2}(r,\theta,\beta)g(l,\beta)h_R(l'-l)\cos\gamma dl d\beta, \tag{A.2.20}$$

which bears a striking resemblance to Eq. (A.2.17). Specifically, in cone-beam reconstruction, the appropriate geometric adjustment factor must take into account the tilt angle τ in addition to the fan angle γ. Thus, the appropriate weighting factor becomes,

$$\cos\gamma\cos\tau = \frac{D}{\sqrt{D^2+u^{\dagger 2}}}\frac{\sqrt{D^2+u^{\dagger 2}}}{\sqrt{D^2+u^{\dagger 2}+v^{\dagger 2}}} = \frac{D}{\sqrt{D^2+u^{\dagger 2}+v^{\dagger 2}}} \tag{A.2.21}$$

where (u,v) are respectively the transaxial and axial detector coordinates of Fig. 2.2, $(u^\dagger, v^\dagger)$ are the equivalent of (u,v) at the imaginary detector containing the origin, and $u^\dagger$ is exactly equivalent to l in this notation. Replacing the $\cos\gamma$ geometric adjustment term in Eq. (A.2.20) with the cone-beam form from Eq. (A.2.21) and rewriting the resultant expression in the cone-beam coordinate system of Fig. (2.2) directly yields,

$$\mu(x,y,z) = \frac{1}{2}\int_0^{2\pi}\int_{-\infty}^{\infty}\left(\frac{D}{x+D}\right)^2 g(u^\dagger,v^\dagger,\beta)h_R(u^{\dagger\prime}-u^\dagger)\cos\gamma\cos\tau du^\dagger d\beta, \tag{A.2.22}$$

which can be more directly expressed in terms of system variables as in Zhu et al. (2008),

$$\mu(x,y,z) = \frac{1}{2}\int_0^{2\pi} \left(\frac{D}{x+D}\right)_\beta^2 g_F\left(\left(\frac{Dy}{x+D}\right)_\beta, \left(\frac{Dz}{x+D}\right)_\beta, \beta\right) d\beta \tag{A.2.23}$$

$$g_F(u,v,\beta) = \int_{-\infty}^{\infty} \frac{D}{\sqrt{u'^2+v^2+D^2}} g_v(u',v,\beta) h_R(u-u') du' \tag{A.2.24}$$

$$g_v(u,v,\beta) = g\left(u\frac{d}{D}, v\frac{d}{D}, \beta\right), \tag{A.2.25}$$

which is the exact form presented in Eqs. (2.2.14)-(2.2.16).

Appendix B

FLUENT Solver Verification Data

B.1 Problem Definition and Objectives

The goal of the simulation presented in Chap. 4 is to assess the effect of krypton addition on laminar flame structure in two dimensions, which will account for such effects as flame stretch and strain. As an important verification step, we demonstrate implementation of an appropriate problem setup and solution procedure in the FLUENT solver following the work of Chander and Ray (2008) and illustrate the applicability of this method to a case with detailed results presented by Bennett et al. (1999).

B.2 Problem Setup

The general setup of the verification problem can be observed in Fig. B.1. We consider a premixed, axisymmetric Bunsen flame stabilized on a burner head. Appropriate boundary conditions are as follows:

- Boundary (1): Outlet: outflow (gradients vanish in all variables but pressure) or pressure outlet
- Boundary (2): Radial far-field: wall (enclosed) or pressure inlet (free)
- Boundary (3): Coflow: velocity inlet or pressure inlet
- Boundary (4): Burner head: wall

- Boundary (5): Fuel inlet: velocity inlet
- Boundary (6): Axisymmetry: axisymmetry

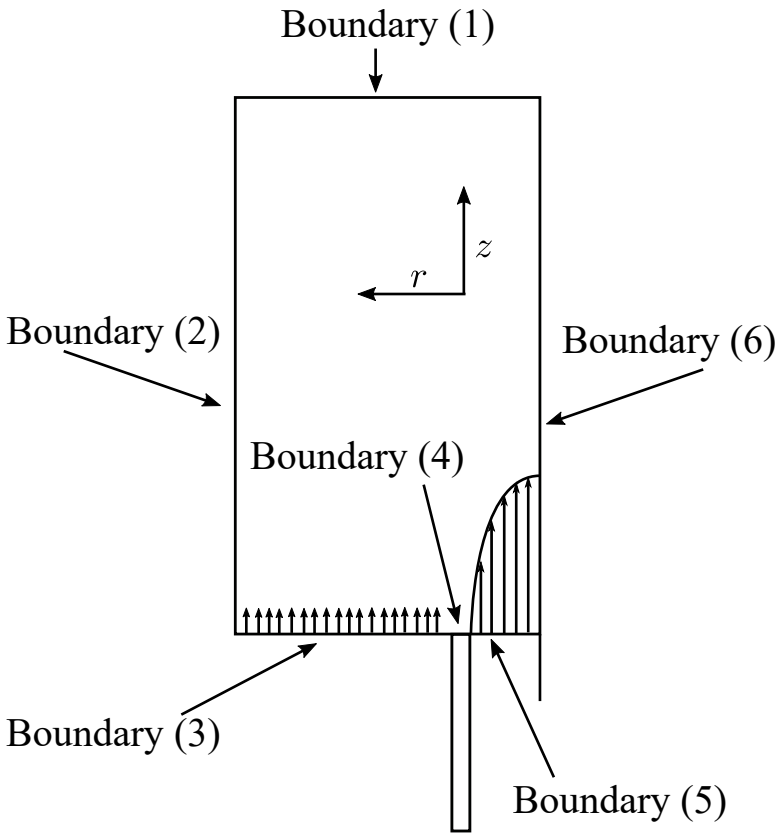

Figure B.1: Schematic of verification calculation.

B.3 Verification Using Bennett et al. (1999)

B.3.1 Description of Verification Case

While a variety of laminar free flame simulations exist in the literature, we use the rich calculation of (Bennett et al., 1999) as a baseline given the similarities to our experimental case in both geometry and stoichiometry. Detailed presentation of major and minor species fields as well as easily comparable centerline profiles are presented, making this a useful set of results on which to perform verification of our problem setup and solution method.

This case involves a rich Bunsen flame at equivalence ratio of $\Phi = 1.243$ (with 11.5 % mole fraction of CH_4) stabilized on an isothermal burner head with temperature $T = 300$ K , inner radius $r_I = 5$ mm, and wall thickness $w_{jet} = 0.5$ mm. Boundary conditions are as follows:

- Boundary (1): Outflow, $\partial()/\partial_z = 0$, p is extrapolated ; $0 < r < 30$ mm, $z = 250$ mm
- Boundary (2): Velocity inlet, $v_z = 0.4$ m/s, $v_r = 0$; $Y = Y_{air}$; $r = 30$ mm, $0 < x < 250$ mm, $T = 300$ K
- Boundary (3): Velocity inlet; $v_z = v_{z,O}\{1 - \exp(-|r - r_I - w_{jet}|/2 \text{ mm }\}$, $v_{z,O} = 0.4$ m/s; $Y = Y_{air}$; $5.5 < r < 30$ mm, $z = 0$ mm; $T = 300$ K
- Boundary (4): Wall, $T = 300$ K; $Y = Y_{air}$; $5 < r < 5.5$ mm, $z = 0$ mm
- Boundary (5): Velocity Inlet; $\phi = 1.243$; fully developed $v_r = 0$, $v_z = v_{z,max}\left[1 - \left(\frac{r}{R}\right)^2\right]$ with $v_{z,max} = 2\bar{v}_z$, $\bar{v}_z = 0.4$ m/s; $0 < r < 5$ mm, $z = 0$ mm, $T = 300$ K
- Boundary (6): Axisymmetry, $\partial()/\partial_r = 0$, $v_r = 0$; $r = 0$ mm, $0 < x < 250$ mm

To solve the case from (Bennett et al., 1999) using the FLUENT solver, we use a mesh inspired by Chander and Ray (2008), with initial resolution of $\Delta r = 50\mu$m $\times$ $\Delta z = 200\mu$m within $0 < z < 25$ mm, $0 < r < 5$ mm and smoothly expanding to the boundaries in similar fashion. This entire mesh was refined by a factor of two to achieve resolution similar to the finest resolution of Bennett et al. (1999).

The solution procedure was as follows. A cold, non-reacting jet solution is first computed on the initial grid described above using a steady-state method. Ignition was accomplished via a transient solver and spark ignition kernel with initial radius 2 mm supplied at 5 mm above the burner, which causes localized ignition – the solver was returned to a steady state configuration after two timesteps of spark ignition. The coarse initial grid was refined only after convergence was achieved.

B.3.2 Key Differences Between Current Case and (Bennett et al., 1999)

Before presenting detailed results, it is helpful to explicitly delineate differences between the present calculation and that of Bennett et al. (1999). These are listed below in Table B.1. Generally, the boundary conditions were able to be matched with those of Bennett et al. (1999) with few exceptions to the degree allowed by the inherent differences between a velocity-vorticity (Bennett and Smooke, 1998) and primitive variable formulation. The numerical solution technique is clearly quite different, as a major goal of the original Bennett et al. (1999) computation was to demonstrate the ability of a particular adaptive gridding approach to enable direct solution of the coupled governing equations using Newton iteration. Advances in computational power since Bennett et al. (1999) have enabled laminar flame calculations at similar resolution without the use of these particular methods, and the calculations here couple a segregated momentum-pressure procedure based on the SIMPLE algorithm to solution of the enthalpy and species equations performed via a hybrid Newton iteration/time-stepping procedure within the CHEMKIN software package (Grcar et al., 1988). Further, details on the radiation model are different – here, the narrow-band optically thin model recommended for modern combustion simulations was used (Sandia National Laboratory, 2003), while Bennett et al. (1999) utilize a different formulation due to Hall (1993) and others. Finally, there exists a slight difference in the mechanism for computing mixture-averaged thermal conductivity that is described in Table B.1.

B.3.3 Results

In terms of results, we compare both 2-D fields and quantitative centerline profiles for a wide variety of important variables, but present only temperature, axial velocity, and Y_{OH} here for the sake of brevity. The flame shape visible in the temperature fields in Figs. B.2(a) and B.2(b) demonstrate that the flame height between the two cases is very similar, but that the FLUENT results demonstrate a higher level of convex curvature. This difference could result from a slight difference in flame speed between the two cases. Specifically, we observe broadly higher temperatures (peak temperature of 2197 K) in the FLUENT

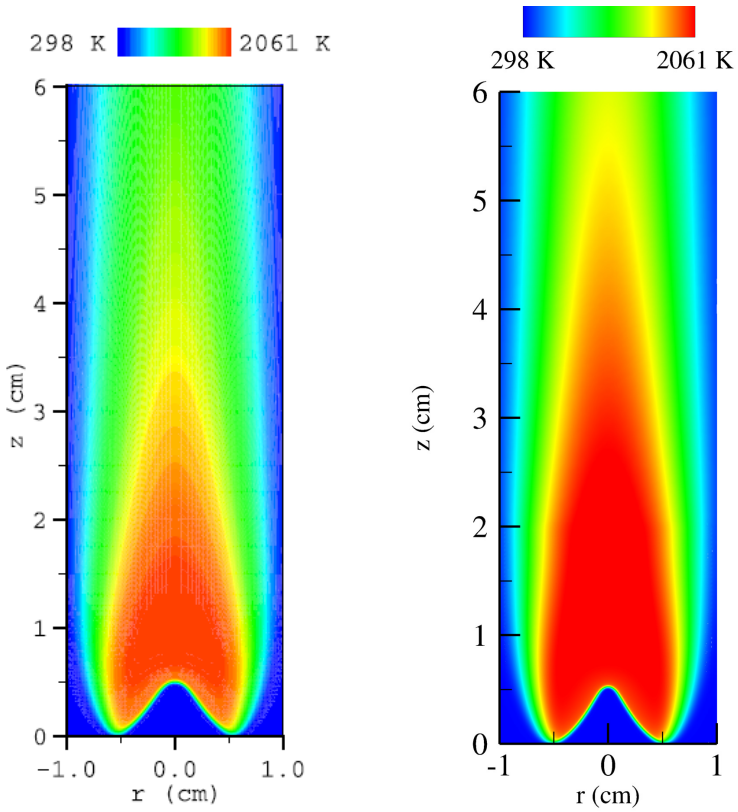

(a) Bennett et al. (1999) (b) FLUENT calculation

Figure B.2: Comparison with validation case: temperature.

calculation of Fig. B.2(b), compared to 2061 K in the literature case of Fig. B.2(a). Such an increase could result in an increase in the computed flame speed. The nature of the difference in the temperature fields can be observed along the centerline as in Fig. B.3, where the flame height is well predicted by the FLUENT calculation, but the downstream temperature is consistently lower in the literature calculation. Note also that the rate of temperature decrease from the peak temperature is almost identical (i.e. the different lines are parallel), implying that the radiation model is functioning appropriately. Quantitative confirmation that the radiation model is giving reasonable results can be found in the fact that their magnitude is on the order of 10^6 W/m^3, which are in line with literature values for this quantity (Chen et al., 2007).

Effects apparent in the temperature data also affect the velocity fields. As shown

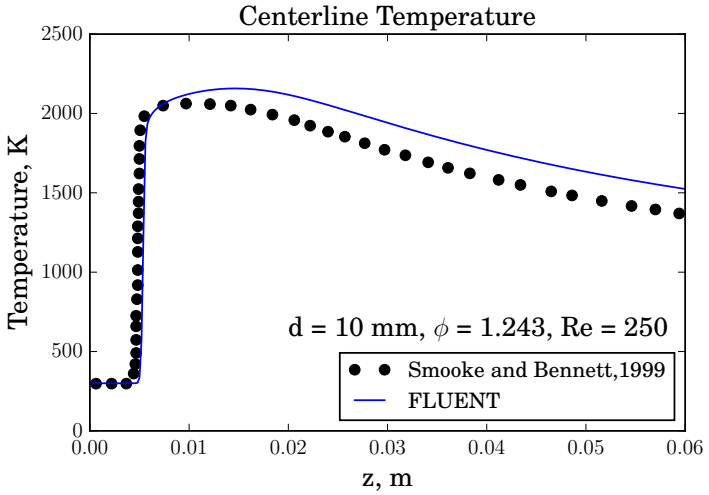

Figure B.3: Quantitative centerline temperature comparison.

qualitatively in Figs. B.4(a) and B.4(b), and quantitatively in Fig. B.5, the axial velocity fields between the two cases appear to be slightly different. The Bennett et al. (1999) inlet appears to undergo a much more substantial drop in velocity as the flow approaches the flame front, and the radial falloff of the maximum velocity in this case also appears to take a different form. This is an interesting result given that the inlet velocity profile of the FLUENT calculation was specified to be exactly equivalent to the literature case – it is possible that this results from the difference in boundary implementation between velocity-vorticity and primitive formulations, as additional verification results for a similar case from Chander and Ray (2008) (not shown here) that was originally solved in FLUENT demonstrate a very similar type of behavior to that observed in these FLUENT results. Generally, the velocity trends are in line with the temperature trends in the sense that the decreased downstream density (resultant from slightly higher temperature) yields consequently higher velocities.

In terms of the different species fields, there exists generally good qualitative agreement and some level of quantitative agreement. Taking OH as an example, as shown in Figs. B.6(a) and B.6(b) we observe very similar structure in both extent and structure of the species distributions. The largest quantitative difference in any of the species fields investigated in this verification procedure, found in the OH field, is shown in further detail

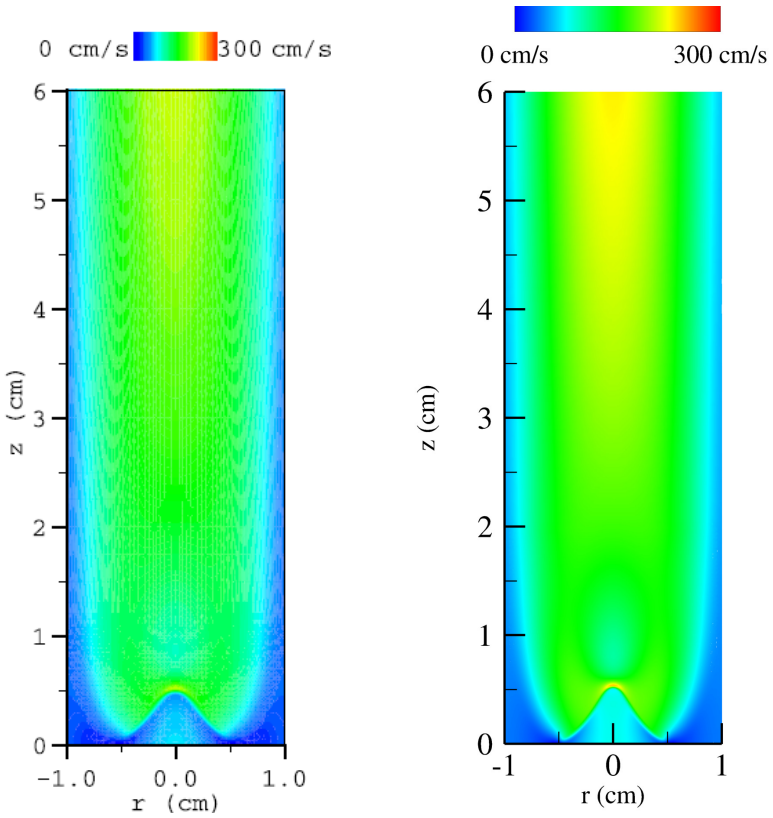

(a) Bennett et al. (1999) (b) FLUENT calculation

Figure B.4: Comparison with validation case: axial velocity

along the centerline in Fig. B.7. Clearly, the secondary reaction zone involving CO and H_2 is well captured downstream of the inner flame cone, though the OH concentrations in the FLUENT calculations are consistently higher than those reported in Bennett et al. (1999). This observation may be related to the slightly higher downstream CO_2 mass fraction in the Bennett et al. (1999) results coupled with the slightly lower downstream CO levels – it appears that additional CO and H_2 are available in secondary reaction zone of the FLUENT flame, creating additional opportunity for slightly higher levels of OH to form. Note that while not shown, other major and minor species are also well-resolved and compare favorably to the results of Bennett et al. (1999).

Thus, in general, the main differences between the current calculations and those of Bennett et al. (1999) are the higher downstream temperature, difference in upstream

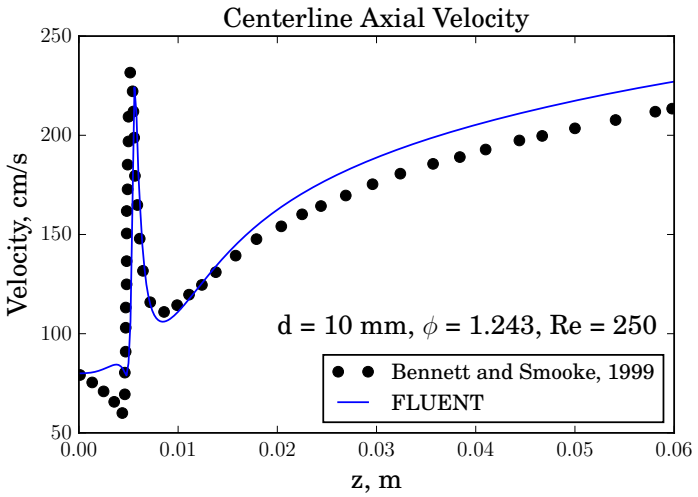

Figure B.5: Quantitative centerline velocity comparison.

velocity, and slight differences in chemistry resulting in the species field differences discussed above. The increased temperature to a degree explains the slightly higher flame speed (and associated concavity) observed in the FLUENT calculations. While these differences remain, the characteristics of the flame itself appear to be well-represented, and the results of this study reflect encouragingly on the viability of our approach to computing 2-D laminar flames with finite-rate chemistry using this solver.

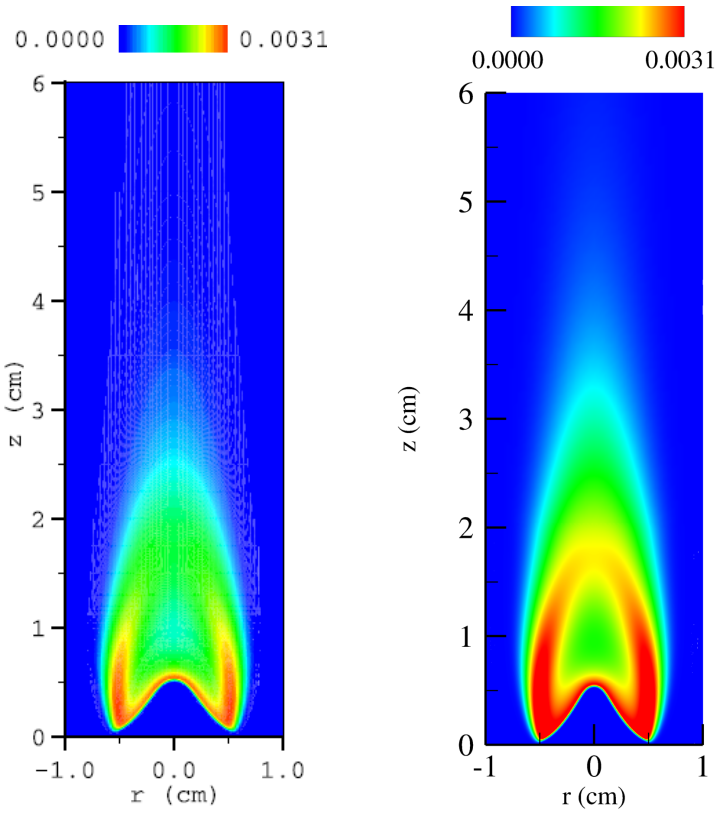

(a) Bennett et al. (1999) (b) FLUENT calculation

Figure B.6: Comparison with validation case: Y_{OH}.

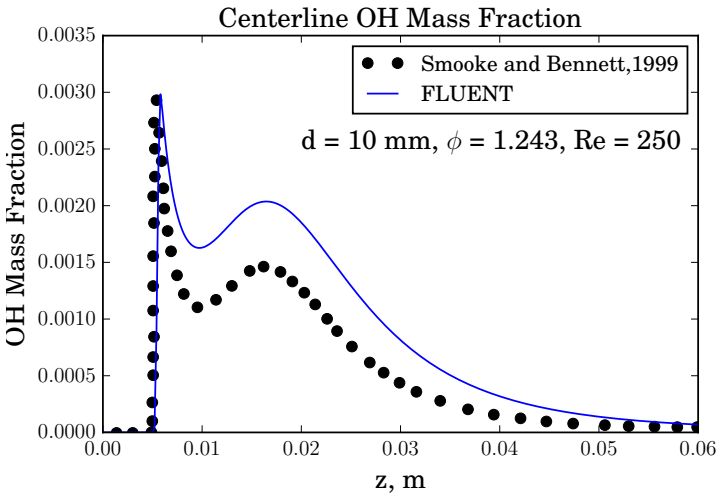

Figure B.7: Quantitative centerline Y_{OH} comparison.

Quantity	**(Bennett et al., 1999)**	**Current Calculation**
Inlet Boundary	Fully Developed, $\bar{v}_I = 0.4$ m/s, T = 300 K, $\phi = 1.243$	Same as Bennett et al. (1999)
Outlet Boundary	Zero flux (except $v_r = 0$)	Zero flux (except pressure)
$r = 0$ Boundary	$v_r = \omega = 0$, no radial gradients	no radial gradients
$r = 3$ Boundary	$v_z = 0.4$, T and Y gradients vanish	$v_z = 0.4$, $T = 300$ K, $Y = Y_{air}$
Wall Boundary	T = 300	Same as Bennett et al. (1999)
Coflow Boundary	$v_z = v_{z,O}\{1 - \exp(-\lvert r - r_I - w_{jet}\rvert/2 \text{ mm}\}$	Same as Bennett et al. (1999)
Numerical Method	Direct Newton solve	Iterative solve (based on SIMPLE)
Mesh	LRR adapted mesh (on T and Y)	Fixed, smoothly varying
Inlet Diffusion	$\rho v_z(Y_n - Y_{n,B}) = \frac{1}{Le_n}\left(\frac{\lambda}{c_p}\right)\frac{\partial Y_n}{\partial z}$	FLUENT Implementation
Formulation	Velocity-vorticity (Bennett and Smooke, 1998)	Primitive variables
Radiation	Optically thin (Hall, 1993)	Optically thin (Grosshandler, 1993)
Viscosity	Wilke	Wilke
Thermal Conductivity	Combination Averaging (Saxena)	Wilke

Table B.1: Differences between FLUENT and Bennett et al. (1999) setups.

Appendix C

Design Drawings: XCT Flow System

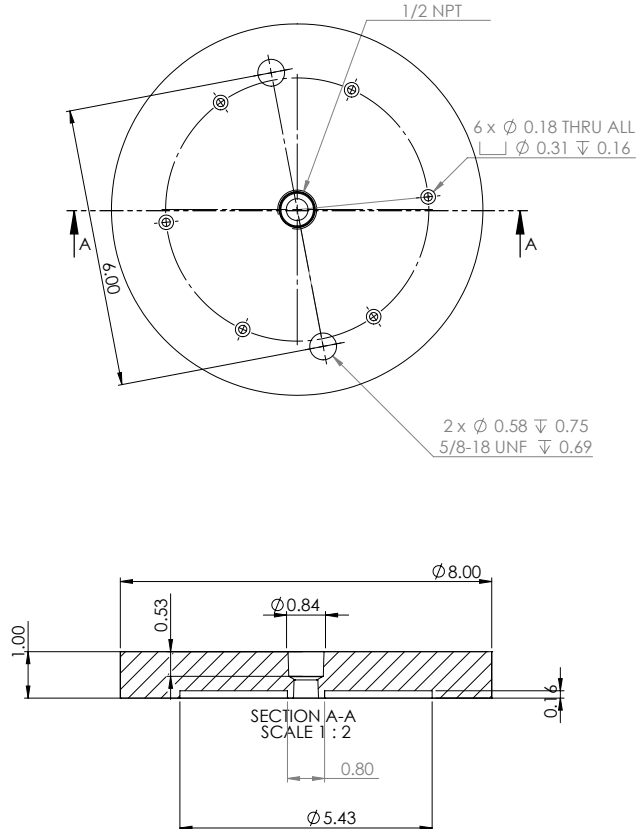

Figure C.1: Technical drawing of custom aluminum plate from Tabletop XCT facility.

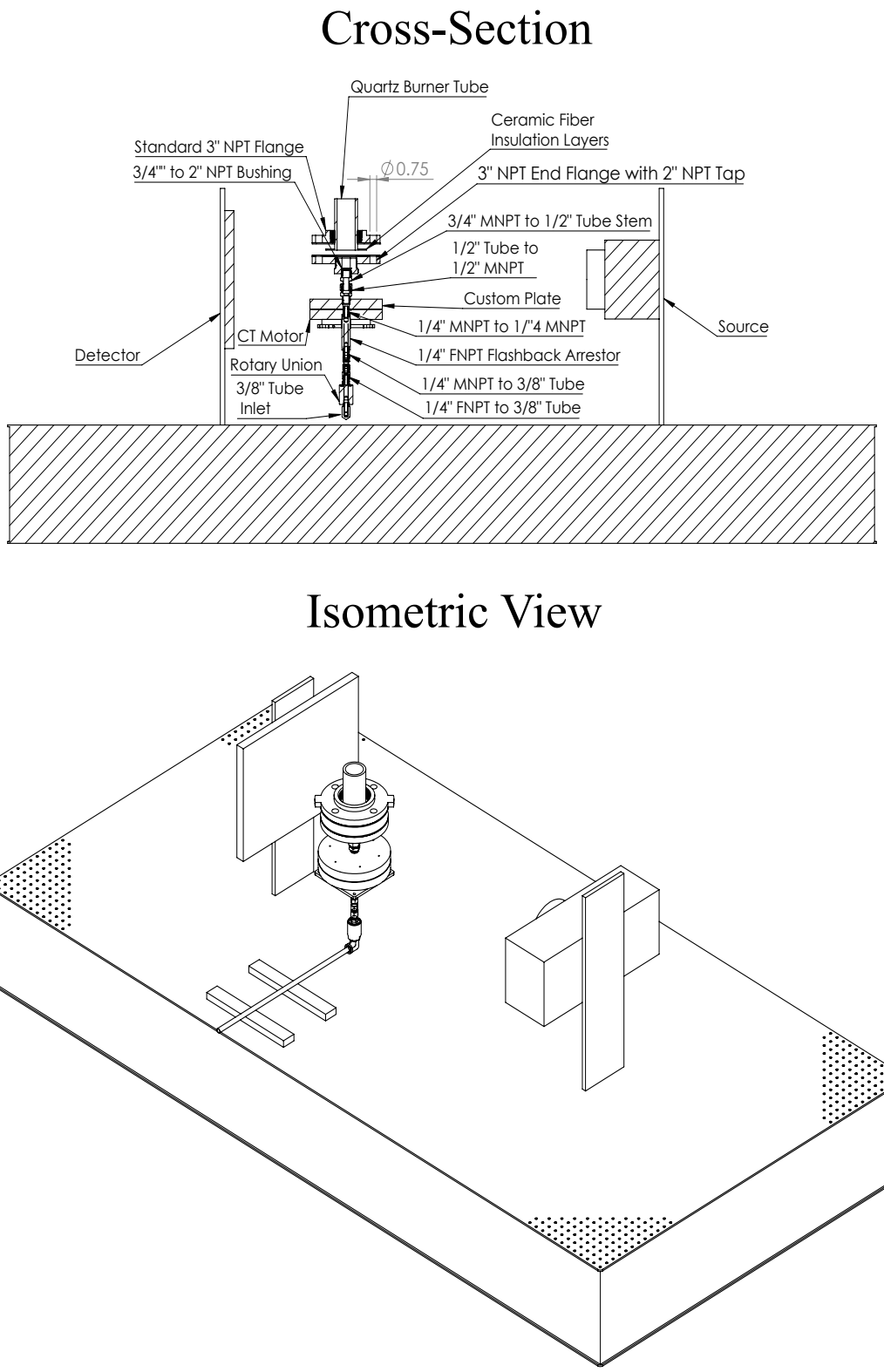

Figure C.2: Technical drawing of flow setup from Tabletop XCT facility.

Appendix D

Registration Algorithm

The following algorithm can be used to register scan b to scan a, which represents a crude greedy search. The implementation is efficient because it relies on a single slice of the 3 PPI section with random geometry to function as a unique registration stencil.

Algorithm 1 Rotation Registration Algorithm

procedure ROTREG($a, b, dtheta, rs$) ▷ Register one reconstruction to another
  $t \leftarrow$ imrotate($b(:,:,rs), dtheta$)
  $s \leftarrow a(:,:,rs)$
  if $||t-s||_2 < ||b-s||_2$ **then**
    $\alpha \leftarrow 1$
  else
    $\alpha \leftarrow -1$
  end if
  $t \leftarrow b(:,:,rs)$ ▷ Iteration on one slice in 3 ppi region to minimize expense
  $s \leftarrow a(:,:,rs)$
  $e \leftarrow \infty$
  $z \leftarrow 0$
  while $c < e$ **do** ▷ Keep rotating while error reduces
    $e \leftarrow c$
    $t \leftarrow$ imrotate($t, \alpha \times dtheta$)
    $c \leftarrow ||t-s||_2$
    $z \leftarrow z+1$
  end while
  return imrotate(b, $z \times \alpha \times dtheta$) ▷ Return rotated reconstruction
end procedure

Appendix E

Rotameter Equation Derivation

The following analysis derives the well-known rotameter correction equation from first principles, and results in an expression identical to that of, e.g., Wojtkowiak and Popiel (1996). Analysis of the rotameter system begins using an assumption that $M < 0.3$ such that the fluid is incompressible. Applying Bernoulli's equation gives:

$$\frac{v^2}{2g} + z + \frac{p}{\rho g} = C, \tag{E.0.1}$$

with C a constant. Applying this equation to the vertical streamline along the tube axis gives,

$$p_a - p_b = \rho g z_b - \rho g z_a + \frac{1}{2}\rho v_b^2 - \frac{1}{2}\rho v_a^2 \tag{E.0.2}$$

where a is directly below the float and b is the balanced point of the float. Invoking continuity such that the volumetric flow rate Q is constant ($Q = v_a A_a = v_b A_b$, with A_b being the annular area between the float and tube wall) gives,

$$\Delta p = \rho g h_f + \frac{1}{2}\rho \left(\frac{Q}{A_b}\right)^2 \left[1 - \left(\frac{A_b}{A_a}\right)^2\right] \tag{E.0.3}$$

with h_f the height of the float (i.e., the physical depth of the float not its height above the bottom of the tube, which is denoted as z). We can then assume that the pressure drop

mostly results from the float such that:

$$\begin{aligned}\Delta p &= \frac{\bar{W}_{Float}}{A_{Float}} + Friction \approx \frac{\bar{W}_{Float}}{A_{Float}}, \\ &= \frac{W_{Float} - B_{Float}}{A_{Float}}, \\ &= \frac{V_f(\rho_f - \rho)g}{A_f}, \end{aligned} \tag{E.0.4}$$

where V_f is the volume of the float, A_f is its cross sectional area, B_f is the buoyant force, and ρ_f is its density. Substituting this in for the pressure drop and solving for the volumetric flow rate gives,

$$Q(z) = \bar{A}_b \sqrt{\frac{2(\Delta p - \rho g h_f)}{\rho\left[1 - \left(\frac{\bar{A}_b}{A_a}\right)^2\right]}} = \bar{A}_b \sqrt{\frac{2g\left(\frac{V_f(\rho_f - \rho)}{A_f} - \rho h_f\right)}{\rho\left[1 - \left(\frac{\bar{A}_b}{A_a}\right)^2\right]}} \tag{E.0.5}$$

The above equation would be valid for inviscid flows. A discharge coefficient C, which depends on Reynolds number, is usually introduced to account for viscosity – in this case, we take C as constant given the low viscosities and similar Reynolds numbers involved. Further, for a given design, if the readout position of the flow is measured and the density is available, the volumetric flow rate can be computed as,

$$Q(z) = C\bar{A}_b(z) \sqrt{\frac{2g\left(\frac{V_f(\rho_f - \rho)}{A_f} - \rho h_f\right)}{\rho\left[1 - \left(\frac{\bar{A}_b(z)}{A_a(z)}\right)^2\right]}} \tag{E.0.6}$$

In the case of a gas-phase flow, the float density is much greater than the gas density, such that $\rho_f \gg \rho$. Further, assuming that $V_f\rho_f/A_f \gg \rho h_F$ (which is generally true, as $\rho_f \approx 1000\rho$ and $V_f/A_f \sim h_f$), we obtain:

$$Q(z) \approx C\bar{A}_b(z) \sqrt{\frac{2g\frac{V_f\rho_f}{A_f}}{\rho\left[1 - \left(\frac{\bar{A}_b(z)}{A_a(z)}\right)^2\right]}} \sim \sqrt{\frac{1}{\rho}} f(z) \tag{E.0.7}$$

Thus, if the density of the fluid were to change for any reason, for a given indicated height z , the indicated volumetric flow rate would change as well. Using the ideal gas law such that $\rho = PW/RT$ with W the molecular weight, we can write,

$$Q(z) \sim \sqrt{\frac{PW}{T}} f(z) \tag{E.0.8}$$

Therefore, to convert between measurements calibrated at a single condition at which the meter was calibrated (Q_{cal}) and those obtained at a different condition(Q_{new}), we obtain:

$$\begin{aligned} \frac{Q_{new}(z)}{Q_{cal}(z)} &= \sqrt{\frac{P_{new}}{P_{cal}} \frac{W_{new}}{W_{cal}} \frac{T_{cal}}{T_{new}}} \\ \therefore Q_{new}(z) &= Q_{cal}(z) \sqrt{\frac{P_{new}}{P_{cal}} \frac{W_{new}}{W_{cal}} \frac{T_{cal}}{T_{new}}} \end{aligned} \tag{E.0.9}$$

Bibliography

Agrawal, A. K., Butuk, N. K., Gollahalli, S. R., and Griffin, D. (1997). Three dimensional rainbow Schlieren tomography of a temperature field. *Applied Optics*, 37(3):479–485.

Al-Hamamre, Z., Voß, S., and Trimis, D. (2009). Hydrogen production by thermal partial oxidation of hydrocarbon fuels in porous media based reformer. *International Journal of Hydrogen Energy*, 34(2):827–832.

Andrews, G. and Bradley, D. (1972). Determination of burning velocities: A critical review. *Combustion and Flame*, 18(1):133–153.

Ansys, Inc. (2009). Fluent 12.0 theory guide.

Babkin, V., Korzhavin, A., and Bunev, V. (1991). Propagation of premixed gaseous explosion flames in porous media. *Combustion and Flame*, 87(2):182–190.

Baek, J. and Pelc, N. J. (2011). Local and global 3D noise power spectrum in cone-beam CT system with FDK reconstruction. *Medical Physics*, 38(4):2122–2131.

Barra, A. J., Diepvens, G., Ellzey, J. L., and Henneke, M. R. (2003). Numerical study of the effects of material properties on flame stabilization in a porous burner. *Combustion and Flame*, 134(4):369–379.

Barra, A. J. and Ellzey, J. L. (2004). Heat recirculation and heat transfer in porous burners. *Combustion and Flame*, 137(1):230–241.

Becker, H. A. and Yamakazi, S. (1978). Entrainment, momentum flux, and temperature in vertical free turbulent diffusion flames. *Combustion and Flame*, 33:123–149.

Bedoya, C., Dinkov, I., Habisreuther, P., Zarzalis, N., Bockhorn, H., and Parthasarathy, P. (2015). Experimental study, 1D volume-averaged calculations and 3D direct pore level simulations of the flame stabilization in porous inert media at elevated pressure. *Combustion and Flame*, 162(10):3740–3754.

Bennett, B. A. V., Fielding, J., Mauro, R. J., Long, M. B., and Smooke, M. D. (1999). A comparison of the structures of lean and rich axisymmetric laminar Bunsen flames: Application of local rectangular refinement solution-adaptive gridding. *Combustion Theory and Modelling*, 3(4):657–687.

Bennett, B. A. V. and Smooke, M. D. (1998). Local rectangular refinement with application to axisymmetric laminar flames. *Combustion Theory and Modelling*, 2(3):221–258.

Bennett, K. and Byer, R. L. (1984). Optical tomography: Experimental verification of noise theory. *Optics Letters*, 7:270–272.

Berger, M. J., Hubbell, J. H., Seltzer, S. M., Chang, J., Coursey, J. S., Sukumar, R., Zucker, D. S., and Olsen, K. (2010). XCOM: Photon cross section database (version 1.5). National Institute of Standards and Technology Online Database.

Birch, A. D., Brown, D. R., Dodson, M. G., and Thomas, J. R. (1978). The turbulent concentration field of a methane jet. *Journal of Fluid Mechanics*, 88(3):431–449.

Blevins, L. G., Renfro, M. W., Lyle, K. H., Laurendeau, N. M., and Gore, J. P. (1999). Experimental study of temperature and CH radical location in partially premixed CH_4/air coflow flames. *Combustion and Flame*, 118(4):684–696.

Boas, F. E. and Fleischmann, D. (2012). CT artifacts: Causes and reduction techniques. *Imaging in Medicine*, 4(2):229–240.

Böhm, B., Heeger, C., Boxx, I., Meier, W., and Dreizler, A. (2009). Time-resolved conditional flow field statistics in extinguishing turbulent opposed jet flames using simultaneous highspeed PIV/OH-PLIF. *Proceedings of the Combustion Institute*, 32(2):1647–1654.

Bouvet, N., Chauveau, C., Gökalp, I., Lee, S.-Y., and Santoro, R. (2011). Characterization of syngas laminar flames using the bunsen burner configuration. *International Journal of Hydrogen Energy*, 36(1):992–1005.

Bradley, D. and Matthews, K. (1968). Measurement of high gas temperatures with fine wire thermocouples. *Journal of Mechanical Engineering Science*, 10(4):299–305.

Brenner, G., Pickenäcker, K., Pickenäcker, O., Trimis, D., Wawrzinek, K., and Weber, T. (2000). Numerical and experimental investigation of matrix-stabilized methane/air combustion in porous inert media. *Combustion and Flame*, 123(1):201–213.

Britter, R. E. (1989). Atmospheric dispersion of dense gases. *Annual Review of Fluid Mechanics*, 21(1):317–344.

Burcat, A. (1984). Thermochemical data for combustion calculations. In *Combustion Chemistry*, pages 455–473. Springer.

Bushberg, J. T., Seibert, J. A., Leidholdt, E. M., and Boone, J. M. (2011). *The Essential Physics of Medical Imaging*. Lippincott, Williams, and Wilkins, 3rd edition.

Byer, R. L. and Shepp, L. A. (1979). Two-dimensional remote air-pollution monitoring via tomography. *Optics Letters*, 4(3):75–77.

Cai, W., Li, X., and Ma, L. (2013). Practical aspects of implementing three-dimensional tomography inversion for volumetric flame imaging. *Applied Optics*, 52(33):8106–8116.

Chae, E. J., Seo, J. B., Goo, H. W., Kim, N., Song, K.-S., Lee, S. D., Hong, S.-J., and Krauss, B. (2008). Xenon ventilation CT with a dual-energy technique of dual-source CT: Initial experience 1. *Radiology*, 248(2):615–624.

Chander, S. and Ray, A. (2008). An experimental and numerical study of stagnation point heat transfer for methane/air laminar flame impinging on a flat surface. *International Journal of Heat and Mass Transfer*, 51(13):3595–3607.

Chaouki, J., Larachi, F., and Dudukovic, M. P. (1997). Noninvasive tomographic and velocimetric monitoring of multiphase flows. *Industrial and Engineering Chemistry Research*, 36(11):4476–4503.

Chen, C. J. and Rodi, W. (1980). *Vertical Turbulent Buoyant Jets: A Review of Experimental Data*. Pergamon.

Chen, Z., Qin, X., Xu, B., Ju, Y., and Liu, F. (2007). Studies of radiation absorption on flame speed and flammability limit of CO_2 diluted methane flames at elevated pressures. *Proceedings of the Combustion Institute*, 31(2):2693–2700.

Coelho, P., Teerling, O., and Roekaerts, D. (2003). Spectral radiative effects and turbulence/radiation interaction in a non-luminous turbulent jet diffusion flame. *Combustion and Flame*, 133(1):75–91.

Coletti, F., Benson, M. J., Sagues, A. L., Miller, B. H., Fahrig, R., and Eaton, J. K. (2014). Three-dimensional mass fraction distribution of a spray measured by X-ray computed tomography. *Journal of Engineering for Gas Turbines and Power*, 136(5):051508.

Crow, S. C. and Champagne, F. H. (1971). Orderly structure in jet turbulence. *Journal of Fluid Mechanics*, 48(3):547–591.

Danielsson, P.-E. and Seger, O. (1990). Generalized and separable Sobel operators. *Machine Vision for Three-Dimensional Scenes*, pages 347–379.

Department of Energy (2017). Annual Energy Outlook. `https://www.eia.gov/outlooks/aeo/`. Last accessed 08-28-2017.

Dowling, D. R. and Dimotakis, P. E. (1990). Similarity of the concentration field of gas-phase turbulent jets. *Journal of Fluid Mechanics*, 218:109–141.

Duke, D. J., Finney, C. E., Kastengren, A., Matusik, K., Sovis, N., Santodonato, L., Bilheux, H., Schmidt, D., Powell, C., and Toops, T. (2017). High-resolution X-ray and neutron computed tomography of an engine combustion network Spray G gasoline injector. *SAE International Journal of Fuels and Lubricants*, 10(2):328–343.

Duke, D. J., Kastengren, A. L., Swantek, A. B., Matusik, K. E., and Powell, C. F. (2016). X-ray fluorescence measurements of dissolved gas and cavitation. *Experiments in Fluids*, 57(10):162.

Dunnmon, J. A., Sobhani, S., Kim, T. W., Kovscek, A., and Ihme, M. (2015). Characterization of scalar mixing in dense gaseous jets using X-ray computed tomography. *Experiments in Fluids*, 56(10):1–17.

Dunnmon, J. A., Sobhani, S., Wu, M., Fahrig, R., and Ihme, M. (2017a). An investigation of internal flame structure in porous media combustion via x-ray computed tomography. *Proceedings of the Combustion Institute*, 36(3):4399–4408.

Dunnmon, J. A., Wu, M., Xia, Y., Sobhani, S., Fahrig, R., and Ihme, M. (2017b). 3-D flame characterization via X-ray computed tomography. In Floryan, J., editor, *Proceedings of the 24th International Congress of Theoretical and Applied Mechanics, (Montreal, Canada, August 2016)*. IUTAM.

Eberhart, C., Lineberry, D., and Frederick, R. (2013). A mechanistic assessment of swirl injection and atomization by X-ray radiographic and optical techniques. In *48th AIAA/ASME/SAE/ASEE Joint Propulsion Conference & Exhibit*, page 3746.

Elsinga, G., Scarano, F., Wieneke, B., and van Oudheusden, B. (2006). Tomographic particle image velocimetry. *Experiments in Fluids*, 41(6):933–947.

Emmerman, P. J., Goulard, R., Santoro, R. J., and Semerjian, H. F. (1980). Multiangular absorption diagnostics of a turbulent argon-methane jet. *Energy*, 85(2):70–77.

Escudero, D. R. and Heindel, T. J. (2014). Acoustic fluidized bed hydrodynamics characerization using X-ray computed tomography. *Chemical Engineering Journal*, 243:411–420.

Fan, L. (1967). Turbulent buoyant jets into stratified or flowing ambient fluids. Technical Report KH-R-15.

Feldkamp, L., Davis, L., and Kress, J. (1984). Practical cone-beam algorithm. *Journal of the Optical Society of America A*, 1(6):612–619.

Feng, J., Okamoto, K., Tsuru, D., Madarame, H., and Fumizawa, M. (2002). Visualization of 3D gas density distribution using optical tomography. *Chemical Engineering Journal*, 86:479–485.

Floyd, J., Geipel, P., and Kempf, A. M. (2011). Computed tomography of chemiluminescence (CTC): Instantaneous 3D measurements and phantom studies of a turbulent opposed jet flame. *Combustion and Flame*, 158:376–391.

Frank, J. H., Shavorskiy, A., Bluhm, H., Coriton, B., Huang, E., and Osborn, D. L. (2014). In situ soft X-ray absorption spectroscopy of flames. *Applied Physics B*, 117(1):493–499.

Fuessel, A., Klemm, H., Boettge, D., Marschallek, F., Adler, J., and Michaelis, A. (2011). Advancement of cellular ceramics made of silicon carbide for burner applications. In *IOP Conference Series: Materials Science and Engineering*, volume 18, page 182001. IOP Publishing.

Glatz, G., Castanier, L. M., and Kovscek, A. R. (2016). Visualization and quantification of thermally induced porosity alteration of immature source rock using X-ray computed tomography. *Energy & Fuels*, 30(10):8141–8149.

Glawe, G. E., Simmons, F. S., and Stickney, T. M. (1956). Radiation and recovery corrections and time constants of several chromel-alumel thermocouple probes in high-temperature, high-velocity gas streams. Technical report, Lewis Flight Propulsion Lab., Cleveland.

Goodwin, D. and Moffat, H. (2006). Cantera. `http://sourceforge.net/projects/cantera`. Last accessed 6-17-2017.

Grass, M., Köhler, T., and Proksa, R. (2000). 3D cone-beam CT reconstruction for circular trajectories. *Physics in Medicine and Biology*, 45(2):329.

Grcar, J. F., Kee, R. J., Smooke, M. D., and Miller, J. A. (1988). A hybrid Newton/time-integration procedure for the solution of steady, laminar, one-dimensional, premixed flames. *Symposium (International) on Combustion*, 21(1):1773–1782.

Grosshandler, W. L. (1993). *RADCAL: A narrow-band model for radiation calculations in a combustion environment*. National Institute of Standards and Technology, Gaithersburg, MD.

Hall, R. J. (1993). The radiative source term for plane-parallel layers of reacting combustion gases. *Journal of Quantitative Spectroscopy and Radiative Transfer*, 49(5):517–523.

Halls, B. R., Heindel, T. J., Kastengren, A. L., and Meyer, T. R. (2014). Evaluation of X-ray sources for quantitative two-and three-dimensional imaging of liquid mass distribution in atomizing sprays. *International Journal of Multiphase Flow*, 59:113–120.

Hansen, N., Tranter, R. S., Moshammer, K., Randazzo, J. B., Lockhart, J. P., Fugazzi, P. G., Tao, T., and Kastengren, A. L. (2017). 2D-imaging of sampling-probe perturbations in laminar premixed flames using Kr X-ray fluorescence. *Combustion and Flame*, 181:214–224.

Hardesty, D. and Weinberg, F. (1973). Burners producing large excess enthalpies. *Combustion Science and Technology*, 8(5-6):201–214.

Hasçakir, B., Glatz, G., Castanier, L. M., and Kovscek, A. (2011). In-situ combustion dynamics visualized with X-ray computed tomography. *SPE Journal*, 16(03):524–536.

Hassel, E. P. and Linow, S. (2000). Laser diagnostics for studies of turbulent combustion. *Measurement Science and Technology*, 11(2):R37.

Heindel, T. J. (2011). A review of X-ray flow visualization with applications to multiphase flows. *Journal of Fluids Engineering*, 133(7):074001.

Heitor, M. and Moreira, A. (1993). Thermocouples and sample probes for combustion studies. *Progress in Energy and Combustion Science*, 19(3):259–278.

Herman, G. T. (1979). Correction for beam hardening in computed tomography. *Physics in Medicine and Biology*, 24(1):81.

Hiller, B. and Hanson, R. K. (1988). Simultaneous planar measurements of velocity and pressure fields in gas flows using laser-induced fluorescence. *Applied Optics*, 27(1):33–48.

Hsieh, J. (2009). *Computed Tomography*. John Wiley and Sons.

Hu, H. (1996). An improved cone-beam reconstruction algorithm for the circular orbit. *Scanning*, 18(8):572–581.

Huang, H. W. and Zhang, Y. (2008). Flame colour characterization in the visible and infrared spectrum using a digital camera and image processing. *Measurement Science and Technology*, 19(8):085406.

Huang, H. W. and Zhang, Y. (2011). Digital colour image processing based measurement of premixed CH_4^+ air and $C_2H_4^+$ air flame chemiluminescence. *Fuel*, 90(1):48–53.

ImPACT Group (2009). Comparative specifications–64-slice CT scanners. Technical Report CEP08027, National Health Service.

Jackson, D. F. and Hawkes, D. J. (1981). X-ray attenuation coefficients of elements and mixtures. *Physics Reports*, 70(3):169–233.

Jasper, A. W., Oana, C. M., and Miller, J. A. (2015). "Third-body" collision efficiencies for combustion modeling: Hydrocarbons in atomic and diatomic baths. *Proceedings of the Combustion Institute*, 35(1):197–204.

Jirka, G. H. (2004). Integral model for turbulent buoyant jets in unbounded stratified flows. Part I: Single round jet. *Environmental Fluid Mechanics*, 4(1):1–56.

Kastengren, A. and Powell, C. F. (2014). Synchrotron X-ray techniques for fluid dynamics. *Experiments in Fluids*, 55(3):1686.

Kastengren, A., Powell, C. F., Arms, D., Dufresne, E. M., Gibson, H., and Wang, J. (2012). The 7BM beamline at the APS: A facility for time-resolved fluid dynamics measurements. *Journal of Synchrotron Radiation*, 19(4):654–657.

Kastengren, A., Powell, C. F., Dufresne, E. M., and Walko, D. A. (2011). Application of X-ray fluorescence to turbulent mixing. *Journal of Synchrotron Radiation*, 18(5):811–815.

Keramiotis, C., Stelzner, B., Trimis, D., and Founti, M. (2012). Porous burners for low emission combustion: An experimental investigation. *Energy*, 45(1):213–219.

Khanna, V., Goel, R., and Ellzey, J. (1994). Measurements of emissions and radiation for methane combustion within a porous medium burner. *Combustion Science and Technology*, 99(1-3):133–142.

Kiefer, J., Weikl, M., Seeger, T., Von Issendorff, F., Beyrau, F., and Leipertz, A. (2009). Non-intrusive gas-phase temperature measurements inside a porous burner using dual-pump CARS. *Proceedings of the Combustion Institute*, 32(2):3123–3129.

Kleijn, C. R. (2001). Heat transfer from laminar impinging methane/air flames. *Proceedings of 2001 ASME-PVP Conference*, 424:259–270.

Kline, S. (1985). The purposes of uncertainty analysis. *Journal of Fluids Engineering*, 107(2):153–160.

Kohse-Höinghaus, K., Barlow, R. S., Aldén, M., and Wolfrum, J. (2005). Combustion at the focus: Laser diagnostics and control. *Proceedings of the Combustion Institute*, 30(1):89–123.

Kojima, J., Ikeda, Y., and Nakajima, T. (2005). Basic aspects of OH (A), CH (A), and C_2 (d) chemiluminescence in the reaction zone of laminar methane–air premixed flames. *Combustion and Flame*, 140(1):34–45.

Lavinskaya, E. A., Martemianov, S., Saulnier, J. B., and Fomin, N. A. (2006). Limited-projection laser tomography of combined gasdynamic flows. *Journal of Engineering and Thermophysics*, 44(31):979–989.

Law, C. (1989). Dynamics of stretched flames. *Symposium (International) on Combustion*, 22(1):1381–1402.

Law, C., Ishizuka, S., and Cho, P. (1982). On the opening of premixed Bunsen flame tips. *Combustion Science and Technology*, 28(3-4):89–96.

Law, C. K. (2010). *Combustion Physics*. Cambridge University Press.

Lee, D., Thakur, S., Wright, J., Ihme, M., and Shyy, W. (2011). Characterization of flow field structure and species composition in a shear coaxial rocket GH_2/GO_2 injector:

modeling of wall heat losses. *Proceedings of the 47th AIAA/ASME/SAE/ASEE Joint Propulsion Conference & Exhibit*, 6125:2011:1–14.

Lesnichii, V., Petrov, N., and Cheremkhin, P. (2013). A technique of measuring spectral characteristics of detector arrays in amateur and professional photocameras and their application for problems of digital holography. *Optics and Spectroscopy*, 115(4):557–566.

Li, X. and Ma, L. (2014). Three-dimensional measurements of turbulent jet flames at kHz rate based on tomographic chemiluminescence. *Proceedings of the 52nd AIAA Aerospace Conference SciTech Forum*, pages 2014–0735:1–8.

Linne, M. (2013). Imaging in the optically dense regions of a spray: A review of developing techniques. *Progress in Energy and Combustion Science*, 39(5):403–440.

Liu, J. F. and Hsieh, W. H. (2004). Experimental investigation of combustion in porous heating burners. *Combustion and Flame*, 138(3):295–303.

Macovski, A. (1983). *Medical Imaging Systems*. Prentice Hall.

MacPhee, A. G., Tate, M. W., Powell, C. F., Yue, Y., Renzi, M. J., Ercan, A., Narayanan, S., Fontes, E., Walther, J., Schaller, J., Gruner, S. M., and Wang, J. (2002). X-ray imaging of shock waves generated by high-pressure fuel sprays. *Science*, 295(5558):1261–1263.

Mayo, S., Josh, M., Nesterets, Y., Esteban, L., Pervukhina, M., Clennell, M. B., Maksimenko, A., and Hall, C. (2015). Quantitative micro-porosity characterization using synchrotron micro-CT and xenon K-edge subtraction in sandstones, carbonates, shales and coal. *Fuel*, 154:167–173.

McGee, H. A. (1991). *Molecular Engineering*. McGraw-Hill.

Meier, G. E. A. (2002). Computerized background-oriented Schlieren. *Experiments in Fluids*, 33:181–187.

Meyer, T. R., Brear, M., Jin, S. H., and Gord, J. R. (2010). Formation and diagnostics of sprays in combustion. *Handbook of Combustion*.

Mi, J., Nobes, D. S., and Nathan, G. J. (2001). Influence of jet exit conditions on the passive scalar field of an axisymmetric free jet. *Journal of Fluid Mechanics*, 432:91–125.

Moffat, R. et al. (1982). Contributions to the theory of single-sample uncertainty analysis. *ASME, Transactions, Journal of Fluids Engineering*, 104(2):250–58.

Moffat, R. J. (1985). Using uncertainty analysis in the planning of an experiment. *Journal of Fluids Engineering*, 107(2):173–178.

Moffat, R. J. (1988). Describing the uncertainties in experimental results. *Experimental Thermal and Fluid Science*, 1(1):3–17.

Mohamad, E. J., Rahim, R. A., Ibrahim, S., Sulaiman, S., and Manaf, M. S. (2006). Flame imaging using laser-based transmission tomography. *Sensors and Actuators A*, 127(2):332–339.

Mujeebu, M. A., Abdullah, M. Z., Bakar, M. A., Mohamad, A., Muhad, R., and Abdullah, M. (2009). Combustion in porous media and its applications—a comprehensive survey. *Journal of Environmental Management*, 90(8):2287–2312.

Mungal, M., Lourenco, L., and Krothapalli, A. (1995). Instantaneous velocity measurements in laminar and turbulent premixed flames using on-line PIV. *Combustion Science and Technology*, 106(4-6):239–265.

Nagarajappa, A. K., Dwivedi, N., and Tiwari, R. (2015). Artifacts: The downturn of CBCT image. *Journal of International Society of Preventive and Community Dentistry*, 5(6):440.

Nagata, R., Appoloni, C. R., and Fernandes, J. S. (2009). Determination of SiC ceramic foams microstructure properties by X-rays microtomography. In *Proceedings of the 2009 International Nuclear Atlantic Conference*, pages 1–8.

Noordally, E., Przybylski, J., and Witton, J. (2004). Porous media combustors for clean gas turbine engines. Technical report, Cranfield University.

Panchapakesan, N. R. and Lumley, J. L. (1993). Turbulence measurements in axisymmetric jets of air and helium. *Journal of Fluid Mechanics*, 246:225–247.

Papakonstantis, I. G., Christodoulou, G. C., and Papanicolaou, P. N. (2011). Inclined negatively buoyant jets 2: Concentration measurements. *Journal of Hydraulic Research*, 49(1):13–22.

Peña, G. D. G., Alrefaai, M. M., Yang, S. Y., Raj, A., Brito, J. L., Stephen, S., Anjana, T., Pillai, V., Al Shoaibi, A., and Chung, S. H. (2016). Effects of methyl group on aromatic hydrocarbons on the nanostructures and oxidative reactivity of combustion-generated soot. *Combustion and Flame*, 172:1–12.

Petersen, E., Kopp, M., Donato, N., and Güthe, F. (2012). Assessment of current chemiluminescence kinetics models at engine conditions. *Journal of Engineering for Gas Turbines and Power*, 134(5):051501.

Pitts, W. M. (1991). Effects of global density ratio on the centerline mixing behavior of axisymmetric turbulent jets. *Experiments in Fluids*, 11(2):125–134.

Poinsot, T., Echekki, T., and Mungal, M. (1992). A study of the laminar flame tip and implications for premixed turbulent combustion. *Combustion Science and Technology*, 81(1-3):45–73.

Poludniowski, G., Landry, G., DeBlois, F., Evans, P. M., and Verhaegen, F. (2009). SpekCalc: A program to calculate photon spectra from tungsten anode X-ray tubes. *Physics in Medicine and Biology*, 54(19):N433–N438.

Pope, S. B. (2000). *Turbulent Flows*. Cambridge University Press.

Prell, D., Kyriakou, Y., and Kalender, W. A. (2009). Comparison of ring artifact correction methods for flat-detector CT. *Physics in Medicine and Biology*, 54(12):247–253.

Prince, J. L. and Links, J. M. (2006). *Medical Imaging Signals and Systems*. Prentice Hall.

Richards, C. D. and Pitts, W. M. (1993). Global density effects on the self-preservation behavior of turbulent free jets. *Journal of Fluid Mechanics*, 254:417–435.

Sandia National Laboratory (2003). International Workshop on Measurement and Computation of Turbulent Premixed Flames. `http://www.sandia.gov/TNF/radiation.html`. Last accessed 08-29-2017.

Santoro, R. J. and Semerjian, H. G. (1981). Optical tomography for flow field diagnostics. *International Journal of Heat and Mass Transfer*, 24(7):1139–1150.

Schumaker, S., Danczyk, S., Lightfoot, M., and Kastengren, A. (2014). Interpretation of core length in shear coaxial rocket injectors from X-ray radiography measurements. In *50th AIAA/ASME/SAE/ASEE Joint Propulsion Conference*, page 3790.

Schumaker, S., Kastengren, A., Lightfoot, M., and Danczyk, S. (2012). A study of gas-centered swirl coaxial injectors using X-ray radiography. Technical report, DTIC Document.

Schumaker, S., Kastengren, A. L., Danczyk, S., and Lightfoot, M. (2015). X-ray fluorescence measurements of turbulent methane-oxygen shear coaxial flames. Technical report, DTIC Document.

See, Y. C. and Ihme, M. (2014). Effects of finite-rate chemistry and detailed transport on the instability of jet diffusion flames. *Journal of Fluid Mechanics*, 745:647–681.

Shimura, M., Ueda, T., Choi, G.-M., Tanahashi, M., and Miyauchi, T. (2011). Simultaneous dual-plane CH PLIF, single-plane OH PLIF and dual-plane stereoscopic piv measurements in methane-air turbulent premixed flames. *Proceedings of the Combustion Institute*, 33(1):775–782.

Sick, V. and Stojkovic, B. (2001). Attenuation effects on imaging diagnostics of hollow-cone sprays. *Applied Optics*, 40(15):2435–2442.

Sijbers, J. and Postnov, A. (2004). Reduction of ring artifacts in high resolution micro-CT reconstructions. *Physics in Medicine and Biology*, 49(14):3881–3895.

Simon, B. A. (2005). Regional ventilation and lung mechanics using X-ray CT. *Academic Radiology*, 12:1414–1422.

Smith, B. D. (1985). Image reconstruction from cone-beam projections: Necessary and sufficient conditions and reconstruction methods. *IEEE Transactions on Medical Imaging*, 4(1):14–25.

Smucker, M. T. and Ellzey, J. L. (2004). Computational and experimental study of a two-section porous burner. *Combustion Science and Technology*, 176(8):1171–1189.

Snyder, R. and Hesselink, L. (1988). Measurement of mixing fluid flows with optical tomography. *Optics Letters*, 13(2):87–89.

Som, S. and Aggarwal, S. K. (2010). Effects of primary breakup modeling on spray and combustion characteristics of compression ignition engines. *Combustion and Flame*, 157(6):1179–1193.

Stelzner, B., Keramiotis, C., Voss, S., Founti, M., and Trimis, D. (2015). Analysis of the flame structure for lean methane–air combustion in porous inert media by resolving the hydroxyl radical. *Proceedings of the Combustion Institute*, 35(3):3381–3388.

Stuck, B. W. (1977). A new proposal for estimating the spatial concentration of certain types of air pollutants. *Journal of the Optical Society of America*, 67(5):668–678.

Su, L. K., Helmer, D. B., and Brownell, C. J. (2010). Quantitative planar imaging of turbulent buoyant jet mixing. *Journal of Fluid Mechanics*, 643:59–95.

Sun, C., Sung, C., He, L., and Law, C. (1999). Dynamics of weakly stretched flames: Quantitative description and extraction of global flame parameters. *Combustion and Flame*, 118(1):108–128.

Swantek, A. B., Duke, D., Kastengren, A., Sovis, N., Powell, C., Bartolucci, L., Scarcelli, R., and Waller, T. (2017). An experimental investigation of gas fuel injection with x-ray radiography. *Experimental Thermal and Fluid Science*, 87:15–29.

Thieme, S. F., Högl, S., and Johnson, T. R. (2011). Lung ventilation. In *Dual Energy CT in Clinical Practice*, pages 91–99. Springer.

Thompson, A. and Vaughan, D. (2005). *X-Ray Data Booklet*. Lawrence Berkeley National Laboratory.

Tranter, R. S., Kastengren, A. L., Porterfield, J. P., Randazzo, J. B., Lockhart, J. P., Baraban, J. H., and Ellison, G. B. (2017). Measuring flow profiles in heated miniature reactors with X-ray fluorescence spectroscopy. *Proceedings of the Combustion Institute*, 36(3):4603–4610.

Trimis, D. and Durst, F. (1996). Combustion in a porous medium-advances and applications. *Combustion Science and Technology*, 121(1-6):153–168.

Tuy, H. K. (1983). An inversion formula for cone-beam reconstruction. *SIAM Journal on Applied Mathematics*, 43(3):546–552.

Vega, B., Dutta, A., and Kovscek, A. R. (2014). CT imaging of low-permeability, dual-porosity systems using high X-ray contrast gas. *Transport in Porous Media*, 101(1):81–97.

Viskanta, R. and Gore, J. (2000). Overview of cellular ceramics based porous radiant burners for supporting combustion. *International Journal on Environmental Combustion Technology*, 1:167–203.

Voss, S., Mendes, M., Pereira, J., Ray, S., Pereira, J., and Trimis, D. (2013). Investigation on the thermal flame thickness for lean premixed combustion of low calorific H_2/CO mixtures within porous inert media. *Proceedings of the Combustion Institute*, 34(2):3335–3342.

Wang, Z. and Andreopoulos, Y. (2010). Density and compressibility effects in turbulent subsonic jets part 1: Mean velocity field. *Experiments in Fluids*, 48:327–343.

Watt, D. W. and Vest, C. M. (1990). Turbulent flow visualization by interferometric integral imaging and computed tomography. *Experiments in Fluids*, 8:301–311.

Wildenschild, D. and Sheppard, A. P. (2013). X-ray imaging and analysis techniques for quantifying pore-scale structure and processes in subsurface porous medium systems. *Advances in Water Resources*, 51:217–246.

Willis, N. P. and Bresler, Y. (1990). Tomographic imaging of time-varying distributions. *Proceedings of SPIE Biomedical Image Processing*, 1245:111–123.

Wojtkowiak, J. and Popiel, C. O. (1996). Visocity correction factor for rotameter. *Transactions of the ASME Journal of Fluids Engineering*, 118:569–573.

Wood, S. and Harris, A. T. (2008). Porous burners for lean-burn applications. *Progress in Energy and Combustion Science*, 34(5):667–684.

Wright, P., Garcia-Stewart, C. A., Carey, S. J., Hindle, F. P., Pegrum, S., Colbourne, S. M., Turner, P. J., Hurr, W. J., Litt, T. K., Murray, S. C., Crossley, S. D., Ozanyan, K. B., and McCann, H. (2006). Towards in-cylinder absorption tomography in a production engine. *Applied Optics*, 44(31):6578–6592.

Wu, M., Keil, A., Cherry, E., Yao, Y., Maier, A., and Fahrig, R. (2016). *CTSim Users' Guide (Version 1.0)*. Stanford University. To be published; documentation available upon request.

Xu, W., Wickersham, A., Wu, Y., He, F., and Ma, L. (2015). 3D flame topography obtained by tomographic chemiluminescence with direct comparison to planar Mie scattering measurements. *Applied Optics*, 54(9):2174–2182.

Xue, L., Suzuki, H., Ohtake, Y., Fujimoto, H., Abe, M., Sato, O., and Takatsuji, T. (2015). Numerical analysis of the Feldkamp–Davis–Kress effect on industrial X-ray computed tomography for dimensional metrology. *Journal of Computing and Information Science in Engineering*, 15(2):021008.

Yip, B. and Long, M. B. (1986). Instantaneous planar measurements of the complete three-dimensional scalar gradient in a turbulent jet. *Optics Letters*, 11(2):64–66.

Zhu, L., Starman, J., and Fahrig, R. (2008). An efficient estimation method for reducing the axial intensity drop in circular cone-beam CT. *International Journal of Biomedical Imaging*, 2008.